N° d'ordre : 40998

Thèse

Présentée à

L'UNIVERSITÉ
DES SCIENCES ET TECHNOLOGIES DE LILLE
Ecole Doctorale des Sciences de la Matière, du Rayonnement et de l'Environnement
UFR de PHYSIQUE

Pour obtenir le grade de

DOCTEUR
Discipline : Sciences des Matériaux

par

Jean-Baptiste PIOCHAUD

MODELLING OF RADIATION INDUCED SEGREGATION IN AUSTENITIC FE ALLOYS AT THE ATOMISTIC LEVEL

Soutenue le 09 janvier 2013 devant la commission d'examen :

S. KENNY	Rapporteur
M F. BARTHE	Rapporteur
F. RIBEIRO	Examinateur
M. NASTAR	Examinateur
C. DOMAIN	Co-encadrant
C.S. BECQUART	Directrice de thèse

MODELISATION A L'ECHELLE ATOMIQUE DE LA SEGREGATION INDUITE PAR L'IRRADIATION DANS LES ALLIAGES AUSTENITIQUES

Dans les réacteurs à eau pressurisée, les internes de cuve sont soumis à d'intenses irradiations induisant le mécanisme de corrosion sous contrainte assistée par l'irradiation qui est initié par le phénomène de ségrégation induite par l'irradiation (SII). La SII observée dans les aciers austénitiques 316 est modélisée à l'échelle atomique en considérant un alliage ternaire modèle Fe–10Ni–20Cr. Pour atteindre cet objectif, nous avons construit un modèle d'interactions de paires pour le système Fe-Ni-Cr afin de simuler la SII à l'échelle atomique en utilisant une approche Monte Carlo cinétique (MCC). Le modèle d'interactions de paires fut déduit à la fois des calculs DFT (Density Functional Theory), disponibles dans les systèmes purs de maille cubiques à faces centrées, mais aussi en effectuant des calculs DFT dans l'alliage Fe-10Ni-20Cr. Les énergies de formation calculées dans cet alliage modèle dépendent fortement de l'environnement local des défauts ponctuels. Nous avons pu ainsi établir une relation liant ces énergies au nombre et à la position des atomes de Ni et de Cr se trouvant à proximité des défauts ponctuels.

Le modèle de pair ainsi obtenu est en bon accord avec les données DFT et avec les coefficients de diffusion expérimentaux calculés à de hautes températures. Dans cette étude, nous montrons cependant qu'un modèle d'interactions de paires uniquement basé sur les interactions entre éléments positionnés sur les sites du réseau (éléments d'alliage et lacune) est incapable de reproduire toutes les données. Une estimation plus précise des barrières de migration est requise pour les espèces migrantes que celle proposée, qui ne prend pas en compte l'environnement du point col. Ce travail montre ainsi qu'il est nécessaire de réaliser des calculs DFT des énergies de migration.

Notre modèle de paires fut utilisé pour simuler la ségrégation thermique hors équilibre (STHE) et la SII en effectuant des simulations de MCC. Dans ce but, un joint de grain (JG) fut modélisé en introduisant de nouvelles interactions pour certains sites du réseau, définis comme étant les sites JG, et ajustées pour reproduire les résultats expérimentaux de STHE. Afin de modéliser la SII, les interactions de paires de tous les interstitiels possibles furent ajustées pour reproduire les calculs DFT obtenus dans l'alliage modèle Fe–10Ni–20Cr sans cependant pouvoir reproduire les résultats expérimentaux de SII. Un accord fut toutefois obtenus lorsque aucune interaction préférentielle n'est prise en compte pour les interstitiels et en favorisant le transport des atomes de Ni par rapport à celui des atomes de Fe et de Cr.

MODELLING OF RADIATION INDUCED SEGREGATION IN AUSTENITIC FE ALLOYS AT THE ATOMISTIC LEVEL

In pressurized water reactors, under irradiation internal structures are subject of irradiation assisted stress corrosion cracking which is influenced by radiation induced segregation (RIS). In this work RIS of 316 stainless steels is modelled considering a model ternary Fe–10Ni–20Cr alloy. For this purpose we have built an Fe-Ni-Cr pair interaction model (PIM) to simulate RIS at the atomistic level using an atomistic kinetic Monte Carlo (AKMC) approach. The pair interactions have been deduced from density functional theory (DFT) data available in the pure fcc systems but also from DFT calculations we have performed in the Fe–10Ni–20Cr target alloy. Point defect formation energies were calculated and found to depend strongly on the local environment of the defect. As a consequence, a rather good estimation of these energies can be obtained from the knowledge of the number and respective positions of the Ni and Cr atoms in the vicinity of point defects.

We were able to build a PIM in reasonable agreement with DFT data and with high temperature diffusion experiments, however, this work shows that a model based only on interaction parameters between elements positioned in perfect lattice sites (solute atoms and vacancy) cannot reproduce all the data. A more accurate estimation of the barriers encountered by the diffusing species is required which has to depend on the saddle point environment. This study therefore shows the need to estimate point defect migration energies using the DFT approach.

Our PIM was used to simulate thermal non equilibrium segregation (TNES) and RIS using AKMC. To this end, the grain boundary (GB) was modelled by assigning additional interactions to sites referred to as GB sites which was set to reproduce TNES experiments. In order to model RIS, pair interaction for all the possible ⟨100⟩ dumbbells was set to reproduce the DFT trends found in our Fe-10Ni-20Cr model alloy without being able to reproduce RIS experiments. Agreement was however obtained when considering no preferential interaction for the dumbbells and a preferential transport for Ni atoms compared to Cr and Fe atoms.

Remerciements

Bien entendu en premier lieu, je tiens à remercier infinirêt Mademoiselle Charlotte Becquart, ma directrice de thèse, et Monsieur Christophe Domain, mon co-encadrant à EDF. Ces trois années passées avec eux m'ont permis de constater leurs innombrables qualités professionnelles et humaines. Je les remercie pour tous ces précieux conseils qu'ils m'ont prodigué et qui m'ont permis de m'améliorer tout au long de ma thèse. Leur complémentarité, leur exemplarité ainsi que leur volontarisme en font pour moi des modèles que j'aimerais suivre à l'avenir.

Ce travail est le fruit d'une collaboration entre plusieurs groupes de recherche dans lesquels j'ai toujours été accueilli chaleureusement. Je tiens ainsi à remercier tous ceux qui ont contribué à l'ambiance privilégiée dont j'ai bénéficié durant ma thèse :

Lors la première année de ma thèse, j'ai été accueilli au sein du Groupe Métallurgie du Département des Matériaux et Mécanique des Composants (MMC) d'EDF R&D. Je tiens tout d'abord à remercier le directeur du département de recherche en fonction à cette époque, Monsieur Jean-Paul Massoud, un homme remarquable qui a tout fait pour faciliter mon intégration dans le groupe. Je tiens également à remercier tous mes collègues doctorants, Raoul Ngayam Happy, Davide Costa et Karim Sebbari, pour les liens d'amitié que nous avons tissés durant cette année aux renardières. Enfin je voudrais remercier Gilles Adjanor pour sa collaboration et pour tous ces moments d'amitié que nous avons partagés ensemble.

Concernant le laboratoire universitaire de Lille 1 où j'ai passé les deux années suivantes de ma thèse, j'ai été accueilli au sein du Laboratoire UMET dirigé par Alexandre Legris que je remercie pour sa bienveillance et son soutien. Je remercie tout le laboratoire et en particulier, Floriane Leaux, Andrée de Backer et Hélène Bultel, qui m'ont accueilli très chaleureusement et avec qui j'ai passé des moments privilégiés durant ces deux années. Une mention spéciale pour ladite « youyou » que je compte à présent parmi mes plus précieux amis.

Enfin, ce travail de thèse a été financé par le projet européen PERFORM 60. J'adresse mes remerciements sincères en particulier à Monsieur Abderrahim Al Mazouzi pour sa gentillesse et son intelligence de travail.

Je remercie sincèrement les membres de mon jury de thèse Steven Kenny, Marie-France Barthe, Maylise Nastar et Fabienne Ribeiro pour leur gentillesse ainsi que pour l'intérêt qu'ils ont porté à mon travail. Un merci particulier à Madame Maylise Nastar pour les nombreuses discutions très enrichissantes que nous avons eu ensemble.

Je termine en remerciant ma famille et mes proches qui ont aussi été très importants pour moi pendant ces années. Je pense tout d'abord à ma famille qui a toujours été présente, et en particulier à mon père et mes grands-parents qui ont consenti à de nombreux sacrifices à une période charnière de ma vie. Je pense également à mes très proches amis, Chris, Ben, Mot, Christian, Sarah, les Juju, Nico et Guillaume, sur qui j'ai toujours pu compter en toutes circonstances. Enfin, je ne saurai exprimer ma gratitude et mon amour pour ma compagne Émilie. Je la remercie pour son soutien indéfectible et pour tous les moments formidables que j'ai passé et que je passerai avec elle. Émilie, je te dédie ce manuscrit de thèse.

À Émilie

List of acronyms

1nn: first nearest neighbours

AFM: Anti-FerroMagnetic

AFM1: Anti-FerroMagnetic simple layer

AFMD: Anti-FerroMagnetic Double layer

AKMC: Atomic Kinetic Monte Carlo

ASS: Austenitic Stainless Steels

bcc: body-centered cubic

CC: Correlation Coefficient

CL: Cubic Lattice

CPA: Coherent Potential Approximation

DFT: Density Functional Theory

dpa: displacement per atom

EAM: Embedded Atom Method

fcc: face-centered cubic

fct: face-centered tetragonal

FISE: Final Initial System Energy

FM: FerroMagnetic

FR: Fully Relaxed

GB: Grain Boundary

GGA: Generalized Gradient Approximation

HF: Hartree and Fock

HK: Hohenberg and Kohn

IASCC: Irradiation Assisted Stress corrosion cracking

KS: Kohn and Sham

LDA: Local Density Approximation

LR: Linear Regressions

LSDA: Local Spin Density Approximation

MC: Monte Carlo

MD: Molecular Dynamics

MIK: Modified Inverse Kirkendall

MMC: Metropolis Monte Carlo

PIM: Pair Interaction Model

PM: ParaMagnetic

PWR: Pressurized Water Reactor

RIS: Radiation Induced Segregation

SIA: Self Interstitial Atoms

SP: Saddle Point

SG: Spin Glass

SQS: Special Quasirandom Structures

SS: Stainless Steels

TIP: Thermodynamics of Irreversible processes

TNES: Thermal Non Equilibrium Segregation

VASP: Vienna Ab initio Simulation Package

Table of contents

Introduction

I   General context of this work

In France, electric power is mainly produced by nuclear reactors. The French nuclear park contains 58 pressurized water reactors (PWR), which have an average age of over 30 years. In the issue about the extension of the lifetime of the nuclear centrals over 60 years, it is important to understand well the evolution of material properties under irradiation. In particular, maintaining good overall mechanical properties is of critical importance for structural components as they impact on the safety of the reactor but also for the cost of maintenance. The reactor is composed of a reactor pressure vessel enclosing the core internals supporting the fuel assemblies containing fissile materials (Fig. 1). In service, at a temperature close to 350°C, internal structures are exposed to harsh conditions: intense neutron irradiation up to 120 dpa[1] (displacement per atom) after 60 years of operation, mechanical and thermal stresses and aggressive corrosive environment. This combination of factors allows, among other effects, the occurrence of radiation induced creep and swelling, thus deeply changing the properties of components significantly irradiated. Moreover, in-service inspections showed in some cases that irradiation increases the formation of cracks in PWR components located inside the vessel (bolts, baffle, etc.). This was attributed to irradiation assisted stress corrosion cracking (IASCC). Stress corrosion cracking which happens when external conditions combine mechanical strains and corrosion is therefore enhanced by irradiation to become a very aggressive phenomenon. These effects, which are prevalent phenomena in irradiated materials, all limit the life time of the in-core components and need to be understood. In this work we focus on the austenitic stainless steels (ASS) which are used in the nuclear industry.

---

[1] The dpa is a standard measure of the damage. It does not measure the amount of residual lattice defects actually created in a material, but rather the "damage energy" deposited in the material by the irradiating particles. This damage energy is evaluated in terms of how many atoms could possibly be permanently displaced from their lattice sites to stable interstitial sites. The Norgett–Robinson–Torrens (NRT) dpa is the damage measure used for engineering applications as recommended by the ASTM [ASTM1993]. In this model, the accumulated displacement per atom (dpa) is given by $0.8E_{MD}/2E_D$, where E_{MD} is the damage energy, i.e. the fraction of the energy of the particle transmitted to the primary knock-on atom (or PKA, i.e. an atom which is displaced from its lattice site by irradiation) as kinetic energy and E_D is the displacement threshold energy (e.g. 40 eV for Fe [ASTM1994]).

1   Introduction
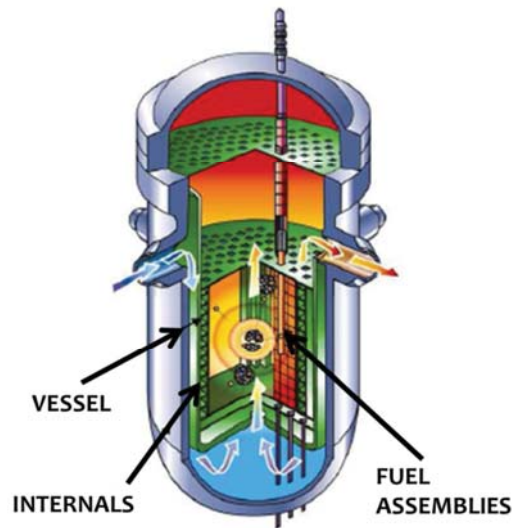
Fig. 1: General view of a pressurized water reactor.

I-1 Radiation induced degradations of austenitic stainless steels

In order to obtain insights on these radiation-induced degradations in ASS, one must first understand what kind of impact irradiation induces at lower scales. Without external solicitations, the only point defects existing in the materials are vacancies, the concentration of which can be determined by their Boltzmann exponential dependence on temperature, as $\exp\left(-E_f^V/k_BT\right)$, where E_f^V is the vacancy formation energy. In irradiated materials, the transfer of energy from an incident projectile to the solid results in the ejections of some atoms from their equilibrium position, giving rise to Frenkel pairs, i.e. creation of an equal number of vacancies and atoms positioned in interstitial positions. In many ferritic or austenitic metals, the most stable configuration of the self-interstitial atom (SIA) is a dumbbell configuration which corresponds to atom pairs sharing the same atomic site. These point defects are created in overconcentration and interact with each other as well as solute atoms, thus leading to the modification of the microstructure. Indeed, the point defects created flow into the material and can rearrange themselves to form a wide variety of defects. The interaction between radiation-induced point defects and solute atoms leads to solute atoms and point defect fluxes which drive the microstructure evolution with time. The type of irradiation particle is known to have a strong influence on the type of damage caused into the materials. Indeed, light ions such as electrons and light protons will produce usually Frenkel pairs distributed relatively homogeneously in the

2 Introduction

materials whereas heavy ions and neutrons will lead to the formation of many defects in localized regions because of displacement cascades[2]. For all these particle types, radiation doses accumulated by the materials are usually estimated in dpa using the Norgett–Robinson–Torrens (NRT) model [NORGETT1975].

Components located inside the vessel are exposed to high neutron irradiations whose effects on structural materials were difficult to predict, especially since inside the vessel doses can reach 120 displacements per atom after 60 years of activity. The significant loss of performance of structural materials described previously is thus induced by microstructural mechanisms assisted or induced by neutron irradiation. Experimental analysis of neutrons irradiated materials showed changes in the microstructure. In particular, a wide variety of non-equilibrium defects are created in irradiated ASS. In the early stages of irradiation, small defects of a few nanometers commonly called "black dots" appear in the materials. The rearrangement of vacancies or interstitials in (111) type planes of the fcc lattice lead to the formation of Franck loops and their formation can result in deep microstructural and mechanical changes. Another important class of defect are the cavities. They can be formed directly from the displacement cascade processes and grow by absorption of mobile defects. When cavities absorb gas atoms such as He, they are called bubbles the stability of which is maintained by the internal gas pressure. Finally, stacking fault tetrahedra can also form by the agglomeration of vacancies.

It has to be mentioned that the appearance of the above-mentioned defects as well as their size and density are strongly dependent on irradiation conditions, irradiation dose and the chemical composition of material but also on the alloy microstructures and in particular how they have been made (cooling rate, cold work, etc.). The evolution of these different populations of defects in concentration, size and mobility as well as their mutual interactions and their interaction with alloying elements create a complex synergy, thus leading to the macroscopic changes observed in irradiated ASS. The main events occurring in neutron irradiated ASS can be summarized as follows.

---

[2] A displacement cascade corresponds to a set of nearby adjacent energetic collisions of atoms.

3   Introduction

➢ Impinging neutrons decelerate in the material through a succession of collisions which create Frenkel pairs. These are composed of SIAs and vacancies which can diffuse, recombine or agglomerate leading to larger defects as Franck loops or cavities. These defects interact with the dislocation network, acting as obstacles to dislocation motion, thus inducing hardening in ASS. Under specific conditions, Franck loops can unfault, thus enhancing significantly their mobility. The glissile loops thus generated can strengthen the initial dislocation network or on the contrary annihilate, thus inducing a softening of the initial dislocation network. When significant fluxes of point defects towards sinks are sustained, the growth of vacancy clusters can induce the formation of voids or cavities which cause swelling. The production of He causes by transmutation reactions can then play a role in this synergy by stabilizing the vacancy clusters.

➢ The preferential binding of alloying elements with point defect fluxes flowing towards point defect sinks lead to a local redistribution of the composition at the vicinity of these sinks. As a result, the so-called radiation induced-segregation (RIS) can be observed at grain boundaries (GB), vacancy clusters, Franck loops and dislocations for example, thus influencing their formation. These radiation induced local redistributions can affect locally the corrosion resistance properties of ASS, thus initiating weaknesses at specific locations of ASS components. As a result of temperature, defects created in overconcentration and RIS, the occurrence of precipitation of a wide variety of second phases is very often observed in irradiated stainless steels [MAZIASZ1993]. A very recent example is the formation of $Cr_{23}C_6$ carbides at dislocation loops in ion irradiated stainless steels [JIN2012]. The precipitates formed induce lattice perturbations which can be the starting point for heterogeneous void formation which can interact with the He atoms. These different phenomena, introduces weaknesses in the material, in particular at grain boundaries which are strong point defect sinks, thus resulting in embrittlement and of inter-granular ruptures. This chain of events and coupled phenomena leads to IASCC, the formation of cracks (Fig. 2) and ultimately to the component failure.

These examples illustrate the complexity of the problem. In particular, the important number and the complexity of microstructural mechanisms involved under nuclear operating conditions as well their coupling prevent from completely understanding IASCC.

4   Introduction

Irradiation dose : 5 - 10 dpa

5 mm   5 mm   25 µm
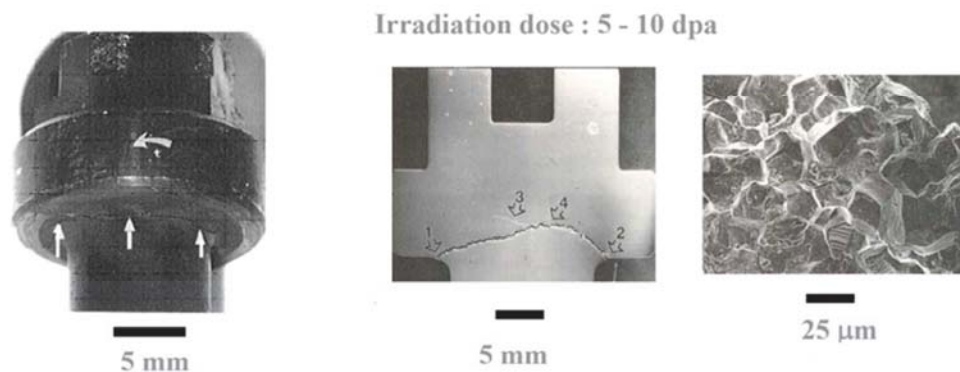
Fig. 2: Neutron-irradiated to 5-10 dpa baffle bolt showing (by arrows) a crack between the trunk and the head of the bolt (left figure). Optical micrograph of a section view of cracked baffle bolt (middle figure). The crack is pointed by arrows. Scanning electron microscopy micrograph of the fracture surface (right figure). The source of the information is EDF (Electricité De France).

I-2 The PERFORM60 project

The available knowledge on the degradation of the internal components of PWRs originates mainly from either the analysis of materials extracted from power reactor components, or tests on materials irradiated in test reactors or using accelerator facilities. These first experimental efforts aimed at revealing the trends in the mechanical property evolution, i.e. the evolution of creep or swelling with temperature, irradiation dose or alloy compositions, for example. However, despite the abundant experimental research made, our current level of understanding of the prevalent mechanisms occurring in irradiated ASS is still limited. This is essentially due to, as stated previously, the important synergy existing between all the different phenomena described above. Furthermore these phenomena usually depend on alloy compositions as well as their irradiation conditions. This decreases dramatically the experimental capabilities since ASS used in the nuclear industry have various compositions, are made of numerous alloying elements and can experience very different irradiation conditions from one reactor to another one, thus increasing the number of possible atomic mechanisms potentially responsible for radiation induced evolutions of ASS. In order to optimize in-service lifetime and avoid costly replacement campaigns, a deeper fundamental understanding of the above-mentioned degradation phenomena is therefore required. In particular, the microstructure evolution due to RIS, which is suspected to play an important role in IASCC [WAS1992, WAS1994A, WAS1994B, BUSBY2002, FUKUYA2004], has

5 | Introduction

therefore to be investigated for its technological importance in the nuclear industry. An important concern is in particular the understanding of the relevant parameters which govern segregation, as well as the ability to design alloys with controlled segregation. RIS depends on the interactions between alloying elements and mobile defects, i.e. the vacancies and interstitials created in overconcentration in irradiated ASS. This phenomenon is strongly composition dependant, and thus the task of predicting the redistribution of alloying elements at sinks due to RIS in a given ASS is not trivial.

In this context, simulation has an important role to play since the experiments pursued have largely identified which processes to model under irradiation and have defined their characteristics, i. e. that experiment can provide empirical data for modelling. In this context, the development of multiscale approaches which can lead to the prediction of macroscopic properties from atomic scale information should provide useful insights into the mechanisms involved.

To this end, the French nuclear operator EDF has initiated the PERFORM60 project. In this venture, multiscale modelling techniques and experiments are combined to gain a deeper understanding of the prevalent degradation mechanisms occurring in ASS. In order to take into account the different time scales and distance scales involved in the long-term evolution induced by the primary radiation damage, the multiscale model has to encompass a set of interlinked models. The typical models are:

> ➢ at the atomic scale, density function theory (DFT) and molecular dynamics (MD) can provide insights on material properties related to, defect formation, diffusion events, point defect and solute interactions or phase stability. MD is also used to model the primary damage (i.e. the displacement cascades). Atomistic Kinetic Monte Carlo method (AKMC) is used to determine diffusion properties as well as the microstructure evolution with time and doses.

> ➢ At an upper scale, object (or event) kinetic Monte Carlo methods, cluster dynamics and phase field methods can model the diffusion and agglomeration of the defects. The mean field methods in the framework of the rate theory are the only ones able to predict the large defects evolution and the global microstructure at long time. They are based on the

6   Introduction

balance of reaction rates between all the point defects but also the network dislocation, grain boundaries, precipitates, gas atoms which is rationalized by the radiation damage theory.

➢ To make the link with the mechanical properties, one usually turns towards dislocation dynamics which accounts for the defect clusters, which are obstacles for the gliding of dislocations, and the interactions among dislocations which can annihilate or agglomerate.

This approach therefore consists in developing a numerical predictive tool by chaining models describing different scales. It can be noted that all the links between the different simulation steps need however to be validated by dedicated experiments. A schematic representation of the multiscale approach used in the PERFORM60 project is given in Fig. 3.
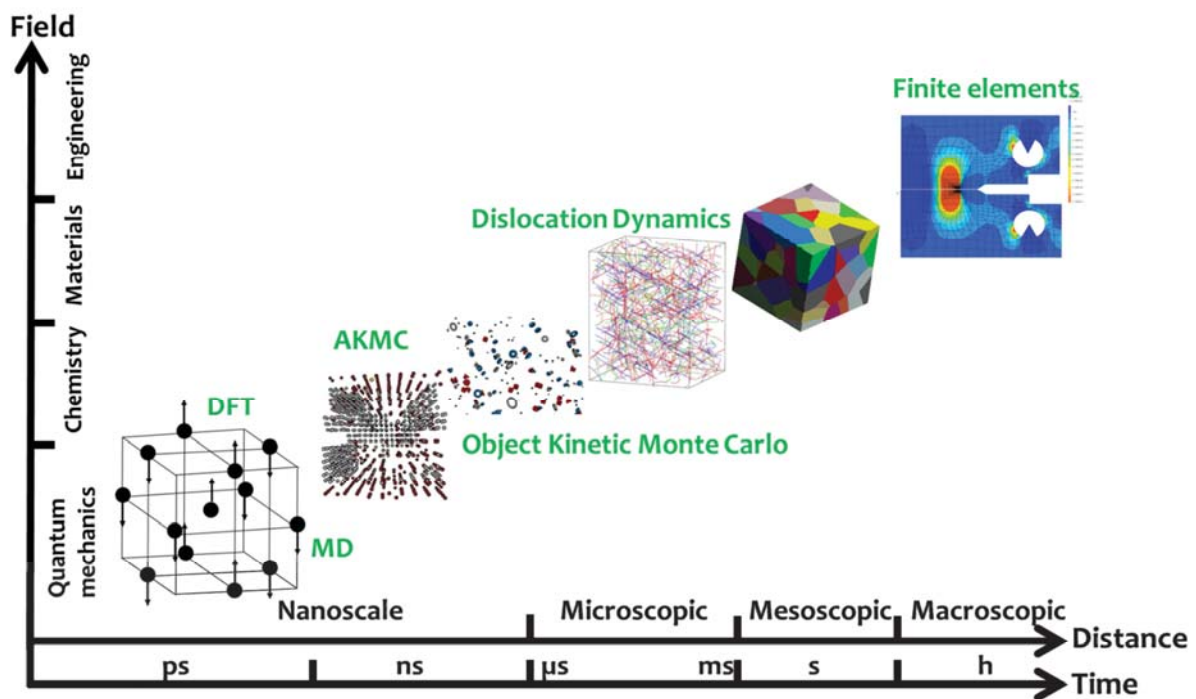
Fig. 3: Schematic representation of the multiscale modelling used in the PERFORM60 project to model IASSC.

7   Introduction

II   Stainless steels and Fe-Ni-Cr model alloys

Stainless steels (SS) are a very important class of alloys. These steels contain at least 11 wt.% of Chromium (Cr) responsible for their stainless properties and they are used for many common applications [LULA1986]. Internals are ASS with a face centred cubic lattice (fcc). ASS constitute a containment barrier protecting the nuclear pressure vessel from irradiation damage because the vessel is the only PWR component that cannot be replaced.

II-1   Materials under investigation

ASS are used because their fcc structure give them remarkable tenacity and ductility properties. In particular, 316L stainless steels have been chosen because of their good mechanical properties and their superior corrosion resistance over a wide range of temperature. These alloys contain three major elements, i.e. iron (Fe) with the highest proportion, a minimum of 16 wt.% Cr to insure the corrosion resistance and minimum of 10 wt.% nickel (Ni) to retain a fcc crystallographic structure from the cryogenic temperature region to the melting point of the alloy.

Metallurgy is to some extend the science of preparing metals and metallic alloys in a controlled macro and microstructure, giving them the expected mechanical properties, i.e. in the case of nuclear materials, hardness, ductility, resistance to corrosion and creep. To this end, in addition to major elements, many solute atoms are introduced in smaller quantity as can be seen in Tab. 1 for a few grades of ASS widely used in the nuclear industry.

Grade	Chemical composition (wt.%)								
	C max	Cr	Ni	Mo	Si max	Mn max	S max	P max	Cu max
AISI-304	0.06	17-20	9-12	-	1	2	0.03	0.045	1
AISI-304L	0.03	17-20	9-12	-	1	2	0.03	0.045	1
AISI-316	0.07	16-19	10-14	2-3	1	2	0.03	0.045	1
AISI-316L	0.03	16-19	10-14	2-3	1	2	0.03	0.045	1

Tab. 1: Chemical composition of different grades of ASS used in the nuclear industry.

Ni and Cr being the main alloying elements of these ASS, a good understanding of the austenitic Fe-Ni-Cr system can provide insights about the property changes occurring in irradiated ASS. In

8   Introduction

the PERFORM60 project, multiscale modelling techniques and experiments on Fe-Ni-Cr model alloys have therefore been combined to gain a deeper understanding of the prevalent degradation mechanisms occurring in 316L SS. To this end, a Fe-Ni-Cr potential has been built to study micro-structure and plasticity in 316L SS by fitting essential materials properties on this target system [BONNY2011B]. Experimentally, two model alloys (Fe-Ni-Cr and Fe-Ni-Cr-Si) close to this target composition (10 at.% Ni and 20 at.% Cr) were also studied using atom probe tomography, transmission electron microscope and positron annihilation spectroscopy to bring additional description and understanding of mechanisms of radiation induced microstructural changes in "simple alloys", thus helping modellers to consider the complexity of 316L SS (large numbers of chemical species) by adopting a step by step approach [VOLGIN2012].

II-2   The Fe-Ni-Cr system

The Fe-Cr-Ni systems are the ternary model alloys considered to understand and model properties of austenitic materials. Fe-Ni-Cr alloys can display a wide variety of magnetic phases. Indeed, depending on the element concentrations, these alloys can enter an anti-ferromagnetic (AFM), spin glass (SG), or ferromagnetic (FM) phase at low temperature as can be observed in Fig. 4 for the $Fe_{80-x}Ni_xCr_{20}$ ternary alloy [MAJUMDAR1983, MAJUMDAR1984]. At operating condition temperatures of nuclear reactors, these steels are paramagnetic (PM). It also can be noted that at 0 K, i.e. at DFT calculation conditions, the target model alloy displays a long range AFM order.
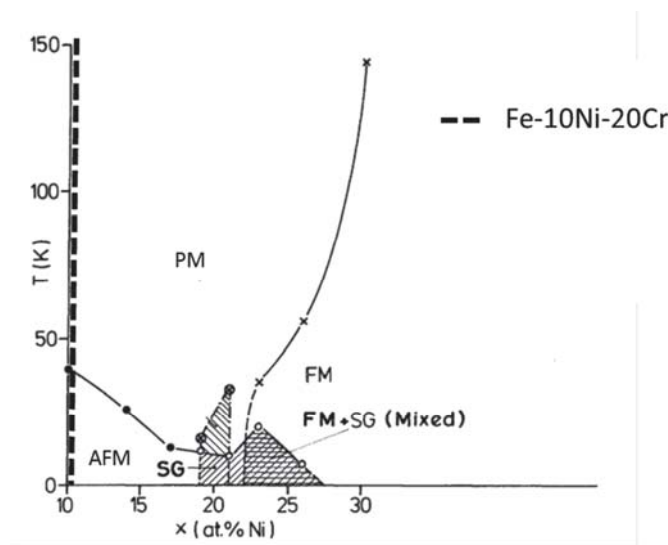
Fig. 4: Phase diagram of $Fe_{80-x}Ni_xCr_{20}$ ternary alloy as a function of both Ni concentration and temperature. PM refers to the paramagnetic, FM refers to ferromagnetic, AFM refers to anti-ferromagnetic and SG refers to spin glass. Dashed line refers to the target composition Fe-10Ni-20Cr. Figure taken from [MAJUMDAR1984].

Four solids phase can be identified in the Fe-Ni-Cr ternary phase diagram at the equilibrium state presented in Fig. 5:

➢ the γ phase which is a fcc solid solution based on γ-Fe and γ-Ni

➢ the α phase which is a body-centred cubic (bcc) solid solution based on α-Fe

➢ the α' phase which is a bcc solid solution based on α-Cr

➢ and the σ phase which is an intermetallic phase which occurs over a wide content of Cr and derived from the Cr-Fe binary.

It can be seen that within the area, delimited in red on Fig. 5, which represents alloys of composition close to the target reference alloy, the alloys can be either a fcc solid solution, or a mixture of two and even three of these different phases.
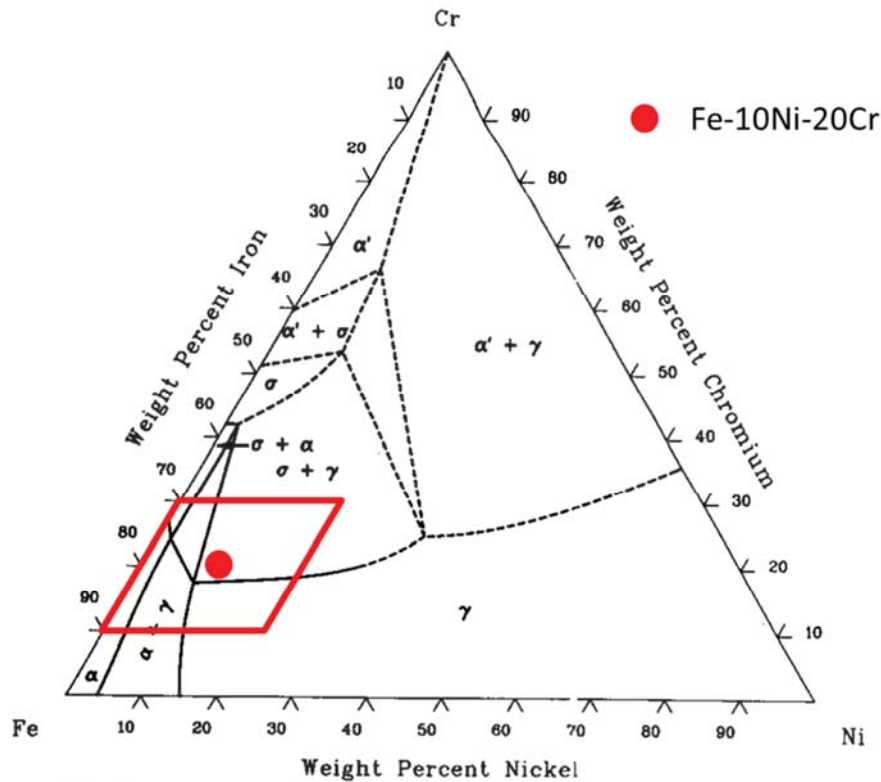
Fig. 5: Fe-Ni-Cr ternary phase diagram at 650°C [RAYNOR1988]. The red point refers to the target composition Fe-10Ni-20Cr. Within the delimited area in red are included alloys in concentration range near the Fe-10Ni-20Cr target composition.

All the other elements impact on the size of the different phase domains of the Fe-Ni-Cr phase diagram which are presented in Fig. 5.

III   Purpose of this work

As mentioned in section I-1, at the operating condition of nuclear reactors, ASS, like most structural alloys, suffer from microstructural changes (void swelling, creep, structural changes, and solute redistribution) leading to a decrease of their performance with time. In addition, all these event impact on one another and their combination allows the occurrence of IASCC at some specific locations and in particular at weakened GB. Ultimately IASCC initiate cracks and then failures in ASS components, thus involving potential safety as well as economic problems in extending the lifetime of the French nuclear centrals over 60 years. Insights about these mechanisms are therefore required to improve their resistance to extreme conditions experienced

11   Introduction

by these components in PWR reactors. Although it is difficult to discriminate the role played by each of these mechanisms on IASCC, the depletion of Cr at grain boundaries is suspected to play the most important part in this process.

As a part of the multiscale modelling effort presented in section I-2, atomistic simulations have thus been initiated to investigate the evolution of microstructure under irradiation and more precisely in this work, the effects of radiation damage on solute redistribution at defect sinks. The aim of our work is to gain insights into RIS process using an atomistic approach, this work thus lies at the base of the multiscale modelling. For this purpose a large amount of DFT calculations have been performed to gain insight about the interactions occurring between point defects, and the two major alloying elements of the Fe-10Ni-20Cr target alloy.

The manuscript is organized as follows. The first chapter introduces the models and theories on which our work is based. The second chapter presents a short bibliographical review of RIS and the properties of point defects in austenitic stainless steels as well as model Fe-Ni-Cr alloys. The third chapter focuses on the results of our DFT calculations, whereas the fourth chapter presents the atomic model we developed to perform AKMC simulations along with some results. We then conclude and propose some perspectives to our work.

Chapter I.   Methods and models

RIS is studied in this work using three atomistic methods: Monte Carlo (MC) methods which are stochastic methods and MD which are deterministic (in principle), as well as DFT ab initio method. The two first methods require a cohesive model, i.e. a model describing the interactions among the atoms, in order to determine, for instance the total energy of the system, activation barriers for diffusion or in the case of MD, interatomic forces. In principle, these data can be obtained from the knowledge of the types of the atoms and their relative positions by solving the Schrödinger equation, i.e. using first principle methods. However, such an approach is only possible for a very limited number of atoms and cannot be used for structural materials for instance. One has to resort to simpler ways such as the use of semi empirical interatomic potentials, or cluster expansion kinds of models. However, developments of first principle methods along with an increase in computational power have made the use of first principles methods much more widespread and in particular DFT calculations are nowadays commonly used to determine data that will contribute to the building of more reliable cohesive models. DFT data can be for instance used to assess the validity of interatomic potentials or build more reliable and transferable potentials. For example, in bcc Fe, in the field of radiation damage, interatomic potentials for MD [ACKLAND2004] or pair interaction model [VINCENT2006A, VINCENT2006B] based on DFT data and specific and simple experiments [DOMAIN2001B] were used to model a multinary alloy representative of RPV steels.

In the first sections, we will present the methods used in this work:

➢ MC methods, which we used to assess the validity of some of the cohesive models derived in the framework of this work as well as to model the microstructure evolution, are presented in section I-1.

➢ MD, which was used only to characterize some of the cohesive models, is presented in section I-2.

The computational approach used in this work to study non equilibrium segregation using MC methods is presented in section II. The different kinds of cohesive models investigated in this work are presented in section III. Finally, the different materials properties that were calculated

to assess the validity of the cohesive models for RIS modelling (chapter IV) will be presented in section IV.

I   <u>Atomistic models</u>

I-1 Monte Carlo Methods

MC methods are a class of computational algorithms which provide approximated solutions to a wide variety of problems (physics, mathematics) by performing statistical sampling calculations. The name comes from the use of random numbers. Statistical mechanics are of very widespread use in computational materials science. In particular, Metropolis MC (MMC) [METROPOLIS1949, METROPOLIS1953] is a method to sample possible states of a system of particles with a known cohesive model. It is used for instance to calculate thermodynamical averages of a system of particles at finite temperatures or to simulate the annealing of a system of particles in order to find configurations corresponding to possible energy minima. The method samples, within a specific statistical ensemble, the phase space of N particles through a random walk along a series of connected configurational changes (building Markov chains). The sampling takes place by making trials that will change the total energy of the system. After each trial, the new energy (i.e. the energy of the trial configuration) is calculated and the decision whether to accept or not the new configuration is based on the energy change. If the new energy is lower than the initial state energy, the trial configuration is accepted and it becomes a new initial condition. If the energy of the trial configuration is higher than the energy of the initial configuration, the acceptance is based on the relative probabilities $P_{trial}/P_{initial} = \exp(-\Delta E/kT)$, where ΔE is the difference between the potential energies of the initial and the trial configurations. One has to keep in mind, that in this scheme, convergence towards equilibrium does not occur following the real physical mechanisms that lead to the transformation from an arbitrary state to the final one. Therefore, the intermediate sampled configurations do not necessarily represent real and existing configurations. In addition, time is not a variable that appears explicitly in the MMC algorithms and no information regarding the kinetics of the evolution towards equilibrium can be obtained. To partially overcome these limitations, one often uses Kinetic Monte Carlo (KMC) techniques, among which AKMC is one of the most versatile method to simulate the evolution of a complex microstructure at the atomic scale, dealing with elementary atomic mechanisms. These

algorithms are based on the residence time algorithm derived by Young and Elcock [YOUNG1966] for the diffusion of a vacancy in ordered alloys. The residence time algorithm is also known as the Bortz-Kalos-Lebowitz algorithm [BORTZ1975].

I-1-a   The metropolis algorithm

As stated previously, MMC simulations sample a given statistical ensemble by performing random configurational changes. In the canonical ensemble (NVT ensemble) the basic steps of a MMC simulation can be summarized as follows:

➢ **Step (1):** A configuration S_n of total energy E_n is accepted.

➢ **Step (2):** One picks a trial configuration S_t of total energy E_t (usually a configuration similar to S_n for instance a configuration in which two atoms of different chemical type have been switched, or a configuration where all the atoms have been slightly displaced at random). If $E_t - E_n < 0$, the trial configuration S_t is accepted, otherwise one pick a random number ζ with value between 0 and 1 and one compute the probability ratio $R = P(S_t)/P(S_n) = \exp\left(\frac{-(E_t - E_n)}{k_B T}\right)$. If $\zeta \leq R$, one makes $S_{n+1} = S_t$, otherwise, one makes $S_{n+1} = S_n$.

➢ **Step (3):** One goes to (2) replacing S_n by S_{n+1}.

The convergence is thus achieved when the step (3) is repeated N times, where N is a sufficiently large number.

Note that a random configuration S_0 is first generated (which is not too far from a realistic configuration) and that the total energy of this system, E_0, is calculated.

It is worth mentioning that at low temperature, the equilibrium state may never be reached owing to the fact that the exchange criterion, $\zeta \leq \exp\left(\frac{-(E_{n+1} - E_n)}{k_B T}\right)$, is never accepted.

I-1-b   The residence time algorithm

The residence time algorithm derived by Young and Elcock [YOUNG1966] is one of the earliest to model the diffusion of point defects in metals. Exchanges between point defects and one of their

first nearest neighbours are performed during the course of the calculation, considering that they are thermally activated events. As a consequence, transitions between two states follow a physical path in the phase space, determined by the activation energies of the point defect diffusion. In contrast with Metropolis algorithm, exchanges are always achieved using the residence time algorithm following a physical diffusion mechanism, and the average time during which the system remains in its state is calculated. KMC methods provide a solution to the Master Equation presented in Eq. I-1, which describes a physical system whose evolution is governed by a known set of transition rates between possible states as:

$$\frac{dP(S,t)}{dt} = -\sum_{S'}\Gamma(S \to S')P(S,t) + \sum_{S'}\Gamma(S' \to S)P(S',t) \qquad \text{Eq. I-1}$$

where $\Gamma(S \to S')$ (respectively $\Gamma(S' \to S)$) refers to the transition probabilities occurring for an unitary time step from the state S to the state S' (respectively from the state S' to the state S). At the steady state, $\frac{dP(S,t)}{dt} = 0$, which means that as many transitions $S' \to S$ as $S \to S'$ are performed during the course of the calculation. In order to model steady state, the principle of detailed balance (Eq. I-2) has to be obeyed:

$$\Gamma(S \to S')P(S,t) = \Gamma(S' \to S)P(S',t) \qquad \text{Eq. I-2}$$

The probability distribution of the steady state is therefore a stationary solution of the master equation presented in Eq. I-1. The basic steps of a KMC simulation applied to the diffusion of point defects can be summarized as follows:

A random configuration S_0 is generated. The total energy of this system, E_0, is calculated.

➢ **Step (1):** During the course of the calculation, at each step, the jump probabilities of each point defects, Γ_D, towards all their possible jumping sites (most of the time their first nearest neighbours), are calculated using the following equation:

$$\Gamma_D = \nu\exp\left(\frac{E_a}{k_BT}\right) \qquad \text{Eq. I-3}$$

where ν corresponds to the attempt frequencies for the jump and E_a corresponds to its activation energy.

- ➢ **Step (2):** The probabilities of all these events are summed.
- ➢ **Step (3):** A random number, ζ, between 0 and $\sum_{i=1}^{N_D} \sum_{j=1}^{N_J} \Gamma_{D_i A_j}$, where the latter term corresponds to the probability sum of all the possible point defect jumps $N_D \times N_J$ (N_D refers to the number of point defect and N_J refers to the number of possible jumps for each defects), is then generated to select one event from all possible events as follows:

$$\sum_{i=1}^{n_D-1} \sum_{j=1}^{N_J} \Gamma_{D_i A_j} + \sum_{j=1}^{n_J-1} \Gamma_{D_{N_D} A_j} \leq \zeta \leq \sum_{i=1}^{n_D-1} \sum_{j=1}^{N_J} \Gamma_{D_i A_j} + \sum_{j=1}^{n_J} \Gamma_{D_{N_D} A_j} \qquad \text{Eq. I-4}$$

where among all the possible transitions $N_D \times N_J$ between each point defects, D, and their first nearest neighbours, A, the jump n_J of the point defect n_D have been chosen. This procedure is presented schematically in Fig. I-1.

- ➢ **Step (4):** The average time step is calculated by considering the inverse sum of the probabilities of all events as follows:

$$\Delta t = \frac{1}{\sum_{i=1}^{N_D} \sum_{j=1}^{N_J} \Gamma_{D_i A_j}} \qquad \text{Eq. I-5}$$

where i runs over all the point defects, D, present in the system, and j runs over their first nearest atoms, A. This relationship then involves that the smaller the sum of probabilities the bigger the KMC time. As a result, time will significantly increase, as could be expected, when one chooses a not very probable event (jump) to take place.

During the course of the calculation, steps 1-4 are repeated until the desired simulation length is reached.
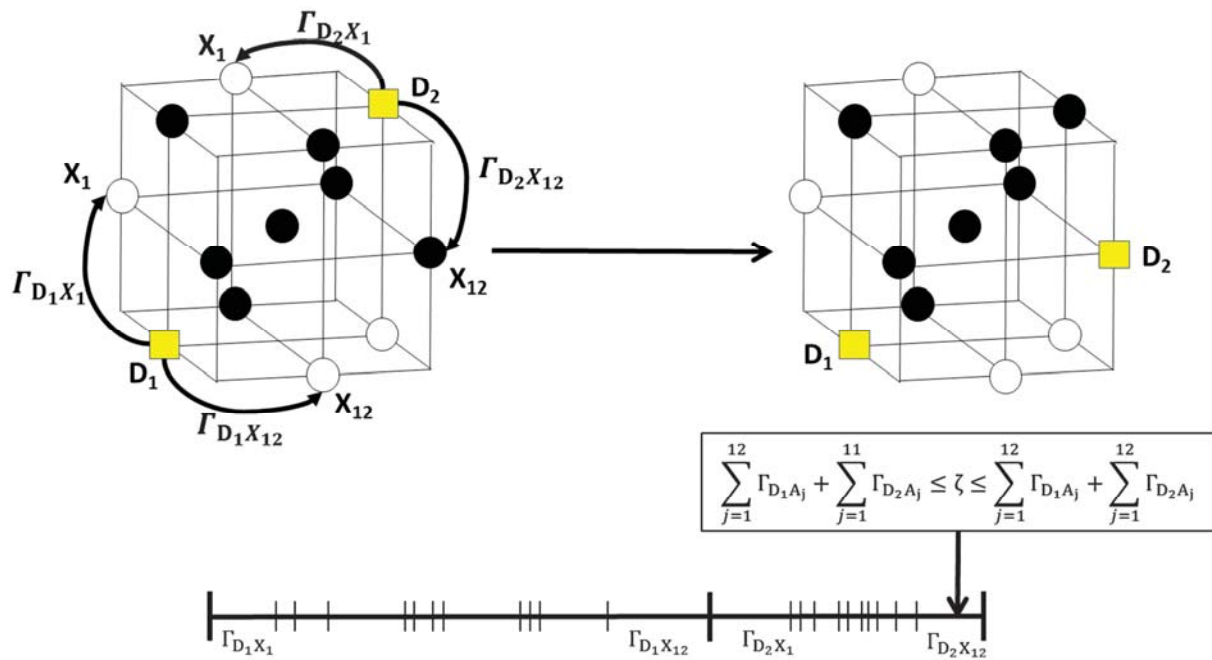
Fig. I-1: Steps 1-4 of the residence time algorithm presented in this section are explained schematically in this figure. Yellow squares refer to two point defects introduced in the lattice. The probabilities of all possible events are summed as presented in the bottom part of this figure. Then, a random number, ζ, is generated to select one jump from all possible jumps, in a stochastic manner, but according to the different jumps probabilities. A new configuration is generated as shown in the right part of the figure. This process is repeated until the end of the simulation.

I-2 Molecular Dynamics

Contrary to MC methods, the evolution of the positions of a collection of atoms is determined in a deterministic manner using MD. In this technique and for classical mechanics (as opposed to ab initio MD where the electrons are explicitly accounted for), atoms introduced in the systems are treated as mass point objects interacting through a force field (an interatomic potential). Their trajectory (i.e. their evolution in time) obeys the classical mechanic equations and the algorithm is essentially an integration of the Newtonian equations of motion over time to yield the particle positions and velocities:

$$f_i = m_i \frac{d^2 r_i}{dt^2}$$

Eq. I-6

18   Chapter I. Methods and models

where f_i refers to the force applied to atoms i, m_i its mass and r_i its position. The forces acting on each atom is simply obtained as the derivative of the interatomic potential as in Eq. I-7.

$$\vec{f_i} = -\frac{\partial V(r_i)}{\partial r_i} \qquad \text{Eq. I-7}$$

Coupled differential equations rule the motion of each atom i of mass m_i, which is solved numerically in an iterative process using different techniques such as the Verlet algorithm or a predictor corrector scheme such as the Gear algorithm [GEAR1971]. MD samples naturally the microcanonical ensemble (NVE) where the number of particles N, the volume V and the energy E of the system are conserved, but the other thermodynamical ensembles (i.e. NPT and NVT ensembles) can be sampled using the Nose Hoover [NOSE1984A, NOSE1984B] or the Andersen algorithm [ANDERSEN1980].

The code that we used, DYMOKA [DOMAIN2001A], can perform calculations in different ensembles:

 ➢ (1) the microcanonical ensemble (N, V, E) but also
 ➢ (2) the canonical ensemble (N, V, T), where the number of particles N, the volume V and the temperature T of the system are conserved and
 ➢ (3) the isothermal-isobaric ensemble (N, P, T) where the number of particles N, the pressure P and the temperature of the system are conserved.

In the simulations done in this work, the equations of motion were integrated using the Verlet algorithm which is simply a Taylor expansion of the position of atom i at time t to obtain its position at time $t + \Delta t$:

$$r_i(t + \Delta t) \cong 2r_i(t) - r_i(t - \Delta t) + \frac{f_i}{m_i}\Delta t^2 \qquad \text{Eq. I-8}$$

Eq. I-8 shows that in order to determine the position of atom i at time $t + \Delta t$, the position of the atoms have to be known at times $t - \Delta t$ and t The difference between atomic positions at times $t - \Delta t$ and $t + \Delta t$ gives access to the velocities at time t as:

19 Chapter I. Methods and models

$$v_i(t) \cong \frac{r_i(t + \Delta t) - r_i(t - \Delta t)}{2\Delta t} \qquad \text{Eq. I-9}$$

Verlet algorithm may be easily implemented and have proved to be accurate enough to allow for the stabilization of the total energy of the system using reasonably large time steps. The iterative process is extremely simple and may be summarized as follows:

> **Step (1):** The initial positions of each atom at times $t - \Delta t$ and t as well as their velocities at time t are stored in the computer memory.

> **Step (2):** The forces applied to atoms introduced in the system can be calculated easily as they are obtained by taking the derivative by any cohesive model designed to define the energy of the collection of atoms as a function of their relative distance as in Eq. I-7.

> **Step (3):** The new atomic positions are determined at the time $t + \Delta t$ using Eq. I-8.

> **Step (4):** Velocities are calculated for each atom by considering their position at time $t + \Delta t$ calculated in the previous step, relative to those calculated at the time $t - \Delta t$, during the time step $2\Delta t$, as in Eq. I-9.

These latter positions and velocities become new input to step 2. Then, steps 2-4 are repeated until the desired simulation length is reached. At each repetition of steps 1-4, the MD time is incremented by the time step Δt. Typically, thousands of millions iterations can be achieved during the course of MD simulations. In practice, the time step depends on the material studied and may be chosen according to typical phonon frequencies to avoid missing intermediate states. Each time step therefore corresponds typically to a few of a femtosecond (10^{-15} s).

II   Computational approach to study non equilibrium segregations

The LAKIMOCA code [DOMAIN2001A] which incorporates both the MMC and the AKMC algorithms was used in this work to simulate RIS and TNES and the computational approach used is presented in the following section.

II-1 The rigid lattice approach

In a material, atoms move around their equilibrium positions. This can be in principle taken into account in AKMC if one disposes of a cohesive model capable of calculating the total energy of

a system as a function of continuous atomic coordinates, as was considered in the recent studies on Fe-Cr alloys by Zhurkin and Terentyev for instance [ZHURKIN2011, TERENTYEV2011]. Despite the fact that relaxations do take place in real systems, they can require a large amount of simulation steps and thus limit the number of point defect jumps that can be simulated in a reasonable amount of time.

In order to use a simple cohesive model and to decrease the computational time, an approach consists in fixing the atomic positions at perfect lattice sites. This so-called rigid lattice approach, does not take into account relaxations explicitly, and as a consequence speeds up the calculations. The validity of this approach should be rather good when the different atom species have similar sizes, as for Fe, Ni and Cr atoms. Furthermore, simplified potentials which only consider a limited number of atomic interactions may be built using this approach, as it is the case for the pair interaction model which will be presented in section III-2-b.

II-2 Modelling irradiation

LAKIMOCA can be used to simulate irradiation with neutrons, ions, or electrons which are treated as external events.

In the case of an electron irradiation simulation, Frenkel pairs (pair formed by a vacancy and the corresponding self-interstitial atom) are introduced randomly in the simulation box, according to a certain dose rate. The corresponding SIA and vacancy can have both correlated (distance between SIA and V below a critical value) or non-correlated (both are introduced randomly) positions. It is assumed, as an acceptable first approximation, that each electron is responsible for the formation of one Frenkel pair.

Neutron irradiation is simulated by introducing cascade debris, as well as randomly distributed Frenkel pairs, according to a rate that is equivalent to the irradiation flux desired. The irradiation dose is calculated in terms of dpa [ASTM1993]. The contribution of each Frenkel pairs is considered to be equal to one displacement, while for each cascade debris the contribution to the damage is computed using the NRT standard [NORGETT1975]:

21   Chapter I. Methods and models

$$\nu_d = \frac{0.8E_{DAM}}{2E_d} \qquad\qquad \text{Eq. I-10}$$

where ν_d is the total amount of defects produced by higher energy irradiation, E_{DAM} is the energy damage induced by the cascade debris generated by primary knock-on atoms and E_d is the threshold displacement energy (40 eV for ferritic and austenitic alloys [ASTM1994]).

Each time a vacancy is introduced in the simulation box, it replaces either a Fe atom or a solute atom on the lattice. The number of atoms of each species (besides Fe) that are removed when introducing the vacancy is stored in a reservoir. Self-interstitial atoms are correspondingly introduced on the lattice by picking at random atoms from the reservoir, if it is not empty, or Fe atoms otherwise. If the site on which a vacancy or a self-interstitial should be introduced is already occupied by a point-defect, there are two possibilities: if the defect to be added is of the same type as the defect already on the site, no new defect is added; if the defect to be added is opposite, recombination occurs (the defect disappears from the lattice).

In this work, only electron irradiation with non-correlated positions between SIA and vacancy is used.

II-3 Modelling a grain boundary

As mentioned in the introduction, RIS mechanism is suspected to play a major factor in weakening of GBs, thus leading to the occurrence of IASCC in irradiated ASS. A reliable description of the GBs is therefore required and in this section, we present the method used to model a GB in AKMC simulations.

A GB is the interface between two grains of different orientations in a polycrystalline material. GBs are therefore highly disordered areas in the material which can contain alloying elements but also an important concentration of defects since they act as strong point defect sinks. As a result, GBs are difficult to model. No such complexity is however considered in AKMC modelling in which a GB is considered as a defined area of the lattice with perfect sites as we rely on a rigid lattice approach. In this area, additional interactions between the sites and the

elements introduced in the lattice (i.e. the solute atoms, the vacancies and the SIAs) are taken into account to capture GB effect as can be seen schematically in Fig. I-2.
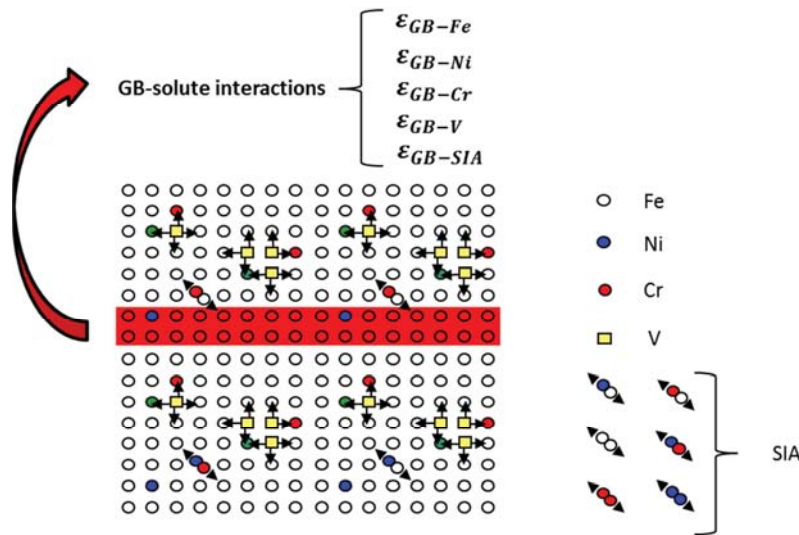
Fig. I-2: Schematic representation of the GB modelling using AKMC. Area in red represents the lattice sites where solute-GB interactions are considered, i.e. ε_{GB-Fe}, ε_{GB-Ni}, ε_{GB-Cr}, ε_{GB-V} and ε_{GB-SIA} in the Fe-Ni-Cr system.

III   Cohesive models

As mentioned previously, the rules that characterize the interactions of the collection of atoms that form the system have to be defined to use MC as well as MD methods. One of the key ingredients of these two kinds of simulations is thus the cohesive model. The various approaches which may be used to determine the total energy of a system of atoms can be divided into two families which broadly depend upon the description of the cohesion, i.e. the electrons.

> ➤ First principle methods which explicitly describe the atoms in terms of nuclei and electrons and take into account the quantic interactions occurring at the atomic scale.

> ➤ Empirical cohesive models which describe the cohesion by mathematical functions adjusted so as to reproduce data pertaining to a given material (its vacancy formation energy, its crystallographic structure, etc.).

A certain number of intermediate techniques such as the tight binding method can also be used. The two families we used in this work are presented in this section.

III-1 First principle methods

The most accurate manner of investigating the energy of a collection of atoms as a function of their relative positions is to model all interactions existing between atoms at the nanoscale. This is provided by the resolution of the Schrödinger equation:

$$H\Psi(\vec{r_1}, \sigma_1, \dots, \vec{r_N}, \sigma_N) = E\Psi(\vec{r_1}, \sigma_1, \dots, \vec{r_N}, \sigma_N) \qquad \text{Eq. I-11}$$

where H is the Hamiltonian operator describing all interactions in the system, Ψ is the associated many-body wavefunction which depends on both spatial and spin coordinates of electrons, and E is the total energy of the system. The Hamiltonian operator describing an ensemble of interacting atoms can be written as:

$$H = -\frac{\hbar^2}{2m_e}\sum_i \nabla_i^2 - \sum_I \frac{\hbar^2}{2M_I}\nabla_I^2 + \frac{1}{2}\sum_{i\neq j}\frac{e^2}{|\vec{r_i}-\vec{r_j}|} + \frac{1}{2}\sum_{I\neq J}\frac{Z_I Z_J}{|\vec{R_I}-\vec{R_J}|} - \sum_{i,I}\frac{eZ_I}{|\vec{r_i}-\vec{R_I}|} \qquad \text{Eq. I-12}$$

where $\hbar$ is the reduced Plank's constant, m_e, e and $\vec{r_i}$ are the electron mass, electric charge and position while M_I, Z_I are the mass and the electric charge of a nucleus at position $\vec{R_I}$.

The main issue to solve the Schrödinger equation is that the many-electron wavefunction $\Psi(\vec{r_1}, \sigma_1, \dots, \vec{r_N}, \sigma_N)$ is a very complex scalar function. Thus, the resolution of the Schrödinger equation, which consist in minimizing the matrix element $\frac{\langle\Psi|H|\Psi\rangle}{\langle\Psi|\Psi\rangle}$, requires a repetition of a huge quantity of operations. In this context, some first principle methods were designed to provide an approximate solution for the quantum many-body problem which may be able to investigate the properties of small systems (few hundred of atoms). A view point consists in making approximations about the many-electron wavefunction itself. This improvement was proposed by Hartree and Fock (HF) who approximated $\Psi(\vec{r_1}, \sigma_1, \dots, \vec{r_N}, \sigma_N)$ by N one-electron orbitals. Another view point consists in finding another physical quantity which may be able to define the system without growing in complexity with increasing electrons. This step was achieved by Hohenberg and Kohn (HK) with the introduction of the DFT, which is based on the electron density rather than the wavefunction. Thus, theoretical approaches giving access to the electronic structure became possible as well as desirable in material sciences due to two major reasons:

24 Chapter I. Methods and models

➢ First principle methods are designed to solve the Schrödinger equation, and provide an accurate description of many material properties, for reasonable computational times.

➢ Both computational power and methods (massively parallel calculation) had been significantly improved during the last decades. Thus, calculations on systems of a few thousands of atoms are currently doable.

Furthermore, it can be noted that several experimental techniques probe the electronic structures of materials like DFT does. This is the case of Scanning Tunneling Microscopy, photon and electron spectroscopies for example.

III-1-a   The variational principle

As briefly mentioned, the resolution of the Schrödinger equation consists in minimizing the matrix element $\frac{\langle\Psi|H|\Psi\rangle}{\langle\Psi|\Psi\rangle}$. The procedure used to achieve this minimization is known as the variational principle. To be more specific, when the system is in the state $|\Psi\rangle$ the functional describing the total energy of the system may be defined as $E[\Psi] = \frac{\langle\Psi|H|\Psi\rangle}{\langle\Psi|\Psi\rangle}$. The variational principle states that the minimization of this functional gives access to the ground state $|\Psi_0\rangle$, and then to the associated ground state properties, e.g. the ground state energy E_0 and the ground state electron density n_0.

III-1-b   The density functional theory

DFT has proved to be a reliable method to investigate the properties of systems studied in all modern sciences (chemistry, physics, materials science, biochemistry, geophysics, etc.). Indeed, the approximate functionals used in DFT provide a good balance between accuracy and computational cost. This allowed much larger systems to be treated than by traditional first principle methods, while retaining much of their accuracy. DFT consists in computing the ground state energy associated to a N-electron system subjected to a fixed external potential V_{ext} which account for electron interactions with the external potential generated by the nuclei. The Hamiltonian operator of these interactions can therefore be written as:

25   Chapter I. Methods and models

$$H = \sum_{i=1}^{N} \left(-\frac{\hbar^2 \nabla_i^2}{2m_e} + V_{ext} \right) + \frac{1}{2} \sum_{i \neq j} \frac{e^2}{|\vec{r_i} - \vec{r_j}|} \qquad \text{Eq. I-13}$$

III-1-c The Born-Oppenheimer approximation

The first approximation which is introduced in DFT is the Born-Oppenheimer approximation. Electrons are treated as moving in the potential generated by motionless nuclei, owing to the fact that mass difference between the nuclei and the electrons is at least three orders of magnitude. As a consequence, the system can be written as a many-electron Hamiltonian containing a term representing the external potential generated by the nuclei:

$$H_e = T_e + V_{int} + V_{ext} \qquad \text{Eq. I-14}$$

where T_e is the electrons kinetic operator, V_{int} is the electron-electron interaction operator and V_{ext} is the operator accounting for the electron interactions with the external potential generated by the nuclei.

III-1-d Hohenberg and Kohn theorems

A significant improvement of the DFT was given by the HK theorems [HOHENBERG1964]. Indeed, they proved that the many-body problem may be formulated by considering electron densities rather than the many-electron wavefunctions as:

$$n(\vec{r}) = \frac{\langle \Psi | n(\vec{r}) | \Psi \rangle}{\langle \Psi | \Psi \rangle} = N \int \Psi^*(\vec{r}, \vec{r_2}, ..., \vec{r_N}) \Psi(\vec{r}, \vec{r_2}, ..., \vec{r_N}) d^3 r_2 ... d^3 r_N \qquad \text{Eq. I-15}$$

where $n(\vec{r}) = \sum_{i=1}^{N} \delta(\vec{r} - \vec{r_i})$ is the density operator, N is the number of particles and r_i are the position vectors associated to each particle. Using this approach, the probability density means that the probability of finding an electron in the volume $d^3 r$ around the position given by the vector r is $n(\vec{r}) d^3 r$.

The first HK theorem states that for all systems of interacting particles exposed to an external potential V_{ext}, this latter term may be determined up to an additive constant, simply by knowing

26 Chapter I. Methods and models

the ground state electron density n_0. In other words, there is a single ground state $|\Psi_0\rangle$ associated to a fixed external potential V_{ext}. Thus, the ground state of the studied system is a functional of the external potential V_{ext}, i.e. $E_0 = E[V_{ext}]$. The second HK theorem states that the minimum of the functional $E[n]$ corresponds to the energy ground state of the system, and its associated electron density (which minimizes $E[n]$) is n_0.

These two theorems allow for a completely different way to solve the Schrödinger equation using the variational principle. Indeed, the most intuitive procedure proposed by HF, consisting in (1) solving the Schrödinger equation (2) then determining the wavefunction (3) finally calculate the electron density. The HK theorems state that many-electron problem may be formulated in terms of electron density (instead of wavefunctions) to compute the energy ground state using a variational approach.

III-1-e   Kohn and Sham equations

However, an emphasis in implementing the latter formalism by using reliable physical basis was provided by Kohn and Sham (KS) in 1965. The exchange-correlation energy functional, which takes into account of all interaction effects of the system, is introduced in the expression of the exact energy functional. The exact energy functional of the system can therefore be written as:

$$E[n] = T_S[n] + E_H[n] + \int V_{ext}(\vec{r})n(\vec{r})d^3r + E_{XC}[n] \qquad \text{Eq. I-16}$$

where $T_S[n]$ is the kinetic energy of a virtual system of N non interacting electrons, $E_H[n]$ which corresponds to the sum of the Hartree terms, i.e. a part of the total Coulomb interaction, and $E_{XC}[n]$ which refers to the exchange-correlation energy functional. It is worth mentioning that $E_{XC}[n]$ may account for (1) the Pauli repulsion between electrons (2) the correction which compensates the fictious nature of both $T_S[n]$ and $E_H[n]$ functionals (3) the correlation effects occurring between two electrons of different spin. Thus, the reliability of the DFT will depend on the ability of finding a relevant functional for $E_{XC}[n]$.

The major improvement achieved by KS was to postulate that the non-interacting part of the system (without taking into account the exchange-correlation part) may be considered as a

virtual system sharing the same electron density as the interacting system. Obviously, in the case where such correspondence exists, the non-interacting system may be subjected to a virtual potential V_{eff} instead of V_{ext} previously introduced, which compensates the fact that we neglected the electron interactions. This is a major improvement since we are able to solve the problem of N non-interacting electron in a fixed potential V_{eff}. Indeed, a set of N Schrödinger equations considering N single particle orbitals ψ_i can be formulated as:

$$\left(-\frac{\hbar^2 \nabla_i^2}{2m_e} - V_{eff}(\vec{r}) \right) \psi_i(\vec{r}) = \varepsilon_i \psi_i(\vec{r}) \qquad \text{Eq. I-17}$$

Moreover, the corresponding electron density can be easily calculated for such a system. The KS equations may be therefore expressed as follows:

$$\begin{cases} n(\vec{r}) = \sum_{i=1}^{N} f_i |\psi_i(\vec{r})|^2 \\ \left(-\frac{\hbar^2 \nabla_i^2}{2m_e} - V_{ext}(\vec{r}) - e^2 \int \frac{n(\vec{r'})}{|\vec{r} - \vec{r'}|} d^3 r' + V_{XC}(\vec{r}, [n]) \right) \psi_i(\vec{r}) = \varepsilon_i \psi_i(\vec{r}) \end{cases} \qquad \text{Eq. I-18}$$

where f_i refers to the occupation factor of orbitals, $V_{XC}(\vec{r}, [n])$ refers to the derivative of the exchange-correlation energy functional. It is worth mentioning that the form given to the effective potential presented in the latter equation corresponds to the necessary condition for the existence of this virtual system associated with the same electron density as the interacting system. The strength of this approach lies in the fact that:

➢ These one-particle equations are suitable within the framework of the DFT.

➢ The Kohn-Sham equations are iteratively solved with a self-consistent approach.

➢ The Kohn-Sham approach to the solution of the N-body problem is rigorously exact up to this point.

III-1-f   Approximation for the exchange-correlation functionals

The needed approximation which allows to solve the Kohn-Sham equations consists in defining the shape of the functional describing the exchange-correlation energy $E_{XC}[n]$.

The first approach used, so-called the Local Density Approximation (LDA), consisted in describing the exchange-correlation energy by an homogeneous electron gas of density $n(r)$. It is worth mentioning that LDA may be extended to local spin density approximation (LSDA) to investigate the magnetic properties of material, using the LDA approach. Despite the fact that both LDA and LSDA are quite rough approximations, they provide a satisfactory description of many systems. However they are less accurate for the study of transition metals. In particular, LSDA predicts a non-magnetic hcp structure instead of a ferromagnetic one for Fe ground state [BURKE2007].

A significant improvement of the LDA approach is obtained using the generalized gradient approximation (GGA) which consists in introducing in $E_{XC}[n]$ a dependence on the gradient of the electron density. Indeed, one of the major results provided by this approach is the prediction of the ferromagnetic α-Fe observed experimentally [DOMAIN2001B, POSTNIKOV2003]. The most widely used parameterizations of GGA are those introduced by Perdew, Wang (PW91) [PERDEW1991, PERDEW1992] and by Perdew, Burke and Ernzerhof [PERDEW1996].

III-2   Empirical cohesive models

The direct electronic structure calculations presented in section III-1 may be performed using both MC and DM techniques. However the computational speed, which is an important issue in numerical simulations, is strongly affected owing to the fact that the first principle methods involve important computational costs. In that context, other rules governing the atomic interactions have to be considered to investigate bigger systems as well as to run longer simulations for instance. To this end, two different types of empirical cohesive models have been investigated to model RIS and TNES:

➢ The EAM potential developed by Bonny [BONNY2011B] in the framework of the PERFORM60 project dedicated to model the Fe-Ni-Cr alloys.

➢ A pair interaction model (PIM) which can be used within the rigid lattice approach described in section II-1.

29   Chapter I. Methods and models

III-2-a   Interatomic potentials

Interatomic potentials provide a good compromise between computational cost and accuracy. Indeed, an interatomic potential is a mathematical function which describes how the total energy of the system depends on the coordinates of atoms. This function is designed to reproduce a certain number of properties of the real systems as accurately as possible. The form of the function chosen often depends on the kind of material the potential is supposed to model. The earliest simulations used simple pair potentials, where the total energy of the system can be obtained as a sum over interactions between two isolated particles as in Eq. I-19.

$$U(r_1, r_2, \dots, r_N) = \sum_i \sum_{j>i} V\big(|\vec{r_i} - \vec{r_j}|\big)$$ Eq. I-19

Well-known examples are the Lennard-Jones or the Morse potentials. For metallic systems, it quickly appeared that this approach is not realistic because such potentials cannot describe correctly the formation of surfaces or of vacancies among other properties. As a result, a whole class of many-body potentials were derived 30 years ago. In this scheme, the total energy of the system, E, is usually obtained as a pair contribution, V_{ij}, which models the repulsion experienced by the nuclei at short distances and a many-body term, $U(\Omega)$, which models the cohesion brought by the electron sea, as in Eq. I-20.

$$E = \frac{1}{2} \sum_i \sum_j V_{ij}\big(|\vec{r_i} - \vec{r_j}|\big) + U(\Omega)$$ Eq. I-20

One of the most used method is the embedded atom method (EAM) [DAW1984], which is based on the simplified description of the electronic density. The EAM approach includes an embedding energies, F_{A_i}, dependent on the local electron density ρ_i of each element A_i, in addition to the sum of pair interactions, $V_{A_i B_j}\big(|\vec{r_i} - \vec{r_j}|\big)$, occurring between all atoms A_i positioned at coordinates vector $\vec{r_i}$ and their first nearest atoms B_j positioned at the coordinates vectors $\vec{r_j}$. The contribution F_{A_i} approximates the many-body contribution of all nearby atoms. The total energy within EAM is therefore given as:

30   Chapter I. Methods and models

$$E = \frac{1}{2} \sum_{\substack{i,j=1 \\ j \neq i}}^{N} V_{A_i B_j}\left(\left|\vec{r_i} - \vec{r_j}\right|\right) + \sum_{i=1}^{N} F_{A_i}(\rho_i) \qquad \text{Eq. I-21}$$

where i and j run over all the lattice sites, F_{A_i} refers to an embedding function that represents the energy required to place the A atom positioned at site i into the electron cloud of electronic density ρ_i. In metal, interactions between two elements positioned at sites i and j respectively can be neglected beyond a certain distance R_{AB}. This distance is called the cut-off energy and is usually chosen so as to take into account the neighbouring shells which contribute significantly to the total energy of the system.

III-2-b   Pair interaction models

PIM requires the description of a limited number of pair interactions between elements positioned at perfect lattice sites, thus being only suitable using the rigid lattice approach described in section II-1.

The total energy of the system, E, is obtained as a sum of pair interactions, $\varepsilon^k_{A_i B_j}$, occuring between all elements A_i positioned at the perfect lattice sites and their nearest elements B_j included until the Nth shell:

$$E = \frac{1}{2} \sum_{k=1}^{N} \sum_{i,j} \varepsilon^k_{A_i B_j} \qquad \text{Eq. I-22}$$

where i runs over each site of the perfect lattice, j runs over each atom positioned in the kth shell and k runs over the shells around the site i. In this approach the cutting radius is the same for all elements and is equal to the distance between two elements positioned at N^{th} neighbours separation from each other.

When using the simplest formulation of this approach, only the interactions between atom pairs positioned at nearest neighbour separations, ε_{AB} (A and B refer to atom type), is required. In

order to model Fe-Ni-Cr alloys, 6 interaction parameters are therefore required as presented schematically in Fig. I-3.
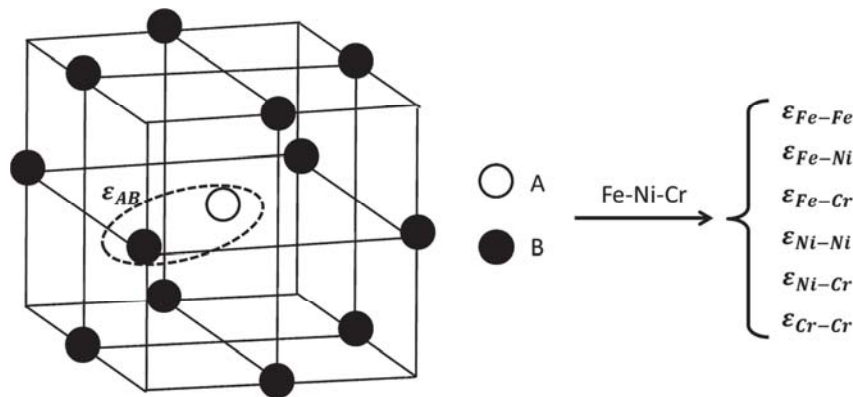
Fig. I-3: Schematic representation of interactions parameters between solute elements in perfect lattice sites, ε_{AB} (A and B refer to atom type). In Fe-Ni-Cr, 6 interaction parameters are considered.

When using this approach, Eq. I-22 can therefore be rewritten as:

$$E = \frac{1}{2}\sum_{i,j} \varepsilon_{A_i B_j} \qquad \text{Eq. I-23}$$

where i runs over each site of a perfect lattice and j runs over each atom positioned in the first shell of the lattice site i (i.e. 12 in the fcc lattice).

However, the study of non-equilibrium segregation in ASS requires the consideration of point defects, i.e. vacancy and SIAs, by which the matter transport occurs. To this end, two other sets of pair interactions are considered for the vacancy (Fig. I-4) and for the SIAs (Fig. I-5).

Similarly to the case of pair interactions between solute atoms presented above, the interactions of the vacancies with their vicinities involve elements positioned at perfect lattice sites. PIM limited to 1nn thus require the knowledge of ε_{VA} (A refers to element type and V to vacancy) interaction energies, the number of which is 4 in the Fe-Ni-Cr system as presented schematically in Fig. I-4.

32   Chapter I. Methods and models
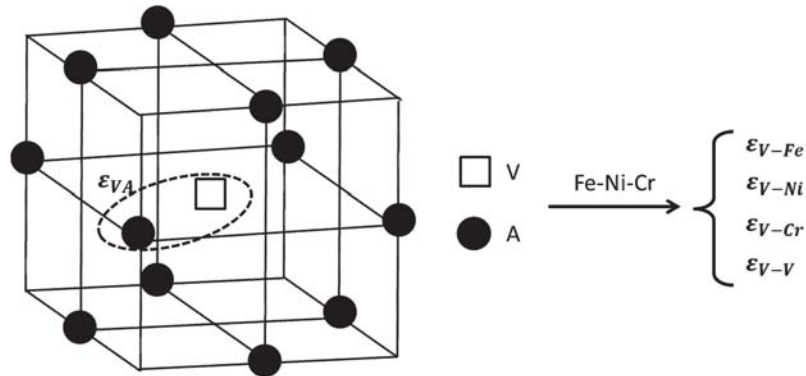
Fig. I-4: Schematic representation of interactions parameters between elements in perfect lattice sites and the vacancy, ε_{VA} (A refers to element type and V to vacancy). In Fe-Ni-Cr, 4 interaction parameters are considered.

The above-mentioned ε parameters are thus defined for all elements positioned at perfect lattice sites, which is the case for the different alloying elements but also the vacancies. Eq. I-23 therefore applies to all these interaction parameters. The consideration of SIAs in the PIM is however more complex. Indeed, atoms are introduced in interstitial sites, thus breaking locally the symmetry of atomic arrangement. We therefore consider two kinds of atoms 1nn to SIAs: atoms positioned in compressive sites, i.e. the atoms 1nn to the interstitial site but closer to dumbbell atoms, and atoms in tensile sites, i.e. the atoms 1nn to the interstitial site but more distant to dumbbell atoms. Pair interaction parameters between the dumbbell atoms; $E^b_{A^{SIA}B^{SIA}}$ (A and B refer to atom type), and between the dumbbell atoms and their 1nn atoms in compressive sites, $E^b_{A^{SIA}C^{1nnc}}$ (A and C refer to atom type), are therefore used as presented schematically in Fig. I-5. In order to avoid tree body interactions, we consider pair interactions of atoms in tensile sites, not with the dumbbell atoms but with the whole dumbbell, $E^b_{C^{1nnt}SIA}$ (C refers to atom type and SIA refers to the whole dumbbell). In Fe-Ni-Cr alloys, 15 additional interaction parameters are therefore considered for the SIAs. It can be noted that these interaction parameters are directly defined as binding energies unlike the above mentioned ε parameters. Thus, one additional parameter used as reference for the dumbbell formation energy has to be considered. Using our PIM, Fe-Fe SIA is chosen as reference formation energy and the associated parameter will be referred to as E^f_{Fe-Fe}.

33   Chapter I. Methods and models
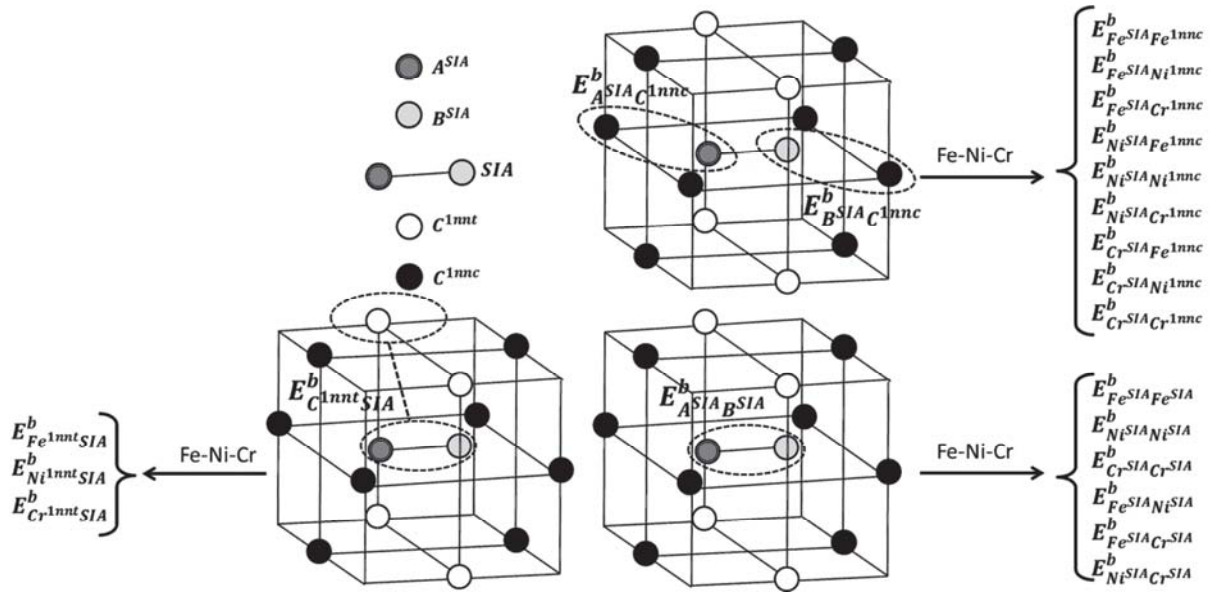
Fig. I-5: Schematic representation of interactions considered between a dumbbell and its first nearest atoms. The dumbbell atoms (A^{SIA} and B^{SIA}) are represented in grey, the atoms positioned in compressive sites (C^{1nnc}) are represented in black, and the atoms positioned in tensile sites (C^{1nnt}) are represented in white. We consider the binding energies between the dumbbell atoms, $E^b_{A^{SIA}B^{SIA}}$, between the dumbbell atoms and their 1nn in compressive sites, $E^b_{A^{SIA}C^{1nnc}}$, and between the whole dumbbell and their 1nn in tensile sites, $E^b_{C^{1nnt}SIA}$. In Fe-Ni-Cr, 15 interaction parameters are considered.

The energy associated to each site, e_{A-B}, where instead of having an element positioned in a perfect lattice site we have a dumbbell A-B is therefore expressed as:

$$e_{A-B} = E^f_{Fe-Fe} - E^b_{A^{SIA}B^{SIA}} - \sum_i E^b_{A^{SIA}C_i^{1nnc}} - \sum_i E^b_{B^{SIA}C_i^{1nnc}} - \sum_j E^b_{C_j^{1nnt}SIA} \qquad \text{Eq. I-24}$$

where i runs over each 1nn atom located in a compressive site of the dumbbell A-B and j runs over each 1nn atom positioned in a tensile site of dumbbell atoms (A and B).

IV   Calculating properties of materials

As mentioned previously, three atomistic methods and three cohesive models are used in this work to investigate the properties of fcc Fe-Ni-Cr systems. In order to check the reliability of empirical cohesive models for RIS modelling using AKMC in chapter IV , a certain number of system properties have been calculated and compared with the data available in the literature, i.e.

DFT and experimental data but also DFT calculations performed in the Fe-10Ni-20Cr target system presented in chapter III. The connection existing between the atomistic models and the cohesive models used in this work are listed below:

➢ DFT is used to investigate the stability of the Fe-10Ni-20Cr target system and to perform point defect calculations.

➢ In the framework of the PERFORM60 project, several Fe-Ni-Cr potentials have been built and are tested in the work. Both point defect formation and binding energies have been calculated using MD (relaxed calculations) or within the framework of the rigid lattice approach (unrelaxed calculations) used to perform MC calculations. The phase stability of the Fe-10Ni-20Cr target system has also been checked using MMC.

➢ A PIM has been built in this work within the framework of the rigid lattice approach. In order to test this cohesive model, both point defect formation and binding energies have been calculated. Segregation profiles and transport coefficients (diffusion coefficients and correlation factors) have also been calculated using AKMC.

In this section, the calculations of these properties of interest for RIS modelling are presented.

IV-1   Migration energy

The migration barriers are key properties to model diffusion at the atomistic level. Indeed, the energies required for atoms to move through the material in various local environments need to be described consistently. Various approaches may be used to estimate the migration energy. The different methods used in this study to estimate these energies are:

➢ The drag method which requires the use of cohesive models able to calculate the total energy of a system as a function of continuous atomic coordinates (using DFT or empirical potentials only).

➢ The final initial state energy (FISE) model which was used to estimate the migration barriers using the rigid lattice approach presented in section II-1.

➢ The cut bond model, which is another approach to estimate the migration barriers in the framework of the rigid lattice model, used by other groups, and in particular by Barbe [BARBE2006] is presented in last section.

IV-1-a   The drag method

A simple method to calculate the required energy for a migrating atom to exchange with a 1nn vacancy is the drag method. Starting from the initial state, small fixed length displacements are applied to the migrating atom towards the final state along the line connecting these states. At each step, the system is allowed to relax only in the plane perpendicular to this line. The lowest energy path connecting initial and final states, called the minimum energy path, is therefore determined. A schematic representation of the drag method is given in Fig. I-6.
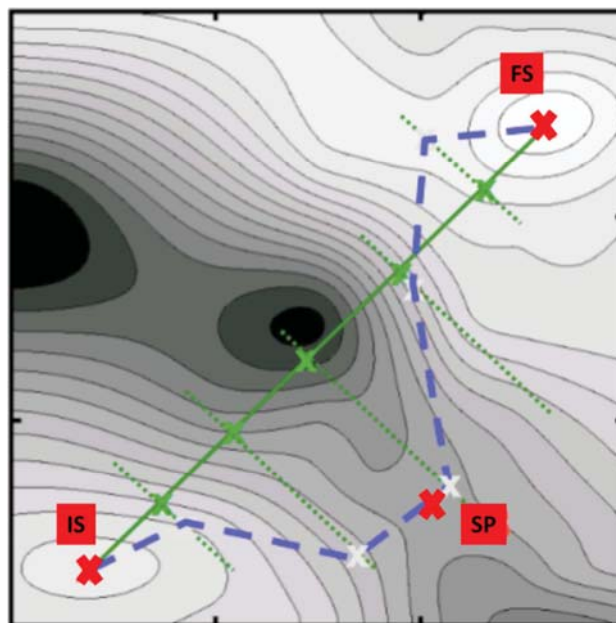
Fig. I-6: Schematic representation of the drag method. The green solid line refers to the line connecting initial and final states. The blue dashed line refers to the minimum energy path found by following the drag method procedure. Green solid crosses refer to the displacement applied to the migrating atom. Red solid crosses define the position of the initial state (IS), the final state (FS) and the saddle point (SP), which corresponds to the highest energy measured along the minimum energy path. Figure taken from http://www.fhi-berlin.mpg.de.

The drag method requires being capable of determining the total energy of the system for any positions of all the atoms. It can thus be applied within the framework of the DFT or using empirical interatomic potentials.

However, even if less time consuming than DFT calculations, full calculations of all the migration barriers encountered by a vacancy during its diffusion in a relatively complex system

36   Chapter I. Methods and models

such as the ternary Fe-Ni-Cr alloy we study is still very much time consuming using a potential and are still limited to relatively small systems and short simulation times [BOCQUET2002].

IV-1-b   The rigid lattice approach

When it is not possible to determine the total energy of the systems for any configurations of the atoms, and thus in particular when one atom is at the saddle point (SP) which is the case of the PIM described in III-2-b, one has to resort to simple models to estimate the activation barrier. We used the FISE model [VINCENT2008, WIRTH1999] in this work whereas other groups [SOISSON1996, LE BOUAR2002, SCHMAUDER2002, BARBE2006] employ the cut bond approach. These two models are presented in the next sections.

IV-1-b-i   FISE model

The FISE model describes the SP energy by considering the energy difference caused by a vacancy-atom exchange, and a term E_{a_0} whose purpose is to capture kinetic information of the system, as follows:

$$E_a = E_{a_0} + \frac{E_{final} - E_{initial}}{2} \qquad\qquad \text{Eq. I-25}$$

where $E_{initial}$ and E_{final} correspond to the total energy of the system before and after the vacancy jump respectively. This model therefore requires a cohesive model to determine the energy difference caused by the vacancy jump. This energy difference can be calculated using either an interatomic potential or a PIM.
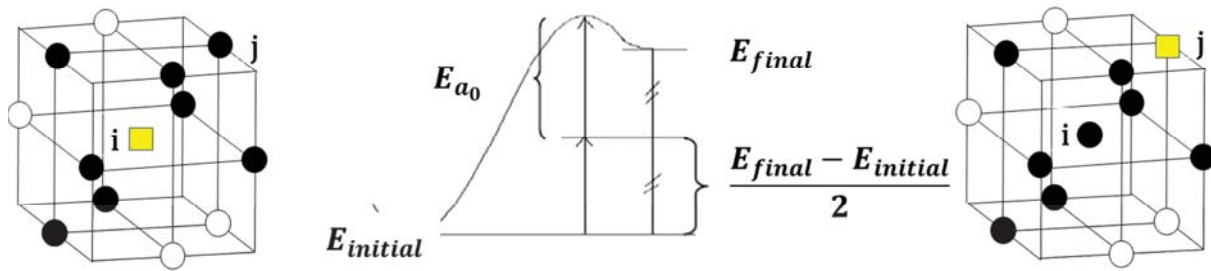
Fig. I-7: Schematic description of the model used in this work (FISE model) to calculate the migration barriers using the AKMC method (rigid lattice approach). Yellow squares refer to point defects. In the initial state of energy $E_{initial}$, the vacancy is positioned at site i, the atom selected to achieve the jump is positioned at site j. After the jump, the total energy of the system becomes E_{final} and the migrating barrier is estimated as $E_a = E_{a_0} + \frac{E_{final} - E_{initial}}{2}$

In bcc Fe with dilute concentration of solutes, good results were obtained using E_{a_0} which only depended on the migrating atom type [VINCENT2008]. However, in some systems and in particular in concentrated systems, the migration energy depends strongly on the local environment at the SP. For example, DFT calculations performed in bcc Fe-Cr concentrated alloys have revealed a strong influence of the number of Cr atom first nearest neighbours of both the initial and final positions of migrating atoms, as well as of the SP [COSTA2012]. Costa et al. have therefore found it necessary to calculate the activation barriers using a value for E_{a_0} which depends on the local environment of the jumping vacancy. In our work, the same approximation as the one used by Vincent [VINCENT2008] is considered (i.e. E_{a_0} value only depends on the migrating atom type).

In the specific case of the vacancy jump presented in Fig. I-7, and using a PIM on a rigid lattice, the activation energy for the vacancy jump can be easily calculated as follows:

$$E_a = E_{a_0} - \sum_k \varepsilon_{A_i B_k} - \sum_k \varepsilon_{V_j B_k} + \sum_k \varepsilon_{A_j B_k} + \sum_k \varepsilon_{V_i B_k} \qquad \text{Eq. I-26}$$

where, before the vacancy jump, the vacancy V_i is positioned at site i and the atom selected to achieve the jump A_j is positioned at site j. After and before the jump, the first nearest neighbours of these two elements are B_k elements, where k runs over their first nearest neighbours.

IV-1-b-ii   Cut bond model

Another approach used by Barbe to study the diffusion properties of Fe-Ni-Cr alloys, [BARBE2006], consists in estimating the SP energy by introducing a second set of interaction parameters ε_{AB}^{SP}, which directly take into account the influence of the local environment of the SP site, on the SP energy. In this so-called cut bond model, activation energies are therefore obtained by considering the energy of the SP, E_{SP}, as well as the energy of the system before the vacancy jump, $E_{initial}$, as follows:

$$E_a = E_{SP} - E_{initial}$$
<div align="right">Eq. I-27</div>
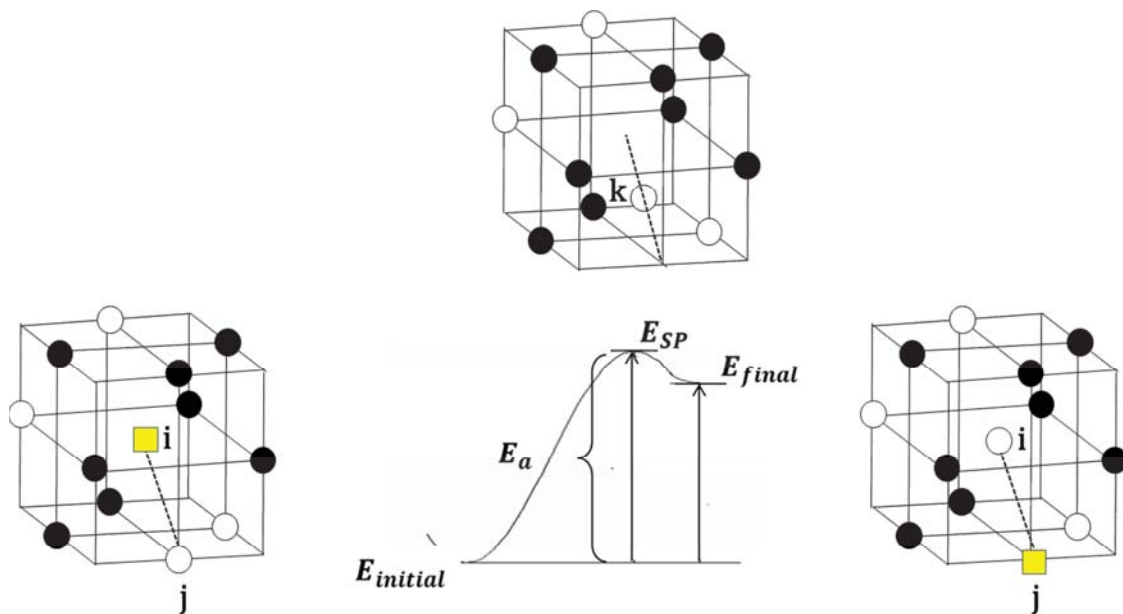
Fig. I-8: Schematic description of the cut bond model which can be used to calculate the migration barriers using the AKMC method (rigid lattice approach). Yellow squares refer to point defects. In the initial state of energy $E_{initial}$, the vacancy is positioned at site i, the atom selected to achieve the jump is positioned at site j. At site k presented in the upper part of the figure, the SP energy, E_{SP}, is estimated by considering interactions between the migrating atom and the SP environment, independently of interaction parameters used in the bulk. The migration barrier is calculated as $E_a = E_{SP} - E_{initial}$

In the specific case of the vacancy jump presented in Fig. I-8, the activation energy is therefore calculated as follows:

$$E_a = \sum_l \varepsilon^{SP}_{A_k B_l} - \sum_l \varepsilon_{A_j B_l} - \sum_l \varepsilon_{V_i B_l} - \varepsilon_{A_j V_i} \qquad \text{Eq. I-28}$$

where, before the vacancy jump, the vacancy V_i is positioned at site i and the atom selected to achieve the jump A_j is positioned at site j. The first nearest neighbours of these two elements are B_l elements where l runs over their first nearest neighbours. It has to be noted that the final state do not play any role into this equation.

IV-2   Cohesive and mixing energies

The cohesive energy is the difference between the energy per atom of a system of free atoms at rest far apart from each other, and the energy of the solid.

In the case of a PIM limited to 1nn interactions, the cohesive energy of a pure A atom matrix, E_c^A, can be obtained as displayed in Eq. I-29. In a fcc phase, the coordination number z is equal to 12 and therefore, by taking account of the double counting, the cohesive energies correspond to 6 times the diagonal interaction parameters ε_{AA}.

$$E_c^A = \frac{z}{2}\varepsilon_{AA} \qquad \text{Eq. I-29}$$

The cohesive energy for an alloy A-B can be approximated using the regular lattice approximation as:

$$E_c^{A_{1-x}B_x} = xE_c^B + (1-x)E_c^A + E_{mix}^{A_{1-x}B_x} \qquad \text{Eq. I-30}$$

where x is the B content, both E_c^A and E_c^B are the cohesive energies of pure A and pure B respectively and $E_{mix}^{A_{1-x}B_x}$ is the mixing energy of an alloy A-B containing x at.% of B atoms. Indeed, in this case of systems of interacting elements, the total energy of the system depends on the relative position between elements introduced in the system. As a result, at the steady state, the mean local environment of each element depends on the temperature and interactions between elements. The mixing energy thus corresponds to the deviation of the total energy from ideality when different interacting elements are introduced in a system to form a mixture. In the

simplest approximation, i.e. the regular solution approximation, the mixing energy of a binary $A_{1-x}B_x$ can be expressed as in Eq. I-31 where $\Omega^{AB}(x)$, which generally depends on the alloy composition, characterises the behaviour of the mixture: ordering or demixing.

$$E_{mix}^{A_{1-x}B_x} = x(1-x)\Omega^{AB}(x) \qquad \text{Eq. I-31}$$

In the simplest case, i.e. when using a PIM limited to the 1nn interactions, Ω^{AB} can be expressed using the Bragg-Williams approximation as follows in Eq. I-32 where z refers to the coordination number.

$$\Omega^{AB} = z(\varepsilon_{AA} + \varepsilon_{BB} - 2\varepsilon_{AB}) \qquad \text{Eq. I-32}$$

Following the usual convention:

- ➢ $\Omega^{AB} > 0$: an ordering tendency will be observed.
- ➢ $\Omega^{AB} < 0$: a demixing tendency will be observed.

Ordering energies have however to be compared to the thermal fluctuations $k_B T$. Indeed, at an infinite temperature, thermal fluctuations are much more important than interaction energies, and hence the system is completely disordered. Thus, a critical temperature, T_c, at which interactions energies are significant compared to thermal fluctuations may be defined as follows:

$$T_c = \frac{\kappa\Omega^{AB}}{2k_B} \qquad \text{Eq. I-33}$$

where κ is a constant equal to 1/3 for a binary system which tend to be ordered, and -1 for a binary system having a demixing tendency [DE FONTAINE1979].

IV-3 Point defect formation energies

IV-3-a Pure systems

The vacancy formation energy represents the energy required to introduce a vacancy in a system or more precisely to remove one atom of the system.

In pure systems, the vacancy formation energy, $E_f^{V/A}$, can be calculated simply by comparing the total energies of pure systems of atoms A, with and without vacancy, i.e. E_{N-1} and E_N respectively as in Eq. I-34, where N is the number of atoms introduced in the defect free lattice.

$$E_f^{V/A} = E_{N-1} - \frac{N-1}{N} E_N \qquad \text{Eq. I-34}$$

Using a PIM limited to the 1nn interactions, the vacancy formation energy is therefore expressed as in Eq. I-35, where z is the coordination number.

$$E_f^{V/A} = z(\varepsilon_{VA} - \frac{\varepsilon_{AA}}{2}) \qquad \text{Eq. I-35}$$

Similarly, the SIA formation energy represents the energy required to introduce an extra atom in a system. In pure systems, the SIA formation energy can be calculated by comparing the total energies of pure systems of atoms A, with and without a SIA, i.e. E_{N+1} and E_N respectively.as:

$$E_f^{SIA/A} = E_{N+1} - \frac{N+1}{N} E_N \qquad \text{Eq. I-36}$$

IV-3-b   Concentrated systems

In pure and infinite systems, the introduction of a point defect is similar whatever the site the defect is positioned in. However, in concentrated alloys, the formula used in Eq. I-34 and in Eq. I-36 cannot be used as all the environments are not equivalent.

For this reason, we used Grandjean's model [GRANJEAN1995] which is a thermodynamic model under the statistical assumption of Bragg-Williams. Using this model, the vacancy formation energies, $E_f^{V/AB}$ and $E_f^{V/ABC}$ for binary and ternary systems respectively, as a function of the concentration can be expressed as follows:

$$E_f^{V/AB} = c_A E_f^{V/A} + c_B E_f^{V/B} + c_A c_B \Omega^{AB} \qquad \text{Eq. I-37}$$

$$E_f^{V/ABC} = c_A E_f^{V/A} + c_B E_f^{V/B} + c_C E_f^{V/C} + c_A c_B \Omega^{AB} + c_A c_C \Omega^{AC} + c_B c_C \Omega^{BC} \qquad \text{Eq. I-38}$$

where c_A is the concentration of the element A, $E_f^{V/A}$ corresponds to the vacancy formation energy in a pure lattice of atoms A and Ω^{AB} refers to the ordering energy between elements A and B. This model is presented in more details in annex 1.

When one tries to estimate the vacancy formation energy using atomistic methods such as DFT, an additional problem arises as the energy calculated depends on the specific atomic configuration used. One has to theoretically determine the energy required to create a vacancy for all possible configurations of the lattice and take into account the chemical potential. Precise estimates of chemical potentials would be however extremely time consuming. This would require sampling of a large number of configurations by, for instance a Monte-Carlo Metropolis procedure. Once the chemical potentials of interest are known, the energy required may be calculated as:

$$\Delta E^V = E_{N-1} - (E_N - \mu_A) \qquad \text{Eq. I-39}$$

$$\Delta E^{SIA} = E_{N+1} - (E_N + \mu_A) \qquad \text{Eq. I-40}$$

Where ΔE^V (ΔE^{SIA}) refers to the required energy to remove (add) one element A from (in) the reference state to form a vacancy (SIA). E_{N-1} (E_{N+1}) and E_N refer to the energy of the concentrated system with and without vacancy (SIA), and μ_A refers to the chemical potential of the species A removed to introduce the vacancy. It has to be noted that ΔE^V and ΔE^{SIA} energies will be usually referred to as point defect formation energies for simplicity purposes.

IV-4 Binding energy

The binding energy represents the energy gained or lost when one brings two elements A and B at a distance where they start "feeling" one another. In a system containing N atoms, the binding energy between two defects A and B, $E_b(A, B)$, is defined as the difference of the two system energies E_1 and E_2, system 1 where A and B do not interact, i.e. the distance between A and B is greater than the potential cut-off, and system 2 where A and B interact. The distance between A

and B may be first nearest neighbour distance, second nearest neighbour distance and so on. The binding energy $E_b(A, B)$ is the difference between the two total system energies, i.e. $E_b(A, B) = E_1 - E_2$. When the size of the simulation box is small, such as in the case of DFT calculations, the binding energies are obtained using the following equation:

$$E_b(A, B) = [E(N - 1 + A) + E(N - 1 + B)] - [E(N - 2 + A + B) + E_{ref}] \qquad \text{Eq. I-41}$$

where $E(N - 1 + A)$ is the energy of a supercell containing only defect A, $E(N - 1 + B)$ the energy of the same supercell containing only defect B, $E(N - 2 + A + B)$ the energy of the same supercell containing A and B, and E_{ref} the energy of the supercell containing no defect. In this scheme, a positive binding energy indicates an attractive interaction. Depending on whether the whole lattice is allowed to relax or not in each calculation, one has access to relaxed or unrelaxed binding energies.

Using a PIM limited to 1nn interactions, the binding energies can be simply deduced from the knowledge of the interaction parameters ε. The binding energy between two atoms A in a solvent C, $E_b^{AA/C}$, can be obtained as in Eq. I-42, whereas the binding energy between two atoms A and B in a solvent C, $E_b^{AB/C}$ can be calculated using Eq. I-43.

$$E_b^{AA/C} = 2\varepsilon_{AC} - \varepsilon_{CC} - \varepsilon_{AA} \qquad \text{Eq. I-42}$$

$$E_b^{AB/C} = \varepsilon_{AC} + \varepsilon_{BC} - \varepsilon_{AB} - \varepsilon_{CC} \qquad \text{Eq. I-43}$$

IV-5   Surface energy

The surface energy quantifies the disruption of atomic bonds that occur when a surface is created. It can be calculated by comparing the energy of a matrix, relative to its energy when a surface has been introduced along the specific direction. Using a PIM limited to 1nn interactions, the necessary energies to create a free surface oriented perpendicular to the $\langle 111 \rangle$ axis in a lattice of atoms A, $E_{surf\langle 111 \rangle}^A$, is presented in Eq. I-44 where a refers to the lattice spacing.

$$E^A_{surf\langle 111\rangle} = \frac{(6\varepsilon_{AV} - 3\varepsilon_{AA})}{\sqrt{3}a^2/8} \qquad\qquad \text{Eq. I-44}$$

IV-6 Surface segregation energy

The surface segregation energy, which characterizes the tendency of atoms to segregate to the surface, is defined as the difference in energy for placing a substitutional impurity or solute atom at different surface atomic layers of an otherwise pure material relative to placing the solute atom in the bulk. Using a PIM limited to 1nn interactions, the surface segregation energy of an atom A initially in a medium of elements C and placed at the interface B/C oriented perpendicular to the $\langle 111\rangle$ axis, $E^{B/C}_{seg\_A\langle 111\rangle}$, is obtained as:

$$E^{B/C}_{seg\_A\langle 111\rangle} = 3(\varepsilon_{AC} + \varepsilon_{BC} - \varepsilon_{AB} - \varepsilon_{CC}) \qquad\qquad \text{Eq. I-45}$$

IV-7 Diffusion properties

Diffusion characterises the movement of particles in the matrix. It is a transport phenomenon which results in mass transport. One of the major issues in the field of diffusion is to establish the link existing between solid-state diffusion and the diffusion coefficients in alloys. Indeed, in irradiated materials, alloying elements move through the material via the jumps of a few point defects, thus involving a kinetic correlation between the successive jumps that each given atom will proceed during the diffusion process. Within the framework of TIP, these correlation effects can be calculated using the five frequency model (section IV-7-b-i) or AKMC simulations (section IV-7-b-ii).

IV-7-a   diffusion equations

In 1855, Fick derived its first law which state that the diffusion flux is proportional to the opposite of the concentration gradient as written in Eq. I-46 which represents the flux of an element B in a solvent A.

45   Chapter I. Methods and models

$$\vec{J_A} = -D_A\vec{\nabla}C_A \qquad\qquad \text{Eq. I-46}$$

$\vec{J_A}$ is the diffusion flux which represents the amount of species A crossing a unit surface per unit of time, D_A the diffusion coefficient or the diffusivity of species A and C_A the concentration of A at a given location of the lattice. However, Fick's first law does not take into account all direct and indirect driving forces acting on each species in the material and from the atomistic point of view, diffusion is considered as a result of the random walk of the diffusing particles. Thus, Fick's first law is frequently insufficient as a condition for describing the flux owing to the fact that the actual driving force for diffusion is not the concentration gradient but the chemical potential gradient.

In thermodynamics, the Onsager reciprocal relations express the equality of certain ratios between flows and forces in thermodynamic systems out of equilibrium, but where a notion of local order exists. More precisely, the Onsager flux equations of TIP provide the general formalism though the postulate of linear relations between the fluxes and the driving forces in multi-component alloys as in Eq. I-48.

$$\vec{J_A} = -\sum_B L_{AB}X_B \qquad\qquad \text{Eq. I-47}$$

X_B corresponds to the driving forces and L_{AB} are the phenomenological coefficients, which do not depend on the driving forces. Thus, correlation effects are taken into account when the non-diagonal terms of the L_{AB} matrix are not equal to zero. These equations are known to be the Onsager flux equations of irreversible processes. Without external solicitations, what is imposed is a gradient of chemical potentials and these equations can be expressed as [ALLNATT1987]:

$$\vec{J_A} = -\sum_B L_{AB}\nabla\mu_B \qquad\qquad \text{Eq. I-48}$$

where $\nabla\mu_B$ gradients correspond to the driving forces of diffusion of matter in materials. Thus, L_{AB} coefficients can be defined as the kinetic response of an alloy to a gradient of chemical. The

46 Chapter I. Methods and models

latter equation can be rewritten as a function of composition gradients which are more accessible for experimentalists, thus leading to the generalised Fick's laws:

$$\vec{J_A} = -\sum_B D_{AB} \nabla C_B \qquad \text{Eq. I-49}$$

where ∇C_B is the composition gradient and D_{AB} is the diffusivity matrix which is be expressed as in Eq. I-50 where C runs over the atomic species considered in the system:

$$D_{AB} = -\sum_C L_{AC} \frac{\partial \mu_C}{\partial C_B} \qquad \text{Eq. I-50}$$

Onsager coefficients can be obtained from the disposition of atoms using Allnatt's equation [ALLNATT1982] presented in Eq. I-51, where R_A refers to the collective displacement (or displacement of the centre-of-mass) of species A at the time t, and V corresponds to the system volume.

$$L_{AB} = \frac{\langle R_A \cdot R_B \rangle}{6 V k_B T t} \qquad \text{Eq. I-51}$$

It can be noted that in the case where species A and B do not interact with each other or that A and B species do not diffuse with the same defects involve that $\langle R_A \cdot R_B \rangle = 0$. As a result, the associated non-diagonal coefficients are equal to zero, i.e. the system is not correlated. Furthermore, Allnatt's equation is calculated using a generalisation of Einstein's equation for the tracer[3], D_A^*, presented in Eq. I-52, where r_A is the displacement of a specie A during the time t.

$$D_A^* = \frac{\langle r_A^2 \rangle}{6t} \qquad \text{Eq. I-52}$$

---

[3] Tracer diffusion corresponds to the spontaneous mixing of molecules taking place in the absence of concentration (or chemical potential) gradient. This type of diffusion can be followed using isotopic tracers, hence the name.

In solid-state diffusion, the atom motion usually takes place via the motion of point defects except when the atoms are very small. One then writes the tracer diffusion coefficients as in Eq. I-53:

$$D_A^* = f_A(zC_V W_A \lambda^2)$$

<div align="right">Eq. I-53</div>

where z is the coordination number, C_V the vacancy concentration, W_A the exchange frequency of an atom A with the vacancy, λ the jump distance and f_A is the correlation factor of atoms A which represent the expression of the correlation between the directions of the successive jumps of this atom type.

IV-7-b   Diffusion in dilute alloys

The next issue in this description is to find the link existing between the above-mentioned flux equations and the related atomic processes. To this end, diffusion coefficients can be obtained using atomistic models which provide a link between the different possible migration barriers encountered by the moving species and the diffusion coefficient or using AKMC simulations. In addition to the AKMC used in this work, we summarize in this section the five frequency model which has been recently used to interpret DFT data in dilute fcc systems presented in chapter II (section II-2-d).

IV-7-b-i   Atomistic models

One of the most used atomistic model is the "five-frequency model" derived by Lidiard and Leclaire [LIDIARD1955, LECLAIRE1956], for dilute alloys, which yields the diffusion rates of impurities by a mono-vacancy mechanism. In this model, one assumes that only monovacancies interact with isolated impurity atoms. It relates the three vacancy jump frequency ratios ω_4/ω_0, ω_2/ω_1 and ω_3/ω_1 (Fig. I-9) to four experimentally obtainable quantities: the ratio of solute and solvent tracer diffusion coefficients (D_B^*/D_A^*), the correlation factor f_B of impurity diffusion and the vacancy flow factor (L_{AB}/L_{BB}). The tracer diffusion coefficient D_B^*, which corresponds to the diffusion coefficient of a solute B in a solvent A, is given by Eq. I-54 in the dilute limit.

$$D_B^* = \frac{1}{6}\lambda^2 \omega_2 c_V z \exp\left(\beta G_{b,1nn}^{V-B}\right) f_B \qquad \text{Eq. I-54}$$

where λ is the length of each jump, f_B is the correlation factor which characterizes the efficiency of B jumps, c_V is the vacancy concentration, z is the coordination number of the lattice, ω_2 is the vacancy jump frequency which characterizes the exchange between B and a vacancy (Fig. I-9) and $G_{b,1nn}^{V-B}$ is the Gibbs free energy of binding between B and a vacancy positioned at 1nn separation. The tracer diffusion coefficient D_A^* or self diffusion coefficient given in Eq. I-55 can be easily deduced from Eq. I-54 by setting all the jump rates equal to ω_0. A value of 0.78 is thus found for f_0 in the fcc phase.

$$D_A^* = \frac{1}{6}\lambda^2 \omega_0 c_V z f_0 \qquad \text{Eq. I-55}$$

The correlation factor of B jumps in the fcc lattice [MANNING1959, MANNING1962, MANNING1964], is expressed in Eq. I-56. It characterizes the fraction of jumps for which the vacancy returns at a 1nn separation of B after dissociation [MANNING1964, KOIWA1983, ALLNATT1993]. Thus, F=1 when $\omega_4 \ll \omega_0$ and means that all paths that return a dissociated vacancy at a 1nn separation from solute atom B are equivalent. It has no impact on the correlation factor in that case. However, the factor F decreases when the relative difference of ω_4/ω_0 ratio increases.

$$f_B = \frac{2\omega_1 + 7\omega_3 F(\omega_4/\omega_0)}{2\omega_1 + 2\omega_2 + 7\omega_3 F(\omega_4/\omega_0)} \qquad \text{Eq. I-56}$$

This factor, F, was exactly calculated by Koiwa and Ishioka using the perturbation theory [KOIWA1983] and is given in Eq. I-57, where $x = \omega_4/\omega_0$ and the coefficients a_i and b_i have to be determined.

$$7F(x) = 7 - \frac{a_1 x + a_2 x^2 + a_3 x^3 + a_4 x^4}{b_0 + b_1 x + b_2 x^2 + b_3 x^3 + b_4 x^4} \qquad \text{Eq. I-57}$$
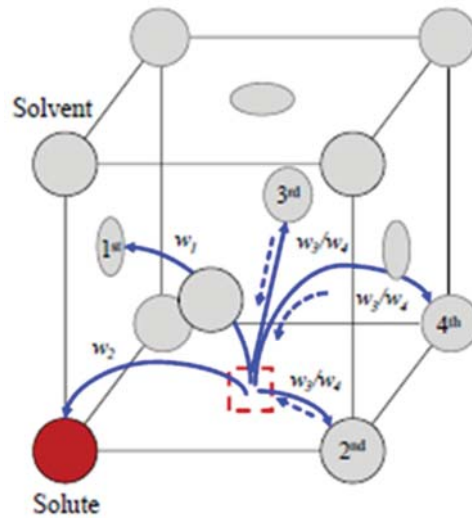
Fig. I-9: Illustration of the five-frequency model. Figure is taken from [TUCKER2008]

The various frequencies or reaction rate ω can be obtained using Eyring-Polanyi equation [EYRING1931, EYRING1935]:

$$\omega = \frac{k_B T}{\hbar} \exp\left(\frac{-\Delta G}{k_B T}\right)$$
Eq. I-58

where the pre-exponential factor corresponds to the mean rate of the reaction, ΔG is the Gibbs free energy of activation (activation energy contains both migration and formation energies), $\hbar$ is Planck's constant, k_B is Boltzmann's constant and T is the temperature. Gibbs free energy G contains contribution of the reference state, which is valid at 0 K, but also the different kind of excitations of this reference state in the case where temperature is considered. In the framework of DFT calculations, Eq. I-58 becomes Eq. I-59:

$$\omega = C_m \exp\left(-\frac{H_m}{k_B T}\right)$$
Eq. I-59

where the pre-exponential factor, C_m, can include the zero-point phonon contribution, but also electronic and magnetic contributions. H_m refers to the migration barrier for the selected atom to jump.

Models similar to the five-frequency model were built to determine phenomenological coefficient for dumbbells in dilute fcc alloys [ALLNATT1983, BARBU1980]. Interstitial mediated diffusion modelling requires however more information than in the case of vacancies. In particular, more dumbbell hopping rates are needed due to the fact that the dumbbell direction as well as its composition can change when hopping events occur. Indeed, one atom of the dumbbell migrates to a 1nn atom and forms a new dumbbell. This process can induce changes in both direction and composition of the migrating dumbbell. As a result, migration properties can evolve significantly during the course of the dumbbell diffusion.

<p style="text-align:center">IV-7-b-ii Kinetic Monte Carlo method</p>

Transport coefficients presented in Eq. I-51 and in Eq. I-52 are frequently used in atomic scale simulations such as AKMC to calculate diffusion coefficients by introducing one vacancy if the diffusion is vacancy mediated, and count the number of jumps the vacancy has done in the course of the simulation. This approach followed by Barashev for instance to study the migration of P and Cu in bcc Fe [BARASHEV2005, BARASHEV2006] and by Barbe [BARBE2006] in Fe-Ni-Cr alloys, is also used in this work.

We calculated the correlation factors using AKMC as the ratio between the quadratic distance really covered, and the quadratic distance which must have been achieved by a random motion:

$$f_{AB} = \frac{\langle R_A . R_B \rangle}{\langle M_A \rangle \lambda^2} \qquad\qquad \text{Eq. I-60}$$

R_A refers to the collective displacement (or displacement of the centre-of-mass) of species A at the time t, M_A corresponds to the number of jumps performed by all species A and λ refers to the distance covered by the migrating species at each jump.

The vacancy concentration, which has a strong impact on the diffusion coefficients (Eq. I-53), cannot be taken into account in AKMC simulations. In order to compare to high temperature diffusion experiments, we considered its influence by introducing the typical Boltzmann exponential dependence with temperature, $\exp\left(-E_f^V / k_B T\right)$, in Eq. I-52 which can therefore be rewritten as:

51   Chapter I. Methods and models

$$D_A^* = \frac{\langle r_A^2 \rangle}{6t} \exp\left(-\frac{E_f^V}{k_B T}\right)$$

Eq. I-61

where E_f^V is the vacancy formation energy which is calculated as a function of the alloy composition using Grandjean's equations presented in Eq. I-37 for a binary and in Eq. I-38 for a ternary.

V   <u>Conclusions</u>

In order to check the reliability of empirical cohesive models for RIS modelling using AKMC, three atomistic methods and three cohesive models are used in this work. The connection existing between the atomistic models and the cohesive models used in this work are summarised in Tab. I-1:

Cohesive model \ Atomistic model	DFT PAW	EAM potential	PIM
DFT (atomic relaxation)	In chapter III: ➢ Magnetic state phase stability of Fe-10Ni-20Cr (sections II and III). ➢ Substitutional formation energy in Fe-10Ni-20Cr (sections IV-2). ➢ Point defect formation in Fe-10Ni-20Cr (section IV-3 and IV-4).		
MD (atomic relaxation)		In chapter IV: ➢ Binding energies in dilute Fe-Ni-Cr (annex 4). ➢ Migration energies in pure fcc systems (section I-2-c). ➢ Phase stability of Fe-10Ni-20Cr alloy (section I-3).	
MC (rigid lattice)		In chapter IV: ➢ Binding energy in dilute Fe-Ni-Cr (section I-2-a). ➢ Vacancy formation in Fe-10Ni-20Cr (section I-2-b). ➢ Stability of the solid solution (MMC) in Fe-10Ni-20Cr (section I-4).	In chapter IV: ➢ Binding energy in dilute Fe-Ni-Cr (section II-2-a). ➢ Point defect formation in Fe-10Ni-20Cr (sections II-1-c and II-1-d). ➢ Substitutional formation energy in Fe-10Ni-20Cr (section II-2-b). ➢ Diffusion coefficient (AKMC) in Fe-10Ni-20Cr (section II-1-c). ➢ Correlation factor (AKMC) in Fe-10Ni-20Cr (section II-2-c). ➢ TNES profiles (MMC and AKMC) in Fe-10Ni-20Cr (section II-2-d). ➢ RIS profiles (AKMC) in Fe-10Ni-20Cr (section II-2-e)

Tab. I-1: Summary of the calculation performed using the three atomistic models used in the work, i.e. the density functional theory (DFT), the molecular dynamics (MD) and the Monte Carlo (MC).

Chapter II.   Bibliography

As stated in the introduction, RIS is a non-equilibrium process that occurs at point defect sinks during irradiation of an alloy at intermediate temperatures. Non-equilibrium segregation at point defect sinks was first observed in binary aluminium alloys [ANTHONY1968] and was found to be a very common phenomenon which occurs in many alloys and under all kinds of irradiation particles, i.e. ions, electrons and neutrons. The discovery of this phenomenon has motivated researches in many materials and in particular in austenitic stainless steels for which RIS was first demonstrated by Okamoto [OKAMOTO1973]. RIS has thus been studied in ASS for three decades in particular because of its technological importance in the nuclear industry as mentioned in the introduction. RIS is due to the preferential binding of solute atoms with fluxes of point defects which are created in overconcentration in irradiated materials. Diffusion mechanisms of segregating as well as depleting alloying elements are therefore of major interest to understand RIS. As a result, many models have been built to study the diffusion mechanisms. In section I, we summarize which insights these models have provided about RIS mechanisms. Finally, it has to be noted that RIS as well as diffusion of atoms through the materials ultimately depend on interaction properties occurring at the atomistic level between the different alloying elements and point defects. For this reason, in section II we therefore summarize the properties available between interacting elements in γ-Fe-Ni-Cr systems.

I   Radiation induced segregation

Non equilibrium segregation was first observed and discussed by Anthony in 1969 in binary aluminium alloys [ANTHONY1968]. Anthony has provided considerable insights in understanding non-equilibrium segregation mechanisms [ANTHONY1969, ANTHONY1970A, ANTHONY1970B, ANTHONY1970C]. In particular, he explained this segregation by the preferential binding between fluxes of excess vacancies and alloying elements. In his experiments, non-equilibrium segregation are due to the diffusion of excess vacancies formed in aluminium alloys after quenching from high temperature. Other experiments use irradiation which creates both vacancies and interstitials, thus increasing the number of mechanism leading to non-equilibrium profiles. In particular, non-equilibrium segregation in austenitic stainless steels was first

demonstrated by Okamoto in an electron and ion bombarded sample of Fe-18Cr-8Ni-1Si [OKAMOTO1973] who proposed another RIS mechanism involving interstitial atoms [OKAMOTO1974]. This conclusion was motivated by the fact that undersized solutes, which are more stable in interstitial sites, diffuse toward defect sinks while oversized solutes diffuse away.

I-1 General trends

Since the above mentioned findings, many experimental and theoretical studies have been conducted in austenitic stainless steels, in order to better understand RIS. In particular, the impact of alloy composition, temperature, irradiation particle type, dose and dose rate has been investigated thoroughly. Very thorough reviews [OKAMOTO1979, MAZIASZ1993, SIMONEN1999, NASTAR2012, KENIK2012], have been recently published and we will thus only summarize in the following section the general trends observed.

The first important topic in understanding RIS is the segregation behaviour of the major components of the stainless steels. In all experiments, Cr atoms deplete and Ni atoms enrich at defect sinks, and in particular at the GB which are strong defect sinks. Fe atoms can enrich or deplete at GB depending upon the alloy composition. These trends are observed whatever the particle irradiation type [ALLEN1997]. Although the irradiation type has a strong influence on the type of defects created as mentioned in the introduction, the data available show the same behaviour for RIS (at least qualitatively) whatever the irradiation type.

Although it seems quite difficult to predict which elements will segregate in a given alloy, it is clear from the large amount of experimental data gathered so far that the size of the migrating elements is one of the controlling criteria of RIS. The size of elements seems however to be the controlling criteria of segregation of minor elements as experiments indicate an enrichment of undersized[4] atoms and a depletion of oversized atoms [REHN1978, NAKATA1987, OKAMOTO1974]. Moreover, other alloying elements, even in small amount, can have a significant impact on the segregation behaviour. For instance, Kato et al. pointed out that the segregation of major

---

[4] Undersized solutes are those which reduce the mean atomic volume of the alloy [KING1966]

elements was significantly affected in austenitic 316L steels modified by oversized elements (Ti, Zr, Hf. V, Nb, Ta) [KATO1992]. Hf and Zr elements were found to particularly inhibit RIS, indicating that they play a role in the enhancement of vacancy-interstitial recombination and/or a reduction of the mobility of the point defects involved in the diffusion processes.

A complicating matter related to the issue of understanding RIS is that the austenitic stainless steels used in the pressure reactors are, like most structural materials in "real life", in metastable states which differ upon the method used to prepare them. As a result, when allowed to, and more precisely, in the presence of point defect overconcentration which will allow for diffusion to take place, they will evolve. As a result Thermal Non Equilibrium Segregations (TNES) are also observed under pure thermal treatments (i.e. without irradiation but in the presence of more point defects than the equilibrium concentration). Allen [ALLEN2007] in particular pointed out that depending upon the alloy cooling conditions, GB segregations in Ni based alloys could even change sign. These results underline the importance of point defects in all these solute redistribution events. Tab. II-1 (taken from [ALLEN2007]) summarizes the segregation trends observed in Fe based alloys for RIS and TNES. One conclusion which can be drawn from these results is that it seems difficult not to account for the role played by SIAs to understand them, as suggested early on by Okamoto [OKAMOTO1974], Johnson and Lam [JOHNSON1976] and Dederichs et al [DEDERICHS1978].

Element	TNES	RIS
P	Enriched	Enriched
Ti	Enriched	Enriched
Mo	Enriched	Depleted
Cr	Enriched	Depleted
Si	Depleted	Enriched
Ni	Depleted (small depletion or no segregation)	Enriched
Fe	Depleted	Depleted

Tab. II-1: Trends in segregation due to TNES and RIS in Fe-base austenitic alloys [ALLEN2007].

The influence of temperature on RIS follows what can be expected from phenomenon induced by point defect fluxes diffusion [NASTAR2012]. When the temperature is too low, the vacancies are immobile and there will be a large amount of recombination with the SIAs. When the

temperature is too high, the very high equilibrium vacancy concentration leads to back diffusion and suppresses segregation.

The effect of radiation particles, dose and dose rate can be understood in the same manner. The higher the flux or the dose rate, the more point defects there will be. As a result, RIS is observed to take place in a range of temperature and dose rate as can be seen in Fig. II-1 taken from Okamoto's review paper [OKAMOTO1979]. Note that Fig. II-1 is the result of modelling but the trends modelled agree with experimental data.
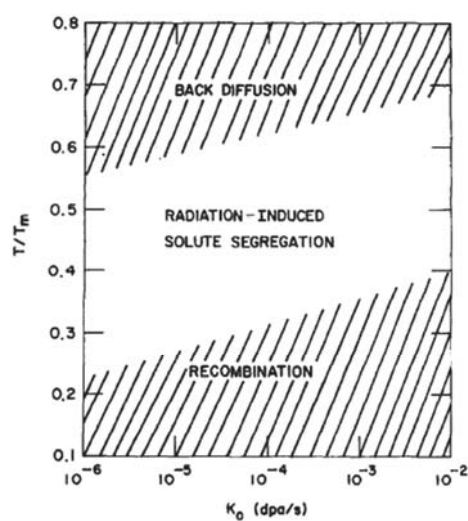
Fig. II-1: Temperature-dose rate diagram for radiation-induced segregation. T_m refers to the melting temperature. Figure taken from [OKAMOTO1979].

The nature of the sinks has also been found to play a role on RIS and more precisely on the segregation profiles as observed experimentally for GBs in ASS irradiated by 5 MeV protons [DUH1998, KAI2004] or by electrons [WATANABE2000A]. These studies indicate that the higher the GB misorientation, the higher RIS. This dependence has been introduced successfully in rate equation models [DUH2001, SAKAGUCHI2004].

Finally, the stability of the bulk phase can be modified in segregated area as the enhancement of the local solute concentration in the vicinity of a point defect sink can reach the solubility limit. As a result of temperature, increased defect concentrations and radiation-induced segregation, precipitation of wide variety of second phases is very often observed in irradiated ASS

[MAZIASZ1993]. A very recent example is the formation of $Cr_{23}C_6$ carbides at dislocation loops in ion irradiated stainless steels [JIN2012].

The following paragraphs summarize the literature regarding the mechanisms put forward to explain RIS in austenitic alloys.

I-2 Solute redistribution processes in alloys

Models based on TIP (section IV-7-a in chapter I) lead to the identification of the different basic mechanisms that could contribute to the global RIS process. The mechanisms leading to the redistribution of solute atoms in the presence of point defect fluxes fall theoretically into two categories. The first one is the solute dragging by point defects which can occur if solute atoms interact with vacancies or self-interstitials to form mobile complexes. In that case, the solute fluxes and the point defect fluxes are in the same direction. The other one is the inverse Kirkendall[5] effect which can also apply to vacancies or SIAs. The distinction between the different mechanisms is not so trivial, and what is really important is the respective direction of the point defect and the solute fluxes. In reality, three situations can arise which are illustrated in Fig. II-2 taken from [NASTAR2012].

➢ The solute flux flows in the same direction as the vacancy flux.

➢ The solute flux flows in the opposite direction to the vacancy flux.

➢ The solute flux flows in the same direction as the SIA flux.

The degree of segregation induced is therefore a balance between the flux of atoms to or from the sinks and back diffusion under radiation-enhanced conditions. Wiedersich [WIEDERSICH1979] was the first to propose a relationship linking the diffusion coefficients of elements via both vacancy and interstitial mechanisms to RIS in a binary alloy A-B. Using simplified flux equation he predicted that under steady state irradiation conditions, the gradient of a solute B at a sink is

---

[5] The Kirkendall effect is illustrated by the motion of the boundary layer between two metals which occurs as a consequence of the difference in diffusion rates of the metal atoms due to preferential exchange of one species with the vacancies. Since the diffusion fluxes are different, there will be a net flow of matter. In that case, the faster diffusing species moves in the opposite direction to the vacancy flux. During irradiation, the inverse situation arises near sinks where gradients in the vacancy and interstitial concentrations can induce a net flux of solute and solvent atoms across a "marker" plane in an initially homogeneous alloy.

57 Chapter II. Bibliography

proportional to $\left(D_A^V/D_B^V - D_A^I/D_B^I\right)$, where D_A^V refers to partial diffusion coefficients of element A via the vacancy mechanism and D_A^I refers to partial diffusion coefficients of element A via the interstitial mechanism.
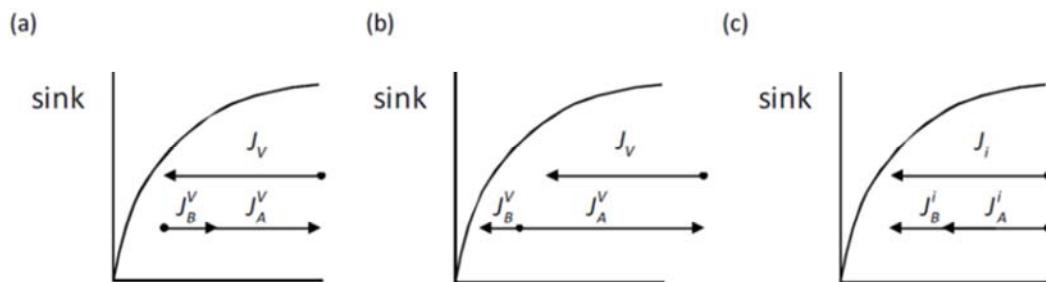
Fig. II-2: Schematic representation of inverse Kirkendall effects induced by (a) vacancy flux and (c) interstitial flux, as well as the drag effect (b) in an A-B binary alloy. This figure is taken from [NASTAR2012] In (a), an enrichment of B occurs if $D_B^V < D_A^V$, a depletion if $D_B^V > D_A^V$. In (b), an enrichment of B and a depletion of A occur. In (c) an enrichment of B occurs if $D_B^I > D_A^I$, a depletion if $D_B^I < D_A^I$.

In the cases of preferential migration of vacancies and/or interstitials via one alloying element or by preferential association of defects with one alloying element in a binary A-B, an element A can either deplete or enrich, relative to the other element B depending on the relative magnitudes of the ratios D_A^V/D_B^V and D_A^I/D_B^I. Thus, the two inverse Kirkendall effects can add or oppose each other in causing solute enrichment or depletion near a sink. It has to be noted that the inverse Kirkendall effect induced by a vacancy flux will always cause depletion at the sink of the faster diffusing element while the inverse Kirkendall effect induced by an interstitial flux as well as solute dragging by point defects will always cause enrichment at the sink of the faster diffusing element.

I-3 RIS in austenitic Fe–Cr–Ni alloys

Most of models which have contributed to improve understanding of RIS in ASS are based on the rate theory. In these models, rate constants $K = v\exp(-E_a/k_BT)$ takes into account kinetic aspect of the different reactions assumed to be the major contributor of solute redistribution at defect sinks. The vibration frequencies, v, as well as the activation energies, E_a, are usually deduced from diffusion experiments performed at high temperatures and adjusted to obtain the

diffusion rates leading to the desired segregation profiles. These models are based on the TIP (section IV-7-a in chapter I) defining a flux as a sum of driving forces multiplied by the phenomenological transport coefficients, L_{AB}.

As mentioned previously, the size of elements seems to play an important role in segregation as experiments indicate an enrichment of undersized atoms and a depletion of oversized atoms [REHN1978, NAKATA1987, OKAMOTO1974]. These observations suggest that interstitial mediated diffusion has a significant impact on RIS, particularly since the depletion of undersized solutes has never been observed despite more than three decades of intensive researches devoted to RIS [ARDELL2008]. This is also supported by the fact that enrichment of the slow diffusing elements and depletion of the fast diffusing elements are not always observed in austenitic stainless steels [OKAMOTO1979, REHN1978]. The preferential association of undersized atoms with the interstitial flux was therefore first assumed as major contributor. This interstitial binding mechanism was proposed by Wiedersich et al. [WIEDERSICH1979] and extended to Fe–Cr–Ni alloys by Lam et al. [LAM1982]. Although the importance of interstitial mediated diffusion was later confirmed by low temperatures experiments performed by Watanabe [WATANABE1997] showing the occurrence of RIS at temperatures at which vacancies were practically immobile (298-323 K), its modelling required large binding energy of mixed dumbbells with Ni atom (~0.75 eV) which is rather inconsistent with the fact that all the components of Fe-Ni-Cr alloys have nearly identical atom radii. Later, Stepanov et al. [STEPANOV2004] showed that the segregation profiles obtained at low temperature (323 K [WATANABE1997]) and at higher temperature (723 K [WATANABE2000B]) in Fe-14.5Ni-20.8Cr alloy could be both reproduced by using a model which takes into account of both interstitial and vacancy mechanisms of diffusion [PECHENKIN1999]. Furthermore a positive binding between vacancy and oversized atoms was found to enhance recombination and inhibit vacancy diffusion, consistently with experimental observation of suppression of both RIS and void swelling with the addition of a small amount of oversized atoms [KATO1992]. It can be noted that Nastar [NASTAR1998] et al. also explained the suppression of RIS by the formation of slowly migrating mixed dumbbells leading to an enhancement of the point defect recombination.

The preferential exchange of a solute with the vacancy as the sole contributor to RIS in Fe–Cr–Ni alloys was proposed by Marwick et al. [MARWICK1978] and modelled by Perks et al.

[PERKS1986]. Comparisons of RIS measurements to calculations using the Perks model, in which the segregation is based on differences in atom-vacancy jump rates of the constituent atoms, have shown that the inverse Kirkendall mechanism (specifically, the preferential coupling of solutes to the vacancy flux) adequately describes RIS in Fe-Cr-Ni alloys and that preferential interstitial effects are not required to explain the observed segregation [DAMCOTT1995, ALLEN1997, ALLEN1998B]. In general, the trends in segregation for austenitic Fe-Cr-Ni alloys as a function of irradiation temperature and dose are also correctly predicted qualitatively using this model (preferential coupling with the vacancy flux). In Fe-based alloys, the atom-vacancy exchange is also supported by the fact that the segregation trends of Fe, Ni and Cr atoms follows the trends predicted by high temperature diffusion measurements. In particular, model calculations showed that increasing the Cr–Fe diffusivity ratio, D_{Cr}^V/D_{Fe}^V, increases the Cr depletion and decreases the Ni enrichment [ALLEN1997]. Model prediction was however found not to be consistent in a Ni-based ternary alloy where the diffusion may be influenced by short range ordering forces known to exist in high Ni content Fe-Cr-Ni alloys. Furthermore, using this model, the inclusion of preferential binding of undersize atoms to the interstitial flux was found to greatly overpredict the measured segregation [ALLEN1998A]. Indeed, if preferential interstitial binding is included, model calculations cannot accurately reproduce segregation measurements unless nonphysical interstitial migration energies are chosen. Comparisons of RIS measurements in austenitic Fe-Cr-Ni alloys with calculations using an inverse Kirkendall model have also shown that composition specific diffusion parameters must be used to accurately predict segregation behaviour, thus limiting the model's predictive capability when no prior segregation measurements exist [DAMCOTT1995, ALLEN1997, ALLEN1998B]. Thus, the dependence of segregation on composition and short range ordering limit the capability of the Perks model to accurately predict segregation in Fe-Cr-Ni alloys for which no prior segregation measurements exist. In particular, ordering is manifested in a tendency to form Ni-Cr pairs in Fe-Ni-Cr alloys and is most pronounced in Ni-based alloys. However, in the majority of previous published calculations using the Perks model, the migration energies for each element are assumed to be equal with differences in segregation rates arising solely from differences in the pre-exponential factors. To include ordering effects, the migration energy term in the exponential must be described as a function of composition. Furthermore, the Perks model is based on Manning's

random alloy model, with the exchange frequencies and correlation factors calculated on the basis of random alloy theory, thus preventing from good predictive capabilities.

Allen et al. obtained a significant improvement in the predictive capabilities of RIS modelling by improving the Perks model [ALLEN1998A] in including composition dependent migration energies which incorporate short range ordering effects. In this new model, known to be the modified inverse Kirkendall (MIK) model, the composition dependent migration energies were obtained using the model first proposed by Grandjean et al. [GRANJEAN1994] to describe RIS in binary Ni-Cu alloys. In Grandjean's model, a single set of input parameters, based on pure element properties, is used to calculate the segregation kinetics at all compositions. Grandjean's method calculates the migration energies based on pair potentials and local composition and includes the possibility of ordering. Results obtained by Allen et al. [ALLEN1998A] showed that the MIK model more accurately predicts RIS than the original Perks model over a wide range of temperatures and doses and leads to a significant improvement of the capability to predict GB compositions in irradiated alloys. Thus, including composition dependent migration energies and short range ordering effects seems to be a key issue in RIS modelling.

However, ordering energies are not introduced in a consistent way using the MIK model, thus making impossible the description of equilibrium properties, although Lam and Wiedersich demonstrated in their study of modifications of subsurface alloy composition during high-temperature sputtering that the effect of the thermodynamic properties on the segregation process cannot be neglected [LAM1981]. This finding is supported by the study of Nastar [NASTAR2005] which shows the important contribution of the thermodynamic properties to the kinetics of RIS, in particular on the formation of the 'W-shaped' profile.

Hackett et al. [HACKETT2009A, HACKETT2009B] used successfully the MIK model to simulate the suppression of RIS by the addition of a small amount of oversized atoms. They found that oversized solute atoms enhance point defect recombination through a solute-vacancy trapping mechanism, resulting in a reduction in grain boundary Cr depletion, supported by the above-mentioned modelling of Stepanov [STEPANOV2004]. These studies revealed that the binding energy was the most important parameter to the trapping model and that large binding energies were required for significant reductions in RIS.

61 Chapter II. Bibliography

I-4 Conclusions

In the framework of rate theory, two mechanisms have been proposed for the occurrence of RIS in Fe–Cr–Ni alloys: (1) The preferential exchange of an alloying element with the vacancy flux (the vacancy mechanism portion of the inverse Kirkendall effect) as the sole contributor to RIS in Fe–Cr–Ni alloys was proposed by Marwick et al. [MARWICK1978] and modelled by Perks et al. [PERKS1986] (2) the preferential association of undersized atoms with the interstitial flux (interstitial binding), in which both interstitial binding and preferential association of solutes with the vacancy flux contribute to the segregation, was proposed by Wiedersich et al. [WIEDERSICH1979] and extended to Fe–Cr–Ni alloys by Lam et al. [LAM1982].

Although the understanding of solute redistribution processes has increased and despite the significant number of experimental and theoretical studies conducted, RIS mechanism is still debatable. In particular, many different models are able to obtain a quantitative description of experimental results, thus making difficult to determine the relative contribution of each basic mechanism presented in Fig. II-2. Indeed, these mechanisms are not necessary exclusive, especially as experiments have proved that both SIAs and vacancies promote segregation process under irradiation.

Although many models have been built to explain the experimental segregation data, assumptions had to be made about input parameters as well as dominant mechanisms because of the lack experimental data, thus making impossible the investigation of the large amount of possible RIS situations that can occur in austenitic stainless steels used in the nuclear industry because of their complexity and the wide variety of alloys used as well as the difference of operating conditions they have to withstand. While a large body of RIS experiments and related thermokinetics data exists for fitting, there is not enough data to accurately determine the complex relationships between all the key variables. In particular, due to the lack of data for the Onsager coefficients, various approximations made throughout the derivation result in an unclear expression of fluxes involving not well defined partial diffusion coefficients.

II   Properties of γ-Fe-Ni-Cr systems

Radiation induced segregation as well as all other defect mediated diffusion mechanisms, depend on the interactions between the point defects and the solute elements. Indeed, the strong interaction between solutes and the point defects generated during irradiation, result in coupled transport of the solute atoms by the point-defect fluxes to and away from sinks. The magnitude of jump frequency ratios between solute atoms and point defect determines whether the solute flow is towards or away from the sinks. In the following sections we will review the knowledge gathered on these issues

II-1   Experimental results

II-1-a   Point defects formation and migration

Experimental data on point defects properties such as the point defect formation energies, migration energies and binding properties are difficult to find in austenitic steels owing to the difficulty to determine them precisely and because they depend on the alloy concentration. In particular, we will show in the third chapter of this manuscript that the point defect formation energies are strongly correlated with their local environment which is difficult to probe. In dilute systems, more experimental data are available, however, the presence of impurities also complicate the problem, as proved by the debate over the vacancy migration energy in bcc Fe which was found to depend strongly on the purity of Fe [TABATA1981]. The vacancy formation energy measured in pure fcc Ni also covers a large range of values [EHRHART1991]. Similarly, the resistivity measurements frequently used to investigate point defect properties in austenitic stainless   steels   [BENKADDOUR1994,   DIMITROV1982,   DIMITROV1984,   DIMITROV1987, DIMITROV1988, DIMITROV1991, DIMITROV1993], may be difficult to interpret. Indeed, the resistivity variation observed during the recovery stages, i.e. when point defects become mobile, are due to two main contributions: (1) the change of local ordering in the material (2) defect annihilations occurring when defects can migrate through the material. Assumptions have therefore to be made to interpret the resistivity profiles [DIMITROV1981].

Despite these difficulties, results are however available for vacancy formation energies and both vacancy and interstitial migration energies in Fe-Ni-Cr alloys [BENKADDOUR1994, DIMITROV1982, DIMITROV1984, DIMITROV1987, DIMITROV1988, DIMITROV1991, DIMITROV1993, MALERBA2006, DIMELFI1980, HUGUENIN1987, HUGUENIN1989, EHRHART1991, SEEGER1998]. Experiments made by Benkaddour et al. and Dimitrov et al. were performed by analysing the change of resistivity variation-rate in electron irradiated austenitic steels while Hugenin et al. performed Positron lifetime experiments. The whole set of results for vacancy formation energies and both vacancy and interstitial migration energies, recently reviewed by Zouari [ZOUARI2012], are summarized from Fig. II-3 to Fig. II-5. The experimental points given in these figures for Fe and Fe-Cr systems, which have a bcc structure, are represented for comparison purpose. Moreover, in pure α-Fe, reported experimental values for the vacancy formation energy range from 1.5 to 2 eV [DE SCHEPPER1983, MAIER1978, SCHAEFER1977, MATTER1979, FURDERER1987, SEEGER1998]. In Fig. II-5 we however reported the most recent values proposed by Seeger in its review of the properties of vacancies in high-purity α-Fe [SEEGER1998]. Similarly, in pure γ-Ni, reported experimental values range from 1.45 to 1.8 eV [EHRHART1991]. Most of these experiments were performed using positron annihilation spectroscopy. However, in Fig. II-5 we reported the value proposed by Ehrhart [EHRHART1991]. This value is indeed recommended as a result of the work of Smedskjaer et al. [SMEDSKJAER1981].

In these experiments, two sets of data are particularly interesting because they were obtained in alloys with compositions close to the one of the ternary system we are interested in, i.e. the γ-$Fe_{70}Ni_{10}Cr_{20}$ austenitic alloy. The main results of the resistivity measurements performed by Benkaddour [BENKADDOUR1994] and Dimitrov [DIMITROV1988] in $Fe_{66-x}Ni_{25}Cr_{8+x}$ $(0 < x < 8)$ and $Fe_{64-x}Ni_{20+x}Cr_{16}$ $(0 < x < 55)$ systems can be summarized as follows:

➢ The mobility of vacancies does not seem to depend on Cr whereas it seems that interstitial mobility linearly increases with decreasing Cr content.

➢ By contrast, Ni content has a slight influence on the point defect mobility. Indeed, vacancy mobility tends to be slightly reduced at higher Ni concentration, whereas the self-interstitial mobility strongly increases with increasing Ni content.

➢ In γ-Fe$_{100-x-y}$Ni$_x$Cr$_y$ alloys, a linear relationship between interstitial activation energies, E$_a$, and both Ni and Cr content, x and y respectively, was thus proposed by Benkaddour by taking into account previous works: E$_a = 0.96 + 0.65y - 0.80x$.

➢ The vacancy formation energies tend to decrease linearly with increasing nickel concentrations.

➢ The addition of impurities as small as 1000 at ppm can deeply impact on point defect migration, as can be shown in Fig. II-3 and in Fig. II-4 were the corresponding values are reported. Indeed, point defects can significantly interact with solute atoms introduced even in very small quantities. This is for instance the case in the Fe-45Ni-16Cr alloy. Indeed, the presence of Ti results in an increase of the effective vacancy migration energy which can be related to the formation of V-Ti complexes by the trapping of vacancies at the beginning of their migration. Similarly, the presence of Si results in an increase of the effective interstitial migration energy which can be related to the interstitial trapping by Si atoms.
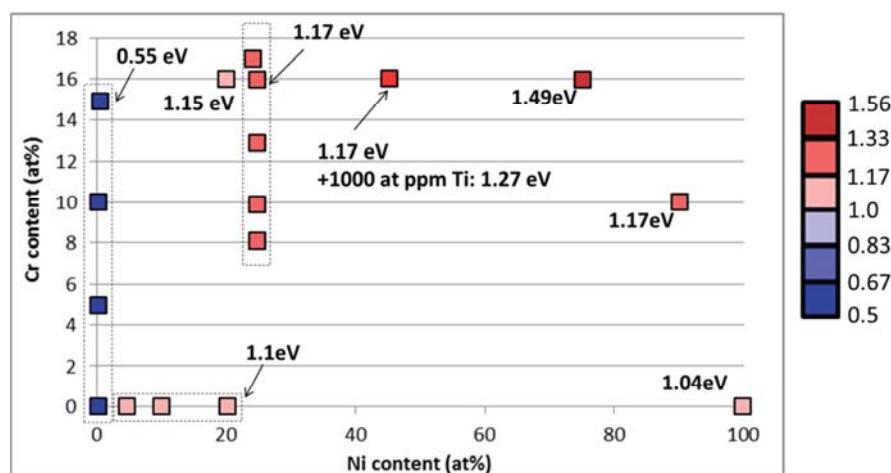
Fig. II-3: Experimental values found in the literature for the vacancy migration energies in Fe$_{100-x-y}$Ni$_x$Cr$_y$ alloys. This picture is inspired from [ZOUARI2012].
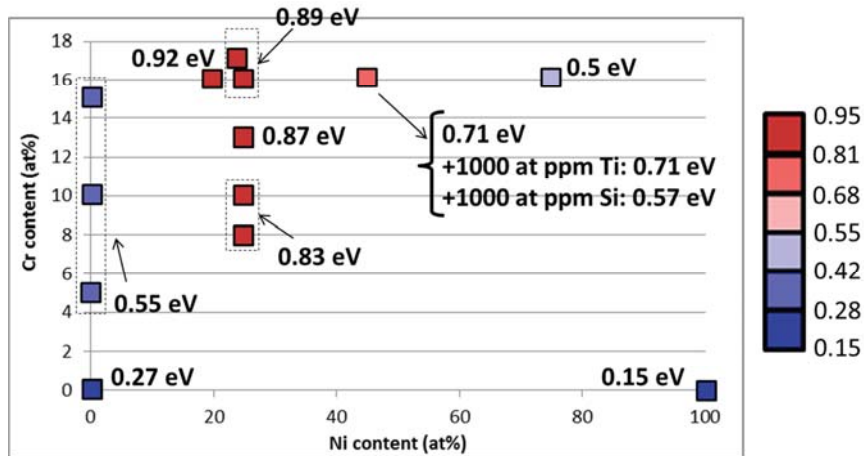
Fig. II-4: Experimental values found in the literature for the self-interstitial migration energies in $Fe_{100-x-y}Ni_xCr_y$ alloys. This picture is inspired from [ZOUARI2012].
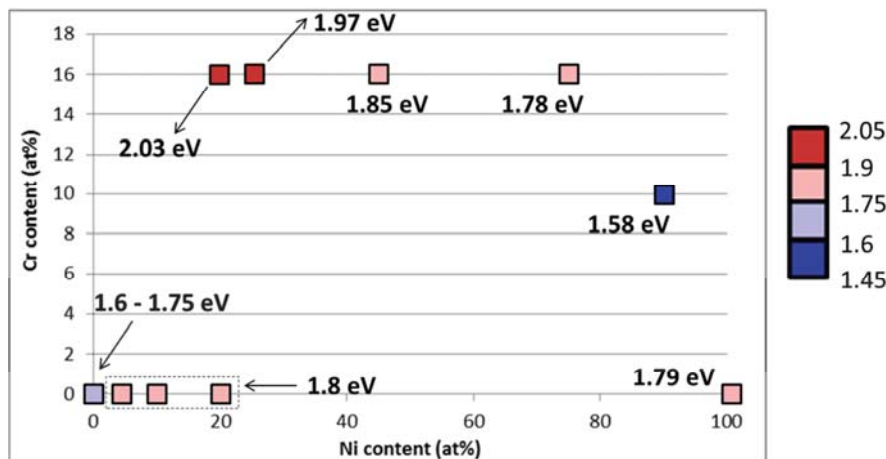
Fig. II-5: Experimental values found in the literature for the vacancy formation energies in $Fe_{100-x-y}Ni_xCr_y$ alloys. This picture is inspired from [ZOUARI2012].

II-1-b   Diffusion properties

Many experimental measurements of the diffusion coefficients are available for Fe-Ni-Cr systems [ROTHMAN1980, MILLION1981, MILLION1985, RUICKOVA1981]. These authors used the radioisotopes ^{59}Fe, ^{63}Ni and ^{51}Cr to measure the diffusion coefficients in different systems. Rothman measured diffusion tracer in the alloys Fe-l5Cr-20Ni, Fe-l5Cr-45Ni, Fe-22Cr45Ni and Fe-l5Cr-20Ni-l.4Si between 960 and 1400°C. Million and Ruickova measured diffusion tracer in the Fe-Cr, Fe-Ni and Cr-Ni alloys as a function of both composition and temperature

66   Chapter II. Bibliography

[MILLION1981, RUICKOVA1981]. These measurements form a reliable data set for the study of diffusion in ternary fcc Fe-Ni-Cr alloys and the evolution of the diffusion coefficients in the binary systems measured by Million [MILLION1981] are given in Fig. II-6 at 1373 K. In the Ni-Cr binary alloy, both Ni and Cr diffusion coefficients are found to decrease with increasing Cr content until a minimum at about 45 at %. Beyond this concentration, the diffusion coefficients slightly increase with increasing Cr content. In the Fe-Ni binary, Both Ni and Fe diffusion coefficients appear to increase linearly with increasing Ni content.
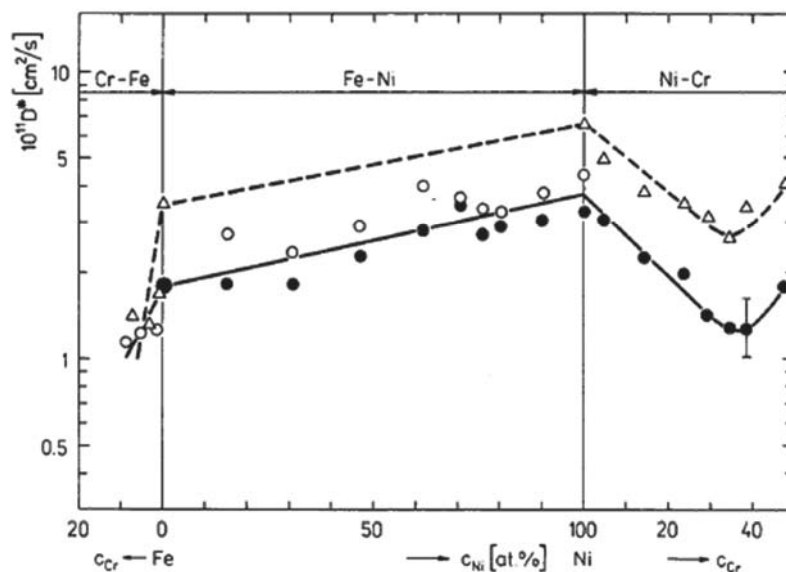
Fig. II-6: Diffusion of components in the fcc phase of binary solid solutions of the Fe-Ni-Cr system at 1373 K. These results consider ^{59}Fe (open circles), ^{63}Ni (black circles) and ^{51}Cr (open triangles) radioisotopes. Results are taken from [MILLION1981].

All the studies performed on Fe-Ni-Cr alloys agree that at all temperatures $D_{Cr}^{V} > D_{Fe}^{V} > D_{Ni}^{V}$ and that there is a constant ratio of about 3/4/9 between Ni, Fe and Cr diffusion coefficient values respectively, i.e. that D_{Cr}^{V}/D_{Ni}^{V} ratio is equal to 3 and that D_{Fe}^{V}/D_{Ni}^{V} ratio is equal to 1.33. The ratios of the diffusion coefficient are found to be independent of temperature within the experimental scatter, thus implying that the pre-exponential factor is the source of this difference between diffusion coefficients [ROTHMAN1980].

II-2 DFT data in pure systems

As mentioned in section II-1, experimental results are relatively scarce in austenitic steels and DFT calculations can be of great help, even if, at the time being, the full complexity of the steel cannot be modelled. This approach has been used widely to investigate ferritic steel point defect properties [DOMAIN2001B, DOMAIN2004, DOMAIN2005, OLSSON2007, TERENTYEV2008] and a good understanding is nowadays emerging from these studies which were done using a dilute alloy approach, i.e. introducing a very small amount of alloying elements in an otherwise perfect Fe supercell. The case of austenitic steels is more complex as these alloys are concentrated alloys. Furthermore, even the dilute approach is quite difficult to pursue since the ground state of Fe crystallizes into a ferromagnetic bcc structure, whereas the austenitic steels or the Fe-Ni-Cr alloys we are interested in are fcc at operating conditions. Experiments have long shown that γ-Fe displays a noncollinear, spiral magnetic structure [ABRAHAMS1962, TSUNODA1989], and considerable experimental efforts have been therefore carried out to stabilize γ-Fe at low temperatures [MEYERHEIM2005, TSUNODA2009, HINES2009]. Unfortunately, these studies were not able to provide insight in the point defect properties so far.

The following sections summarize the knowledge regarding the behaviour of point defects in the three elements constituting our alloy acquired so far from DFT calculations. As the Fe-Ni-Cr alloy we are interested in has been experimentally obtained as a substitutionnally disordered fcc solid solution, we mostly focus on the properties of elements in the fcc structure. DFT calculations in concentrated Fe-Ni-Cr alloys have been performed only for phase stability considering a "grey" material using the Coherent Potential Approximation (CPA).

II-2-a   Ground states

The modelling of γ-Fe based austenitic steels is a major topic of interest because they are key materials in many industrial applications. It could seem simpler to determine point defect properties theoretically than experimentally, however in the case of austenitic steels, the first task which consists in modelling the fcc reference state (i.e. the alloy without any point defect) is not trivial. Indeed, despite the important improvement made in DFT calculation over the last decades, the numerous studies conducted on dilute γ-Fe have revealed the difficulty of modelling

this metastable phase at 0K [HERPER1999, SPIŠÁK2000, SPIŠÁK2002, DOMAIN2001B, JIANG2003, KONG2006, KLAVER2012]. These studies showed that there are many competing magnetic structures lying between 0.08 and 0.15 eV per atom above the bcc ferromagnetic ground state. This point enhances the difficulty of modelling a relevant reference state to calculate physical properties in γ-Fe. Another critical issue is to model the PM state in γ-Fe. Indeed, as mentioned in the introduction, austenitic steels are PM at temperatures where nuclear reactors operate. It is therefore necessary to properly model the PM state using first principle methods which have not been so far successful.

A clever strategy used by Klaver et al. [KLAVER2012] in dilute austenitic Fe-Ni-Cr alloys was to calculate properties in multiple collinear magnetic structures selected as possible reference states for austenite, and then define which features was in common in order to extrapolate them to the PM state. Using this approach, Klaver et al. have investigated solute-solute, vacancy-solute and dumbbell-solute interactions, among other things, in dilute austenitic Fe-Ni-Cr alloys. The single layer anti-ferromagnetic (AFM1) state, the double layer anti-ferromagnetic (AFMD) state and the ferromagnetic high spin (fm-HS) state were considered as possible reference states in the face centred tetragonal (fct) phase. Indeed these magnetic ordering were found to exhibit stability in both structure and against introduction of point defects. Most of the information summarized in this section for pure γ-Fe comes from the work of Klaver et al. [KLAVER2012].

The ground state of Ni is fcc and displays a FM ordering at low temperature. DFT calculations are therefore more reliable because the ground state of γ-Ni can be modelled easily and Ni properties are better known than the properties of γ-Fe and γ-Cr.

Cr has a bcc crystal structure and exhibits the so-called incommensurate spin-density wave (SDW) at low temperature, which is not easy to capture in DFT [HAFNER2001, HAFNER2002, COTTENIER2002]. Moreover, it is worth mentioning that so far, the DFT calculations indicate that fcc Cr is not stable against point defect addition. Indeed, point defect addition in the pure fcc Cr system induces the occurrence of a non-magnetic phase [DOMAIN], the associated negative formation energies of which are unphysical and stem from the instability of the reference state with respect to the distortion induced by the point defect addition. For this reason, point defect properties are not available in fcc Cr.

69 Chapter II. Bibliography

II-2-b   Point defects formation and clustering

In the pure γ-Fe system, Klaver et al. [KLAVER2012] found that the ⟨100⟩ dumbbell is the most stable interstitial for all reference states considered, with a formation energy lying between 3.2 and 3.6 eV. This is in agreement with experimental results obtained for γ-Fe as well as other fcc metals [EHRHART1974, WOLLENBERGER1983, SCHILLING1978, YOUNG1978, FORSCH1974]. It can be noted that in the AFM states, the most stable dumbbell is the one oriented perpendicular to the AFM magnetic planes, with a small symmetry-breaking effect of approximately 0.1 eV. These dumbbells are found to aggregate strongly into pairs and into small defect clusters in (100) and (111) planes, which is favourable for dislocation loop nucleation. Similar results were found in γ-Ni for self-interstitials, with a strong tendency to form tri-interstitial (binding energy of 1.71 eV) [DOMAIN] and in bcc Fe where large binding interaction were found for interstitial complexes using DFT [OLSSON2008] and MD [TERENTYEV2008].

Regarding the mixed dumbbells, Klaver et al. found that Ni was very unlikely to be found in mixed [100] Fe-Ni dumbbells, whatever the magnetic state. Pure Ni-Ni dumbbells are even more unlikely to form. Cr on the other hand can form mixed dumbbells whatever the magnetic state, in agreement with what was found in bcc Fe [OLSSON2007]. Thus, there is of a general order of preference for the different atomic species with Cr being the most stable in interstitial site, followed by Fe and finally Ni. These results are however not in agreement with the experimentally derived size factors for Ni and Cr solutes estimated by Straalsund in 316 SS and in the pure materials [STRAALSUND1974].

In the same work, the vacancy formation energy is between 1.8 and 1.95 eV. Although the divacancy binding is found to be rather weak, thus suggesting that the nucleation of voids will face a nucleation barrier at elevated temperatures. Vacancy cluster are found to be very stable, for example, 2.5 eV for the binding energy of a six-vacancy cluster, which is favourable for void nucleation.

Point defect properties were calculated using DFT in pure fcc Ni systems [WIMMER2008, JANOTTI2004, KRCMAR2005, TUCKER2008] in the past. It was found that for this element, the GGA method fails to predict a correct value of the vacancy formation energy probably because surface effects are not well reproduced [MATTSSON2002, CARLING2000].

Besides this issue, the experimental data are in general in good agreement with the theoretical ones for this element. This is for instance the case for both vacancy and ⟨100⟩ dumbbell migration energies, the experimental values of which are 1.04±0.04 eV and 0.15±0.01 eV [EHRHART1991] in excellent agreement with DFT calculations [TUCKER2008].

II-2-c Solute-solute and defect-solute interactions

Fig. II-7 to Fig. II-9 present the binding energies between pairs of Ni and Cr obtained by Klaver et al. [KLAVER2012] in the pure γ-Fe system. These results show that there is non-negligible attraction between pairs of Ni atoms until the second nearest neighbours in the AFM states. Moreover, Cr-Cr repulsion occurs at 1nn separation. Less clear trends are observed for Ni-Cr interactions for which interaction properties strongly depend on the magnetic ordering. Ni-Cr interactions are however found to be weak in general. These results show that at typical operating temperatures for nuclear applications, the solid solution is stable with small tendency for locally enhanced Ni-Ni and reduced Cr-Cr ordering in dilute alloys.
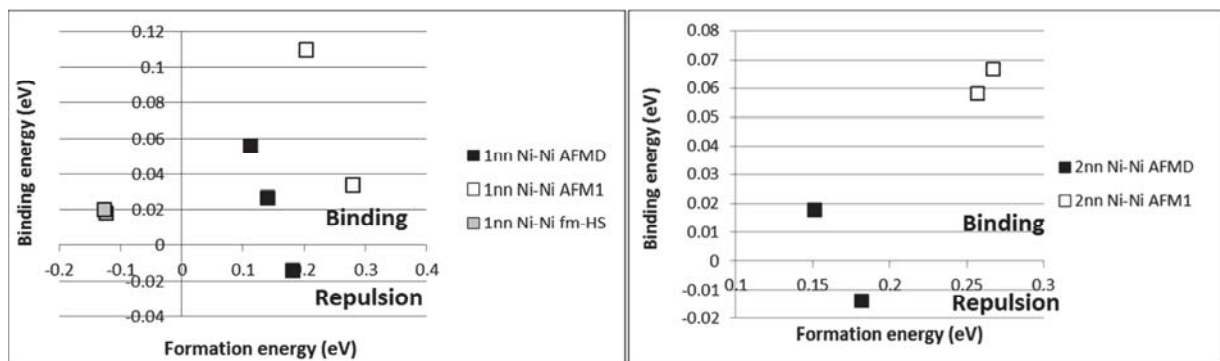
Fig. II-7: Binding energy of 1nn Ni-Ni pairs (left figure) and 2nn Ni-Ni pairs (right figure) in pure fct Fe as a function of the formation energy. We include AFM1 (open squares), AFMD (black squares) and fm-HS (grey squares) magnetic states. Results are taken from [KLAVER2012].
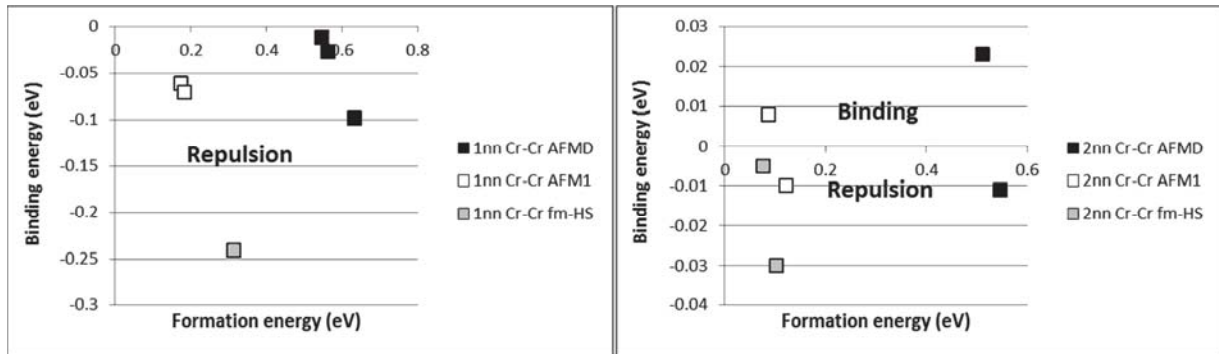
Fig. II-8: Binding energy of 1nn Cr-Cr pairs (left figure) and 2nn Cr-Cr pairs (right figure) in pure fct Fe as a function of the formation energy. We include AFM1 (open squares), AFMD (black squares) and fm-HS (grey squares) magnetic states. Results are taken from [KLAVER2012].
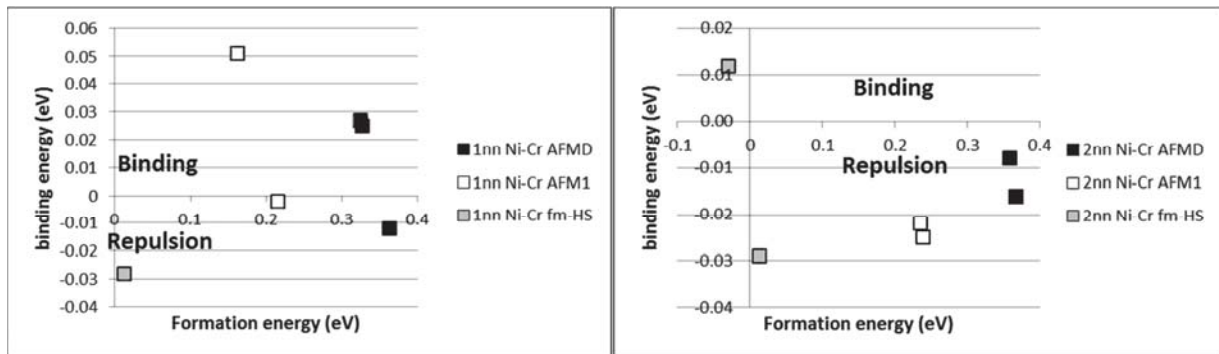
Fig. II-9: Binding energy of 1nn Ni-Cr pairs (left figure) and 2nn Ni-Cr pairs (right figure) in pure fct Fe as a function of the formation energy. We include AFM1 (open squares), AFMD (black squares) and fm-HS (grey squares) magnetic states. Results are taken from [KLAVER2012].

Fig. II-10 and Fig. II-11 present the vacancy-solute binding energies obtained by Klaver et al. [KLAVER2012] in the pure γ-Fe system. These results show that a non-negligible attraction exists between pairs of vacancy and Ni at 1nn separation while weak interactions are observed at 2nn separation in AFM states. Furthermore, repulsion between pairs of vacancy and Cr is generally observed until 2nn separation.

72   Chapter II. Bibliography
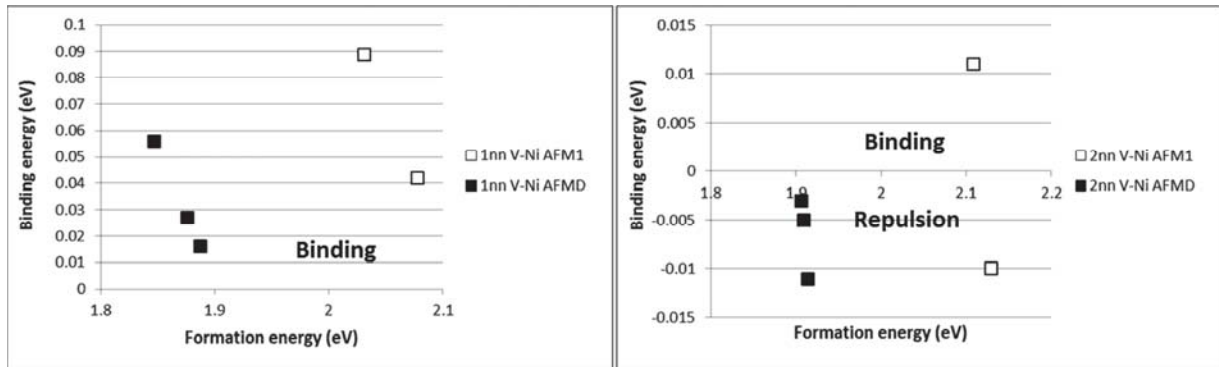
Fig. II-10: Binding energy of 1nn V-Ni pairs (left figure) and 2nn V-Ni pairs (right figure) in pure fct Fe as a function of the formation energy. We include AFM1 (open squares) and AFMD (black squares) magnetic states. Results taken are from [KLAVER2012].
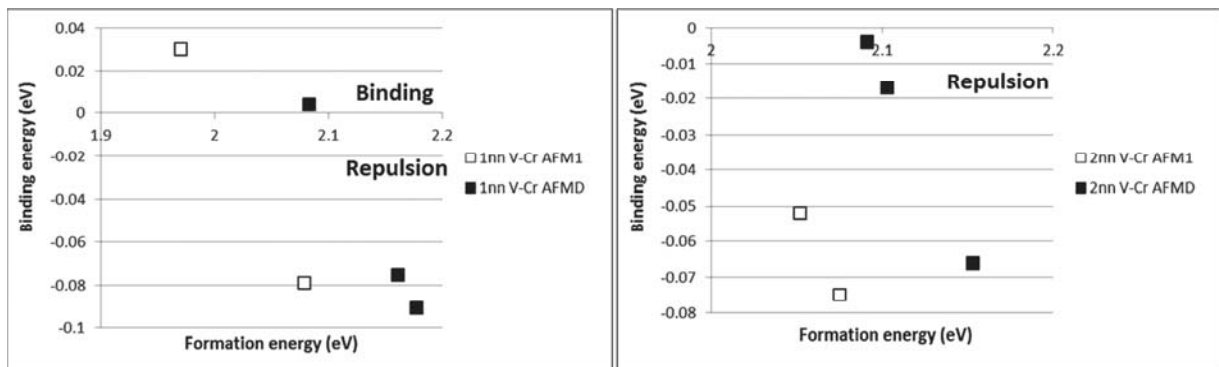
Fig. II-11: Binding energy of 1nn V-Cr pairs (left figure) and 2nn V-Cr pairs (right figure) in pure fct Fe as a function of the formation energy. We include AFM1 (open squares) and AFMD (black squares) magnetic states. Results are taken from [KLAVER2012].

Fig. II-12 to Fig. II-15 present the binding energies obtained by Klaver et al. [KLAVER2012] in the pure γ-Fe system of both Ni and Cr atoms positioned at 1nn and 2nn separation of Fe-Fe dumbbell oriented along different non-equivalent axis. These results show that 1nn Ni atoms generally display weak interactions with the Fe-Fe dumbbell, except when positioned in compressive sites where the Ni atoms are repelled by the dumbbell in both AFM1 and AFMD phases. Cr atoms always bind with Fe-Fe dumbbells positioned at a 1nn separation, however the magnitude of this interaction is generally weak. In both the fct afmI and afmD states Ni is most stable in the tensile 2nn sites with a binding energy up to approximately 0.1 eV.

73 Chapter II. Bibliography
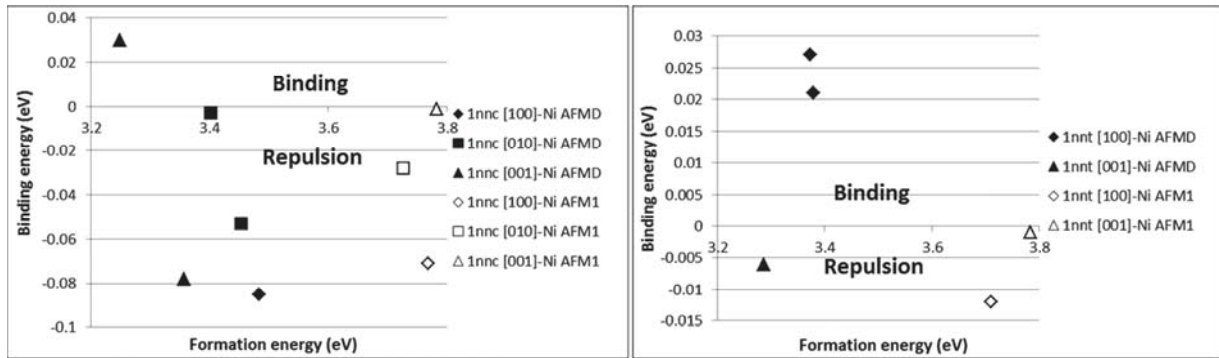
Fig. II-12: Binding energy for ⟨100⟩ Fe-Fe SIAs to substitutional Ni in 1nn compressive sites (1nnc in left figure) and in tensile sites (1nnt in right figure) in pure fct Fe as a function of the formation energy. We include AFM1 (open symbols) and AFMD (black symbols) magnetic states. We include [100] (diamonds), [010] (squares) and [001] (triangles) Fe-Fe SIAs. Results are taken from [KLAVER2012].
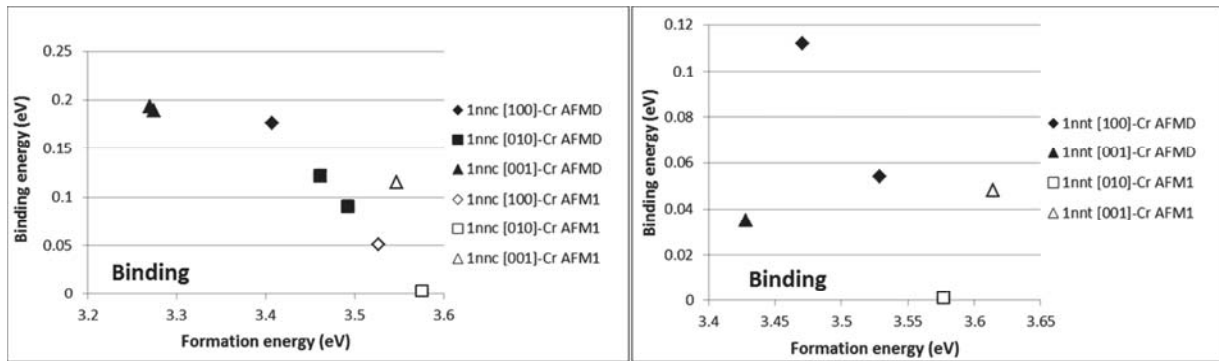
Fig. II-13: Binding energy for ⟨100⟩ Fe-Fe SIAs to substitutional Cr in 1nn compressive sites (1nnc in left figure) and in tensile sites (1nnt in right figure) in pure fct Fe as a function of the formation energy. We include AFM1 (open symbols) and AFMD (black symbols) magnetic states. We include [100] (diamonds), [010] (squares) and [001] (triangles) Fe-Fe SIAs. Results are taken from [KLAVER2012].

74 Chapter II. Bibliography
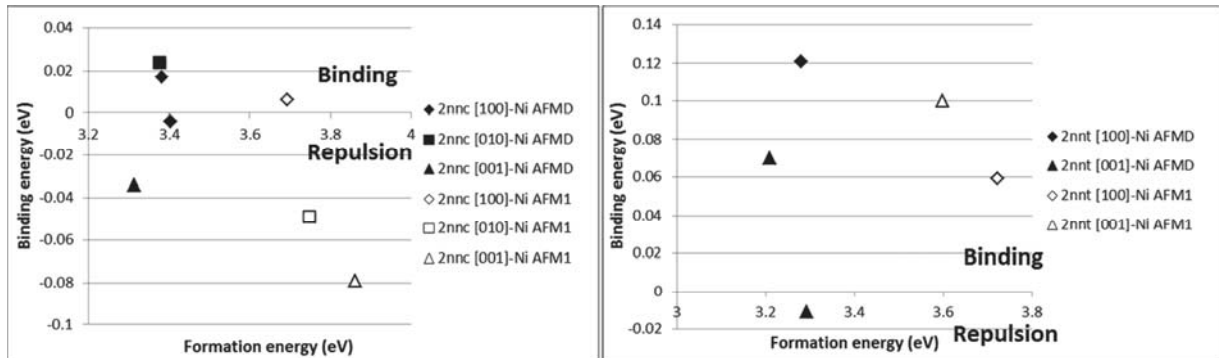
Fig. II-14: Binding energy for ⟨100⟩ Fe-Fe SIAs to substitutional Ni in 2nn compressive sites (2nnc in left figure) and in 2nn tensile sites (2nnt in right figure) in pure fct Fe as a function of the formation energy. We include AFM1 (open symbols) and AFMD (black symbols) magnetic states. We include [100] (diamonds), [010] (squares) and [001] (triangles) Fe-Fe SIAs. Results are taken from [KLAVER2012].
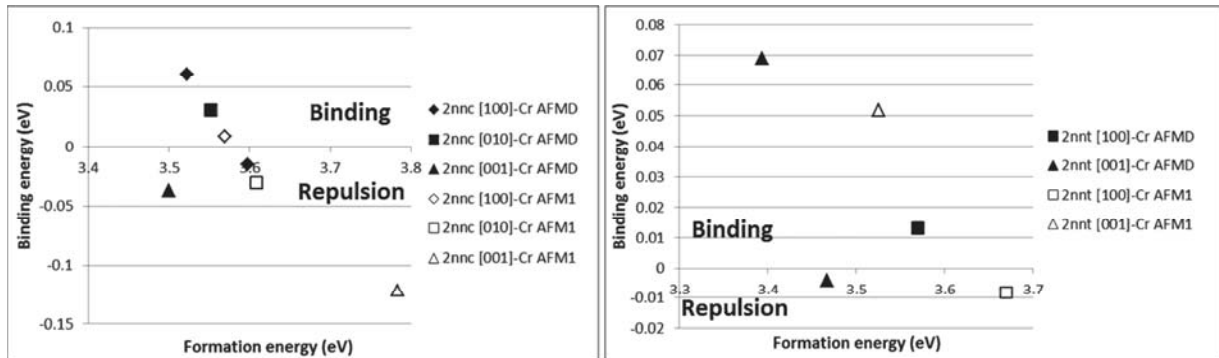
Fig. II-15: Binding energy for ⟨100⟩ Fe-Fe SIAs to substitutional Cr in 2nn compressive sites (2nnc in left figure) and in 2nn tensile sites (2nnt in right figure) in pure fct Fe as a function of the formation energy. We include AFM1 (open symbols) and AFMD (black symbols) magnetic states. We include [100] (diamonds), [010] (squares) and [001] (triangles) Fe-Fe SIAs. Results are taken from [KLAVER2012].

Tab. II-2 presents the solute-solute, vacancy-solute and SIA-solute binding energies until 2nn separation which have been calculated in the pure γ-Ni system by Tucker [TUCKER2008]. These results show the same trends for the binding of the vacancy with Cr and Fe atoms. Indeed, both Cr and Fe atoms are repelled until the third nearest neighbour separation whereas a significant binding is being felt at the fourth nearest neighbour separation. No significant interactions seem to occur beyond this distance. However, although most of the vacancy-solute binding energies are repulsive, they are relatively weak. For instance, as listed in Tab. II-2, the 1nn solute-vacancy binding energies are -0.05 eV for Cr and -0.02 eV for Fe. The binding energy between a ⟨100⟩

75 Chapter II. Bibliography

Ni-Ni dumbbell and a Fe atom positioned in a 1nn site was also found to be weak, whereas a value of about 0.18 eV was obtained for the binding energy of the ⟨100⟩ Ni-Ni dumbbell and a Cr atom positioned at 1nn separation. Tab. II-2 indicates also that no significant differences are observed between compressive and tensile sites. Finally, two Fe atoms seem to repel each other in 1nn position, the same applies for an Fe atom and a Cr atom. No significant interaction is found when the two atoms are further apart. Two Cr atoms attract each other but only if there 2nn.

Binding energy (eV)	distance	fcc FM
Fe-Fe	1nn	-0.11
	2nn	0.02
Cr-Cr	1nn	0.04
	2nn	0.11
Fe-Cr	1nn	-0.16
	2nn	0.01
V-Fe	1nn	-0.02
	2nn	-0.01
V-Cr	1nn	-0.05
	2nn	0.01
V-V	1nn	0.02
	2nn	0.12
<100>-Fe	1nnc	0.01
	1nnt	0.03
<100>-Cr	1nnc	0.18
	1nnt	0.15

Tab. II-2: Solute-solute and vacancy-solute binding energies until the 2nn in pure fcc Ni. Binding energies for ⟨100⟩ Ni-Ni SIAs to substitutional solutes in 1nn compressive sites (1nnc) and in 1nn tensile sites (1nnt) in pure fcc Ni. Results are taken from [TUCKER2008].

The prediction of relatively weak Cr-vacancy binding in pure γ-Ni as well as the Cr-vacancy repulsion in pure γ-Fe largely rules out vacancy drag mechanisms that could play a role in RIS and have sometimes been invoked to explain TNES [ARDELL2008]. However, in both pure systems, Cr is found to bind significantly to ⟨100⟩ SIAs suggesting that the interstitial mechanism could play a role for Cr atoms. The vacancy-Ni binding observed in pure γ-Fe is small but is likely to be cumulative. This result is consistent with the positive binding of

vacancies to oversized solutes found to be the mechanism inducing the suppression of both RIS and void swelling with the addition of a small amount of oversized atoms first observed by Kato et al. [KATO1992] and supported by the modelling of Stepanov et al. [STEPANOV2004] and Hackett et al. [HACKETT2009B] (section I-3). This result is also consistent with the reduction in the experimentally determined vacancy formation energy with increasing Ni content in Fe-Cr-Ni austenitic alloys [DIMITROV1984] mentioned in section II-1-a.

II-2-d   Vacancy migration and diffusion

Fig. II-16 present the vacancy migration barriers in the pure γ-Fe system for AFM1 and AFMD magnetic ordering. It is striking that the migration energies may be completely different depending on which path is chosen for the vacancy-solute exchange. In particular, the Fe-vacancy exchange, the migration energy of which range is about 1 eV in both AFM1 and AFMD states, is very sensitive to the local magnetic environment.
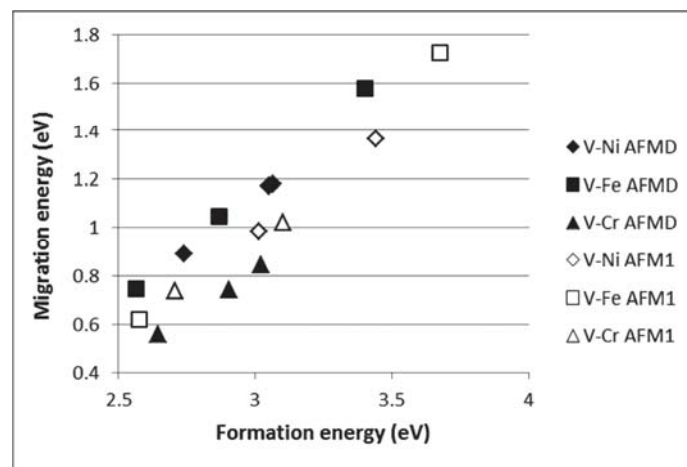
Fig. II-16: Migration energy involving 1nn V-Cr (triangles), V-Ni (diamonds) and V-Fe (squares) exchange in pure fct Fe as a function of the formation energy. We include AFM1 (open symbols) and AFMD (black symbols) magnetic states. Results are taken from [KLAVER2012].

Calculations made by Tucker in the pure γ-Ni system showed that the vacancy migration barrier heights are respectively 0.82, 0.95, and 1.08 eV when the migrating atom are respectively a Cr, Fe, and Ni atom [TUCKER2008]. The same ordering of the vacancy migration barriers with the migrating atom type is found in pure γ-Fe in both AFM1 and AFMD. Indeed, migration barrier

of Ni atoms are found to be significantly higher than those of Cr atoms, and Fe self-diffusion generally lie between Ni and Cr migration values as can be seen in Fig. II-16.

It can be noted that this sequence obtained for the migration energies in both γ-Fe and γ-Ni systems, i.e. Cr atoms have a lower barrier for migration via vacancy exchange relative to Fe or Ni atoms, is consistent with diffusion experiment presented in section II-1-b. These results seem therefore to support the modelling of Perks [PERKS1986] presented in section I-3, which assume the preferential exchange of an alloying element with the vacancy flux as the sole contributor to RIS in Fe–Cr–Ni alloys (Cr depletion through the IK mechanism). However, correlation effects have to be taken into account in order to drawn reliable conclusions. DFT data of the pure systems [TUCKER2008, KLAVER2012] was therefore used in the five frequency model provided by Lidiard and LeClaire [LIDIARD1955, LECLAIRE1956] presented in chapter I (section IV-7-b-i) to obtain insights about the mechanisms involved in the vacancy diffusion process in Ni base (Ni-Fe and Ni-Cr) and Fe base (Fe-Ni and Fe-Cr) dilutes alloys. Using this model, Klaver et al. [KLAVER2012] found that Ni diffusion was significantly slower than that of both Cr and Fe in γ-Fe, especially at typical operating temperatures for nuclear energy applications. The relative ordering between Cr and Fe diffusion was however found to be dependent on the magnetic reference state chosen to determine the activation barriers. Cr is also found to be the fastest diffusing species in γ-Ni followed by Fe and then Ni. The calculation of the vacancy wind, which allows determining the relative direction of solute flow relative to the vacancy flux, shows that in γ-Ni the vacancy diffusion mechanism was found to change as a function of temperature resulting in vacancy–solute drag below 460 K, while above vacancy–solute exchange is the dominant diffusion mechanism [TUCKER2010]. In the case of the γ-Fe system, vacancy wind calculation indicates that Cr solutes will diffuse opposite to the vacancy flux and that Ni is more likely to diffuse with the vacancy flux than opposite it.

Another important point is that the enhanced diffusivity of Cr is found to be primarily due to differences in migration barriers and binding energies, not pre-exponential factors. This result is in strong disagreement with high temperature measurements [ROTHMAN1980] (section II-1-b) which have attributed the source of fast Cr diffusion to the pre-exponential factors. This finding [TUCKER2010] can have a significant impact because, although diffusion coefficients that involve changes in migration energy or pre-factor can both lead to Cr depletion via the vacancy, it can

completely change the temperature dependence and the mechanisms by which Cr diffusion is promoted.

II-3   Properties of concentrated Fe-Ni-Cr

Paramagnetic Fe-Ni-Cr alloys have been modelled by DFT using the mean field CPA [FAULKNER1982]. Indeed, CPA method is a powerful analytical technique for calculations of density of states in solid solutions. For example, for a binary alloy containing x at.% of element A and 1-x at.% of element B, the idea of the CPA is to replace the components A and B by an effective medium in which the lattice site can be occupied by A with the probability x, or by B with the probability 1–x. CPA is thus an approximation based on the concept of an effective medium, which replaces the real environment seen by an electron by a grey material.

This method therefore allows treating Fe-Ni-Cr alloys considering a substitutional disorder on a fcc underlying lattice neglecting the local lattice relaxation and short range order [PITKÄNEN2009, DELCEZG2012]. The paramagnetic state is modelled using the disordered local magnetic local approach. Taking into account configurational and magnetic entropies, formation energies as a function of temperature have been determined.

Pitkänen et al. [PITKÄNEN2009] have studied the phase stability of paramagnetic Fe-Ni-Cr alloys at high temperature (above 1000K) between ferrite, austenite and the two-phase of duplex steels. As a function of composition, the stability region of ferrite, austenite and ferrite-austenite are in qualitative good agreement with experimental data. For Fe-10Ni-20Cr, above 1000K, the equilibrium phase is found to be duplex in rather agreement with experimental data.

Using the same approach, the vacancy formation energy has been calculated in a 32 site primitive cell [DELCEZG2012]. As forces are not calculated, the vacancy relaxation configuration was obtained by minimising the energy as a function of first nearest neighbour of the vacancy and supercell volume only. For Fe-10Ni-20Cr, the relaxed vacancy formation energy was found to be 1.95 eV. Using DFT, Vitos and Johansson have also demonstrated that the elastic properties of paramagnetic Fe-Cr-Ni alloys depend strongly on the local magnetic moment [VITOS2009]. The same authors obtained a theoretical description of the stacking fault energy in Fe-Cr-Ni alloys as a function of composition and temperature [VITOS2006], the results of which

were used by Bonny [BONNY] to build the Fe-Ni-Cr potentials presented in chapter IV (section I).

III Conclusions

Many models have been developed to simulate RIS. However, most of them are based on rate theory in which the mechanisms by which RIS occurs have been assumed, thus limiting their predictive capability. Different models assuming different simple mechanisms for RIS were found to obtain a quantitative representation of segregation profiles. If one uses Perks model, one finds that Cr depletion at GB is mainly due to the higher diffusivity of Cr atoms compared to that of Fe and Ni atoms, in line with the high temperature diffusion measurements where Cr is found to be the faster diffusion element in Fe-Ni-Cr alloys. Using Lam's model or Pechenkin's model, the migration of undersized atoms via mixed dumbbells is supposed, in line with the occurrence of RIS at low temperatures and with the enrichment of undersized atoms and a depletion of oversized atoms usually observed at the GB in ASS. Although these models seem to capture at least a part of the global RIS mechanism, these results suggest that the RIS theory proposed by the rate theory is too simple to reflect its true nature.

The picture emerging from DFT data used in the framework of the five frequency model is that RIS mechanisms are much more complex than the assumptions made in models based on rate theory. In particular, diffusion mechanism can change as a function of temperature as found in the pure γ-Ni system [TUCKER2010]. Furthermore, these studies also show that the change in diffusion coefficient was primary due to the difference of binding and migration energies, not pre-exponential factors as was concluded by high temperature diffusion experiments.

These findings along with those of Allen [ALLEN1998A] who identified the need for modelling to include species dependence migration energies and short range ordering effects to explain RIS data over a significant composition range, show that RIS modelling require the use of an atomistic approach and a reliable cohesive model. Furthermore, reliable description of the transport coefficients entering equations for the fluxes of point defect and solute atoms within the framework are required to be used as input parameter for rate theory. Indeed, although transport coefficients can be obtained from tracer diffusion experiments or interdiffusion experiments, not

all coefficients can be determined, thus decreasing the performance of these models. One however can turn to models taking into account interacting atoms distributed on a rigid lattice such as AKMC or the Self-Consistent Mean-Field (SCMF) kinetic theory proposed by Nastar [NASTAR2000] which have been later adapted by Barbe to take into account the dumbbell mechanism [BARBE2006B].

A cohesive model taking into account interacting atoms distributed on a rigid lattice has already been built by Barbe in the Fe-Ni-Cr system [BARBE2006], but at a time when only DFT data in the pure γ-Ni system were available. The recent study of Klaver et al. [KALVER2012], the purpose of which is to calculate properties in multiple collinear magnetic structures selected as possible reference states in the pure γ-Fe system using DFT, can help to provide a cohesive model suitable for the study of RIS in 316L SS (Fe-based alloys). Indeed, the good description of thermodynamic properties was found to have a significant contribution on the segregation process and cannot be neglected [LAM1981, NASTAR2005]. Although data are available in the pure systems, a suitable cohesive model requires also data in the concentrated systems which are limited in the literature.

81 Chapter II. Bibliography

Chapter III.   First principle study of point defects in a fcc Fe-10Ni-20Cr model alloy

In order to investigate deeper the properties of austenitic stainless steels used in the nuclear industry, in this chapter concentrated Fe-Ni-Cr alloys are studied using DFT presented in chapter I (section III-1). To our knowledge, DFT studies were performed in concentrated austenitic Fe-Ni-Cr alloys are few and do not investigate point defect properties [VITOS2003, DELCZEG2012]. However, from a fundamental point of view, concentrated austenitic Fe-Cr-Ni alloys, i.e. ASS used in the nuclear industry only formed by their major alloying elements, are key model systems to investigate their complex magneto-structural behaviour. In particular, the chemical disorders as well as the magnetic properties need to be considered to explain a wide range of properties of these alloys like point defect properties. Thus, in what follows, we model the austenitic steels by a ternary alloy containing 70 at.% of Fe, 20 at.% of Cr and 10 at.% of Ni. The influence of the local environment on vacancy and $\langle 100 \rangle$ self-interstitial formation energies has therefore been studied in a fcc Fe-10Ni-20Cr model alloy by analysing an extensive set of first principle calculations based on density functional theory. Chemical disorder has been considered and a large set of possible collinear magnetic structures have been investigated to determine the most relevant reference state to perform point defect calculations. Two different convergence methods have been also used to characterize the importance of the method on the results.

This chapter is organized as follows. In section I, computational details used to perform the DFT calculations are presented. In section II, defect free calculations are performed in four different magnetic phases to define the most suitable reference for point defect calculations in the Fe-10Ni-20Cr model alloy. The magnetic structure of the reference state chosen is analysed in more details in section III. In section IV-1, an estimate of chemical potentials needed to perform both point defect and substitution formation calculations in concentrated alloys is proposed. In sections IV-2 and IV-3, an emphasis is given to the calculation of both point defect and substitution formation energies in concentrated alloy. In section IV-4, a link existing between the point defect formation and the local environment establish. Finally, we list our conclusions in the last section.

I   Modelling the austenitic steels

I-1   Calculation details

The first principle calculations were performed using the DFT code VASP (Vienna ab initio Simulation Package) [KRESSE1993, KRESSE1994, KRESSE1996A, KRESSE1996B], a plane wave code that implements the projector augmented wave (PAW) method. The standard PAW potentials supplied with VASP were used. Exchange and correlation were described by the Perdew-Wang functional [PERDEW1981], adding a non-local correction in the form of the generalized gradient approximation (GGA). The Vosko-Wilk-Nusair interpolation was applied for the correlation part of the exchange correlation functional [VOSKO1980]. Potentials with 8, 6 and 10 valence electrons were used for Fe, Cr and Ni respectively. Block Davidson algorithm was used to minimize the energy of the system with respect to the free parameters of a set of basis functions used to represent the wave function.

Two set of calculations were performed in this work. Reference states calculations were performed in supercells of 256 atoms containing 180 Fe atoms (70 at. %), 50 Cr atoms (20 at. %) and 26 Ni atoms (10 at. %). In this first set of calculations, the local magnetic moments on atoms were initialized to impose the desired magnetic ordering and then allowed to relax. Four different collinear magnetic structures were compared to select the most relevant reference state for the point defect calculations. In a second set of calculations, formation energies of point defects were calculated in supercells of 256 ±1 atoms, with supercell dimensions held fixed at the equilibrium values of the reference state selected and ionic positions free to relax.

For the reference state calculations, two different calculation methods were considered in order to analyse its impact on the observed properties. Fully relaxed (FR) calculations were performed in which the fractional ionic coordinates and the supercell shape and volume were allowed to relax. Cubic lattice (CL) calculations were also performed in which lattice was kept fcc and only the fractional ionic coordinates and the supercell volume were allowed to relax.

All the above mentioned set of calculations were performed using an energy cutoff of 300 eV for the plane wave basis set [KRESSE1999, BLÖCHL1994] and a 2^3 Monkhorst-Pack grid to sample the Brilloin zone. First-order (N=1) Methfessel and Paxton smearing of the Fermi surface

[METHFESSEL1989] was used throughout with smearing width, σ, set to 0.3 eV. Periodic boundary conditions have been applied to the system.

I-2   Treatment of substitutional disorder

It has been shown in the introduction that Fe-Ni-Cr alloys are chemically disordered materials in a wide range of composition. Thus, short-range order effects should not play an important role in the energetics of our model alloy.

In simulation, the main difficulty for studying defect properties in a disordered alloy is to properly consider the environment effects. As previously mentioned in chapter II (section II-3), the CPA averages them completely and certain quantities like formation energies are difficult to investigate due to its mean field approach. To overcome this difficulty, the influence of the local environment is addressed by generating a ternary alloy close to the composition of stainless steels of types 316 where disorder was considered by designing Special Quasirandom Structures (SQS) which mimic the most relevant radial correlation functions of an infinite solid solution [ZUNGER1990]. This method allows a significant reduction of the lattice size when the supercell approach is used, the approach of which takes into account the local lattice relaxation and short range order, unlike CPA. Two different SQSs of 256 atoms were generated and used in this work (SQSa and SQSb).

I-3   Treatment of the magnetism

As shown in previous studies, the magnetic properties of γ-Fe-Cr-Ni systems drive, at least in part, the properties of these systems. Thus, the magnetic properties need to be considered in order to properly model austenitic alloys. As mentioned in chapter II (section II-2-a), the γ-Fe ground state most likely consists of a noncollinear, spiral magnetic structure. However, it seems difficult to investigate such configurations using VASP as we will show next. Ionic as well as electronic structure minimizations were therefore performed in the defect free supercell using four different initial collinear magnetic structures to select the most relevant reference state for the point defect calculations. The initial local magnetic moments were then set to impose these magnetic orderings. Since our systems do not have any symmetry, the magnetic moments on atoms had the possibility to evolve and the relaxed local magnetic moments were determined by

85   Chapter III. First principle study of point defects in a fcc Fe-10Ni-20Cr model alloy

integrating the spin density within spheres centred on the atoms using sphere radii of 1.302, 1.323 and 1.286 for Fe, Ni and Cr respectively.

We considered the PM phase which was modelled by generating two different SQSs (SQSa and SQSb) for the six component $\left(Fe_{0.5}^{\uparrow}Fe_{0.5}^{\downarrow}\right)_{70}\left(Ni_{0.5}^{\uparrow}Ni_{0.5}^{\downarrow}\right)_{10}\left(Cr_{0.5}^{\uparrow}Cr_{0.5}^{\downarrow}\right)_{20}$ alloy to take into account both chemical and magnetic disorder in the lattice. From these SQSs, three other magnetic states were built by initializing the moments to impose the desired magnetic ordering. We considered the single-layer antiferromagnetic (AFM1) state in which (100) planes contain moments in directions alternatively parallel and anti-parallel (↑↓↑↓…), the double-layer antiferromagnetic (AFMD) state in which pairs of (100) planes contain moments in directions alternatively parallel and anti-parallel (↑↑↓↓…) and the FM state in which all moments point in the same direction. These different magnetic orderings are represented schematically in Fig. III-1.
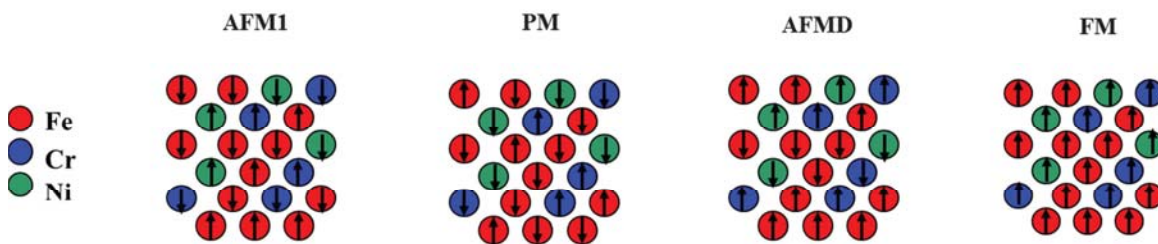
Fig. III-1: Schematic representation of the different kind of magnetic orderings investigated in this work. We considered the ferromagnetic (FM), anti-ferromagnetic simple layer (AFM1), anti-ferromagnetic double layer (AFMD) and paramagnetic (PM) orderings. Arrows indicate the local moments (either "up" or "down") carried by each atom.

II   Reference state for the point defect calculations

II-1   Non-collinear spin state calculations

As non-collinear spin states can occur in some fcc Fe alloys we have calculated four Fe-10Ni-20Cr systems with Fe-Cr or Fe-Ni interstitials located at different lattice sites, while allowing non-collinear spin states. The calculations were started from the collinear solutions for these

systems. Since our systems do not have any symmetry, the magnetic moments on atoms had the possibility to move away from the collinear state. However, in none of the four systems did this actually happen. The collinear solution appeared to be at least a stable local energy minimum. The presence of interstitials significantly influences the magnetic moments on atoms inside or close to the dumbbells. Yet, despite the magnetic disturbance due to interstitials, magnetic moments on all atoms remained collinearly aligned. In one system the moments on all Cr and Ni atoms were initialized to be aligned non-parallel to the anti-ferromagnetic and collinear aligned Fe atoms. In this case the system converged back to a collinear solution for all atoms. These results do not represent definite proof that there are no non-collinear solutions in our SQS systems, as starting calculations with strongly non-collinear initial moments on all atoms would have a greater chance of finding non-collinear solutions than starting from collinear initial moments on the Fe atoms. However, convergence for such calculations would likely be very difficult. For our work, we are satisfied that collinear spin configurations are at least quite a stable local energy minimum and the lack of non-collinearity throughout our systems leaves open the possibility that they are the global minimum.

II-2   Collinear spin state calculations

The DFT calculations performed in the Fe-10Ni-20Cr alloys displayed, depending on the initial magnetic ordering considered, a wide variety of relaxed magnetic structures close in energy can be observed as observed in dilute γ-Fe. As a consequence, the total energy of the system depends on the magnetic initial conditions applied to the system. It is thus important to compare different initial magnetic structures to select the most appropriate reference state. To this end, we considered in this work four different initial magnetic orderings presented in section I-3 which have been tested in two different SQSs referred as the SQSa and the SQSb structures in Fig. III-2.
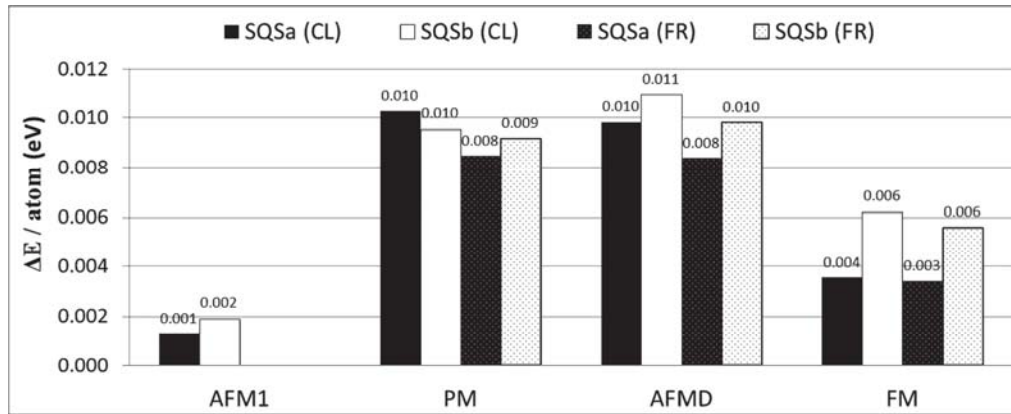
Fig. III-2: Energy difference per atom, ΔE/atom, between distinct magnetic states. We considered the ferromagnetic (FM), anti-ferromagnetic simple layer (AFM1), anti-ferromagnetic double layer (AFMD) and paramagnetic (PM) orderings. We considered two different special quasi-random structures (SQSa and SQSb). We considered the full relaxed calculation method (FR) and the cubic lattice calculation method (CL).

As already found in previous work for the γ-Fe, we found many minima very close in energy corresponding to different magnetic states as can be seen in Fig. III-2. When relaxing these four magnetic structures we found that the AFM1 state was the most stable state for each SQS as can be seen in this figure. This result is in agreement with the detailed magnetic measurements performed in polycrystalline $Fe_{80-x}Ni_xCr_{20}$ alloys by Majumdar et al. for this composition and at 0 K [MAJUMDAR1989].

For each magnetic phase tested, the relaxed moments on Cr and Ni atoms can be deduced from the magnetic properties of their Fe 1nn as we will discuss later. By contrast, the behaviour of Fe moments is less predictable. Although the magnitude of Fe moments is slightly ruled by its local chemistry, a number of moment flips occur during the course of the calculation, depending on the initial magnetic condition initialized. In particular, multiple relaxed magnetic structures were obtained when relaxing the PM phase, thus inducing important change of magnetic interactions felt at each lattice site and of the total energy of the system. These changes even happened when using atomic position and moments of a firstly converged calculation as input parameters to restart a second run. This behaviour is illustrated in Fig. III-3 which represents the change of moments carried by Fe atoms between these two calculations plotted as a function of Fe moment of the first run. It can be seen that an important number of Fe moment have been soften during the course of the first calculation. These soften moments which lie between -1 and 1 μ_B are

subjected to significant changes when restarting the first calculation. This behaviour is certainly due to the competition between many magnetic states close in energy, however this behaviour couldn't be restrained. As a result, the PM phase which correspond to the magnetic phase of ASS at temperatures at which nuclear reactors operates, couldn't be used as reference state to perform the point defect calculations.
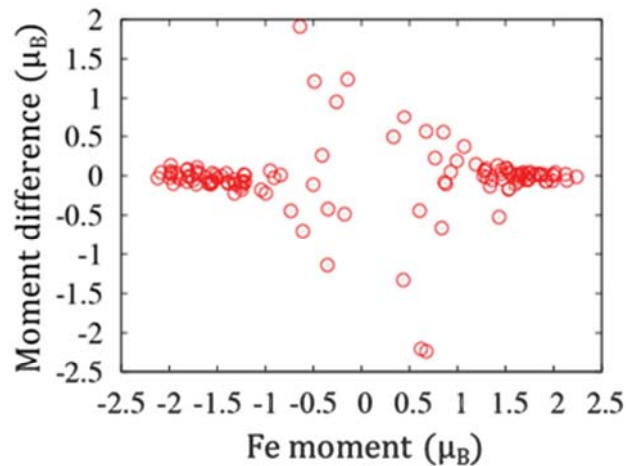
Fig. III-3: Fe moments obtained from a firstly converged calculation initialized to impose the PM phase are displayed in abscissa. This calculation was then used as input parameters to restart a second run of which Fe moments were used to calculate the moment difference (relative to those found for the first run) displayed in ordinate.

The other magnetic phases investigated, i.e. the AFM1, AFMD and FM states, are less prone to such spontaneous moment flips on Fe. In particular, the AFM1 state has the most robust magnetic structure since for each SQS studied, very few moments flips occurred on Fe atoms and hence the AFM1 phase was retained after relaxation. However, the AFMD and FM phases may sometimes be destabilized during the course of the calculation. For all these reasons, the AFM1 state was selected as the best (and unique) candidate to perform the point defect calculations:

The energy differences of a few meV per atom observed between FR and CL methods in Fig. III-2, are due to the fact that both ferromagnetic and anti-ferromagnetic states transform into fct structures when the CL constraint is removed. By contrast, no such energy difference is observed

---

89   Chapter III. First principle study of point defects in a fcc Fe-10Ni-20Cr model alloy

in the PM state where the crystallographic phase remains fcc. Two different AFM1 states were therefore selected as reference states:

➢ Using the CL method, the AFM1 reference state is fcc with lattice parameter of 3.518 Å. In what follows this reference state will be referred as the fcc AFM1 state.

➢ Using the FR method, the AFM1 reference state has lattice parameters close to an fct phase, so that a = 3.492 Å, b = 3.503 Å and c = 3.566 Å. Thus, in what follows this reference state will be referred as the fct AFM1 state.

The final atomic positions for SQSa and SQSb in the fct AFM1 phase are presented in annex 2. SQSa is used to perform the point defect calculations in the fct AFM1 reference state.

III   <u>General properties of the reference state</u>

III-1   General features of the local magnetic moments

An analysis of the local magnetic moments indicates that in the AFM1 state of our model alloy, the relaxed local moments carried by the Ni atoms, m_{DFT}^{Ni}, and the Cr atoms, m_{DFT}^{Cr}, depend strongly on the sum of the moments of their Fe first nearest neighbours (1nn) as can be seen in Fig. III-4. These trends are clear in this picture where Cr atoms tend to be anti-ferromagnetic with the sum of the moments of Fe 1nn as is the case in bcc Fe-Cr alloys [KLAVER2006] and their local magnetic moments range from -1.5 μ_B to 1.5 μ_B. Conversely, the Ni moments are ferromagnetic with the sum of the moments of Fe 1nn, as is the case in bcc Fe-Ni alloys [OLSSON2010] and their local magnetic moments range from -0.3 μ_B to 0.4 μ_B. It has to be noted that Fe forms 70 at.% of our model alloy and therefore many Fe-rich environments exist. Thus, as the magnetic moments of Fe atoms range between -2 μ_B and 2 μ_B as we will see next, it is not surprising that the sums of the moments of Fe 1nn displayed in Fig. III-4 lie between -10 μ_B and 15 μ_B.
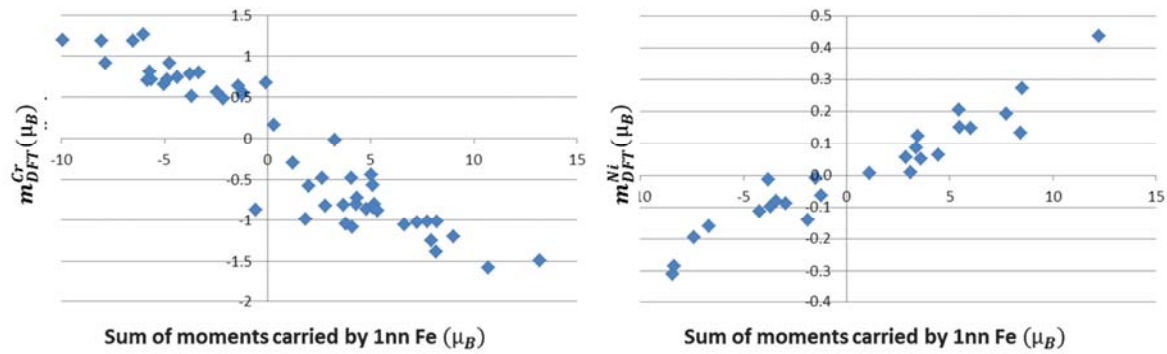
Fig. III-4: Magnitude of the Cr moments, m_{DFT}^{Cr}, versus the sum of the moments of their Fe 1nn (left figure). Magnitude of the Ni moments, m_{DFT}^{Ni}, versus the sum of the moments of their Fe 1nn (left figure).

In contrast, the behaviour of Fe moments remains unclear: the magnitudes of moments on Fe atoms, whose absolute values lie between 1 μ_B and 2 μ_B, do not depend on the magnetic features of their neighbour atoms. The magnitude of Fe atom moments however depends slightly on the species in its neighbourhood and particularly shows a slight trend with the number of first nearest atoms of Ni and Cr. This point will be illustrated in more details in section IV-4.

III-2   Analysis of the magnetic robustness against point defect addition

As previously mentioned, depending on the initial magnetic condition considered, Fe moments can be destabilized during the course of the calculation. Numerous moment flips occurring on Fe atoms destabilize the PM phase whereas the magnetic phase is retained for Fe atoms initialized in the AFM1 phase. Indeed, we observed that Fe moments generally kept the same sign during the course of the calculation and that their magnitude slightly depended on the number of their Ni and Cr 1nn (Fig. III-18). However, both magnitude and sign of moments carried by both Cr and Ni atoms are completely ruled by their local environment. In particular, Cr and Ni moments are found to be respectively anti-ferromagnetic and ferromagnetic with the sum of the moments carried by their Fe 1nn. Although the AFM1 state, chosen to be the reference state, was not subjected to high magnetic instabilities, we observed competing structures close in energy, owing to a small number of Fe atoms whose moments were free to evolve spontaneously. Previous work on pure fcc iron had already showed this kind of behaviour [HERPER1999, SPIŠÁK2002, KLAVER2012]. This is therefore not surprising that point defect addition induces a few magnetic instabilities in the whole lattice. Indeed, even if the strongest changes are located

91   Chapter III. First principle study of point defects in a fcc Fe-10Ni-20Cr model alloy

in the vicinity of the dumbbell, for no apparent reason, spin flips may occur on a few Fe atoms positioned anywhere in the lattice as can be seen in Fig. III-5. Point defect addition may sometimes bring a sufficient perturbation and then destabilize the moment carried by a few atoms positioned far from the point defect. Similar results have been found for Fe-Ni alloys [ABRIKOSOV2007]. These results point to a potential source of variability of point defect formation energies.
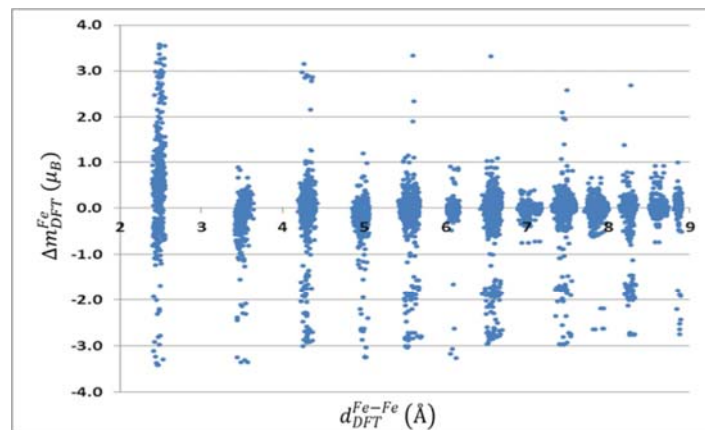
Fig. III-5: Variations of local magnetic moments carried by Fe atoms due to Fe-Fe dumbbell addition in the AFM1 reference state, Δm_{DFT}^{Fe}, as a function of the distance from the point defect created, d_{DFT}^{Fe-Fe}. Fe-Fe dumbbell was introduced in the AFM1 reference state at 40 different sites, oriented along both [100] and [010] directions at each site. This figure represents the merging of these 80 calculations.

IV   Point defect formation energies

Point defect formation and substitutional formation energies have been calculated in the AFM1 reference state. These calculations were calculated at many sites of the lattice in order to consider the local environment effect. Thus, these energies should rather considered as the required energies ΔE to introduce a point defect (respectively to substitute an atom by another one) at different lattice sites of a reference state and are therefore different from a formation energy (respectively a substitutional formation energy) in the strictest sense. Thus, in what follows ΔE^V will refer to the required energies to introduce a vacancy and $\Delta E^{[100]Fe-Fe}$ will refer to the required energies to introduce an Fe-Fe dumbbell oriented in the [100] axis for instance. These energies will be however often referred to as point defect formation energies for simplicity purposes. Similarly, $\Delta E^{Fe \to Cr}$ will refer to the required energies to substitute one Fe atom by one

Cr atom for instance. These energies will be however often referred to as substitutional formation energies for simplicity purposes.

In this work we focused on vacancies and ⟨100⟩ dumbbells. Vacancies have been introduced by removing one Fe atom from the reference state and dumbbells have been introduced by replacing one Fe atom from the reference state by two atoms sharing the same atomic site. Point defect calculations were performed at many sites (at least 40 sites) to analyse the impact of the local environment on formation energies. For comparison purposes, both vacancies and dumbbells were introduced on the same atomic sites using the same reference state. It has to be noted that all atomic sites selected to introduce the point defects are Fe atoms carrying a magnetic moment "up" (in a plane "up"). Both ionic and electronic minimizations of the defect lattices were then done at constant volume, i. e. by fixing the supercell dimensions at the equilibrium values obtained for the reference states. Calculations were not done at constant pressure in order to save computational cost because several hundred of calculations are needed to consider each point defect and to investigate the influence of the local environment. In particular, many calculations have to be performed to accurately analyse the dumbbells. Indeed, they can be formed by six different combinations of elements (Fe-Fe, Fe-Ni, Fe-Cr, Ni-Ni, Cr-Cr and Ni-Cr dumbbells) which can be oriented either parallel (oriented along the [010] axis) or perpendicular (oriented along the [100] axis) to the AFM1 magnetic planes.

As already mentioned in Chapter I, the point defect formation energies were calculated by considering the difference between the energy of the defect lattice, that is to say either E_{N-1} for the vacancies or E_{N+1} for the dumbbells, and the energy of the reference state E_N, where N refers to the number of atoms of the reference state. However, as these lattices do not have the same number of atoms, we need to define the chemical potentials for one Fe atom, μ_{Fe}, one Ni atom, μ_{Ni}, and one Cr atom, μ_{Cr}, to be able to calculate all the point defect energies as follow:

$$\Delta E^V = E_{N-1} - (E_N - \mu_{Fe})$$ Eq. III-1

$$\Delta E^{Fe-A} = E_{N+1} - (E_N + \mu_A)$$ Eq. III-2

$$\Delta E^{A-B} = E_{N+1} - (E_N - \mu_{Fe} + \mu_A + \mu_B)$$ Eq. III-3

Where ΔE^V refers to the required energy to remove one Fe atom from the reference state to form a vacancy, ΔE^{Fe-A} refers to the required energy to introduce an atom A in the reference state to form a dumbbell Fe-A (A refers to the element type), ΔE^{A-B} refers to the required energy to introduce two atoms A and B to form a dumbbell A-B (A and B refer to elements different than Fe atom) in place of an Fe atom initially positioned in substitutional site in the reference state. A schematic description is given in Fig. III-6.
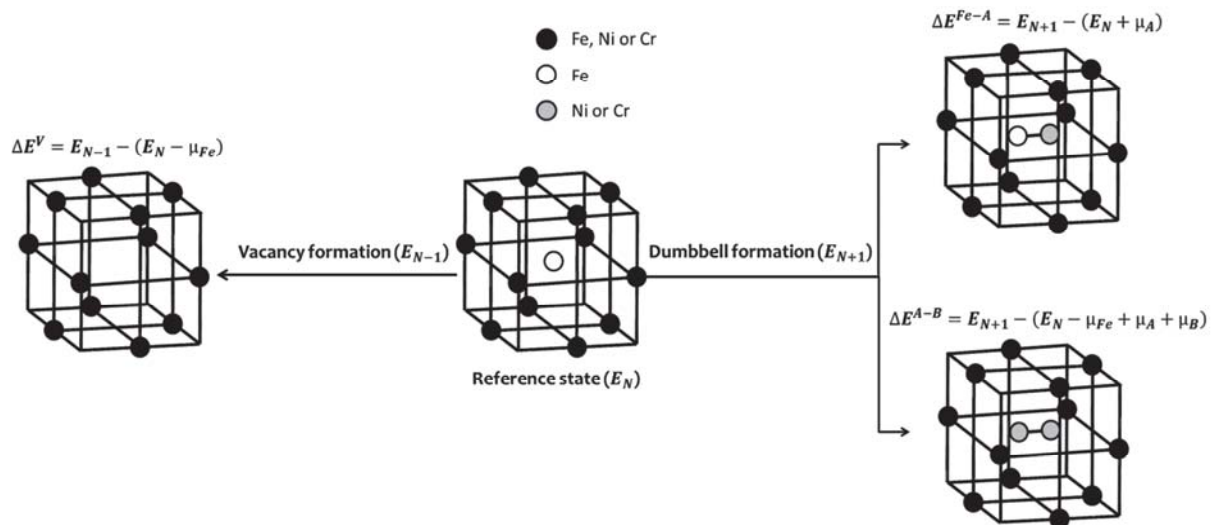
Fig. III-6: Schematic representation of the calculation of the point defect formation energy. Vacancies and dumbbells were introduced on the same atomic sites (Fe atoms carrying a magnetic moment "up", i.e. in a plane "up") using the same Fe-Ni-Cr reference state of total energy E_N. To create a vacancy, one Fe atom is removed from the reference state. The total energy of the defect lattice is E_{N-1}. To create a Fe-A dumbbell (A can refer to Fe, Ni or Cr), an Fe atom initially positioned at a lattice site is introduced, with another atom A, in the two interstitial sites. To create a A-B dumbbell (A and B can refer to Ni or Cr), the Fe atom initially positioned at a lattice site is removed from the reference state and two atoms A and B are introduced in the two interstitial sites. The total energy of the defect lattice is E_{N+1}.

IV-1   Determination of the "chemical potential"

As it will see next, many substitution calculations were performed in the Fe-10Ni-20Cr model alloy in order to obtain an estimate of the required chemical potentials needed to calculate the point defect formation energies presented in this section. These calculations have been also used to calculate substitutional formation energies as follows:

$$\Delta E^{A \to B} = (E_B + \mu_A) - (E_A + \mu_B) \qquad\qquad \text{Eq. III-4}$$

where E_A refers to the energy of the initial state containing one more element A and one less element B relative to the final state, and μ_A refers to the chemical potential of A atoms. A schematic representation of these calculations is given in Fig. III-7.
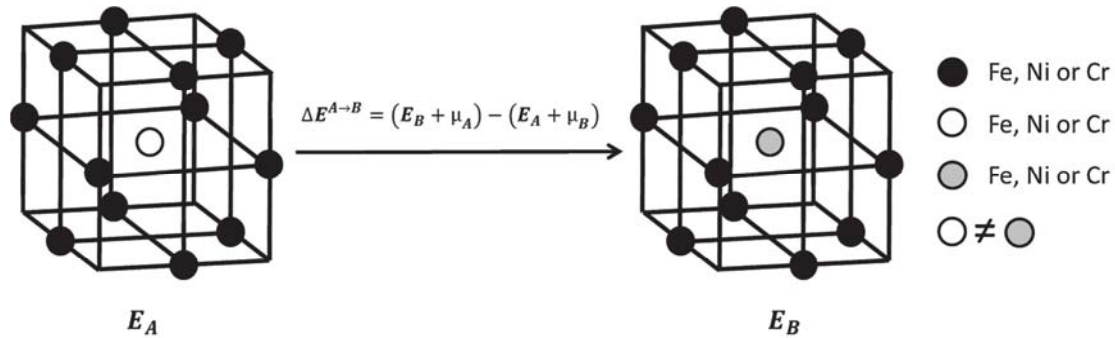
Fig. III-7: Schematic representation of the substitution calculation performed to calculate the substitutional formation energies in the Fe-Ni-Cr reference state of total energy E_N. The lattice represented in the left hand side correspond to the initial state of energy E_A and contains one more element A (white circle) and one less element B (grey circle) relative to the final state of energy E_B represented in the right hand side.

As we consider a concentrated Fe-Ni-Cr system in this work, we can expect chemical potentials defined above to be substantially different than the formation energies of elements in their pure reference states. Thus in this section we suggest an approach to calculate these quantities.

Although naturally defined at constant temperature and pressure, the chemical potential can also be calculated in constant volume and temperature simulations:

$$\left.\frac{\partial G}{\partial N_\alpha}\right|_{P,T,N_{\beta \neq \alpha}} = \left.\frac{\partial F}{\partial N_\alpha}\right|_{P,T,N_{\beta \neq \alpha}} = \mu_\alpha$$

At finite temperature, excess chemical potential differences $\Delta\mu_{ex} = \left(\mu_B - \mu_B^{id}\right) - \left(\mu_A - \mu_A^{id}\right)$, where μ_B refers to the chemical potential of the B specie and μ_B^{id} refers to the ideal contribution of μ_B, are usually calculated using Widom-type substitution techniques [WIDOM1963]. In principle, this can be done either at constant pressure or at constant volume. This consists, in short, in simulating the non-substituted reference system "A" of energy E_A (containing N_A A-type

95 Chapter III. First principle study of point defects in a fcc Fe-10Ni-20Cr model alloy

atoms and N_B B-type atoms) with a Monte-Carlo procedure, and estimating the excess chemical potential difference by canonical averages of the exponential of the substitution energy $\Delta^{A \to B} E = E_B - E_A$:

$$\Delta^{A \to B} \mu_{ex} = -\beta^{-1} \ln \langle \exp(-\beta \Delta^{A \to B} E) \rangle_A$$

where, $\beta = (k_B T)^{-1}$, $\langle \ \rangle_A$ denotes the canonical average on the "A" system configurations. Stating the ratio of the ideal gas contributions gives [FRENKEL1996]:

$$\Delta^{A \to B} \mu = -\beta^{-1} \ln \langle \frac{N_B}{N_A + 1} \exp(-\beta \Delta^{A \to B} E) \rangle_A \qquad \text{Eq. III-5}$$

In practice, to obtain accurate estimates of the chemical potential differences, it is safer to realise the inverse substitution starting from a "B" system of energy E_B with an additional B atom (containing N_A-1 A-type atoms and N_B+1 B-type atoms) as a reference, and to make a canonical average on the "B to A" substitution energies $\Delta^{B \to A} E = E_A - E_B$:

$$\Delta^{B \to A} \mu = -\beta^{-1} \ln \langle \frac{N_A}{N_B + 1} \exp(-\beta \Delta^{B \to A} E) \rangle_B$$

For the purpose of calculating defects formation energies from Eq. III-1 to Eq. III-3, estimates of the chemical potentials of the species involved in the defects are required. Precise estimates of chemical potentials by DFT methods would be extremely time consuming. This would require, depending on temperature, to sample a large number of configurations by a Monte-Carlo Metropolis procedure. Thus, the estimates of chemical potentials will present here may not be considered as physical and realistic ones, but just zero Kelvin reference energies in VASP for the addition or the removal of a given type of atom in our AFM1 Fe-10Ni-20Cr reference configuration (hereafter simply called chemical potential and referred to as $\mu_A^{FeNiCr/DFT}$, where A refers to the element type) thus neglecting any entropic contribution. It can be noted that $\mu_A^{FeNiCr/DFT}$ will be therefore used in the calculation of formation defined from Eq. III-1 to Eq. III-3.

The zero Kelvin equivalent of Widom-type substitution techniques and associated Monte-Carlo procedure for estimates of $\Delta\mu$ would be estimate from the minimum value of substitution

energies, sampled. Indeed, the limit of Eq. III-5 for $\beta^{-1} \xrightarrow[T \to 0]{} 0$, the ideal gas contribution vanishes and:

$$\Delta^{A \to B}\mu_{ex} = -\beta^{-1}\ln\langle\exp(-\beta\Delta^{A \to B}E)\rangle_A$$

$$\approx -\beta^{-1}\ln\left(\frac{1}{n}\sum_{i=1}^{n}\exp(-\beta\Delta^{A \to B}E_i)\right)$$

$$= -\beta^{-1}\ln\left(\frac{1}{n}\exp\left(-\beta\min_k(\Delta^{A \to B}E_k)\right)\sum_{i=1}^{n}\exp\left(-\beta\left(\Delta^{A \to B}E_i - \min_k(\Delta^{A \to B}E_k)\right)\right)\right)$$

$$= -\beta^{-1}\ln\left(\frac{1}{n}\exp\left(-\beta\min_k(\Delta^{A \to B}E_k)\right)\left(1 + \sum_{i=1,i\neq j}^{n}\exp\left(-\beta\left(\Delta^{A \to B}E_i - \min_k(\Delta^{A \to B}E_k)\right)\right)\right)\right)$$

$$= -\beta^{-1}\ln\left(\exp\left(-\beta\min_k(\Delta^{A \to B}E_k)\right)\right) - \beta^{-1}\ln\left(\frac{1}{n}\right) - \beta^{-1}\ln\left(1 + \sum_{i=1,i\neq j}^{n}\exp(-\beta\varepsilon_i)\right)$$

$$\xrightarrow[\beta^{-1} \to 0]{} \min_k(\Delta^{A \to B}E_k)$$

$$\Delta^{B \to A}\mu \xrightarrow[\beta^{-1} \to 0]{} \min_k(\Delta^{B \to A}E_k)$$

Where j is such that $\Delta^{A \to B}E_i = \min_k(\Delta^{A \to B}E_k)$, $\varepsilon_i = \Delta^{A \to B}E_i - \min_k(\Delta^{A \to B}E_k) > 0$ for any $i \neq j$, and where the sum is made on the substitution energies sampled in the AFM1 configuration. Similarly, we have $\Delta^{B \to A}\mu \xrightarrow[\beta^{-1} \to 0]{} \min_k(\Delta^{B \to A}E_k)$.

Now, applying this method to the estimate of reference chemical potential of Fe, Ni and Cr in the AFM1, we estimate the three differences of reference chemical potentials as follows:

$$\mu_{Cr}^{FeNiCr/DFT} - \mu_{Fe}^{FeNiCr/DFT} = \frac{1}{2}(\Delta^{Fe \to Cr}\mu - \Delta^{Cr \to Fe}\mu) \qquad \text{Eq. III-6}$$

97   Chapter III. First principle study of point defects in a fcc Fe-10Ni-20Cr model alloy

$$\mu_{Ni}^{FeNiCr/DFT} - \mu_{Fe}^{FeNiCr/DFT} = \frac{1}{2}\left(\Delta^{Fe\to Ni}\mu - \Delta^{Ni\to Fe}\mu\right) \qquad \text{Eq. III-7}$$

$$\mu_{Ni}^{FeNiCr/DFT} - \mu_{Cr}^{FeNiCr/DFT} = \frac{1}{2}\left(\Delta^{Cr\to Ni}\mu - \Delta^{Ni\to Cr}\mu\right) \qquad \text{Eq. III-8}$$

by calculating the minimum of substitution energy on most of the 180 Fe, 50 Cr and 26 Ni atoms of the reference state. Advanced estimation techniques which rigorously combine so called "forward" and "backward" estimates $\Delta^{\alpha\to\beta}\mu$ and $-\Delta^{\beta\to\alpha}\mu$ [ADJANOR2011, BENNETT1976] cannot be applied for the present method, as no actual Monte-Carlo sampling is done in this simplified approach, and simple arithmetic average is taken in the previous equations. This system of three equations (from Eq. III-6 to Eq. III-8) provides in fact only two independent equations, the last one being the difference of the former two, it cannot be used to solve the values of the μ_α, but only for checking the good reliability of the estimates (if the numerical estimate yielded by the difference of the first two is close to the estimate of the last one, this supports the accuracy of the estimates, as they were not calculated with the same substitutions). The total energy of system calculated with VASP can provide us the additional equation needed to estimate the reference chemical potentials (Eq. III-9). Indeed, as the calculation where made at constant volume, and neglecting all entropic contributions, we have $E_A \approx F(V)$ and:

$$F(V) = G(V) - PV = \sum_{\alpha} N_\alpha \mu_\alpha^{FeNiCr/DFT} - PV \qquad \text{Eq. III-9}$$

The substitution energy calculations performed in the AFM1 reference state using VASP, $\Delta^{B\to A}\mu$, and used to obtain an estimate of zero Kelvin reference energies for the addition or the removal of a given type of atom using equations III-6 to III-9, i.e. $\mu_{Fe}^{FeNiCr/DFT}$, $\mu_{Ni}^{FeNiCr/DFT}$ and $\mu_{Cr}^{FeNiCr/DFT}$, are listed in Tab. III-1.

Substitution energy (eV)	Number of calculations	Average value	Minimum value	Maximum value
$\Delta\mu^{Fe\to Ni}$	40	2.66	2.50	2.86
$\Delta\mu^{Ni\to Fe}$	26	-2.72	-2.81	-2.59
$\Delta\mu^{Fe\to Cr}$	40	-1.17	-1.43	-0.95
$\Delta\mu^{Cr\to Fe}$	40	1.13	0.86	1.32
$\Delta\mu^{Ni\to Cr}$	26	-3.87	-4.07	-3.55
$\Delta\mu^{Cr\to Ni}$	40	3.81	3.49	4.06

Tab. III-1: Minimum, maximum and average values of substitution energies, $\Delta^{B\to A}\mu$ (A and B refer to the element type), performed to obtain an estimate of zero Kelvin reference energies in VASP for the addition or the removal of a given type of atom in the AFM1 Fe-10Ni-20Cr system, i.e. $\mu_{Fe}^{FeNiCr/DFT}$, $\mu_{Ni}^{FeNiCr/DFT}$ and $\mu_{Cr}^{FeNiCr/DFT}$, are presented along with the number of calculation performed.

The results of these calculations are presented in Tab. III-2 with the calculation of chemical potentials in pure fcc systems, μ_A^0, as well as their relative differences. It can be noted that reference chemical potentials calculated in AFM1 reference state, $\mu_A^{FeNiCr/DFT}$, never exceed their associated bulk chemical potentials, μ_A^0. This result indicates that all elements are more stable in Fe-10Ni-20Cr reference state than in their respective pure phases of lowest energies found using VASP ($\mu_A^{FeNiCr/DFT} - \mu_A^0 < 0$ for all elements A). Elements are thus found to be more stable in a SQS (solid solution) than in a precipitate, thus indicating no tendencies for phase separation in the Fe-10Ni-20Cr reference state.

Alloying elements	Fe	Ni	Cr
μ_A^0 (eV)	-8.118	-5.470	-9.020
$\mu_A^{FeNiCr/DFT}$ (eV)	-8.125	-5.472	-9.269
$\mu_A^{FeNiCr/DFT} - \mu_A^0$ (eV)	-0.07	-0.002	-0.249

Tab. III-2: Reference chemical potentials calculated using VASP, in pure fcc system, μ_A^0, along with those calculated in the AFM1 Fe-10Ni-20Cr system, $\mu_A^{Fe-10Ni-20Cr}$ are presented. All calculations were performed using the same computational conditions as those presented in section I-1. The magnetic ordering considered for the calculations were the AFM1, FM and non-magnetic phases in pure systems of Fe, Ni and Cr respectively.

It has to be mentioned again that the estimates of chemical potentials $\mu_A^{FeNiCr/DFT}$ presented in this table may not be considered as physical and realistic ones as it is the case for chemical potential

presented in annex 3. This can only represent a zero Kelvin reference energies in VASP for the addition or the removal of a given type of atom in our AFM1 Fe-10Ni-20Cr reference alloy. In any case, the use of wrong chemical potentials may cause a global shift in the formation energy values thus obtained, but it does not change the trends observed with the local environment.

IV-2   Substitution formation energy

The calculations performed in section IV-1 were used to perform substitutional formation energy calculations using the reference chemical potentials $\mu_{Fe}^{FeNiCr/DFT}$, $\mu_{Ni}^{FeNiCr/DFT}$ and $\mu_{Cr}^{FeNiCr/DFT}$ presented in Tab. III-2 For each set of substitutional formation energy calculations, the minimum, maximum and average values are listed in Tab. III-3 along with the number of calculations performed.

For each set of calculations, i.e. Fe→Ni, Ni→Fe, Fe→Cr, Cr→Fe, Ni→Cr and Cr→Ni substitutional energies, an energy range of about 0.4 eV is usually obtained, underlying the importance of the local environment. In particular, we show in this section that these energies slightly depend on the number of chemical elements first nearest neighbours to the substitution sites, i.e. 1nn_Fe, 1nn_Cr and 1nn_Ni as schematically presented in Fig. III-8.

Substitutional formation energy (eV)	Number of calculations	Average value	Minimum value	Maximum value
$\Delta E_{DFT}^{Fe \to Ni}$	40	0.01	-0.16	0.21
$\Delta E_{DFT}^{Ni \to Fe}$	26	-0.06	-0.15	0.06
$\Delta E_{DFT}^{Fe \to Cr}$	40	-0.02	-0.29	0.19
$\Delta E_{DFT}^{Cr \to Fe}$	40	-0.02	-0.29	0.17
$\Delta E_{DFT}^{Ni \to Cr}$	26	-0.07	-0.28	0.25
$\Delta E_{DFT}^{Cr \to Ni}$	40	0.02	-0.31	0.26

Tab. III-3: Minimum, maximum and average values of substitutional formation energies, $\Delta E_{DFT}^{A \to B}$ (A and B refer to the element type), are presented along with the number of calculations performed.
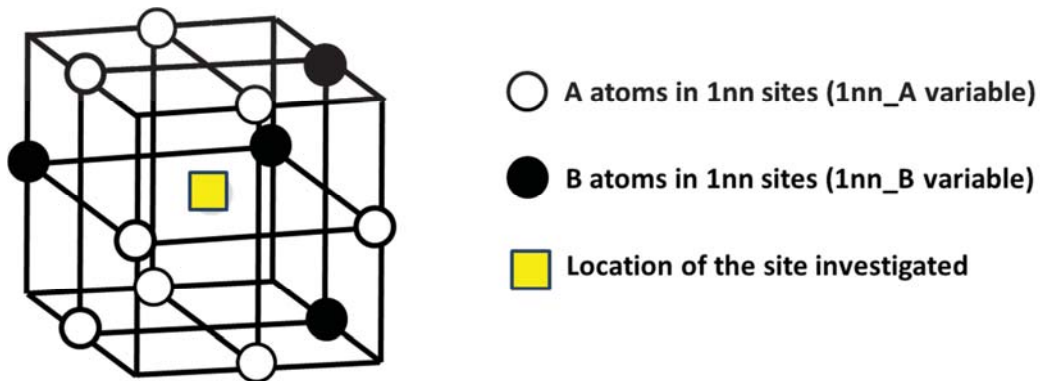
Fig. III-8: Representation of the first nearest neighbours of an atomic site. The 1nn_A variable (respectively the 1nn_B variable) refers to the number of A atoms (respectively the number of B atoms) first nearest neighbour (1nn sites) to the site investigated. In this example 1nn_A = 8 and 1nn_B = 4.

No clear trends are observed for the substitutional formation energies involving one Fe and one Ni atom, i.e. $\Delta E_{DFT}^{Fe \rightarrow Ni}$ and $\Delta E_{DFT}^{Ni \rightarrow Fe}$ energies respectively. In particular, absolutely no trends were observed for $\Delta E_{DFT}^{Ni \rightarrow Fe}$ energies. It can however be mentioned that $\Delta E_{DFT}^{Fe \rightarrow Ni}$ energies slightly decrease with the number of first nearest Ni to the substitution sites as can be seen in Fig. III-9.
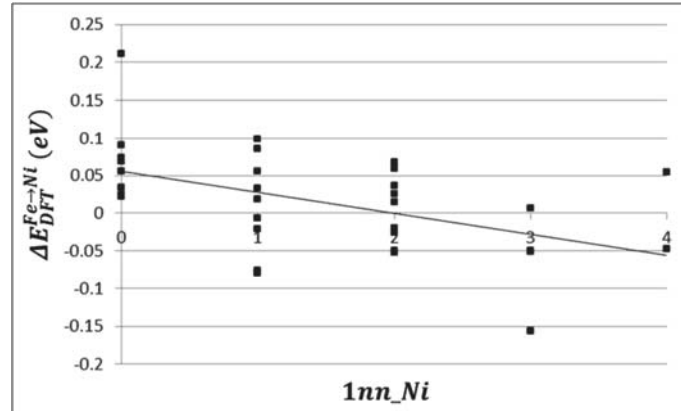
Fig. III-9: Fe→Ni substitutional formation energies, $\Delta E_{DFT}^{Fe \rightarrow Ni}$, as a function of the number of 1nn of Ni, 1nn_Ni.

Better trends are observed for the substitutional formation energies involving one Fe and one Cr atom, i.e. $\Delta E_{DFT}^{Fe \rightarrow Cr}$ and $\Delta E_{DFT}^{Cr \rightarrow Fe}$ energies respectively. In particular, these energies show clear trends with the number of first nearest Cr to the substitution sites as can be seen in Fig. III-10. Furthermore, $\Delta E_{DFT}^{Cr \rightarrow Fe}$ energies are found to slightly increase with the number of first nearest Fe

101   Chapter III. First principle study of point defects in a fcc Fe-10Ni-20Cr model alloy

to the substitution sites as can be seen in Fig. III-11 while no particular trends are found for $\Delta E_{DFT}^{Fe \rightarrow Cr}$.
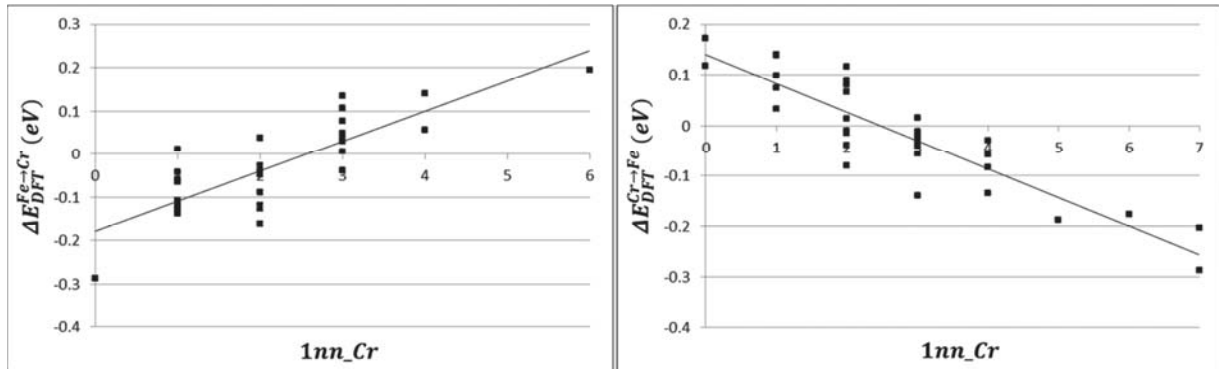
Fig. III-10: Fe➔Cr substitutional formation energies, $\Delta E_{DFT}^{Fe \rightarrow Cr}$, as a function of the number of 1nn of Cr, 1nn_Cr (left figure). Cr➔Fe substitutional formation energies, $\Delta E_{DFT}^{Cr \rightarrow Fe}$, as a function of the number of 1nn of Cr, 1nn_Cr (right figure).
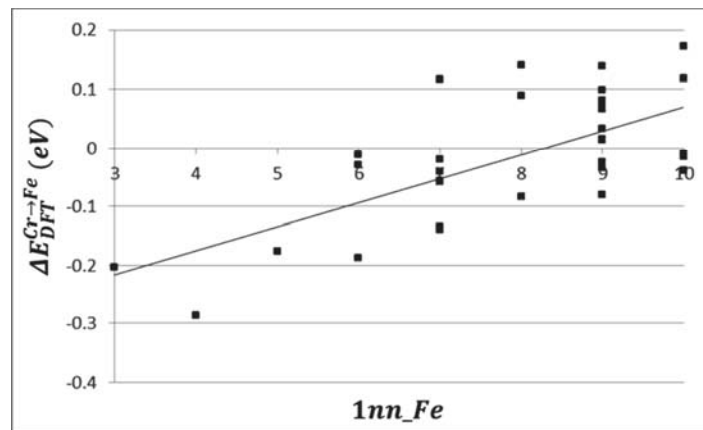
Fig. III-11: Cr➔Fe substitutional formation energies, $\Delta E_{DFT}^{Cr \rightarrow Fe}$, as a function of the number of 1nn of Fe, 1nn_Fe.

Again, clear trends are observed for the substitutional formation energies involving one Cr and one Ni atom, i.e. $\Delta E_{DFT}^{Ni \rightarrow Cr}$ and $\Delta E_{DFT}^{Cr \rightarrow Ni}$ energies respectively, with the number of first nearest Cr to the substitution sites as can be seen in Fig. III-12. Furthermore, better trends are found with the number of first nearest Fe to the substitution sites relative to those found previously as can be seen in Fig. III-13.

102   Chapter III. First principle study of point defects in a fcc Fe-10Ni-20Cr model alloy
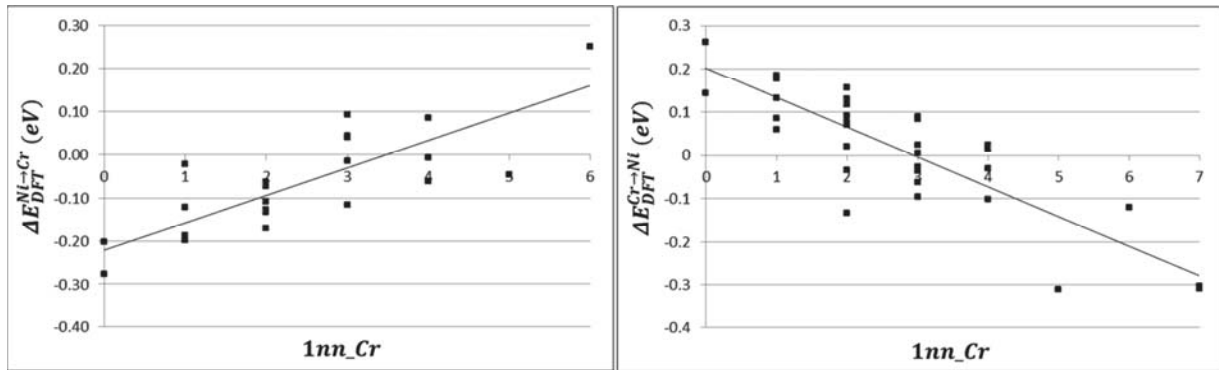
Fig. III-12: Ni→Cr substitutional formation energies, $\Delta E_{DFT}^{Ni\rightarrow Cr}$, as a function of the number of 1nn of Cr, 1nn_Cr (left figure). Cr→Ni substitutional formation energies, $\Delta E_{DFT}^{Cr\rightarrow Ni}$, as a function of the number of 1nn of Cr, 1nn_Cr (right figure).
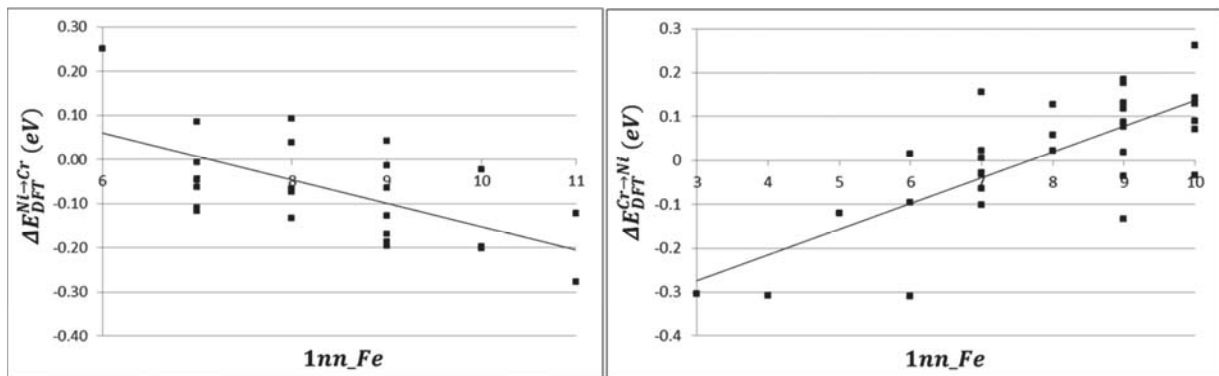
Fig. III-13: Ni→Cr substitutional formation energies, $\Delta E_{DFT}^{Ni\rightarrow Cr}$, as a function of the number of 1nn of Fe, 1nn_Fe (left figure). Cr→Ni substitutional formation energies, $\Delta E_{DFT}^{Cr\rightarrow Ni}$, as a function of the number of 1nn of Fe, 1nn_Fe (right figure).

IV-3   Point defect formation energies

Tab. III-4 presents, for each point defect studied, the mean value calculated for the formation energies along with the energy range, the mean square deviation, the number of calculations performed and the calculation method used. We obtained an important energy range for each set of point defect formations, proving again the key role played by the local environment. In particular, we can see in Fig. III-14 for the case of the vacancy, the key role played by the local chemistry and in particular by the number of Ni and Cr first nearest neighbours of point defects on formation energy values, ΔE_{DFT}^{V}. Indeed, the vacancy formation energy is found to slightly decrease with both higher Ni content and lower Cr content.

103   Chapter III. First principle study of point defects in a fcc Fe-10Ni-20Cr model alloy

Our results can be compared with the formation energy values found by Klaver et al. [KLAVER2012] in dilute Fe-Ni-Cr austenitic alloys presented in chapter II (section II-2-b), where, especially for the dumbbell formation energies, significant differences are observed. Indeed, the mean value found for the vacancy formation energies is similar in the fct AFM1 γ-Fe system and in our model alloy while dumbbell formation is found to be significantly higher in the fct AFM1 γ-Fe. It can however be noted that the same general order of preference for the different alloying elements to be found in dumbbell sites. Indeed, Fe atom is found to be the most stable in interstitial site followed by Cr and Ni atoms in the fct AFM1 γ-Fe system according to Klaver et al [KLAVER2012]. In particular, Ni is found to be very unlikely to be found in mixed Fe-Ni dumbbells. Ni-Ni dumbbells are even more unlikely to form. Cr on the other hand can form mixed dumbbells. These results are however not in agreement with the experimentally derived size factors for Ni and Cr solutes in type 316 SS and in the pure materials [STRAALSUND1974].

Reference state	Point defect formation energy (eV)	Number of calculations	Energy range	Mean value
fct AFM1	ΔE_{DFT}^{V}	60	1.76-2.19	1.96
	$\Delta E_{DFT}^{[100]\ Fe-Fe}$	60	2.61-3.34	3.02
	$\Delta E_{DFT}^{[010]\ Fe-Fe}$	40	2.72-3.50	3.06
	$\Delta E_{DFT}^{[100]\ Fe-Ni}$	60	2.81-3.80	3.37
	$\Delta E_{DFT}^{[010]\ Fe-Ni}$	40	3.12-3.96	3.48
	$\Delta E_{DFT}^{[100]\ Fe-Cr}$	40	2.68-3.31	3.05
	$\Delta E_{DFT}^{[010]\ Fe-Cr}$	40	2.76-3.41	3.04
	$\Delta E_{DFT}^{[100]\ Ni-Ni}$	40	3.23-3.95	3.65
	$\Delta E_{DFT}^{[100]\ Cr-Cr}$	40	2.97-3.71	3.31
	$\Delta E_{DFT}^{[100]\ Ni-Cr}$	40	2.94-3.79	3.35
fcc AFM1	$\Delta E_{DFT}^{[100]\ Fe-Fe}$	40	2.75-3.51	3.05
	$\Delta E_{DFT}^{[010]\ Fe-Fe}$	40	2.79-3.56	3.05

Tab. III-4: Energy range found for each set of formation energy calculations is presented along with the mean value, the number of calculations and the reference state used. For instance, ΔE_{DFT}^{V} refers to the vacancy formation energy.
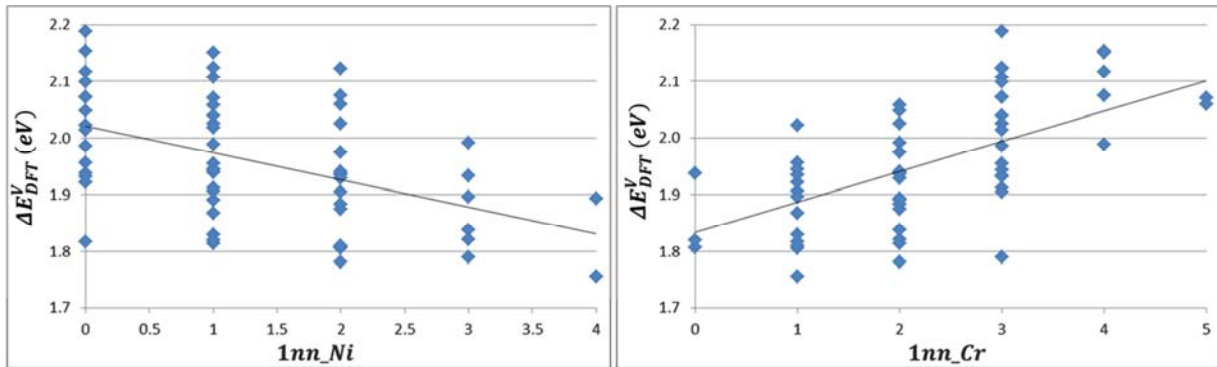
Fig. III-14: Evolution of the vacancy formation energy, ΔE_{DFT}^{V}, as a function of the number of first nearest Ni atoms surrounding the vacancy, 1nn_Ni (left figure). Evolution of the vacancy formation energy, ΔE_{DFT}^{V}, as a function of the number of first nearest Cr atoms surrounding the vacancy, 1nn_Cr (right figure). These figures display the merging of 60 vacancy calculations performed in the fct AFM1 reference state.

IV-4   Link between the local environment and the formation energies

Fig. III-14 clearly shows that a relationship between the local environment of the point defect and its formation energy exist. We are now going to investigate this issue in more details in the following paragraphs. In particular, we are going to show that an estimate of the point defect formation energy can be obtained from the knowledge of the local environment of the point defect. For this purpose, we first need to establish a nomenclature of the different sites in the close vicinity of the point defect. The nomenclature used to describe the local environment of point defects is presented in Tab. III-5.

The simplest set of variables which describes the atomic arrangement surrounding the point defects is the one which only consider the number of alloying elements positioned in their nearest shells. We considered in this work the first (1nn), second (2nn) and third (3nn) nearest neighbours of the point defect center of mass. They will be referred in the next sections to as inn_A, where i indicates the shell (1st, 2nd or 3nd) and A indicates the chemical type of the neighbour considered. The case of the 1nn variables is schematically represented in Fig. III-8.

In contrast to the vacancy, the specific orientation of the dumbbell induces anisotropic relaxations for atoms belonging to its first shells. As could be expected, the eight 1nn atoms in compressive sites (black spheres in Fig. III-15) are repelled by the dumbbell as can be observe

105   Chapter III. First principle study of point defects in a fcc Fe-10Ni-20Cr model alloy

in Fig. III-16. The opposite behaviour is observed for the four 1nn atoms in tensile sites (white spheres in Fig. III-15). The magnetic behaviour is strongly related to the distance between atoms as indicated by the behaviour of Fe whose ground state can switch from low spin to high spin by simply changing its lattice constant [DOMAIN2001B]. Therefore, it can be expected that 1nn atoms positioned in compressive sites contribute differently to the formation energies than those positioned in tensile sites. We have thus considered two different variables to describe the first nearest atoms of a dumbbell defect, by introducing in the notation "t" when the atom is positioned in a tensile site or "c" when the atom is positioned in a compressive site. 1nnc_Ni thus refers to a Ni atom which is situated at 1nn separation of a dumbbell and in a compressive site, i.e. one of the black spheres in Fig. III-15. It has to be noted that atoms in the fourth shell surrounding Fe-Fe dumbbell also split into tensile and compressive sites as can be seen in Fig. III-16.
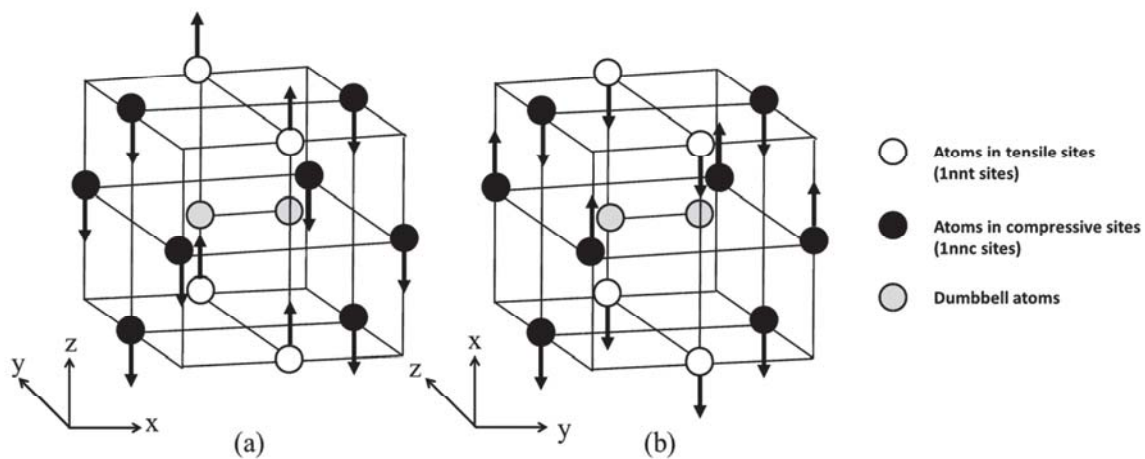
Fig. III-15: Representation of atoms at 1nn separation to a dumbbell defect oriented either along the [100] direction (figure a) or along the [010] direction (figure b), in a fcc lattice. Atoms positioned in compressive sites (1nnc sites) are represented in black and atoms in tensile sites (1nnt sites) are represented in white. Dumbbell atoms are represented in grey. Arrows indicate the local moments in both figures and the magnetic planes of the AFM1 reference state. 1nnt_A variables (respectively 1nnc_A variables) refer to the number of A atoms located in tensile sites (respectively in compressive sites). In the case of mixed dumbbells, i.e. Fe-Ni and Fe-Cr dumbbells, "Fe" or "S" is introduced in the variable notation (1nncFe_A and 1nncS_A respectively) to consider compressive atoms positioned in the plane near either the Fe or the solute atom of the mixed dumbbell.
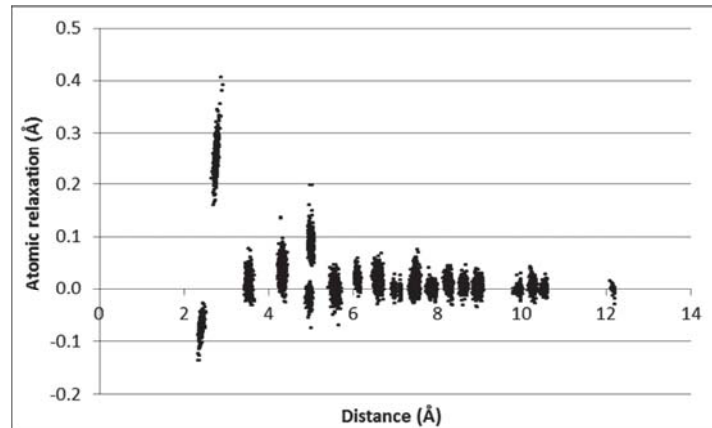
Fig. III-16: Relaxation of the Fe atoms relative to the lattice spacing as a function of their distance from the Fe-Fe dumbbells. A positive relaxation indicates that the atoms are repelled by the dumbbell. The 80 Fe-Fe dumbbells calculations performed with the FR method are represented.

It also can be assumed that for both Fe-Ni and Fe-Cr mixed dumbbells, first nearest atoms positioned in compressive sites may behave differently when located closer to the Fe atom than the solute atom of the mixed dumbbell. These two different kinds of compressive sites have been therefore differentiate by introducing in the variable notation either "Fe" or "S" respectively when they were positioned in the plane near either the Fe or the solute atom of the mixed dumbbell. The 1nncFe_Ni variable thus refers to the number of Ni atoms positioned in compressive sites, located closer to the Fe atom of the mixed dumbbell. No such differentiation was considered for tensile sites since they are equidistant from the two atoms which form the dumbbell.

More complicated variables such as the ones presented in Fig. III-17, can be defined to determine if a more accurate description of the point defect vicinity could provide better predictions of the point defect formation energies. In particular, many kinds of pairs as well as triplets variables can be considered. However, these variables have not been used in the next sections because we found that they do not bring any substantial improvements in the estimate of the point defect formation energies.

107   Chapter III. First principle study of point defects in a fcc Fe-10Ni-20Cr model alloy

Local variables	Number
1nn_A	12
1nnc_A	8
1nncFe_A	4
1nncS_A	4
1nnt_A	4
2nn_A	6
3nn_A	24

Tab. III-5: Variable notations used to describe the local environment surrounding the point defects are represented along with the number of their atomic sites. 1nn_A, 2nn_A and 3nn_A variables refer to the number of atoms A, respectively first second and third nearest neighbours to the point defect. 1nnc_A and 1nnt_A variables refer to the number of atoms A positioned in compressive and in tensile sites respectively. 1nncFe_A and 1nncS_A variables refer to the number of atoms A positioned in compressive sites, located closer to the Fe atom of the dumbbell and closer to the solute atom of the dumbbell respectively.
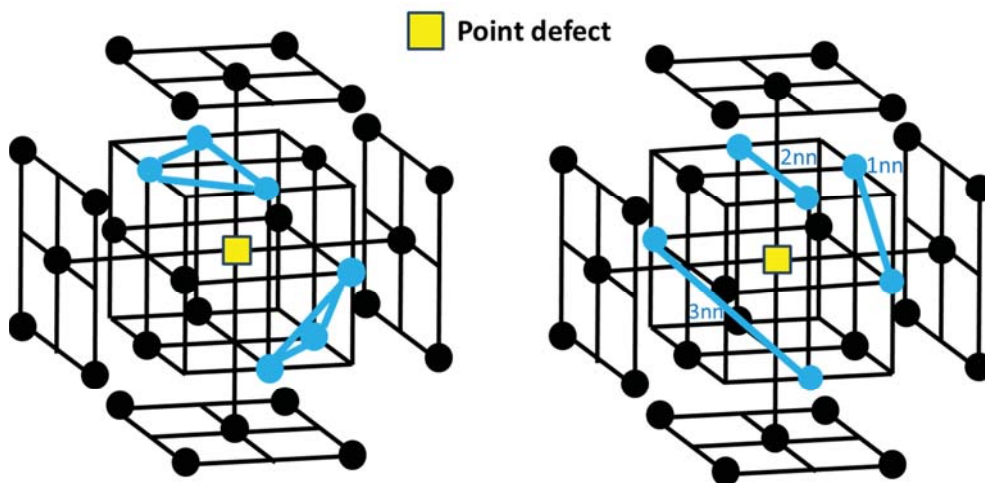
Fig. III-17: Schematic representation of the multiplets (pairs and triplets) tested to estimate the point defect formation energy.

The trends observed from Fig. III-9 to Fig. III-14 prove the strong influence of local environment on local energies of the system. This result is not surprising since the study of the reference state indicates that local properties, such as the magnetic moments strongly depend on properties of their closest neighbourhood as shown in section III-1. Indeed, the analysis of the local magnetic moments performed in the AFM1 state of our model alloy has indicated that the relaxed local moments carried by both Cr and Ni atoms depend strongly on the sum of the moments of their Fe first nearest neighbours. Although moments carried by Fe atoms do not depend on the magnetic

features of their neighbour atoms, the magnitude of Fe atom moments are found to slightly depend on the species in its neighbourhood and particularly shows a slight trend with the number of first nearest atoms of Ni and Cr. In order to illustrate this point, magnitude of Fe moments obtained in the AFM1 reference state using VASP, $\left|m_{DFT}^{Fe}\right|$, have been estimated using linear regressions (LRs). Variables tested to characterise the local environment of Fe atoms are those used to characterise the local environment of vacancies, i.e. the 1nn_A (A refer to the element type) variables as presented in Tab. III-5.

The adequacy between the multiple LRs involving two or more variables, and local physical quantities calculated using the DFT was estimated using the Pearson product-moment correlation coefficient , $r_{X_{DFT}X_{LR}}$, which is obtained by dividing the covariance obtained for a certain local physical quantity X, by the product of their standard deviations as follows:

$$r_{X_{DFT}X_{LR}} = \frac{\sum_{k=1}^{n}(X_{DFT}^{k} - \overline{X_{DFT}^{k}})\left(X_{LR}^{k} - \overline{X_{LR}^{k}}\right)}{\sqrt{\sum_{k=1}^{n}\left(X_{DFT}^{k} - \overline{X_{DFT}^{k}}\right)^{2}\sum_{i=1}^{n}\left(X_{LR}^{k} - \overline{X_{LR}^{k}}\right)^{2}}}$$
Eq. III-10

where DFT means that the local physical quantity X was calculated using the DFT, LR means that the local physical quantity X was calculated using a linear regression and n refers to the number of DFT calculation performed in the set considered. This relation measure the strength of the linear relationship between the two sets of data X_{DFT}^{k} and X_{LR}^{k} respectively. The Pearson correlation is +1 in the case of a perfect positive linear relationship and −1 in the case of a perfect negative linear relationship. For intermediate values, the more the Pearson correlation approaches the zero value, the less correlation exists between the two set of data X_{DFT}^{k} and X_{LR}^{k} respectively.

Fig. III-18 compares the magnetic moment magnitude of Fe atoms obtained using VASP, $\left|m_{DFT}^{Fe}\right|$, with its best estimation obtained by a linear function of two variables, $\left|m_{LR}^{Fe}\right|$. A correlation coefficient (CC) of 0.65 is obtained with this LR which takes into account the number of Ni and Cr 1nn. The signs obtained for the adjusted parameters show a tendency for Fe moments to decrease when Fe atoms are positioned in Cr-rich or Ni-poor environments.

109 Chapter III. First principle study of point defects in a fcc Fe-10Ni-20Cr model alloy
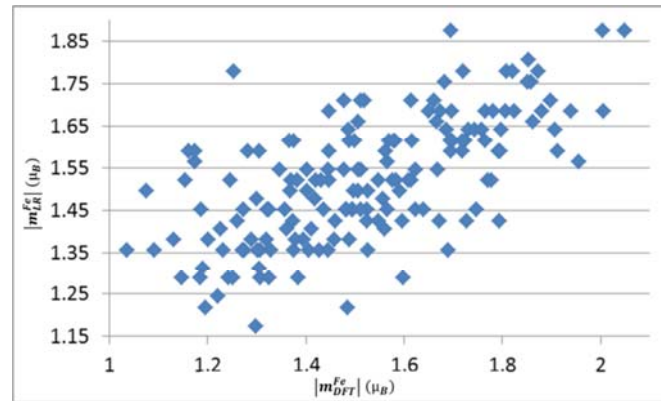
Fig. III-18: Magnitudes of magnetic moments carried by Fe atoms obtained in the AFM1 reference state using VASP, $\left|m_{DFT}^{Fe}\right|$, are compared with their best estimations, i.e. $m_{LR}^{Fe} = 0.09 \times 1nn\_Ni - 0.07 \times 1nn\_Cr + 1.55$, where 1nn_Ni is the number of Ni 1nn and 1nn_Cr is the number of Cr 1nn. CC of 0.65 is obtained between these two sets of data.

It is therefore not surprising that local energies of the system like the point defect formation energies also strongly depend on properties of the point defect neighbourhoods. Trends presented in Fig. III-14 for the vacancy formation are however weak. The strategy in this section is therefore to perform LRs between the point defect formation energies obtained using DFT and the variables which describe the local environment surrounding the different point defects created described in Tab. III-5. The results for each point defect are summarized in Tab. III-7 which presents the best parameter values for the linear regressions as well as the correlation coefficient. As can be seen in Tab. III-4, many calculations were performed for each set of point defect to consider a sufficient variety of local environments surrounding the point defects and hence to allow for the convergence of the LR parameters. As our purpose is to try to identify which variables are the most relevant ones to estimate the point defect formation energies, we performed a systematic study which will show that a good estimate of the formation energies can be obtained through the knowledge of a few simple local variables.

It is worth mentioning that LR parameters have the dimension of an energy and can be considered, to a first approximation, as being representative of the average interactions between point defects and alloying elements located in their vicinity.

110   Chapter III. First principle study of point defects in a fcc Fe-10Ni-20Cr model alloy

IV-4-a   Vacancy

The first LR presented in Tab. III-7 refers to the vacancy formation energy. It can be seen that the LR which considers only the number of Ni and Cr atoms 1nn to the vacancy (1nn_Fe, 1nn_Cr and 1nn_Ni), was sufficient to obtain a good value of 0.74 for the CC. Parameter values assigned to these variables have a negative sign and a positive sign respectively, showing that to a first approximation, it costs on average, a higher energy to introduce a vacancy near Cr than Ni 1nn atoms. The correlation existing between these two sets of energies as can be seen in Fig. III-19. These results are in strong agreement with the work of Klaver et al. [KLAVER2012] in which Ni was found to bind to vacancy and V-Cr interactions were repulsive. Although Fe atoms impose the moment carried on both Cr and Ni atoms as shown in section III-1, no dependence of the evolution of the vacancy formation energy was found with first nearest atoms of Fe. Better estimates can be obtained by performing LRs considering more variables. In particular, we obtained an improved CC value of 0.80 using the four-parameter LR which takes into account 1nn Ni atoms and the number of Cr atoms in the first three shells surrounding the vacancy. This weak improvement obtained, underlines that the first shell of atoms surrounding the vacancies provides the greatest contribution to their formation energies. However, this result is again consistent with previous works [KLAVER2012], which showed a more important interaction length between Cr and vacancy than between Ni and vacancy in dilute fcc Fe.
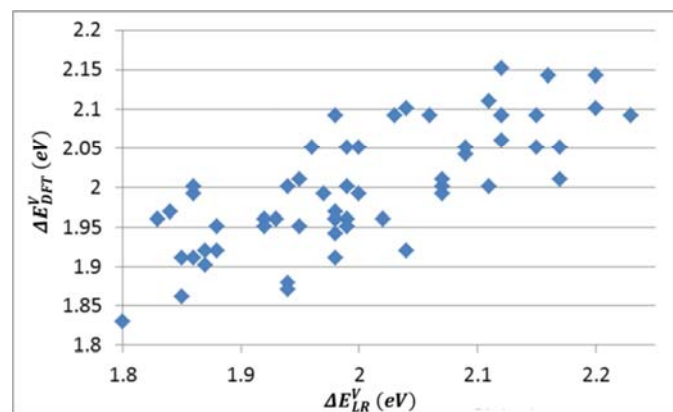
Fig. III-19: Vacancy formation energies obtained using DFT, ΔE_{DFT}^V, compared with their values estimated using the LR 1 in Tab. III-7, i.e. $\Delta E_{LR}^V = -0.04 \times 1nn\_Ni + 0.05 \times 1nn\_Cr + 2$, where 1nn_Ni is the number of Ni 1nn and 1nn_Cr is the number of Cr 1nn to the vacancy. CC of 0.74 is obtained between these two sets of energies.

111   Chapter III. First principle study of point defects in a fcc Fe-10Ni-20Cr model alloy

IV-4-b   Fe-Fe ⟨100⟩ dumbbell

Similarly to what has been done in the case of vacancies, LRs of the DFT data were performed for each dumbbell studied. However, in this case, we separated the contributions of atoms in tensile sites from those in compressive sites as can be seen in Tab. III-5. In this section, the DFT formation energies of Fe-Fe dumbbells oriented along the [100] axis, $\Delta E_{DFT}^{[100]Fe\text{-}Fe}$, and along the [010] axis, $\Delta E_{DFT}^{[010]Fe\text{-}Fe}$, are compared to their values estimated using LRs, $\Delta E_{LR}^{[100]Fe\text{-}Fe}$ and $\Delta E_{LR}^{[010]Fe\text{-}Fe}$ respectively. In Tab. III-7, LRs numbered from 2 to 5 refer to [100] dumbbell formation while LRs numbered from 6 to 9 refer to [010] dumbbell formation in the fct AFM1 reference state. LRs numbered from 10 to 17 were performed in the fcc AFM1 reference state to analyse the impact of the calculation method on results.

The results obtained in the fct phase show first that, as in the case of the vacancy, the knowledge of the number of Cr and Ni 1nn to the Fe-Fe ⟨100⟩ dumbbell allows a correct estimation of the formation energies. Indeed, the 2rd and 6th LRs presented in Tab. III-7 provide good estimates of $\Delta E_{DFT}^{[100]Fe\text{-}Fe}$ and $\Delta E_{DFT}^{[010]Fe\text{-}Fe}$ energies with CC values of 0.66 and 0.71 respectively. Much better results are however obtained by performing the LRs using variables which take into account of tensile and compressive sites. In particular, the 5th and 9th LRs presented in Tab. III-7 provide better estimates of $\Delta E_{DFT}^{[100]Fe\text{-}Fe}$ and $\Delta E_{DFT}^{[010]Fe\text{-}Fe}$ energies with CC values of respectively 0.75 and 0.82. This proves the different role played by atoms positioned in tensile and compressive sites. The correlation existing between DFT values and values obtained for these two latter LRs can be seen in Fig. III-20 and in Fig. III-21 respectively. Indeed, as could be expected, the different parameter values obtained for these LRs confirm that both Cr and Ni atoms positioned in tensile and compressive sites do not contribute equally to the ⟨100⟩ Fe-Fe formation energy. The most prominent element proving this feature is the negative parameter values obtained for the 1nnt_Ni variable, whereas the parameter values assigned to the 1nnc_Ni variable are positive. Furthermore, the relative importance between compressive and tensile sites was investigated in Tab. III-7 by performing two-parameter LRs taking into account Cr and Ni atoms positioned either in tensile (8th and 12th LRs) or in compressive sites (7th and 11th LRs). The better CC values of 0.70 and 0.79 found when we use these latter LRs, i.e. by only considering

compressive sites in the estimate of $\Delta E_{DFT}^{[100]Fe\text{-}Fe}$ and $\Delta E_{DFT}^{[010]Fe\text{-}Fe}$ energies respectively clearly show the higher influence of compressive sites.
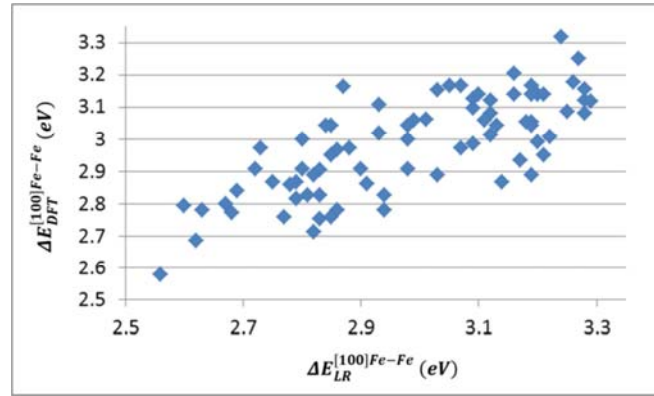
Fig. III-20: Formation energies of Fe-Fe dumbbells oriented along the [100] direction obtained using the DFT, $\Delta E_{DFT}^{[100]Fe-Fe}$, compared with their values estimated using the LR 5 in Tab. III-7, i.e. $\Delta E_{LR}^{[100]Fe-Fe} = 0.08 \times$ 1nnc_Ni $- 0.11 \times$ 1nnc_Cr $- 0.05 \times$ 1nnt_Ni $- 0.07 \times$ 1nnt_Cr $+ 2.9$. 1nnc_Ni and 1nnc_Cr variables correspond respectively to the number of Ni and Cr 1nn, positioned in compressive sites. 1nnt_Ni and 1nnt_Cr variables correspond respectively to the number of Ni and Cr 1nn, positioned in tensile sites. CC of 0.75 is obtained between these two sets of energies.
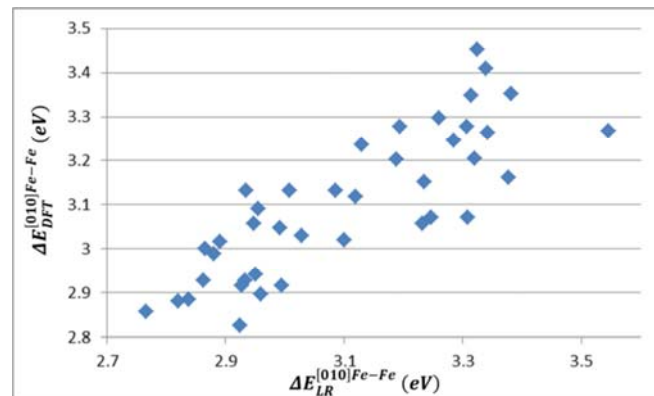
Fig. III-21: Formation energies of Fe-Fe dumbbells oriented along the [010] direction obtained using the DFT, $\Delta E_{DFT}^{[010]Fe-Fe}$, compared with their values estimated using LR 9 in Tab. III-7, i.e. $\Delta E_{LR}^{[010]Fe-Fe} = 0.15 \times$ 1nnc_Ni $-$ $0.06 \times$ 1nnc_Cr $- 0.04 \times$ 1nnt_Ni $- 0.07 \times$ 1nnt_Cr $+ 3.1$. 1nnc_Ni and 1nnc_Cr variables correspond respectively to the number of Ni and Cr 1nn, positioned in compressive sites. 1nnt_Ni and 1nnt_Cr variables correspond respectively to the number of Ni and Cr 1nn, positioned in tensile sites. CC of 0.82 is obtained between these two sets of energies.

113   Chapter III. First principle study of point defects in a fcc Fe-10Ni-20Cr model alloy

Unlike the case of vacancies, it cost a higher energy to introduce an Fe-Fe ⟨100⟩ dumbbell near Ni atoms than Cr atoms, but, this result does not seem contradictory since in one case, one Fe atom is removed to form a vacancy, and in the other case, one Fe atom is added to form an Fe-Fe ⟨100⟩ dumbbell. These results are in agreement with previous findings on binding energies of single Ni and Cr solutes to ⟨100⟩ Fe-Fe self-interstitial dumbbells, in pure fcc Fe [KLAVER2012], where Ni and Cr in compressive sites generally exhibited negative and positive binding energies respectively.

One interesting issue to note is that the LR did not yield similar coefficients for dumbbells oriented differently, i.e. whether the Fe-Fe dumbbells were oriented along the [100] direction, i.e. perpendicular to the AFM1 magnetic planes (LRs numbered from 2 to 5 in Tab. III-7), or along the [010] direction, i.e. parallel to the AFM1 magnetic planes (LRs numbered from 6 to 9 in Tab. III-7). In particular, a global shift of parameter values toward higher energies is observed when performing LR on $\Delta E_{DFT}^{[010]\text{Fe-Fe}}$ energies. These differences could be however expected owing to the fact that the local magnetic environment felt by dumbbell atoms introduced in the reference state strongly depends on the dumbbell axis relative to the AFM1 magnetic planes. Although that on average there are as many atoms 1nn to the dumbbell with magnetic moments up as down, these are not equivalently distributed between the compressive and tensile sites. This is illustrated from Fig. III-22 to Fig. III-24, which represent the initial magnetic moments of the Fe, Cr and Ni atoms 1nn to the dumbbell (i.e. as measured in the defect free reference state), m_{DFT}^{A} (A refers to the element type) plotted as a function of their ionic relaxations, i.e. the displacement of atoms underwent after the dumbbell was introduced. The ionic relaxations will be noted as $\delta d_{DFT}^{[100]\text{Fe-Fe}}$ .or $\delta d_{DFT}^{[010]\text{Fe-Fe}}$ depending on whether the dumbbell was introduced along the [100] or the [010] axis. Note that the sign of the ionic relaxation is a simple way of visualising whether the atom is in a compressive site ($\delta d > 0$) or in a tensile one ($\delta d < 0$).

These figures clearly show significant differences whether Fe-Fe dumbbells were oriented along the [100] direction or along the [010] direction. Depending on the orientation of the dumbbell axis, the Fe moments are not distributed equivalently between tensile and compressive sites, as can be seen in Fig. III-22. Indeed, when the dumbbell is introduced with its axis parallel to the

114   Chapter III. First principle study of point defects in a fcc Fe-10Ni-20Cr model alloy

AFM1 magnetic planes, most of the initial moments on Fe atoms in tensile sites are positive whereas most of the initial moments of Fe atoms in compressive sites are negative. As noted previously small perturbations in the spin orientation of the atoms can be found in the AFM1 reference state as discussed in section III-2. However, when the dumbbell is introduced with its axis perpendicular to the AFM1 magnetic planes, most of the initial moments of Fe atoms in tensile sites are positive, but the initial moments of Fe atoms in compressive sites can be positive as well as negative. This arises from the specific configuration of the AFM1 structure. Indeed, compressive sites lie within two magnetic planes "down" whereas tensile sites lie within a single magnetic plane "up" when interstitials are introduced with their axis perpendicular to the AFM1 magnetic planes, as can be seen in Fig. III-15. Similarly, tensile sites lie within a single magnetic plane "down", whereas compressive sites lie within two magnetic planes having, on average, the same amount of Fe atoms with moments "up" and "down" when interstitials are introduced with their axis parallel to the AFM1 magnetic planes. As a result, moments carried by Cr and Ni atoms (imposed by the sum of the moments of their neighbour 1nn Fe atoms as shown in Fig. III-4) present significant differences whether the Fe-Fe dumbbell is oriented along the [100] direction or along the [010] direction as shown in Fig. III-23 and in Fig. III-24 respectively. The mean values of the moments displayed in these figures are summarized in Tab. III-6.
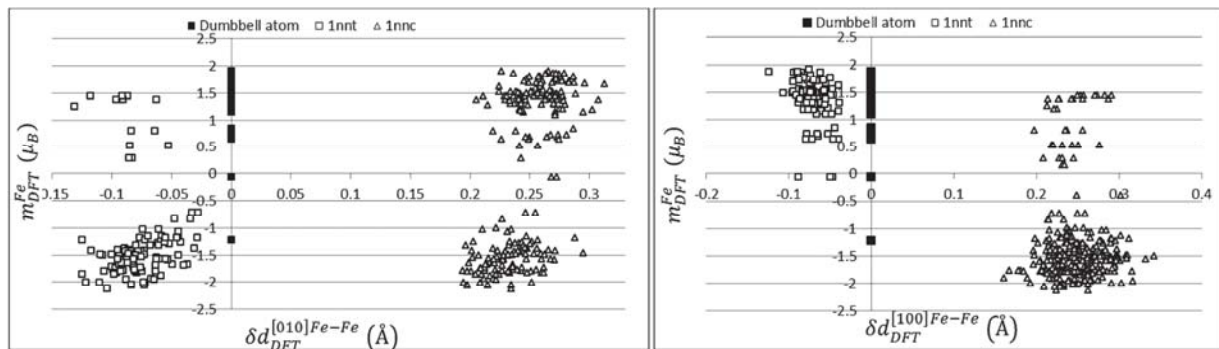
Fig. III-22: Magnetic moments of Fe atoms 1nn to Fe-Fe dumbbells measured in the defect-free reference state, m_{DFT}^{Fe}, as a function of their ionic relaxations, i.e. $\delta d_{DFT}^{[100]Fe-Fe}$ or $\delta d_{DFT}^{[010]Fe-Fe}$ depending on whether dumbbells were introduced along the [100] (right figure) or the [010] axis (left figure). Atoms in tensile sites (1nnt) are represented in open squares and atoms in compressive sites (1nnc) represented with open triangles. Moments of Fe atoms positioned at sites (defect-free reference state) selected to introduce the dumbbells are also represented along the zero abscissa (black squares).

         http://doc.univ-lille1.fr
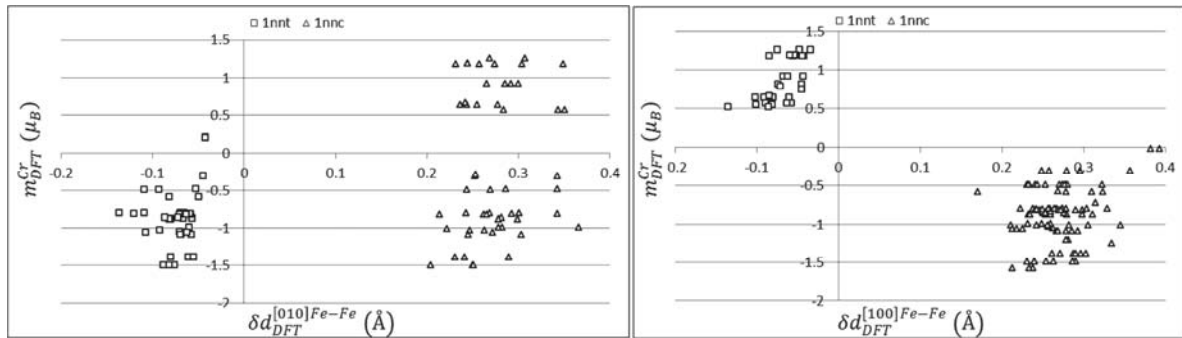
Fig. III-23: Magnetic moments of Cr atoms 1nn to Fe-Fe dumbbells measured in the defect-free reference state, m_{DFT}^{Cr}, as a function of their ionic relaxations, i.e. $\delta d_{DFT}^{[100]Fe-Fe}$ or $\delta d_{DFT}^{[010]Fe-Fe}$ depending on whether dumbbells were introduced along the [100] (right figure) or the [010] axis (left figure). Atoms in tensile sites (1nnt) are represented in open squares and atoms in compressive sites (1nnc) represented with open triangles.
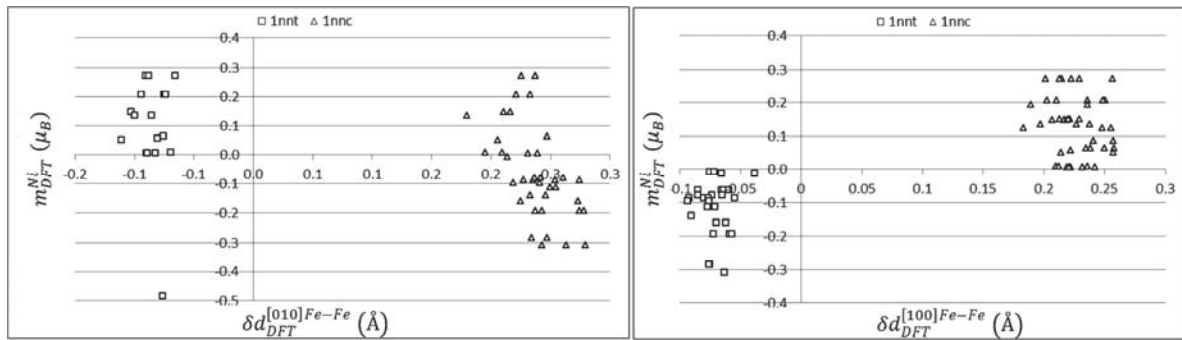
Fig. III-24: Magnetic moments of Ni atoms 1nn to Fe-Fe dumbbells measured in the defect-free reference state, m_{DFT}^{Ni}, as a function of their ionic relaxations, i.e. $\delta d_{DFT}^{[100]Fe-Fe}$ or $\delta d_{DFT}^{[010]Fe-Fe}$ depending on whether dumbbells were introduced along the [100] (right figure) or the [010] axis (left figure). Atoms in tensile sites (1nnt) are represented in open squares and atoms in compressive sites (1nnc) represented with open triangles.

Point defect type	Site type	$\langle m_{DFT}^{Fe} \rangle$ (μ_B)	$\langle m_{DFT}^{Cr} \rangle$ (μ_B)	$\langle m_{DFT}^{Ni} \rangle$ (μ_B)
Vacancy	1nn	-0.34	-0.47	-0.01
[100] dumbbell	1nnt	1.41	0.87	-0.13
	1nnc	-1.29	-0.89	0.13
[010] dumbbell	1nnt	-1.23	-0.90	0.09
	1nnc	0.05	-0.19	-0.05

Tab. III-6: Mean value of magnetic moments of Fe, Ni and Cr 1nn to point defects measured in the defect-free reference state, $\langle m_{DFT}^{A} \rangle$ (A refers to the element type), are calculated for each point defect types considered. Average values are calculated on sites first nearest neighbours to the vacancy (1nn) and on compressive and tensile sites of dumbbells (1nnc and 1nnt respectively).

Despite these differences and knowing the key role played by atoms in compressive sites in the evaluation of the formation energy as shown by the LRs presented previously, we find that the dumbbell formation energies are nevertheless similar on average whether the dumbbell is oriented along the [100] or the [010] direction, as can be seen in Tab. III-4. This result suggests that it is the chemical composition of the first shell of atoms surrounding the Fe-Fe dumbbells which provides the biggest contribution to the formation energy values and that the position (tensile or compressive site) and thus magnetism intervenes at second order. This is confirmed by the fact that the parameter values of the LRs are similar for the [100] and the [010] Fe-Fe dumbbell.

Fig. III-25 to Fig. III-27 represent the final magnetic moments of the Fe, Cr and Ni atoms 1nn to Fe-Fe dumbbells (i.e. the magnetic moment measured in the lattice containing the dumbbell and after it was allowed to relax), M_{DFT}^{A} (A refers to the element type), plotted again as a function of the atom ionic relaxations.

It can first be noted that the magnetic distributions visible on Fig. III-22 to Fig. III-24 have been retained during the relaxation of the lattice containing the dumbbell. Furthermore, whatever the orientation of the dumbbell axis, the magnitude of moments carried by Fe and Cr atoms measured in the reference state, i.e. $\left|m_{DFT}^{Fe}\right|$ and $\left|m_{DFT}^{Cr}\right|$ respectively, has been globally reduced for the atoms in the compressive sites (1nnc) and enhanced for those in the tensile sites (1nnt) during the relaxation of the lattice. It can also be noted that the reference state seems to be more stable against the addition of a [010] dumbbell than a [100] dumbbell for which significant instabilities of moments are observed for the moments carried by the Fe atoms in compressive sites as can be seen in Fig. III-25. Indeed, Fe atoms positioned in compressive sites of [100] oriented dumbbells are prone to important moment variations, which can even sometimes alter locally the AFM1 ordering. This is not observed for the [010] oriented dumbbells. Thus, the AFM1 magnetic structure seems more robust against addition of [010] Fe-Fe dumbbells, which may account for the better correlation coefficient values obtained systematically for the LRs. This behaviour can be easily understood since [010] dumbbell atoms lie inside AFM1 planes whereas [100] dumbbell atoms lie in between two magnetic planes, thus breaking the AFM1 symmetry. Moments carried by [100] dumbbell atoms are therefore expected to be more prone to unpredictable variations of Fe moments owing to their proximity with both magnetic planes "up"

117   Chapter III. First principle study of point defects in a fcc Fe-10Ni-20Cr model alloy

and "down". This behaviour has been confirmed by performing dumbbell calculations with different initial magnetic configurations (up-up, up-down and down-down). In Fig. III-25, it can also be noted that the moments carried by the dumbbell atoms are significantly reduced compared to the moment of the Fe atom which was (defect-free reference state) at the site the dumbbell was created (Fig. III-22). Furthermore, the moments of Fe dumbbells are more reduced when introduced along the [010] (negative sign on average) than along [100] direction (positive sign on average).

In the lights of these results, a few simple arguments based on magnetic interactions can explain the differences obtained when looking for the relationship (LR) between the dumbbell formation energy and the local environment for the two kinds of dumbbells investigated so far. As mentioned previously, the chemical composition of the first shell surrounding ⟨100⟩ Fe-Fe dumbbells seems to provide the greater contribution to the formation energy values. Indeed, we found that, for the two different orientations considered for this point defect type, the more first neighbour Ni atoms the larger the dumbbell formation energy, whereas the more first neighbour Cr atoms the lower the dumbbell formation energy. However, Fe-Fe dumbbell atoms introduced along the [100] axis have positive moments, whereas their first nearest Cr and Ni exhibit, in compressive sites, negative and positive moments respectively. In this case, it is clear that moment interactions between the point defects and these atoms are favourable since, on average, Fe atoms of dumbbells have anti-ferromagnetic interactions with Cr atoms and ferromagnetic interactions with Ni atoms. Magnetic interactions are however less favourable for the [010] oriented dumbbell, of which dumbbell Fe atoms have negative moments while moments of both Cr and Ni in compressive sites have negative as well as positive values. These results are consistent with LR presented in Fig. III-20 and in Fig. III-21. Indeed, in both cases, Cr atoms positioned in compressive sites tend to decrease the formation energy as shown by the negative values found for the parameter values, but a lower value is found for the [100] dumbbell, which indicates that the magnetic environment is more appropriate for energetically favourable interactions between the Fe atoms of the dumbbell and their Cr 1nn. Similarly, in both cases, Ni atoms positioned in compressive sites tend to increase the formation energy as shown by the positive values found for the parameters, but a lower value is found for [100] dumbbells. It is worth mentioning that, although not predominant in the contribution to the formation energy,

magnetic interactions can nevertheless bring a significant contribution, as proved by the important variability obtained for these parameter values.
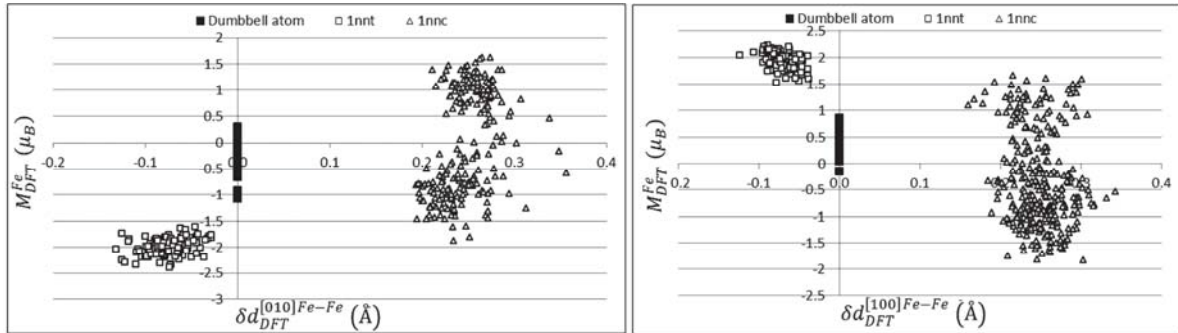
Fig. III-25: Magnetic moments of Fe atoms 1nn to Fe-Fe dumbbells measured in the defect lattices, M_{DFT}^{Fe}, as a function of their ionic relaxations, i.e. $\delta d_{DFT}^{[100]Fe-Fe}$.or $\delta d_{DFT}^{[010]Fe-Fe}$ depending on whether dumbbells were introduced along the [100] (right figure) or the [010] axis (left figure). Atoms in tensile sites (1nnt) are represented in open squares and atoms in compressive sites (1nnc) represented with open triangles. Moments of dumbbell Fe atoms are also represented along the zero abscissa (black squares).
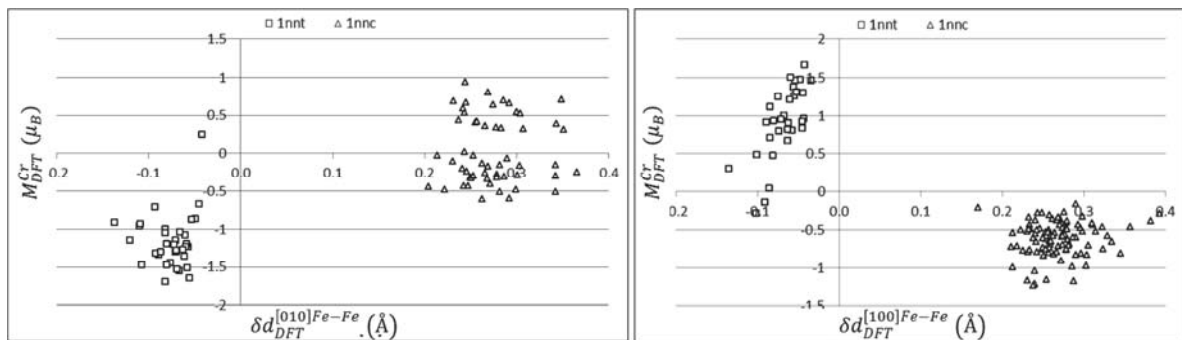
Fig. III-26: Magnetic moments of Cr atoms 1nn to Fe-Fe dumbbells measured in the defect lattices, M_{DFT}^{Cr}, as a function of their ionic relaxations, i.e. $\delta d_{DFT}^{[100]Fe-Fe}$.or $\delta d_{DFT}^{[010]Fe-Fe}$ depending on whether dumbbells were introduced along the [100] (right figure) or the [010] axis (left figure). Atoms in tensile sites (1nnt) are represented in open squares and atoms in compressive sites (1nnc) represented with open triangles.

119   Chapter III. First principle study of point defects in a fcc Fe-10Ni-20Cr model alloy
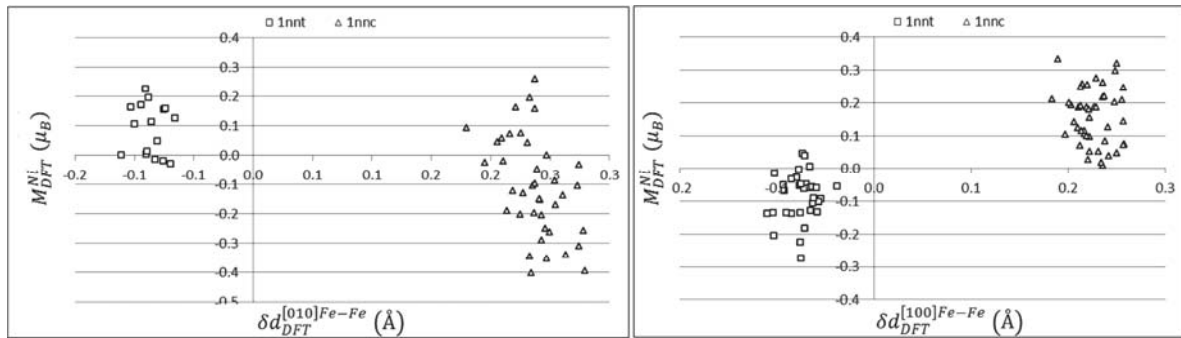
Fig. III-27: Magnetic moments of Ni atoms 1nn to Fe-Fe dumbbells measured in the defect lattices, M_{DFT}^{Ni}, as a function of their ionic relaxations, i.e. $\delta d_{DFT}^{[100]Fe-Fe}$ .or $\delta d_{DFT}^{[010]Fe-Fe}$ depending on whether dumbbells were introduced along the [100] (right figure) or the [010] axis (left figure). Atoms in tensile sites (1nnt) are represented in open squares and atoms in compressive sites (1nnc) represented with open triangles.

The same general conclusions as those presented in this section for the fct phase can be drawn for calculations performed in the fcc phase. Furthermore, no important changes in the LR parameters are observed relative to those obtained in the fct phase, as can be seen in Tab. III-7, showing that changing crystallographic phase does not involve major changes in the effective interactions, thus showing once more that magnetism intervenes at second order. However, one must note that the estimate of the formation energies using our LR method is less suitable in the fcc phase where the CC obtained are smaller than those found in the fct phase.

IV-4-c   Mixed ⟨100⟩ dumbbell

In this section, the results obtained for mixed dumbbells are analysed. As two different atoms form the dumbbells, the position of atoms positioned in compressive sites relative to mixed dumbbells was also considered in LR variables as can be seen in Tab. III-5. The results obtained for the LRs, numbered from 18 to 51 in Tab. III-7 follow the same trends as those observed for the Fe-Fe dumbbells. First of all, Cr and Ni positioned in compressive sites were also found to impact strongly on the values of the formation energies calculated. Furthermore, in this case, the more accurate the variables used to describe the first shell of point defects in the LRs, the better the estimates of point defect formations. Thus, the best CC values were also obtained by differentiating the compressive sites lying in the planes positioned below and above relative to the plane perpendicular to the dumbbell axis, i.e. by using the1nncFe_A and 1nncS_A variables defined in Tab. III-5.

The analysis of the parameter values assigned to these variables shows that the formation energies depend on how the Cr and Ni atoms in compression sites are positioned with respect to the mixed dumbbell. Let's, for instance, consider the case of the Fe-Ni [100] dumbbell. The 22th LR which estimates the DFT formation energies of the Fe-Ni [100] dumbbell, shows that on average, as in the case of the ⟨100⟩ Fe-Fe dumbbell, it costs more energy to introduce the dumbbell near Ni atoms than near Cr atoms (It can however be noted that the values obtained for the LR parameters both have a negative sign while, as mentioned in the previous section, a positive value was found for the parameter value of the 1nnc_Ni variable in the case of ⟨100⟩ Fe-Fe dumbbell). Better estimates are however found using the LRs 23 to 26 for which the analysis of parameter values of the variables clearly shows that interaction properties of atoms in compressive sites are strongly affected by their position relative to the dumbbells atoms. Indeed, the presence of Cr atoms positioned in compressive sites tends to decrease the formation energy whatever their position relative to the mixed dumbbell, although this tendency is more pronounced when Cr atoms are located closer to the Fe atom in the dumbbell (the magnitude of parameter values assigned to the 1nncFe_Cr variable is more important). Parameter values assigned to the number of Ni atoms in compressive sites have however opposite signs depending on their location. The occurrence of Ni atoms in compressive sites located next to the Fe atom of the [100] Fe-Ni dumbbell, tend to increase the formation energy, as was found for the ⟨100⟩ Fe-Fe dumbbell in the previous section. However, when located next to the Ni atom of the [100] Fe-Ni dumbbell, they tend to decrease the formation energy. These more favourable interactions found for Ni-Ni pairs are in agreement with results obtained by Klaver et al. [KLAVER2012], which generally found a modest attraction of Ni-Ni pairs in pure fcc Fe.

No such behaviour was observed for the [010] oriented dumbbell, for which both Cr and Ni atoms in compressive sites seem to have similar influence on the formation energy, whatever their positions relative to the mixed dumbbells. Indeed, there are very few differences between the parameter values of the variables associated with these sites (it has however to be mentioned that the magnitude of the parameter values found for the 1nncFe_Ni variable is more important than those found for the 1nncS_Ni variable, but they have the same sign). It is therefore not surprising that equivalent CC values are obtained between the 30th LR which only considers the number of Cr and Ni atoms in both tensile and compressive sites, and those obtained for the LRs

31 to 34 which takes into account also the position of these atoms relative to the dumbbell. It has also to be mentioned that the parameter values found for the 30th LR do not exhibit important differences relative to those found for the Fe-Fe [010] dumbbell in the 22th LR. This confirms the fact that, unlike the case of the [010] oriented dumbbell, the Ni atom of the Fe-Ni [010] dumbbell has a limited impact on the effective interactions found between Fe-Fe [010] dumbbells and their local environment as listed in Tab. III-7.

These different effective interactions found between the Ni atom in the dumbbell (oriented either along the [100] or the [010] axis) and its first nearest Ni in compressive sites, though, do not necessarily contradict each other owing to the strong influence of the magnetic state on the binding energies found by Klaver et al. [KLAVER2012]. In particular, Ni-Ni pairs generally exhibited modest attractions in the AFM1 state but repulsive binding in the AFMD state.

It is worth mentioning that, in line with the tendency found previously for the ⟨100⟩ Fe-Fe dumbbell, in the case of ⟨100⟩ Fe-Ni dumbbell, an overall increase of parameter values of the compressive sites located the closest to the Fe atom of the dumbbell (i.e. 1nncFe_Ni and 1nncFe_Cr variables in Tab. III-7), occurs for the [010] oriented dumbbell as compared to what is observed for the [100] oriented dumbbell.

Fig. III-28 to Fig. III-30 represent the final magnetic moments of the Fe, Cr and Ni atoms 1nn to Fe-Ni dumbbells (i.e. the magnetic moment measured in the lattice containing the dumbbell and after it was allowed to relax), M_{DFT}^{A} (A refers to the element type), plotted again as a function of the atom ionic relaxations.

In the case of the Fe-Ni dumbbell, the trends are similar to those displayed in Fig. III-25 to Fig. III-27 for the ⟨100⟩ Fe-Fe dumbbell. Indeed, moments measured in the reference state are, on average, enhanced with the addition of the [100] Fe-Ni dumbbell, whereas with the addition of the [010] Fe-Ni dumbbell, the moment amplitudes are generally reduced in both compressive and tensile sites. The most significant differences are observed for the moments measured on atoms in compressive sites, located next to the Ni atom of the mixed dumbbell, which are considerably less reduced in magnitude than when the atoms is next to the Fe atom of the dumbbell. Furthermore, as can be seen in Fig. III-28, the mean values of moments found for the Fe atom of the mixed dumbbell are all respectively positive for the [100] oriented dumbbell and negative for the [010] dumbbell, as previously found for the ⟨100⟩ Fe-Fe dumbbells. The amplitude of the

moment values are however more important for the mixed dumbbells than for the ⟨100⟩ Fe-Fe dumbbells. The mean values of moments carried by the Ni atom of the mixed dumbbell are negative for both kinds of dumbbell. Lower values are nevertheless found for the Ni atom of the [010] oriented dumbbell. This is very due to their close proximity to the Fe atom of the dumbbell of which moment is very negative. These results underline again the significant impact of the direction of the dumbbell axis.

Arguments based on magnetic interactions seem again in agreement with the different LR parameter values assigned to the 1nncS_Ni variable, between [100] and [010] oriented dumbbells. Indeed, Ni atoms of [100] oriented dumbbell atoms have negative moments, as well as most of their first nearest Ni positioned in compressive sites. In this case, it is clear that moment interactions between the point defects and these atoms are rather favourable since, Ni-Ni interactions are ferromagnetic. By contrast, magnetic interactions are not favourable in the case of [010] oriented dumbbell owing to the fact that there is a little more anti-ferromagnetic than ferromagnetic Ni-Ni interactions. These results are therefore consistent with LR parameters of which the 1nncS_Ni variable exhibit negative values (unfavourable interactions) for [100] oriented dumbbells and positive values for [010] oriented dumbbells. Furthermore, the overall increase of parameter values of 1nncFe_Ni and 1nncFe_Cr variables in Tab. III-7 occurring for the [010] oriented dumbbell as compared to what is observed for the [100] oriented dumbbell can be explained using the same arguments as in the case of ⟨100⟩ Fe-Fe for the parameter values of 1nnc_Ni and 1nnc_Cr.

In the case of the Fe-Cr dumbbells, we found that it is necessary to take into account the position of Cr and Ni atoms in compression sites relative to the mixed dumbbell to obtain good estimates of the DFT formation energies. Indeed, whatever the direction of the dumbbell axis, bad estimates (small CC values) were found for both 39th and 47th LRs which consider atoms in compressive sites without taking into account their position relative to the mixed dumbbell. In both cases, the CC values were considerably enhanced by describing more accurately the first shell surrounding the Fe-Cr dumbbells, as can be seen for the LRs 40 to 42 for the [100] oriented dumbbell, and for the LRs 48 to 51 for the [010] oriented dumbbell. Indeed, the addition of one Cr in in the dumbbell seems to have a strong impact on the point defect local environment

whatever the direction axis considered for Fe-Cr dumbbells. In particular, the parameter values of the two variables (1nncS_Cr and 1nncFe_Cr) describing the effective interactions between Cr atoms in compressive sites and the two atoms of dumbbells exhibit opposite signs. Negative values of the parameter are obtained when the Cr atoms in compressive sites are close to the Fe atom of the dumbbell which indicates favourable interactions. However, when the Cr atoms in compressive sites are close to the Cr atom of the mixed dumbbell, these interactions are unfavourable, in agreement with the strong Cr-Cr repulsion found by Klaver et al. [KLAVER2012], in pure fcc Fe with three different magnetic structures. It may be mentioned that a very similar repulsive binding is also found for Cr-Cr pairs in bcc FM Fe [OLSSON2010] at 1nn separation.

Fig. III-31 to Fig. III-33 represent the final magnetic moments of the Fe, Cr and Ni atoms 1nn to Fe-Cr dumbbells (i.e. the magnetic moment measured in the lattice containing the dumbbell and after it was allowed to relax), M_{DFT}^{A} (A refers to the element type), plotted again as a function of the atom ionic relaxations.

In the case of the Fe-Cr dumbbell, the trends are similar to those observed for the Fe-Fe dumbbell and the mixed Fe-Ni dumbbell. The most significant differences are observed for moments measured on atoms in compressive sites, located closer to Ni atoms of dumbbells, which were considerably less reduced in magnitude than when located closer to Fe atoms of dumbbells.
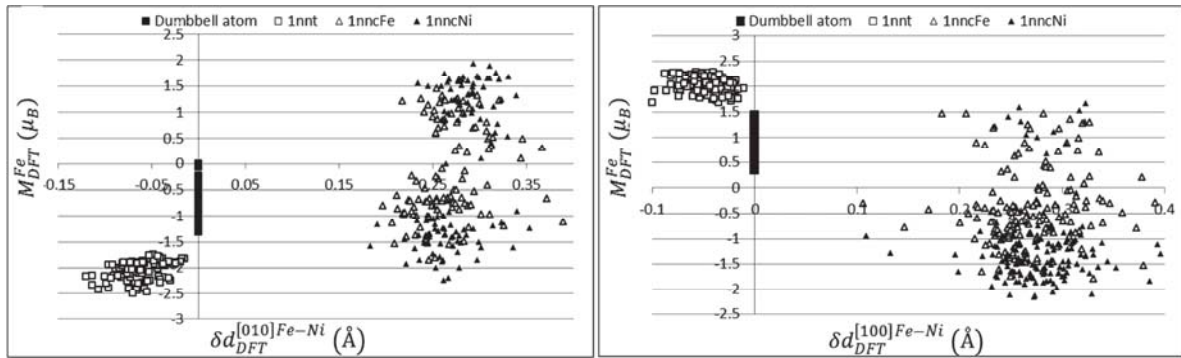
Fig. III-28: Magnetic moments of Fe atoms 1nn to Fe-Ni dumbbells measured in the defect lattices, M_{DFT}^{Fe}, as a function of their ionic relaxations, i.e. $\delta d_{DFT}^{[100]Fe-Ni}$ .or $\delta d_{DFT}^{[010]Fe-Ni}$ depending on whether dumbbells were introduced along the [100] (right figure) or the [010] axis (left figure). Atoms in tensile sites (1nnt) are represented in open squares. Atoms in compressive sites located closer to the Fe atom of the dumbbell (1nncFe) are represented in open triangles and those located closer to the Ni atom of the dumbbell (1nncNi) are represented in black triangles. Moments of dumbbell Fe atoms are also represented along the zero abscissa (black squares).

Fig. III-29: Magnetic moments of Cr atoms 1nn to Fe-Ni dumbbells measured in the defect lattices, M_{DFT}^{Cr}, as a function of their ionic relaxations, i.e. $\delta d_{DFT}^{[100]Fe-Ni}$ .or $\delta d_{DFT}^{[010]Fe-Ni}$ depending on whether dumbbells were introduced along the [100] (right figure) or the [010] axis (left figure). Atoms in tensile sites (1nnt) are represented in open squares. Atoms in compressive sites located closer to the Fe atom of the dumbbell (1nncFe) are represented in open triangles and those located closer to the Ni atom of the dumbbell (1nncNi) are represented in black triangles.

125   Chapter III. First principle study of point defects in a fcc Fe-10Ni-20Cr model alloy
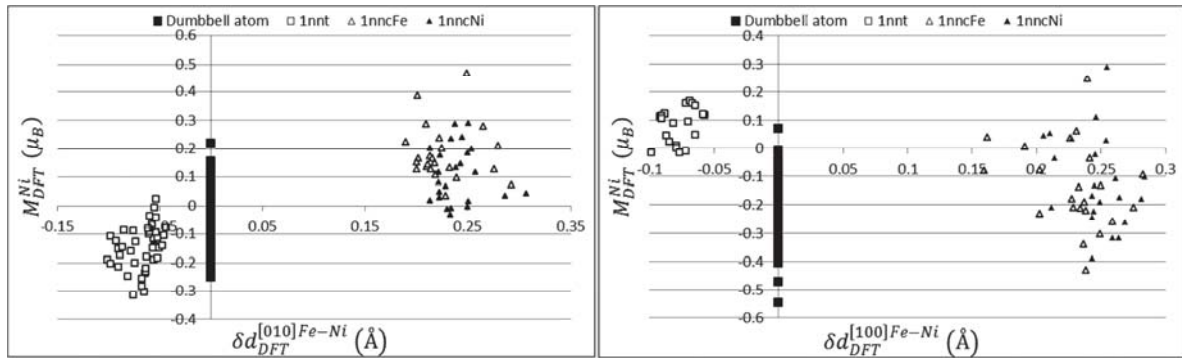
Fig. III-30: Magnetic moments of Ni atoms 1nn to Fe-Ni dumbbells measured in the defect lattices, M_{DFT}^{Ni}, as a function of their ionic relaxations, i.e. $\delta d_{DFT}^{[100]Fe-Ni}$ .or $\delta d_{DFT}^{[010]Fe-Ni}$ depending on whether dumbbells were introduced along the [100] (right figure) or the [010] axis (left figure). Atoms in tensile sites (1nnt) are represented in open squares. Atoms in compressive sites located closer to the Fe atom of the dumbbell (1nncFe) are represented in open triangles and those located closer to the Ni atom of the dumbbell (1nncNi) are represented in black triangles. Moments of dumbbell Ni atoms are also represented along the zero abscissa (black squares).
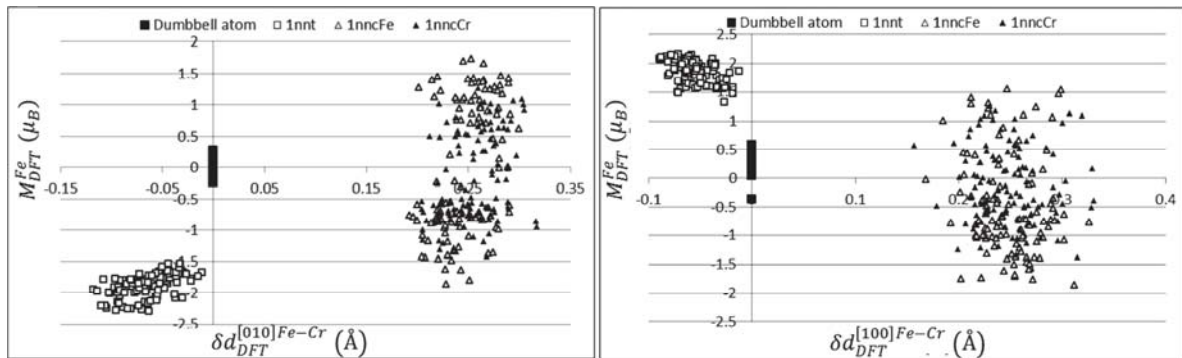
Fig. III-31: Magnetic moments of Fe atoms 1nn to Fe-Cr dumbbells measured in the defect lattices, M_{DFT}^{Fe}, plotted as a function of their ionic relaxations, i.e. $\delta d_{DFT}^{[100]Fe-Cr}$ .or $\delta d_{DFT}^{[010]Fe-Cr}$ depending on whether dumbbells were introduced along the [100] (right figure) or the [010] axis (left figure). Atoms in tensile sites (1nnt) are represented in open squares. Atoms in compressive sites located closer to the Fe atom of the dumbbell (1nncFe) are represented in open triangles and those located closer to the Ni atom of the dumbbell (1nncNi) are represented in black triangles. Moments of dumbbell Fe atoms are also represented along the zero abscissa (black squares).
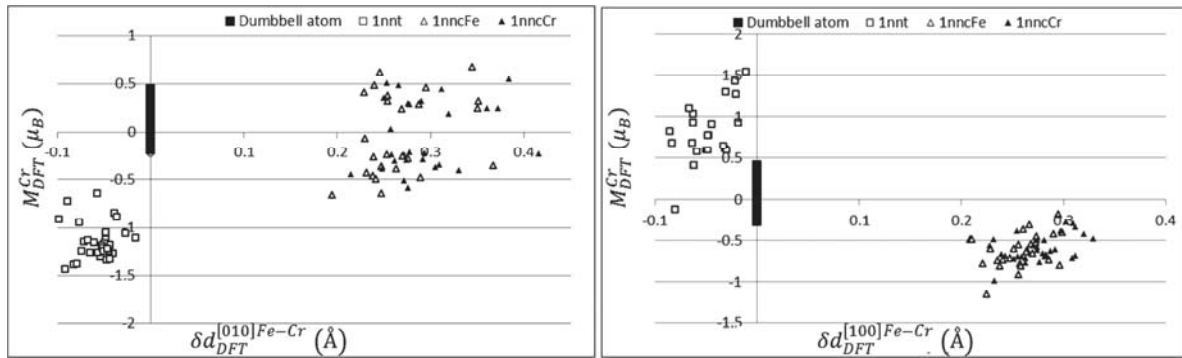
Fig. III-32: Magnetic moments of Cr atoms 1nn to Fe-Cr dumbbells measured in the defect lattices, M_{DFT}^{Cr}, plotted as a function of their ionic relaxations, i.e. $\delta d_{DFT}^{[100]Fe-Cr}$ .or $\delta d_{DFT}^{[010]Fe-Cr}$ depending on whether dumbbells were introduced along the [100] (right figure) or the [010] axis (left figure). Atoms in tensile sites (1nnt) are represented in open squares. Atoms in compressive sites located closer to the Fe atom of the dumbbell (1nncFe) are represented in open triangles and those located closer to the Ni atom of the dumbbell (1nncNi) are represented in black triangles. Moments of dumbbell Cr atoms are also represented along the zero abscissa (black squares).
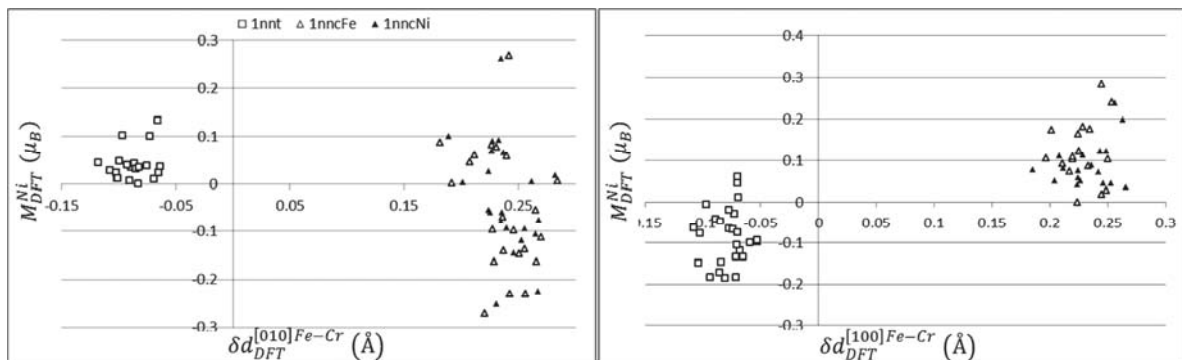
Fig. III-33: Magnetic moments of Ni atoms 1nn to Fe-Cr dumbbells measured in the defect lattices, M_{DFT}^{Ni}, plotted as a function of their ionic relaxations, i.e. $\delta d_{DFT}^{[100]Fe-Cr}$ .or $\delta d_{DFT}^{[010]Fe-Cr}$ depending on whether dumbbells were introduced along the [100] (right figure) or the [010] axis (left figure). Atoms in tensile sites (1nnt) are represented in open squares. Atoms in compressive sites located closer to the Fe atom of the dumbbell (1nncFe) are represented in open triangles and those located closer to the Ni atom of the dumbbell (1nncNi) are represented in black triangles.

127 Chapter III. First principle study of point defects in a fcc Fe-10Ni-20Cr model alloy

LR number	LR type	phase	1nn_Ni	1nn_Cr	1nnc_Ni	1nnc_Cr	1nncFe_Ni	1nncFe_Cr	1nncS_Ni	1nncS_Cr	1nnt_Ni	1nnt_Cr	CC
1	ΔE_{LR}^{V}	fct	-0.04	0.05	-	-	-	-	-	-	-	-	0.74
2			0.03	-0.10	-	-	-	-	-	-	-	-	0.66
3	$\Delta E_{LR}^{[100]Fe-Fe}$		-	-	0.07	-0.11	-	-	-	-	-	-	0.70
4		fct	-	-	-	-	-	-	-	-	-0.02	-0.05	0.16
5			-	-	0.08	-0.11	-	-	-	-	-0.05	-0.07	0.75
6			0.081	-0.07	-	-	-	-	-	-	-	-	0.71
7	$\Delta E_{LR}^{[010]Fe-Fe}$		-	-	0.14	-0.08	-	-	-	-	-	-	0.79
8		fct	-	-	-	-	-	-	-	-	-0.03	-0.09	0.34
9			-	-	0.15	-0.06	-	-	-	-	-0.04	-0.07	0.82
10			0.06	-0.07	-	-	-	-	-	-	-	-	0.59
11	$\Delta E_{LR}^{[100]Fe-Fe}$		-	-	0.10	-0.08	-	-	-	-	-	-	0.61
12		fcc	-	-	-	-	-	-	-	-	0.04	-0.06	0.27
13			-	-	0.10	-0.08	-	-	-	-	-0.01	-0.06	0.65
14			0.07	-0.06	-	-	-	-	-	-	-	-	0.62
15	$\Delta E_{LR}^{[010]Fe-Fe}$		-	-	0.13	-0.07	-	-	-	-	-	-	0.70
16		fcc	-	-	-	-	-	-	-	-	-0.04	-0.08	0.31
17			-	-	0.14	-0.05	-	-	-	-	-0.05	-0.07	0.75
18			-0.03	-0.09	-	-	-	-	-	-	-	-	0.52
19			-	-	-0.02	-0.11	-	-	-	-	-	-	0.65
20			-	-	-	-	-	-0.14	-	-0.07	-	-	0.65
21			-	-	-	-	0.03	-0.15	-	-	-	-	0.60
22	$\Delta E_{LR}^{[100]Fe-Ni}$	fct	-	-	-0.03	-0.10	-	-	-	-	-0.04	0.05	0.67
23			-	-	-	-	-	-0.13	-0.10	-0.07	-	0.09	0.73
24			-	-	-	-	-	-0.14	-0.07	-0.08	-0.05	-	0.72
25			-	-	-	-	0.04	-0.14	-	-0.07	-0.07	-	0.70
26			-	-	-	-	0.03	-0.14	-0.08	-0.08	-	-	0.70
27			0.03	-0.07	-	-	-	-	-	-	-	-	0.44
28			-	-	0.08	-0.09	-	-	-	-	-	-	0.66
29			-	-	-	-	0.14	-0.07	-	-	-	-	0.60
30	$\Delta E_{LR}^{[010]Fe-Ni}$	fct	-	-	0.09	-0.06	-	-	-	-	-0.08	-0.03	0.70
31			-	-	-	-	0.12	-0.08	-	-0.07	-0.06	-	0.71
32			-	-	-	-	0.16	-	0.07	-	-0.12	-0.04	0.71
33			-	-	-	-	0.15	-0.04	0.06	-	-0.09	-	0.70
34			-	-	-	-	0.12	-0.10	0.03	-0.09	-	-	0.70
35			0.01	0.00	-	-	-	-	-	-	-	-	0.14
36			-	-	0.01	0.00	-	-	-	-	-	-	0.08
37			-	-	-	-	-	-0.08	-	0.08	-	-	0.56
38	$\Delta E_{LR}^{[100]Fe-Cr}$	fct	-	-	-	-	0.02	-0.07	-	-	-	-	0.37
39			-	-	-0.01	0.01	-	-	-	-	0.05	0.08	0.25
40			-	-	-	-	-	-0.07	-	0.09	0.04	0.07	0.61
41			-	-	-	-	0.01	-0.07	-	0.09	-	0.05	0.59
42			-	-	-	-	0.02	-0.08	0.01	0.08	-	-	0.57
43			0.07	-0.01	-	-	-	-	-	-	-	-	0.42
44			-	-	0.12	0.04	-	-	-	-	-	-	0.56
45			-	-	-	-	0.14	-	-	0.12	-	-	0.64
46			-	-	-	-	0.10	-0.11	-	-	-	-	0.60
47	$\Delta E_{LR}^{[010]Fe-Cr}$	fct	-	-	0.13	0.06	-	-	-	-	-0.06	-0.04	0.06
48			-	-	-	-	0.14	-	0.13	0.16	-0.05	-	0.80
49			-	-	-	-	0.13	-0.05	0.11	0.12	-	-	0.79
50			-	-	-	-	0.14	-	0.14	0.13	-	-0.02	0.78
51			-	-	-	-	0.12	-0.08	-	0.09	-	-0.02	0.69

Tab. III-7: LRs of interest used to estimate the required energies ΔE to introduce a point defect at different lattice sites of the AFM1 reference state using DFT, i.e. ΔE_{DFT}^{V} and ΔE_{DFT}^{Fe-A} energies, are presented. The obtained parameter values assigned to variables displayed at the top of the rows are summarized for each LR along with the crystallographic phase, the number assigned to each LR and the LR type which indicates which DFT data set was fitted. Variable considered, i.e. 1nn_A, 1nnc_A, 1nnt_A, 1nncS_A and 1nncFe_A (A refers to the element type), are listed in Tab. III-5.

IV-4-d   Parameters for the PIM

The above mentioned information obtained about SIAs, which will be used in chapter IV to build our PIM, are summarised in this section. Indeed, the effective interactions listed in Tab. III-7 as well as the SIA formation energies listed Tab. III-4 will be used to determine all the energies of the PIM presented in Fig. I-5. Tab. III-7 includes however too many results to incorporate them easily in the PIM. Among all the LRs which estimate SIA formation energies in the fct phase, we thus decided to consider the mean values of the effective interactions of LRs with a CC higher than 0.6 and to directly assign them to energies of the PIM presented in Fig. I-5. The values thus obtained are listed in Tab. III-8. To be more specific:

- $E^b_{Fe^{SIA}Ni^{1nnc}}$ ($E^b_{Fe^{SIA}Cr^{1nnc}}$) binding energy was obtained by taking the mean values of both values assigned to 1nncFe_Ni (1nncFe_Cr) for LRs numbered from 18 to 51 and values assigned to 1nnc_Ni (1nnc_Cr) for LRs numbered from 2 to 9.

- $E^b_{Ni^{SIA}Ni^{1nnc}}$ ($E^b_{Ni^{SIA}Cr^{1nnc}}$) binding energy was obtained by taking the mean values of values assigned to 1nncS_Ni (1nncS_Cr) for LRs numbered from 18 to 34.

- $E^b_{Cr^{SIA}Ni^{1nnc}}$ ($E^b_{Cr^{SIA}Cr^{1nnc}}$) binding energy was obtained by taking the mean values of values assigned to 1nncS_Ni (1nncS_Cr) for LRs numbered from 35 to 51.

- $E^b_{Ni^{1nnt}SIA}$ ($E^b_{Cr^{1nnt}SIA}$) binding energy was obtained by taking the mean values of values assigned to 1nnt_Ni (1nnt_Cr) for LRs numbered from 2 to 9 and from 18 to 51.

Note that in the following table we considered in fact the opposite of mean values owing to the fact that using our convention, a negative binding energy implies repulsion. The interactions of Ni and Cr solutes with $\langle 100 \rangle$ dumbbells in Fe-10Ni-20Cr are consistent with what would intuitively be expected of moderately oversized and undersized solutes, respectively. Despite the small positive energy for $E^b_{Ni^{SIA}Ni^{1nnc}}$, Ni is generally repelled from the compressive sites but shows positive binding in the tensile sites. Cr exhibits the opposite tendencies, except for $E^b_{Cr^{SIA}Cr^{1nnc}}$ for which non negligible repulsion is obtained.

	$E^b_{Fe^{SIA}Ni^{1nnc}}$	$E^b_{Fe^{SIA}Cr^{1nnc}}$	$E^b_{Ni^{SIA}Ni^{1nnc}}$	$E^b_{Ni^{SIA}Cr^{1nnc}}$	$E^b_{Cr^{SIA}Ni^{1nnc}}$	$E^b_{Cr^{SIA}Cr^{1nnc}}$	$E^b_{Ni^{1nnt}SIA}$	$E^b_{Cr^{1nnt}SIA}$
E^b (eV)	-0.09	0.10	0.02	0.08	-0.10	-0.11	0.05	0.01

Tab. III-8: Values obtained for $E^b_{C^{1nnt}SIA}$ and $E^b_{A^{SIA}B^{1nnc}}$ (A and B refer to the element type) binding energies of the PIM presented in Fig. I-5, when taking the mean values of effective energies of LRs presented in Tab. III-7 with a CC higher than 0.7.

V   <u>Conclusions</u>

We have determined point defect formation energies in a fcc Fe-10Ni-20Cr model alloy. To select the most appropriate reference state, we modelled PM, AFM1, AFMD and FM structures. The most stable state obtained with the VASP code is the AFM1, which was therefore used for the point defect calculations. A study of this reference state showed that the moments of the Cr and Ni atoms are ruled by the moments of their nearest neighbour Fe atoms. We estimated $\mu_A^{Fe-10Ni-20Cr}$ (A refers to the element type) chemical potentials for Fe, Ni and Cr atoms, by calculating the minimum of substitution energy on most of the 180 Fe, 50 Cr and 26 Ni atoms of the reference state. Our extensive set of point defect calculations based on the first principle method shows an important energy range for each set of point defect formations as can be seen in Fig. III-34, thus underlying the importance of the local environment in concentrated alloys.
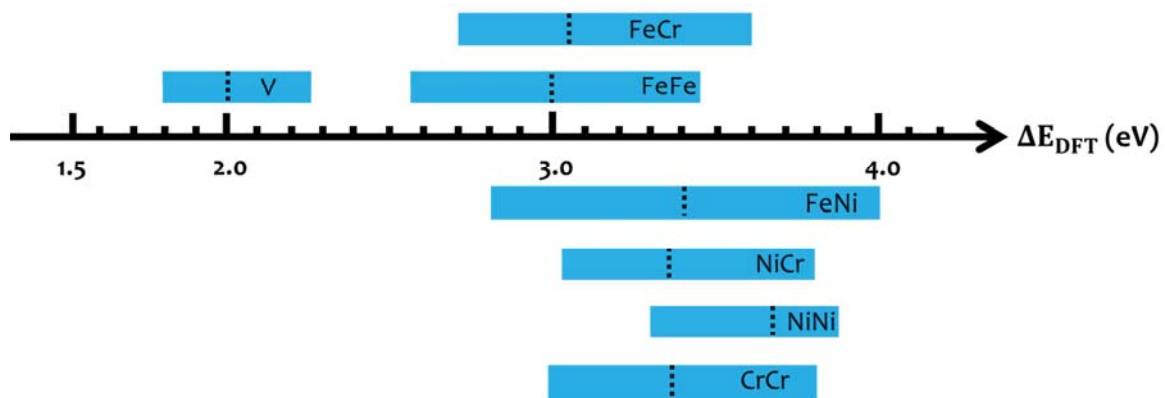
Fig. III-34: Schematic representation of each set of point defect calculations, ΔE_{DFT}, performed in this work. The blue bars correspond to the range of formation energy and the dashed lines correspond to the mean values of ΔE_{DFT} energies.

To investigate the role played by the local environment, a nomenclature of the different sites in the close vicinity of the point defect was established. The linear regressions performed using the variables defined in this nomenclature pointed out the key role played by the first shell surrounding the point defects in the formation energy value obtained when a point defect is created. The main results can be summarized as follows:

➤ The simple knowledge of the number of Ni and Cr atoms 1nn to the vacancy (1nn_Ni and 1nn_Cr respectively) was sufficient to estimate with a reasonable agreement DFT data. Values obtained for the best LR showed that the more first neighbour Ni atoms the lower the vacancy formation energy, whereas the more first neighbour Cr atoms the larger the vacancy formation energy.

➤ Inversely, LR usually showed that the more first neighbour Ni atoms the larger the dumbbell formation energy, whereas the more first neighbour Cr atoms the lower the vacancy formation energy.

➤ Dumbbell formation energies was best estimated by LR using the variables describing the effective interactions between Cr and Ni atoms in compressive sites and dumbbell atoms (i.e. 1nnc_Ni and 1nnc_Cr for self-interstitials and 1nncFe_Ni, 1nncFe_Cr, 1nncS_Ni and 1nncS_Cr for mixed dumbbells).

➤ Chemical composition of the first shell of atoms surrounding the Fe-Fe dumbbells which provides the biggest contribution to the formation energy values and that the position (tensile or compressive site) and thus magnetism usually intervenes at second order.

➤ Different LR coefficients were usually obtained between dumbbells oriented along the [100] direction, i.e. perpendicular to the AFM1 magnetic planes, or along the [010] direction, i.e. parallel to the AFM1 magnetic planes. These differences of effective interactions were consistent with the change of magnetic environment felt by dumbbell atoms between [100] and [010] dumbbells.

➤ The interactions of Ni and Cr solutes with point defects in fcc Fe-10Ni-20Cr are consistent with what would intuitively be expected of moderately oversized and undersized solutes, respectively. Ni binds to the vacancy and is generally repelled from the compressive sites of ⟨100⟩ dumbbells but shows positive binding in the tensile sites. Cr exhibits the opposite tendencies. The same conclusions can be drawn for the SIA formation energies. Indeed, Ni is found to be very unlikely to be found in mixed Fe-Ni

dumbbells or to from Ni-Ni dumbbells. Cr on the other hand can form mixed dumbbells. These results are however not in agreement with the experimentally derived size factors for Ni and Cr solutes in type 316 SS and in the pure materials [STRAALSUND1974].

132   Chapter III. First principle study of point defects in a fcc Fe-10Ni-20Cr model alloy

Chapter IV.   Cohesive models and RIS modelling

As shown in the introduction, one work package within the European project PERFORM60 is dedicated to the modelling of RIS in 316L stainless steels. The aim of our work is to gain insights into RIS process using an atomistic approach. In order to achieve this goal, a reliable cohesive model able to mimic properties of 316L stainless steels must be available. At the same time, low computational cost simulations are required to obtain long simulation times in big systems. In order to attain this objective, two different kinds of cohesive models were developed in PERFORM60, one of them by G. Bonny, which we tested extensively and the other one by us. These cohesive models and their properties are presented in the following sections.

I   EAM Fe-Ni-Cr interatomic potentials developed by G. Bonny

The EAM formalism presented in chapter I (section III-2-a) was taken as a natural choice because it provides a good balance between the good reproduction of system properties and the simplicity of its formalism. Adjustment details used by Bonny to build potentials using this approach are presented. The potentials thus obtained are then compared to DFT data.

I-1   Adjustment of EAM potentials

In the literature two different EAM Fe-Ni-Cr (N and H) potentials were developed by Grujicic and Zhou [GRUJICIC1993] and Smith and Was [SMITH1989], respectively. However, in these works the full parameterization of the potential was not reported. The requirement of the PERFORM60 project was thus to build a single EAM potential suitable to study the micro-structure and plasticity in 316L stainless steels. Although, many attempts have been made by Bonny [BONNY2011B], the requirements with respect to micro-structure and plasticity were found to be essentially different and not necessarily compatible. Six different potentials based on two different sets of single atom potentials have been therefore built [BONNY] and are summarized below.

A first set of ternary potentials was built by using the pure element potentials found in the literature for Fe [ACKLAND1997, MENDELEV2003, ACKLAND2004, DUDAREV2005, MALERBA2010],

Cr [OLSSON2005, BONNY2011A] and Ni [MISHIN2004]. An emphasis was given to select pure element atom potentials to reproduce:

➢ A meta-stable fcc phase in the composition range of interest, i.e. 8-30% of Ni concentration and 5-25% of Cr concentration.

➢ A stable stacking fault energy in reasonable agreement with thermodynamic calculations.

➢ Formation energies of vacancy and self-interstitial atoms in reasonable agreement with DFT values, and in particular, predict the $\langle 100 \rangle$ dumbbell as most stable SIA configuration.

For that purpose, the Fe potential of Ackland [ACKLAND1997], the Cr potential of Olsson [OLSSON2005] and the Ni potential of Mishin [MISHIN2004] were selected as best candidates to fulfil these constraints, and in particular, for the purpose of modelling the metastable fcc phase. The adjustment of the ternary potential was furthermore done with a number of constraints which can be summarized as follows:

➢ Strong underestimation of the stable stacking fault energy for Cr.

➢ Overestimation of vacancy migration barriers.

➢ Overestimation of vacancy-vacancy binding.

However, given these constraints, no suitable compromise was found to adjust all the properties in a unique ternary potential. Three different potentials were then built:

➢ The first of the potentials aims at reproducing the elastic properties of the material (P-100826).

➢ Two other potentials were built which focus more on defect energies and defect migration (P-100819 and P-100831).

Another strategy employed by Giovanni Bonny to build an Fe-Ni-Cr potential was to adjust pure element potentials over the properties of interest. These potentials were then used to build the ternary potential. Again, by following this procedure, no suitable compromise was found to adjust all the properties in a unique ternary potential. Three different potentials were then built:

➢ The first of the potentials is aimed at reproducing the elastic properties of the material (P-110307).

➢ Two other potentials were built to focus more on defect energies and defect migration (P-20120216 and P-20120323).

This set of six different EAM potentials summarized in Tab. IV-1 presented below, have been tested to determine whether some of them could be used to model RIS in Fe-Ni-Cr alloys.

Potential name	Modelling purpose
P-100826	Plasticity
P-100819	RIS
P-100831	RIS
P-110307	Plasticity
P-20120216	RIS
P-20120323	RIS

Tab. IV-1: Different EAM potentials built by Bonny [Bonny] and tested in this work are summarized. Potential names and their modelling purpose are specified.

I-2   Properties predicted by the EAM potentials

In order to check the reliability of the different potentials presented in Tab. IV-1, basic properties have been compared to DFT data available in dilute systems, i.e. γ-Fe and γ-Ni. An emphasis was therefore first given in calculating vacancy-vacancy, vacancy-solute and solute-solute binding energies. An accurate calculation of migration barriers is also key issue to model diffusion at the atomistic level using AKMC. Thus, vacancy-solute migration barriers have been calculated in dilute systems using the drag method presented in chapter I (section IV-1-a).

I-2-a   Binding energies in the dilute fcc Fe-Ni-Cr alloys

In order to compare with the DFT results presented in chapter II (section II-2-c) for the pure systems, two different sets of calculations were performed using five different potentials presented in Tab. IV-1:

➢ In a first set of calculations, both atoms and supercell were allowed to relax. These calculations, which are presented in Tab. 3-1 and in Tab. 3-2 of the annex 4 are referred to the relaxed calculations.

➢ However, as specified in chapter I (section II-1), both vacancy-solute exchanges performed in AKMC and solute-solute exchanges performed in MMC are done using the rigid lattice approach, i.e. no kind of relaxation is taken into account using this model. Thus, calculations referred to as "unrelaxed calculations" were also performed. These

135   Chapter IV. Cohesive models and RIS modelling

calculations presented in Tab. IV-2 and in Tab. IV-3, were done at the equilibrium lattice spacing in order to characterize the potentials presented in Tab. IV-1 using the rigid lattice approximation.

Interaction properties were not calculated using the P-20120223 potential owing to the fact it has been released recently.

It can be noted that these calculations were also performed by two other groups to check the good implementation of the methods available in the PERFORM60 project [ZHURKIN, AL TOOQ]. The three groups get the same agreement on values provided by the potentials.

DFT data available in dilute fcc systems and presented in chapter II (section II-2-c) have been added in the following tables to simplify the comparison between results obtained using DFT and the potentials. It may be mentioned again that calculations performed in the γ-Fe system usually spread over a wide range of values owing to the fact that DFT calculations were performed in different magnetic states. The reported energy range is the one found by Klaver et al. in the AFM states [KLAVER2012], because the phase magnetic diagram shows a long range antiferromagnetic order at the composition of our model alloy, at 0 K[MAJUMDAR1984].

Binding energies obtained using the different potentials tested are in general bad agreement with DFT data. In Tab. IV-2, it can be seen that in pure γ-Ni, all the potentials tested strongly overestimate the binding of vacancies positioned at 1nn separation while they all strongly underestimate the binding of vacancies positioned at 2nn separation. Furthermore, except for P-20120216, the weak binding found between 1nn Fe-Cr as well as the repulsion found between 2nn Fe-Cr are in total disagreement with DFT results. The other 1nn binding energies calculated using the rigid lattice method are however in rather good agreement in pure γ-Ni. This is however not the case for 2nn binding energies, in particular, the strong Cr-Cr binding found using DFT is usually not reproduced. Among the different potentials tested in pure γ-Ni, it can be noted that the worst agreement with DFT data is obtained using both P-100826 and P-110307 potentials. Indeed, at least two 1nn binding energies display opposite values relative to DFT data while only one important difference is observed for both P-100819 and P-100831 potentials and that P-20120216 potential is in rather good agreement. The bad agreement of both P-100826 and

P-110307 potentials could however be expected since they were built to reproduce plasticity properties as mentioned in Tab. IV-1. Regarding the 2nn binding energies, the agreement with DFT values is even worse, particularly for both P-100819 and P-100831 although they have been built for RIS modelling. It can be noted that, as for the 1nn interaction, the P-20120216 potential seem to provide a good description of 2nn interaction.

Distance	Cohesive model	Binding energy (eV)					
		V-V	Fe-V	Cr-V	Fe-Fe	Cr-Cr	Fe-Cr
1nn	DFT	0.02	-0.02	-0.05	-0.11	0.04	-0.16
	P-100819	0.15	-0.15	-0.1	-0.16	0.01	0.02
	P-100826	0.14	-0.05	0.01	0	0.19	0.06
	P-100831	0.15	-0.15	-0.1	-0.16	0.01	0
	P-110307	0.33	0.03	-0.01	-0.01	0.01	0
	P-20120216	0.24	-0.11	-0.04	-0.09	0.06	-0.07
2nn	DFT	0.12	-0.01	0.01	0.02	0.11	0.01
	P-100819	0.02	0.02	-0.02	-0.12	-0.05	-0.09
	P-100826	0.02	0.04	0	0.01	-0.04	-0.04
	P-100831	0.02	0.03	-0.03	-0.09	-0.07	-0.08
	P-110307	0.01	-0.03	-0.03	0	0	0
	P-20120216	0.07	0	0.01	0.03	0.05	0.01

Tab. IV-2: Binding energies calculated in the pure γ-Ni system using the rigid lattice method. Results are compared to DFT data [TUCKER2008]. We consider five different Fe-Ni-Cr potentials presented in Tab. IV-1.

In Tab. IV-3, it can be seen that in pure γ-Fe, except the P-20120323 potential, all the potentials tested strongly overestimate the binding of vacancies positioned at 1nn separation. Also, none of the potentials reproduce well the 1nn Cr-Cr binding energy range of DFT. Indeed, both P-100819 and P-100831 potentials strongly overestimate the repulsion of 1nn Cr-Cr predicted by the DFT, while a binding is found using the other potentials. The agreement for 2nn interactions with DFT data is good for none of the potentials. It can however be noted that a better agreement is obtained for the P-110307 potential, but 2nn interaction are found to be very weak. 1nn interactions are rather in accordance with DFT data using both P-100819 and P-100831 although that both 1nn Cr-V and 1nn Cr-Cr repulsions as well as 1nn Ni-V attraction are strongly overestimated. However, the agreement with DFT data is very poor using the other potentials,

particularly the P-20120216 potential which displays opposite trends with DFT data for Cr-V, Ni-Ni and Cr-Cr interactions.

Distance	Cohesive model	Binding energy (eV)					
		V-V	Ni-V	Cr-V	Ni-Ni	Cr-Cr	Ni-Cr
1nn	DFT	0.04 to 0.18	0.02 to 0.09	-0.09 to 0.00	-0.01 to 0.11	-0.10 to -0.01	-0.01 to 0.05
	P-100819	0.28	0.22	-0.16	0.1	-0.16	-0.01
	P-100826	0.28	0.05	-0.04	-0.01	0.04	-0.05
	P-100831	0.28	0.21	-0.16	0.1	-0.16	-0.02
	P-110307	0.3	-0.04	-0.05	-0.01	0.01	-0.01
	P-20120216	0.1	0.03	0.06	-0.09	0.12	-0.01
2nn	DFT	-0.09 to 0.02	-0.01 to 0.03	-0.08 to 0.00	-0.01 to 0.07	-0.01 to 0.02	-0.03 to -0.01
	P-100819	-0.04	-0.09	-0.02	-0.14	0.01	-0.01
	P-100826	-0.04	-0.02	0.03	0.02	0.06	0.06
	P-100831	-0.04	-0.09	-0.02	-0.13	0.01	0
	P-110307	0.1	0.03	0.01	0	0.01	0
	P-20120216	0.05	0.02	0.03	0.03	0.06	0.02

Tab. IV-3: Binding energies calculated in the pure γ-Fe system using the rigid lattice method. Results are compared to DFT data [KLAVER2012]. We consider five different Fe-Ni-Cr potentials presented in Tab. IV-1.

Another point worthy of mention is that, for P-100819 and P-100831 potentials both dedicated to atomistic studies related to the micro-structural evolution of Fe-Ni-Cr alloys, very different results may be obtained between relaxed and unrelaxed calculations as can be seen in Tab. 3-3 and in Tab. 3-4 presented in annex 4. This point is important because it is the relaxed binding energies of the potentials which were adjusted on DFT results. Thus, Properties of these potentials are in worse agreement using the rigid lattice method owing to the fact that their properties were adjusted on relaxed calculations. This property is mainly observed in the γ-Ni where significant differences were calculated for almost all 1nn interactions and 2nn solute-solute interaction. This may cause important deviations between MC models using the rigid lattice approach and those which take into account atomic relaxations.

None of the potentials developed in the framework of the PERFORM-60 project and presented in Tab. IV-1 are able to reproduce accurately the binding energies calculated using DFT in both γ-Ni and γ-Fe systems:

- ➢ None of the potentials provide a good reproduction of 2nn interactions in pure γ-Fe.
- ➢ P-100819 and P-100831 potentials, which are dedicated to the study of RIS in Fe-Ni-Cr alloys, are the most appropriate potentials in γ-Fe but do not reproduce well both 1nn and 2nn binding energies in pure γ-Ni.
- ➢ The P-20120216 potential, which is dedicated to the study of RIS in Fe-Ni-Cr alloys, is in very good agreement with DFT values in γ-Ni but is not appropriate in γ-Fe.
- ➢ As could be expected, for both P-100826 and P-110307 potentials, which are dedicated to the study of plasticity in Fe-Ni-Cr alloys, the agreement is very poor in both γ-Ni and γ-Fe systems.

As could be expected, potentials dedicated to the RIS modelling, i.e. P-100819, P-100831 and P-20120216 potentials provide the best agreement, although none of them are in prefect accordance with DFT data. In particular, P-20120216 potential is found to best model γ-Ni whereas both P-100819 and P-100831 potentials are found to best model γ-Fe. Despite the discrepancy of binding energies in pure γ-Fe system due to the choice of the reference state, as the austenitic steels we want to model alloys containing a high content of Fe atoms, both P-100819 and P-100831 can be considered as the best potentials for our study. It should be borne in mind that, due to the lack of data, the AFM states are just supposed to be reliable for the calculation of binding energies in the γ-Fe system using DFT.

I-2-b   Vacancy formation in the Fe-10Ni-20Cr alloy

DFT results obtained for our Fe-10Ni-20Cr model alloy and presented in Fig. III-14 have been compared with the P-20120216 potential. Evolution of excess energy caused by the vacancy creation, ΔE^V, as a function of the local environment to the vacancy is compared between the DFT and the P-20120216 potential in Fig. IV-1 and in Fig. IV-2. The same sites as those considered in DFT calculations to introduced vacancies were tested using the P-20120216 potential. Clearly, the local environment surrounding the vacancy has a very different influence on ΔE^V using the potential or the DFT as can be seen in these graphs. In particular, the number of Fe 1nn to the vacancy has a pronounced influence on the evolution of the formation energy

139   Chapter IV. Cohesive models and RIS modelling

using the potential as can be seen in Fig. IV-2 whereas no particular trends were observed using DFT. Similarly, the number of Cr 1nn to the vacancy has opposite effect on the evolution of the formation energy between DFT and the P-20120216 potential as can be seen in Fig. IV-1. Thus, as could be expected, ΔE^V estimated using the P-20120216 potential is unable to reproduce the values found using DFT as can be seen in Fig. IV-2 (left figure).
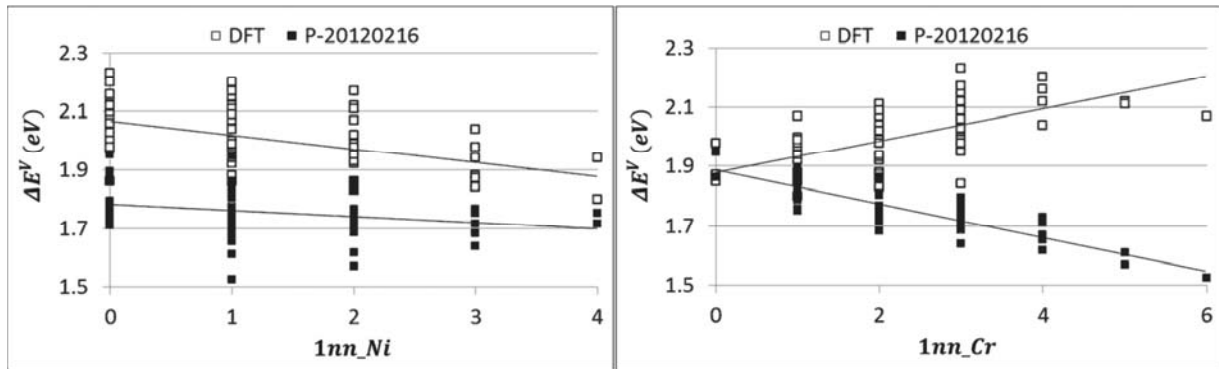
Fig. IV-1: Vacancy formation energy, ΔE^V, versus the number of Ni atoms 1nn to vacancies (1nn_Ni in left figure). Vacancy formation energy, ΔE^V, versus the number of Cr atoms 1nn to vacancies (1nn_Cr in right figure). We include calculation performed using DFT (open squares) and using P-20120216 potential (black squares) in the Fe-10Ni-20Cr model alloy.
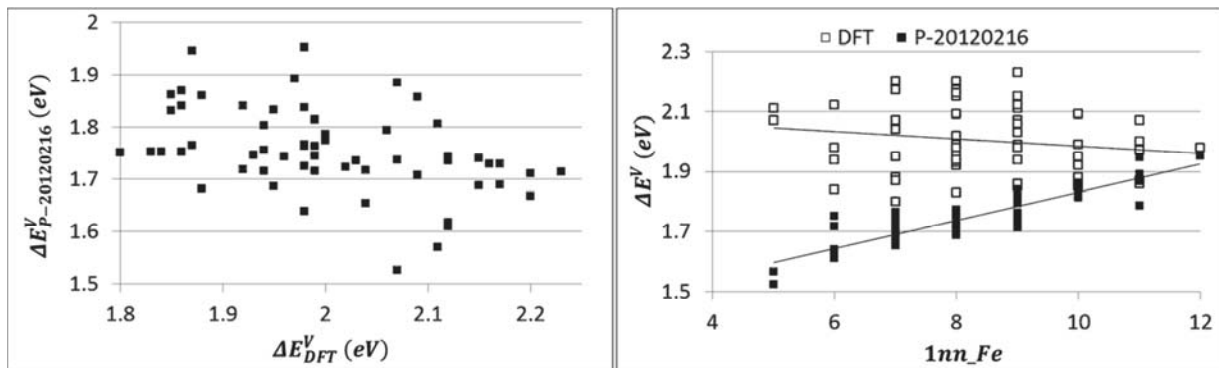
Fig. IV-2: Vacancy formation energy, ΔE^V, versus the number of Fe atoms 1nn to vacancies (1nn_Fe in right figure). We include calculation performed using DFT (open squares) and using P-20120216 potential (black squares) in the Fe-10Ni-20Cr model alloy. In left figure, vacancy formation energy calculated using P-20120216 potential, $\Delta E^V_{P-20120216}$, as a function of the vacancy formation energy calculated using DFT, ΔE^V_{DFT}.

140   Chapter IV. Cohesive models and RIS modelling

I-2-c   Migration energy in the pure fcc systems

In Tab. IV-4, vacancy-solute migration barriers calculated using both P-100831 and P-100819 potentials are compared to DFT data. Firstly, it can be noted that agreement between DFT and the pure potentials is poor. Indeed, as mentioned in section I-1, these ternary potentials are based on both [ACKLAND1997] and [MISHIN2004] single potentials which overestimate the DFT values by 0.40 and 0.11 eV respectively in pure Ni and Fe systems. Since these values cannot be corrected by fitting the alloy potential, an emphasis was given to reproduce their good relative weigh, i.e. that the relative jump frequencies using the DFT data in a given matrix is the same as by using the potentials. Unfortunately, no good compromise was obtained as can be seen in Tab. IV-4. In particular, strong discrepancy of Cr diffusion barriers were obtained in fcc systems. Indeed, using these potentials, Cr is found to be a low diffusing element in fcc system while DFT predicts precisely the opposite.

System	Migrating atom	Migration barrier (eV)		
		DFT	P-100831	P-100819
Pure γ-Ni	Fe	0.95	1.08	1.04
	Ni	1.08	1.19	1.19
	Cr	0.82	0.95	1
Pure γ-Fe	Fe	1.05	1.45	1.45
	Ni	0.88	1.28	1.13
	Cr	0.64	1.4	1.4

Tab. IV-4: Vacancy-solute migration barriers calculated using both P-100831 and P-100819 potentials. Results are compared to DFT data available in the pure fcc systems [TUCKER2008, KLAVER2012].

I-3   Stability of the fcc phase

We have investigated the stability of fcc phase for two potentials. The first step is to determine the correct lattice parameters with temperatures and compositions. Since materials expand with increasing temperature, the lattice constant must be determined for every simulation temperature. To that purpose, the lattice parameter at 0K, 300K and 600K over the whole concentration range was calculated using both P-100819 and P-100831 potentials. In particular, $Fe_{70}Ni_{30-x}Cr_x$ ternary alloys are investigated in Fig. IV-3 and in Fig. IV-4.

The 0K calculations converged very well but are not in agreement with the linear increase observed for $Fe_yNi_{100-y-x}Cr_x$ alloys with increasing Cr content [BAER1958, ARTSISHEVSKAYA2008, KARMAZIN1982, MARUCCO1994]. Furthermore, the lattice parameter is found to decrease with increasing temperature rather than increase as might be expected. Indeed, higher temperatures result in smaller lattice parameters as can be observed in Fig. IV-3 and in Fig. IV-4. This anomalous behaviour seems to be induced by the introduction of Cr atoms in the lattice, even at low concentration, and to be enhanced by increasing concentration of Cr. This is also supported by the fact that a positive thermal expansion is observed at zero concentration of Cr.
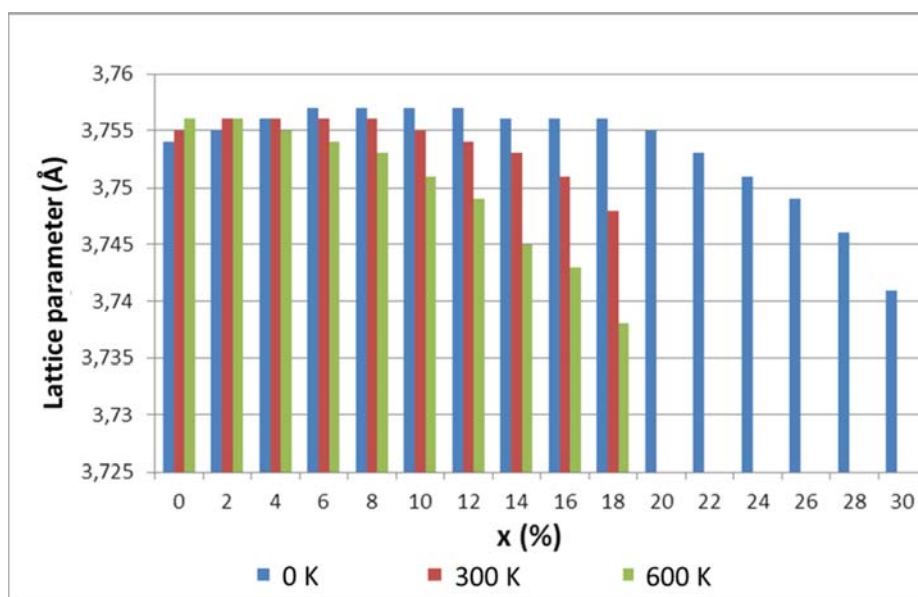
Fig. IV-3: Lattice parameter predicted by the P-100831 potential for Fe-10Ni-20Cr ternary alloys as a function of the Cr content. 10,000 steps of MD were performed for each simulation in lattices containing 4000 atoms ($10\times10\times10$ a_0^3). Beyond 18 at% of Cr, fcc lattice is not retained at finite temperatures.

142   Chapter IV. Cohesive models and RIS modelling
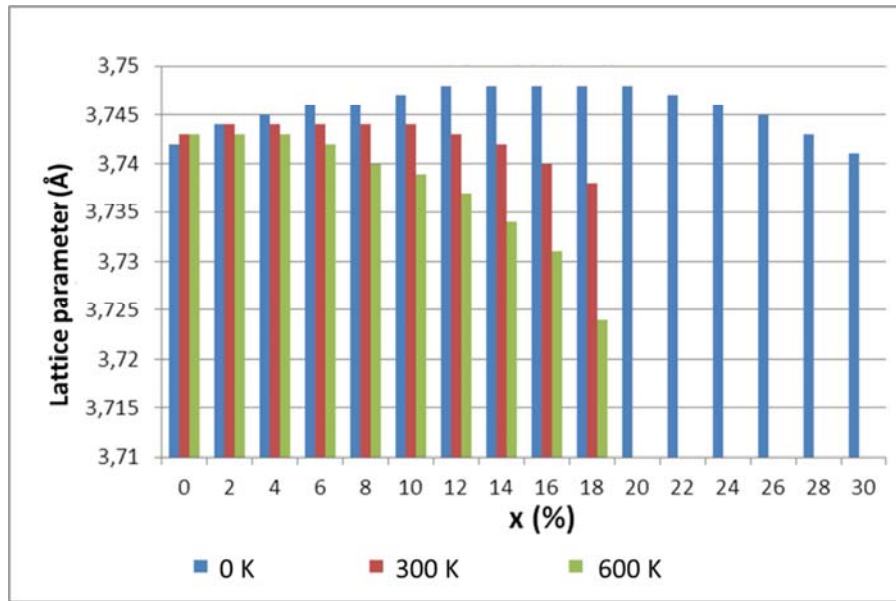
Fig. IV-4: Lattice parameter predicted by the P-100819 potential for Fe-10Ni-20Cr ternary alloys as a function of the Cr content. 10,000 steps of MD were performed for each simulation in lattices containing 4000 atoms ($10\times10\times10$ a_0^3). Beyond 18 at% of Cr, fcc lattice is not retained at finite temperatures.

Furthermore, we were not able to calculate the lattice parameter for many compositions of the ternary alloy. Further analysis showed that the plotting of the lattice parameter as a function of the pressure revealed anomalous behaviours. In particular, these curves were not linear at negative pressures over a wide concentration range, suggesting that a transition phase occurred. This feature was confirmed by the representation of the lattice given in Fig. IV-5 where it is clear that the fcc phase is not retained at finite temperatures. As a consequence, the zero-pressure point couldn't be reached. In Fig. IV-3 and in Fig. IV-4, the lattice parameters which are not represented at 300 K and 600 K, i.e. for Cr content exceeding 18%, correspond to the compositions at which the phase transitions occurred.

143   Chapter IV. Cohesive models and RIS modelling
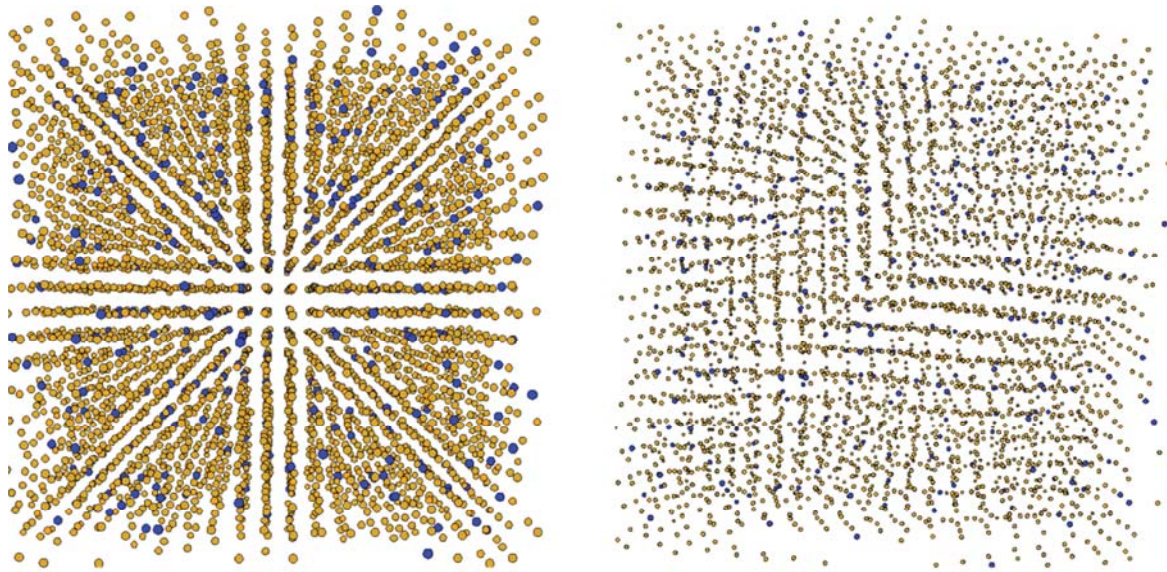
Fig. IV-5: fcc arrangement is presented for Fe-10Ni-20Cr ternary alloys with Cr content below (left figure) and above (right figure) 18 at%.

We showed in this section that the potentials available in the literature [ACKLAND1997, OLSSON2005, MISHIN2004] of which P-100819 and P-100831 ternary potentials are based on (see section I-1), are not reliable for the study of RIS. In particular, at the target composition of 10% Ni and 20% Cr with the latter potentials, we found that at finite temperature and under strain the fcc phase is not (meta)stable and a spontaneous transformation to an anomalous phase takes place.

I-4   Stability of the solid solution

The phase stability as well as its order properties predicted by a cohesive model is an important point to consider in atomic simulations. As mentioned in the introduction, according to the Fe-Ni-Cr phase diagram, several different phases should coexist at temperature conditions encountered in nuclear reactors. However, 316L SS are frozen in a meta-stable austenitic phase during the fabrication process [VOLGIN2012], which is intended to survive for the life time of the component. In particular, the quench does not allow for the appearance of order in the material which is a solid solution. The stability of the solid solution is therefore investigated in this section by performing MMC simulations. Again, these calculations were performed by two other

144   Chapter IV. Cohesive models and RIS modelling

groups [ZHURKIN, AL TOOQ] to check the good implementation of the methods available in the PERFORM60 project.

Very different behaviours may be observed depending on the potential studied as summarized from Tab. IV-5 to Tab. IV-9. The most important information may be summarized as follows:

> In fcc Ni-20Cr alloy, the P-100819 potential shows a strong tendency for phase ordering as can be seen in Tab. IV-5. Further analyses indicate that the binary system segregates into two regions, i.e. pure Ni region and Ni-Cr region. The ratio between Ni and Cr atoms in the Ni-Cr region is approximately equal to 2, which indicates the formation of the Ni_2Cr phase. This observation is in agreement with the expected results from the experimental phase diagram [NASH1991]. However, the P-100819 potential shows a strong tendency for phase demixing in fcc Fe-10Ni-20Cr alloy. Indeed, both Ni and Cr atoms segregate to different regions of the Fe matrix.
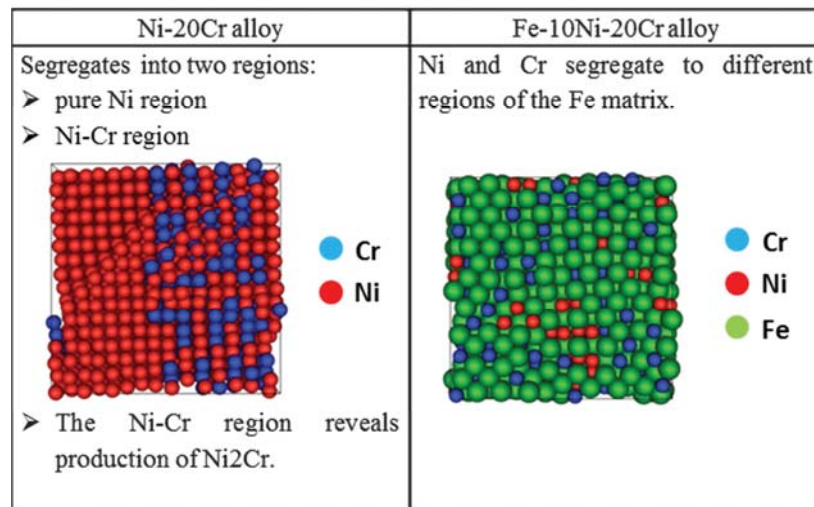
Tab. IV-5: Summary of relaxed MC simulations performed by Al Tooq et al. [AL TOOQ] using the P-100819. Bulk calculations performed in a lattice containing 4000 atoms ($10 \times 10 \times 10 \; a_0^3$) at 600K.

> The P-100826 potential, which is dedicated to the study of plasticity, shows that Cr atoms have a strong tendency to precipitate over a wide range of temperature in fcc Fe-10Ni-20Cr alloy. Indeed, when performing both relaxed and unrelaxed calculations, big precipitates of Cr are formed in the lattice, even at high temperature. The type of MC method used was found to have an influence on the behaviour of Ni atoms in the lattice.

Indeed Ni atoms segregate until 900K using relaxed MC methods [ZHURKIN] while Fe and Ni showed a strong tendency for phase ordering using unrelaxed MC methods, as can be seen in Tab. IV-6 and in Tab. IV-7 respectively.

System type	T (K)	Fe-10Ni-20Cr alloy
Bulk	100	➢ Ni and Cr Phase separation ➢ Big Cr precipitates ➢ Small Ni precipitates
Bulk	300-900	➢ Cr precipitates ➢ Dissolution of Ni precipitates (fully achieved at 900K)
Bulk	1400-1900	➢ Small Cr precipitates ➢ Solid solution
Free surface	100-1400	Cr depletes at the free surface and at small cavity surfaces.
Free surface	100-300	Ni depletes at the free surface

Tab. IV-6: Summary of relaxed MC simulations performed by Zhurkin et al. [ZHURKIN] using the P-100826. Calculations performed in supercells of 4000 atoms ($10\times10\times10$ a_0^3).

System type	T (K)	Fe-10Ni-20Cr alloy
Bulk	100-1400	➢ Big Cr precipitates ➢ Tendency for phase ordering between Fe and Ni (formation of lines of Ni in the Fe matrix)	
Free surface	100-1400	➢ Big Cr precipitates ➢ Tendency for phase ordering between Fe and Ni (formation of lines of Ni in the Fe matrix) ➢ Ni enrichment at the free surface.	
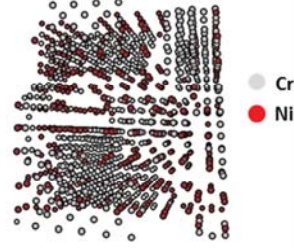
Tab. IV-7: Summary of unrelaxed MC simulations performed using the P-100826. Calculations performed in supercells of 4000 atoms ($10\times10\times10$ a_0^3).

➢ In fcc Ni-20Cr alloy, the P-110307 potential shows a weak tendency for phase precipitation. Indeed, calculation performed by Al Tooq et al. [AL TOOQ] showed the formation of small cluster of Cr atoms at 600K. However, the P-110307 potential shows also strong tendency for phase ordering over a wide range of temperature and using both

relaxed and unrelaxed MC methods as can be seen in Tab. IV-8 and in Tab. IV-9. Indeed, Ni and Cr atoms are arranged into planes alternated with pure Fe planes, even at high temperature.

T (K)	Ni-20Cr alloy	Fe-10Ni-20Cr alloy
100-900		➤ Strong tendency for phase ordering ➤ Formation of pure Fe planes alternated with Cr-Ni planes
900-1400		➤ solid solution
600	Weak tendency for phase precipitation ● Cr ● Ni	➤ Strong tendency for phase ordering ● Cr ● Ni ➤ Formation of pure Fe planes alternated with Cr-Ni planes
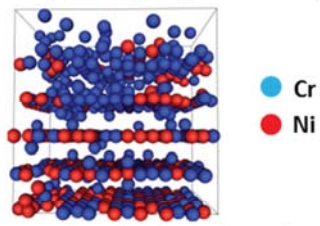
Tab. IV-8: Summary of relaxed MC simulations performed by Al Tooq et al. and Zhurkin et al. [ZHURKIN , AL TOOQ] using the P-110307. Bulk calculations performed in a lattice containing 4000 atoms ($10\times10\times10$ a_0^3).

T (K)	Fe-10Ni-20Cr alloy
100-900	➤ Strong tendency for phase ordering ○ Cr ● Ni ➤ Formation of pure Fe planes alternated with Cr-Ni planes
900-1400	➤ solid solution

Tab. IV-9: Summary of unrelaxed MC simulations performed using the P-110307. Bulk calculations performed in a lattice containing 4000 atoms ($10\times10\times10$ a_0^3).

➤ Finally, Zhurkin et al. [ZHURKIN] have observed the formation of a big Cr precipitate, containing almost of the Cr atom of the simulation box, stable at least up to 2000 K using the P-20120323 potential. At low T, the Cr precipitate is surrounded by Ni atoms, whereas at high T, the Ni atoms move back to the matrix.

147   Chapter IV. Cohesive models and RIS modelling

We can conclude that none of the potentials are able to reproduce the solid solution observed in 316L SS used for nuclear applications. Indeed, except for the P-100819, all potentials show strong tendencies for either phase ordering or phase precipitation over a wide range of temperature (including temperatures well above operating temperatures encountered in PWR reactors).

It can be mentioned that the P-100819 is however the best potential regarding MC simulations since it predicts the formation of the Ni$_2$Cr phase [NASH1991]. However, it also predicts that Ni and Cr atoms segregate completely to different regions in the Fe matrix which is not in accordance with the solid solution of Fe-Ni-Cr alloys [RAYNOR1988]. Furthermore, the fcc phase was found to be unstable using this potential (as well as using P-100831).

I-5   Conclusions

We have tested a set of EAM potentials (provided by Bonny [BONNY]) dedicated to model the Fe-Ni-Cr system. Investigations made on binding energies as well as migration barriers indicate that neither the thermodynamic nor the kinetic aspect of Fe-Ni-Cr alloys are correctly reproduced using these potentials. The biggest issues may be summarized as follows:

- Agreement between DFT and plasticity potentials is found to be very poor.
- Strong disagreements are found for Fe-Cr, Cr-V and Fe-V binding energies in pure Ni using the P-100831 potential.
- A general better agreement is found using the P-100819 potential even if strong disagreements are found for Cr-V and Fe-Cr binding energies in the pure fcc Ni.
- Using both P-100831 and P-100819 potentials, the thermal expansion coefficient was found to be negative for the majority of composition studied and the fcc phase is found to be unstable for the target composition (Fe-10Ni-20Cr).
- Despite the fact that P-20120216 was consistent with the DFT data available in the pure fcc Ni, strong disagreements were found for Cr-V, Ni-Ni as well as Cr-Cr interactions in pure Fe.

148   Chapter IV. Cohesive models and RIS modelling

➢ We observed for each potential strong tendency for either phase ordering or phase precipitation in the Fe-10Ni-20Cr target alloy, thus allowing for the appearance of the solid solution usually at too high temperatures

II   Pair Fe-Ni-Cr interaction model

As reviewed in the previous section, none of the potentials presented in Tab. IV-1 are able to provide a reliable description of DFT data available in pure and concentrated systems, migration energies as well as the meta-stable phase of 316L SS components (solid solution) at operating temperatures encountered in PWR reactors. Furthermore, the fcc phase is not stable for many ternary alloys. For all these reasons, it was decided to build a PIM.

II-1   Adjustment of the PIM

In building our PIM, much emphasis was put on obtaining good interaction properties as well as reliable diffusion properties in fcc systems. In the following section, we present our strategy to adjust the interaction parameters to reproduce:

➢ DFT data available in dilute fcc systems.
➢ The evolution of the DFT vacancy formation energy with its local environment presented in Fig. III-14 for the Fe-10Ni-20Cr model alloy.
➢ Tracer diffusion coefficients of elements as a function of the composition, in Fe-Ni and Ni-Cr binaries.

II-1-a   Properties of dilute and concentrated fcc Fe-Ni-Cr alloys

As mentioned in chapter I (section II-1), AKMC simulations are performed in a rigid lattice. Interaction parameters of a PIM limited to 1nn interactions between elements positioned at perfect lattice positions, ε_{AB} presented in Fig. I-3 and in Fig. I-4, can thus be used to determine the total energy of an alloy. A system of 10 consistent equations is therefore required to deduce the interaction parameters in the Fe-Ni-Cr system. This set of equations is presented in this section.

149   Chapter IV. Cohesive models and RIS modelling

Among the 10 interaction parameters required to model Fe-Ni-Cr alloys, 8 of them were deduced from DFT calculation performed in pure systems:

- ➢ The diagonal interaction parameters ε_{AA} were deduced by using the cohesive energies of the pure systems, E_c^{Fe}, E_c^{Ni} and E_c^{Cr} respectively.

- ➢ The binding energies in pure γ-Fe, $E_b^{NiNi/Fe}$, $E_b^{CrCr/Fe}$ and $E_b^{NiCr/Fe}$ were used to deduce the non-diagonal interaction parameters ε_{AB}.

- ➢ Both ε_{VFe} and ε_{VV} interaction parameters, were deduced by considering the formation energy in pure γ-Fe, $E_f^{V/Fe}$, the binding energy between two vacancies in pure γ-Fe, $E_b^{VV/Fe}$.

The last interaction parameters, i.e. ε_{VNi} and ε_{VCr}, were adjusted so as to reproduce the influence of the local environment on energy excess caused by the creation of a vacancy (i.e. ΔE_{DFT}^V). Indeed, we showed in chapter III (section IV-4-a) that ΔE_{DFT}^V can be nicely estimated from the knowledge of the number of Ni and Cr 1nn to the vacancy, while the number of 1nn Fe atoms does not have any impact. This relationship can be represented by the following function:

$$\Delta E_{LR}^V = \delta E^{V/Cr} \times 1nn\_Cr + \delta E^{V/Ni} \times 1nn\_Ni + C \qquad \text{Eq. IV-1}$$

where $\delta E^{V/Cr}$ ($\delta E^{V/Ni}$) represents the average variation of energy to introduce a vacancy near one Cr (Ni) atom, $1nn\_Cr$ corresponds to the number of Cr 1nn to the vacancy introduced in the lattice and C is the LR constant found for the intercept (the value of ΔE_{LR}^V when both $1nn\_Cr$ and $1nn\_Ni$ are equal to 0). The LR presented in Fig. III-19 shows that $\delta E^{V/Cr} = 0.05$ and that $\delta E^{V/Ni} = -0.04$.

In order to reproduce the same evolution as ΔE_{DFT}^V when using the PIM, we defined two energies $\delta E^{V/Fe \to Ni}$ and $\delta E^{V/Fe \to Cr}$ respectively, which represent the energy change due to the creation of a vacancy in an Fe site, and where among the 1nn, there is one less Fe atom and one more Ni atom (Cr atom respectively). The final expression found for the excess energy caused by the introduction of the vacancy using our PIM, ΔE_{PIM}^V, is displayed in Eq. IV-2.

$$\Delta E_{PIM}^V = (\varepsilon_{VFe} - \varepsilon_{FeFe}) \times 1nn\_Fe + (\varepsilon_{VNi} - \varepsilon_{FeNi}) \times 1nn\_Ni + (\varepsilon_{VCr} - \varepsilon_{FeCr}) \times 1nn\_Cr + \mu_{Fe} \qquad \text{Eq. IV-2}$$

This equation display 3 terms between parenthesis which represent the energy costs to introduce a vacancy near 1 Fe, 1 Ni and 1 Cr respectively. It can be seen that the relative balance between these energies drive the evolution of the vacancy formation energy as a function of the local environment when removing one Fe atom at different lattice sites of the same lattice to create the vacancies. The remaining pair interactions (ε_{VNi} and ε_{VCr}) have therefore been obtained by identifying the parameter values between Eq. IV-1 and Eq. IV-2. This was achieved by varying the local environment felt by the vacancy in Eq. IV-2. We considered two different cases: (1) a change of one more Fe and one less Ni in vacancy vicinity, i.e. $\delta E^{V/Fe \to Cr}$ presented in Eq. IV-3 (2) a change of one more Fe and one less Cr in vacancy vicinity, i.e $\delta E^{V/Fe \to Ni}$ presented in Eq. IV-4.

$$\delta E^{V/Fe \to Cr} = (\varepsilon_{VFe} + \varepsilon_{FeCr}) - (\varepsilon_{FeFe} + \varepsilon_{VCr})$$

Eq. IV-3

$$\delta E^{V/Fe \to Ni} = (\varepsilon_{VFe} + \varepsilon_{FeNi}) - (\varepsilon_{FeFe} + \varepsilon_{VNi})$$

Eq. IV-4

Both energies $\delta E^{V/Fe \to Ni}$ and $\delta E^{V/Fe \to Cr}$ have thus been designed to impose the evolution of ΔE_{PIM}^V with the local environment. In order to impose ΔE_{PIM}^V with the same evolution as ΔE_{DFT}^V, we identified both $\delta E^{V/Fe \to Cr}$ and $\delta E^{V/Fe \to Ni}$ values with the parameter values in Eq. IV-1, i.e. $\delta E^{V/Cr}$ and $\delta E^{V/Ni}$. We found that $\delta E^{V/Fe \to Ni} = -0.04$ and $\delta E^{V/Fe \to Cr} = 0.05$, the values of which are used in Fig. IV-6 to represent the evolution of ΔE_{DFT}^V as a function of the evolution of ΔE_{PIM}^V.
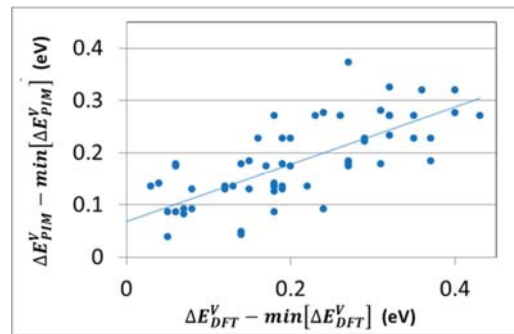
Fig. IV-6: Evolution of ΔE_{DFT}^V as a function of the evolution of ΔE_{PIM}^V estimated using $\delta E^{V/Fe \to Ni} = -0.04$ and $\delta E^{V/Fe \to Cr} = 0.05$ values.

II-1-b   Diffusion properties

Following the procedure of Barbe [BARBE2006], we attempted to reproduce the tracer diffusion coefficient values measured in experiment of Ruickova, in Ni-Cr and Fe-Ni binaries, at 1373 K and 1378 K respectively [RUICKOVA1981]. These results have been summarized in chapter II (section II-1-b).

Vacancy formation energies as the function of the concentration were therefore estimated, for both Ni-Cr and Fe-Ni binaries, using Grandjean's equation presented in Eq. I-37. This model predicts that a positive value of the binary ordering energy, Ω^{AB}, i.e. a tendency for phase ordering in a binary AB, will cause a minimum of diffusion for all the migrating atoms. Thus, the quadratic variations obtained using this model for the binary, are convenient to reproduce the shape of these diffusion measurement which display a well-defined minimum for the Ni-Cr binary as can be seen in Fig. IV-9. Grandjean's equation also depends on the vacancy formation energies calculated in the pure fcc Ni and Cr systems which can be calculated analytically using our cohesive model. These parameters can hence be adjusted to reproduce the good position of the diffusion minimum. As a result, we put an emphasis on reproducing:

➢ The good ratio between the tracer diffusion coefficients observed in the Ni-Cr binary, i.e. a ratio equal to 3 between Cr and Ni atoms respectively ($D_{Cr} > D_{Ni}$) upon all the composition range.

➢ The good ratio between the tracer diffusion coefficients observed in the Fe-Ni binary, i.e. a ratio equal to 1.33 between Ni and Fe atoms respectively ($D_{Ni} > D_{Fe}$) upon all the composition range.

➢ The good position of the minimum of diffusion coefficients observed in the Ni-Cr binary, i.e. for a concentration of about 45% of Cr. As noted previously, the minimum is imposed by a positive value for Ω^{NiCr}, and its position depends on the ratio between the formation energy in the pure fcc Ni, $E_f^{V/Ni}$, and the formation energy in the pure fcc Cr, $E_f^{V/Cr}$.

➢ The good reproduction of the diffusion coefficient evolution in the Fe-Ni binary alloy, which increase linearly with the concentration until the Ni_3Fe composition.

Diffusion coefficients presented in Eq. I-61 combine Einstein's equation which is evaluated for each element using AKMC and the Boltzmann exponential dependence with temperature, $\exp(-E_f^V/k_BT)$, where E_f^V is calculated using Grandjean's equations . It can be mentioned that in practice, the evolution of diffusion coefficients is almost completely imposed by the exponential term. The relative difference obtained between the diffusion coefficients of alloying elements is however induced by the part of diffusion coefficients calculated using AKMC through the values of migration barriers as a function of the local environment and the values of attempt frequencies.

II-1-c   Optimisation of the PIM

Both $\delta E^{V/Fe\rightarrow Ni}$ and $\delta E^{V/Fe\rightarrow Cr}$ energies presented in section II-1-a were found to have a strong impact on the diffusion coefficients. In particular, the set used to reproduce the evolution of the DFT vacancy formation energies with the local environment presented in Fig. IV-6, cannot be used to obtain the good position for the minimum values of diffusion coefficients in the Ni-Cr binary. As a result, we attempted to optimize our cohesive model by using another set of values for $\delta E^{V/Fe\rightarrow Ni}$ and $\delta E^{V/Fe\rightarrow Cr}$, being able to both reproduce the same trends as ΔE_{DFT}^V as well as the shape of the experimental diffusion coefficient evolution with composition. The best compromise was found by using $\delta E^{V/Fe\rightarrow Ni} = -0.01$ and $\delta E^{V/Fe\rightarrow Cr} = 0.01$ (instead of $\delta E^{V/Fe\rightarrow Ni} = -0.04$ and $\delta E^{V/Fe\rightarrow Cr} = 0.05$) for which ΔE_{PIM}^V is compared to ΔE_{DFT}^V in Fig. IV-7. It can be mentioned that Barbe's model does not reproduce the same trends as ΔE_{DFT}^V as can be seen in Fig. IV-8.
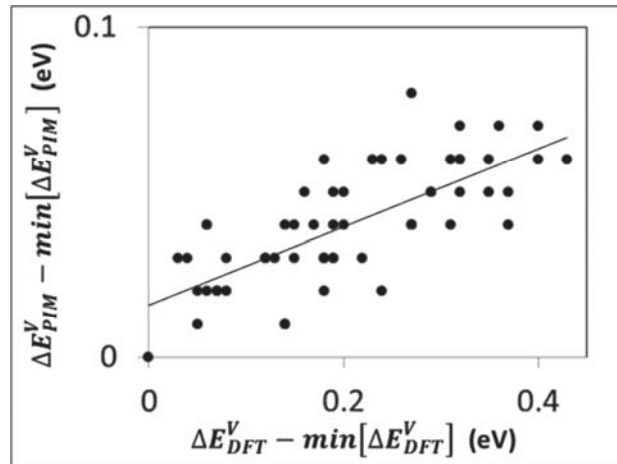
Fig. IV-7: Evolution of ΔE_{DFT}^{V} as a function of the evolution of ΔE_{PIM}^{V} estimated using $\delta E^{V/Fe \to Ni} = -0.01$ and $\delta E^{V/Fe \to Cr} = 0.01$ values.
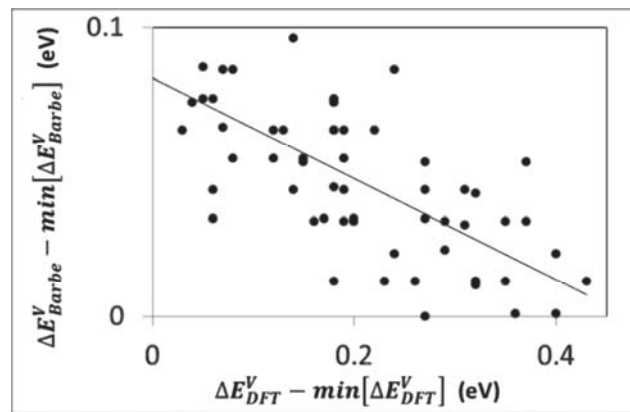
Fig. IV-8: Evolution of ΔE_{DFT}^{V} as a function of the evolution of ΔE_{BARBE}^{V} estimated using Barbe's PIM

Furthermore, we imposed that the formation energy in the pure fcc Ni is 0.07 eV above the formation energy in pure Cr to make sure that the minimum of the diffusion coefficients in the Ni-Cr binary system is obtained for a concentration of about 45% of Cr in agreement with the experimental data. The relative difference between these formation energies having been adjusted accordingly, and given the constraint of the PIM, the only way by which the depth of the minimum may be adjusted was to play on the Ni-Cr binding energy in the pure fcc Fe. The existence of the diffusion minimum is insured by choosing the value of $E_b^{NiCr/Fe}$ lying between -0.01 and 0.01 eV. The best agreement for the other energies fitted was however obtained by taking 0.01 eV for $E_b^{NiCr/Fe}$. Similarly, the good reproduction of the evolution of diffusion

154 Chapter IV. Cohesive models and RIS modelling

coefficients observed in the Fe-Ni binary was achieved by imposing that the formation energy in pure Fe is 0.18 eV above the formation energy in pure Ni. It is worth mentioning that this constraint is in agreement with DFT results which predicted a smaller value for the vacancy formation the pure fcc Ni as can be seen in Tab. IV-19. The parameters thus obtained by optimizing interaction energies in Fe-Ni-Cr alloys as well as diffusion properties in binary systems are presented in Tab. IV-10.

ε_{AB} (eV)	Fe	Ni	Cr	V
Fe	-0.73	-	-	-
Ni	-0.74	-0.74	-	-
Cr	-0.75	-0.77	-0.7	-
V	-0.2	-0.22	-0.21	0.28

Tab. IV-10: Interaction parameter values, ε_{AB} (A and B refer to the element type), between elements positioned at perfect lattice sites in the Fe-Ni-Cr system.

	Ni	Fe	Cr
E_{a_0} (eV)	0.50	0.53	0.48
ν (s^{-1})	$2.06 \cdot 10^{16}$	$2.78 \cdot 10^{16}$	$6.27 \cdot 10^{16}$

Tab. IV-11: Attempt frequencies, ν, and E_{a_0} energy values of the FISE model for each alloying elements.

The diffusion coefficients obtained in the Ni-Cr binary system are presented in Fig. IV-9 along with the experimental values of Ruickova at 1373 K [RUICKOVA1981]. AKMC simulations were performed in a system containing 4096 atoms including one vacancy and by making 2.0E6 measurements of at least 10 jumps per atom of each solute. Furthermore, the good reproduction of diffusion experiments in the Ni-Cr binary system was obtained using the attempt frequencies and the E_{a_0} energies of the FISE model presented in Tab. IV-11. We imposed the good ordering for the attempt frequencies and for the E_{a_0} energies to obtain $D_{Cr}^V > D_{Fe}^V > D_{Ni}^V$ as in the diffusion experiments. In particular, we imposed the same ratio between the attempt frequencies as the expected diffusion ratio (observed experimentally at 1300 K), i.e. that D_{Cr}^V/D_{Ni}^V ratio is equal to 3 and that D_{Fe}^V/D_{Ni}^V ratio is equal to 1.33. These parameters are those used in all the simulation presented below.

155 Chapter IV. Cohesive models and RIS modelling

The diffusion coefficients obtained in the Ni-Cr binary alloy are presented in Fig. IV-9 along with experimental values of Ruickova at 1378 K [RUICKOVA1981]. Although the shape of diffusion measurement is relatively well reproduced, it was impossible to adjust the magnitude as well as the good D_{Fe}^V/D_{Ni}^V ratio in the Ni-Cr binary alloy. The same remark can be done for the diffusion coefficients of Cr and Fe atoms in the ternary alloys presented in Fig. IV-10 and in Fig. IV-11. The D_{Cr}^V/D_{Fe}^V ratio seems to be equal to 2 in the whole composition range which is rather consistent with diffusion experiments. However, calculations performed using our cohesive model cannot reproduce these experimental results.
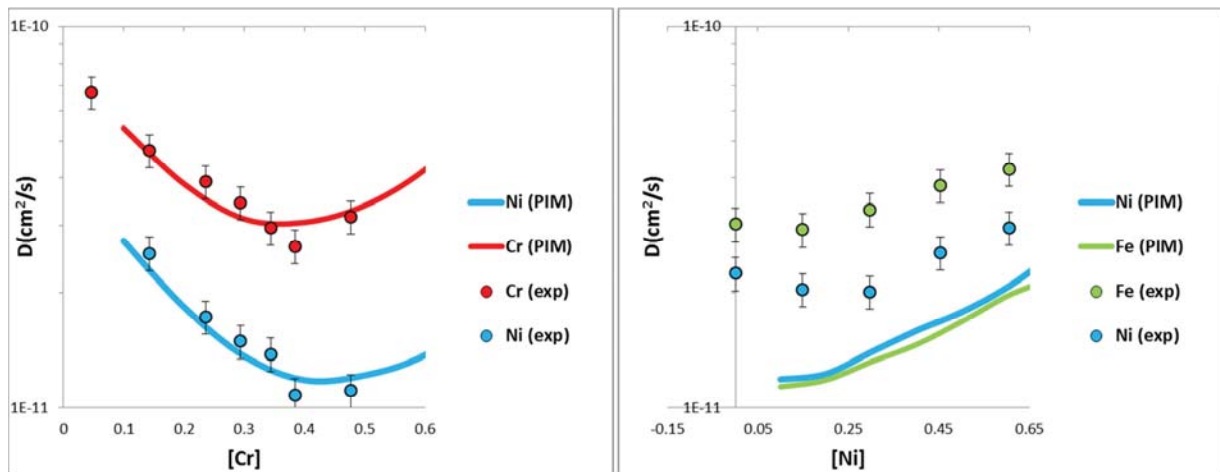
Fig. IV-9: Tracer diffusion coefficient of Ni and Cr atoms in the Ni-Cr binary plotted as a function of the Cr concentration (left figure). Tracer diffusion coefficient of Ni and Fe atoms in the Fe-Ni binary plotted as a function of the Ni concentration (right figure). Symbols refer to experimental measurement made by Ruickova [RUICKOVA1981] at 1373 K presented in Fig. II-6. Lines refer to diffusion coefficient calculated using our PIM. Calculations performed in a system containing 4096 atoms ($8\times8\times16$ a_0^3) including one vacancy.
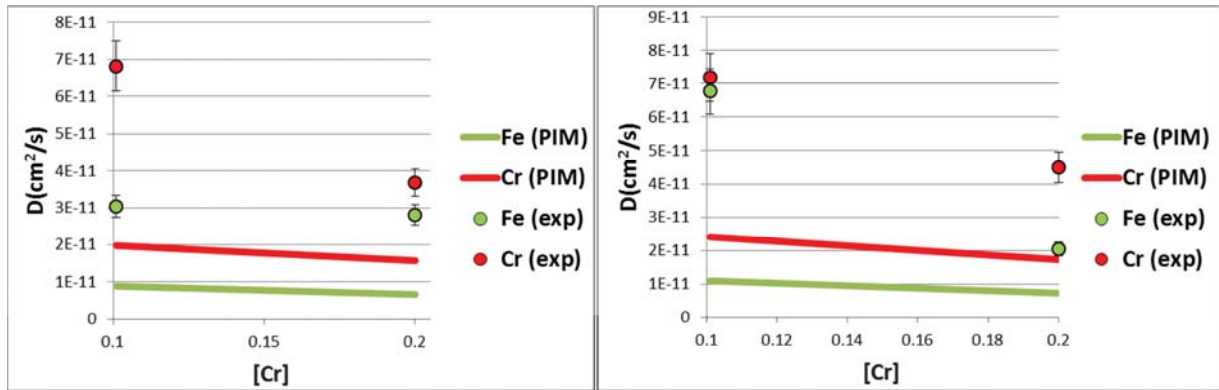
Fig. IV-10: Tracer diffusion coefficient of Fe and Cr atoms in the $Fe_{45-x}Ni_{55}Cr_x$ ternary (right figure) and in the $Fe_{65-x}Ni_{35}Cr_x$ ternary (left figure) plotted as a function of the Cr concentration. Symbols refer to experimental measurement made by Ruickova [RUICKOVA1981] at 1378 K. Lines refer to diffusion coefficient calculated using our PIM. Calculations performed in a system containing 4096 atoms ($8 \times 8 \times 16$ a_0^3) including one vacancy.
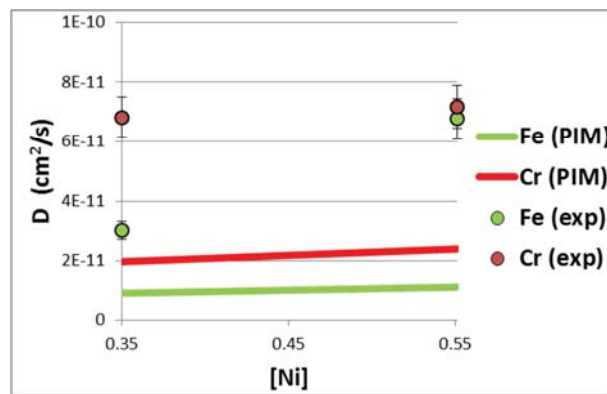
Fig. IV-11: Tracer diffusion coefficient of Fe and Cr atoms in the $Fe_{80-x}Ni_xCr_{20}$ ternary plotted as a function of the Ni concentration. Symbols refer to experimental measurement made by Ruickova [RUICKOVA1981] at 1378 K. Lines refer to diffusion coefficient calculated using our PIM. Calculations performed in a system containing 4096 atoms ($8 \times 8 \times 16$ a_0^3) including one vacancy.

Although we obtained for the Fe-Ni binary alloy (Fig. IV-9) and the ternary alloy (Fig. IV-10 and Fig. IV-11) the same tendencies between the calculated diffusion coefficients and the experimental diffusion coefficients, the calculated diffusion coefficients are found to be less than one order of magnitude smaller than experimental diffusion coefficients. This point can have significant consequences at low temperatures. Unfortunately, this issue cannot be solved due to the approximation made in the FISE model (only three E_{a_0} parameters). As a result, our PIM cannot reproduce well the diffusion coefficients in all the range of composition of fcc Fe-Ni-Cr

157   Chapter IV. Cohesive models and RIS modelling

alloys and at all the temperatures, as it was obtained previously by Barbe [BARBE2006]. In particular, Barbe was able to reproduce the diffusion experiments presented in Fig. IV-9 as well as obtaining a D_{Cr}^V/D_{Ni}^V ratio equal to 3 and a D_{Fe}^V/D_{Ni}^V ratio equal to 1.33 in the all composition range. In order to understand the lacks of our PIM regarding diffusion, we compared it to Barbe's model. We found that the bad agreement obtained for the diffusion coefficient values is due to the too low variability of migration barriers using our PIM and the FISE model (Eq. I-26) compared to simulations which use Barbe's cut bond model (Eq. I-28). Indeed, as can be seen in Fig. IV-12, the migration barriers encountered by the vacancy, E_a, cover a wider range of values with the cut bond model than with our model (FISE model). In particular, many low migration barriers, i.e. below 0.3 eV, are found using the cut bond model while E_a is above 0.4 eV in the vast majority of the jumps using our model. The influence of the local environment on the barrier, which is almost exclusively assumed by the pair interaction parameters presented in Tab. IV-10, is not sufficiently well described. In particular, we had to impose $\delta E^{V/Fe \to Ni} = -0.01$ and $\delta E^{V/Fe \to Cr} = 0.01$ to reproduce both the trends for ΔE_{DFT}^V (Fig. IV-7) and for the shape of diffusion coefficient experiments (Fig. IV-9). Given these fitting constraints, the final values for these parameters are too small to induce a significant variability of the migration barriers with the local environment. Furthermore, the choice made to take E_{a_0} parameter defined in Eq. I-26 as only depending on the migrating atom type, seems to be too great an approximation. The best agreement with diffusion coefficients was found by taking E_{a_0} equal to 0.53, 0.50 and 0.48 eV when the migrating atom was Fe, Ni and Cr respectively and changing these values does not extend the range covered by the migration barrier. It appears thus that the local environment at the SP has to be taken into account as it has been done by Costa in the Fe-Cr [COSTA2012] and by Barbe in the Fe-Ni-Cr [BARBE2006].
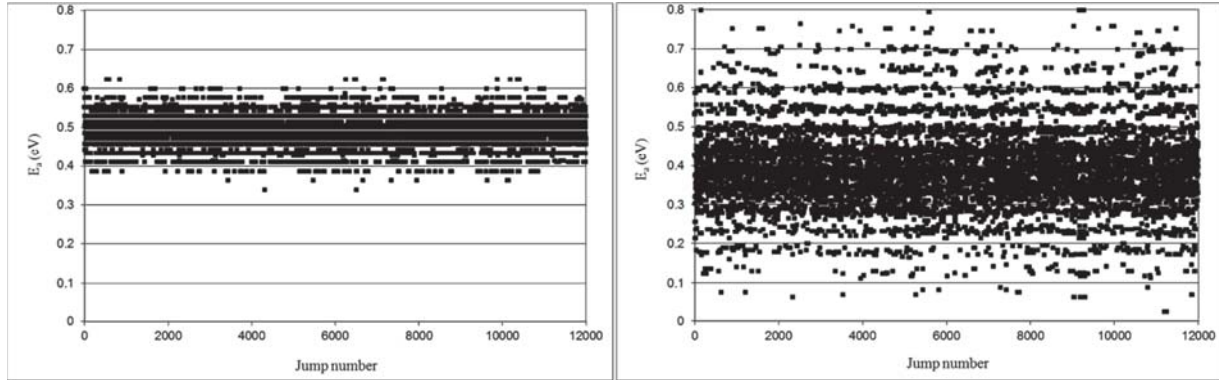
Fig. IV-12: Representation of activation energies, E_a, calculated during the course of AKMC simulations using our cohesive model and the FISE model (left figure) and using the cohesive model of Barbe and the cut bond model [BARBE2006] (right figure). Calculations performed in a system containing 4096 atoms ($8\times8\times16\ a_0^3$) including one vacancy in the Fe-45Ni-16Cr system

II-1-d   Treatment of dumbbells

In order to compare our PIM to DFT results performed in the Fe-10Ni-20Cr alloy, the SIA formation energies were calculated in a similar fashion as those determined in chapter III. We therefore calculated the reference chemical potentials using our PIM and following the same procedure as the one described in chapter III (section IV-1). In particular, the calculations were performed in the same SQS and at the same sites for comparison purpose. The reference chemical potentials thus obtained using the PIM for Fe, Ni and Cr, i.e. $\mu_{Fe}^{FeNiCr/PIM}$, $\mu_{Ni}^{FeNiCr/PIM}$ and $\mu_{Cr}^{FeNiCr/PIM}$ respectively, are listed in Tab. IV-12.

Alloying element	Fe	Ni	Cr
μ_A^0 (eV)	-4.4	-4.45	-4.2
$\mu_A^{FeNiCr/PIM}$ (eV)	-4.43	-4.56	-4.42
$\mu_A^{FeNiCr/PIM} - \mu_A^0$ (eV)	-0.03	-0.11	-0.22

Tab. IV-12: Reference chemical potentials calculated using our PIM, in the pure fcc system, μ_A^0, and in the Fe-10Ni-20Cr model alloy, $\mu_A^{FeNiCr/PIM}$.

As in the case of reference chemical potentials calculated using VASP, i.e. $\mu_{Fe}^{FeNiCr/DFT}$, $\mu_{Ni}^{FeNiCr/DFT}$ and $\mu_{Cr}^{FeNiCr/DFT}$ presented in Tab. III-2, all elements are more stable in the Fe-10Ni-

159   Chapter IV. Cohesive models and RIS modelling

20Cr reference state than in their respective pure phases ($\mu_A^{FeNiCr/PIM} - \mu_A^0 < 0$ for all elements A), thus indicating no tendencies for phase separation in the Fe-10Ni-20Cr target system.

As in the case of pair interactions between alloying elements and the vacancy, the binding energies presented in Fig. I-5 for the SIAs were set to reproduce the influence of the local environment on energy excess caused by the creation of the different types of SIAs using DFT. Among the 12 binding energies defined between the SIAs and their 1nn, we found values for 8 of them as summarised in Tab. III-8. Indeed, the energies were determined between the SIAs and their 1nn of Ni and Cr (in tensile and compressive sites) owing to the fact that they have a strong influence on the SIA formation energies. As no particular interactions were found between SIAs and their 1nn of Fe, the 4 remaining parameters were set to zero as can be seen in Tab. IV-13 and in Tab. IV-14.

$E^b_{A^{SIA}B^{1nnc}}$ (eV)			
A^{SIA} \ B^{1nnc}	Fe	Ni	Cr
Fe	0.00	-0.09	0.1
Ni	0.00	0.02	0.08
Cr	0.00	-0.1	-0.11

Tab. IV-13: Interaction parameter values between dumbbell atoms and their 1nn positioned in compressive sites, $E^b_{A^{SIA}B^{1nnc}}$, where A^{SIA} refers to elements A positioned in interstitial sites and B^{1nnc} refers to elements B 1nn to A and positioned in compressive sites.

$E^b_{A^{1nnt}SIA}$ (eV)	Fe	Ni	Cr
SIA	0.00	0.05	0.01

Tab. IV-14: Interaction parameter values between the SIA and their 1nn positioned in tensile sites, $E^b_{A^{1nnt}SIA}$, where SIA refer to dumbbells and A^{1nnc} refer to elements A 1nn to SIA and positioned in tensile sites .

The 6 remaining parameters, i.e. the binding energies between atoms in the dumbbell, $E^b_{A^{SIA}B^{SIA}}$, were deduced by adjusting them to reproduce the average value of formation energies listed in Tab. III-4. We also checked that the mean values of formation energies for the two possible mixed dumbbell configurations (A-B and B-A dumbbells) were as close as possible. After adjustment, comparison between our PIM and DFT data are presented in Tab. IV-16 and the

160   Chapter IV. Cohesive models and RIS modelling

associated parameters are presented in Tab. IV-15. It can be noted that the reference formation energy E_{Fe-Fe}^{f} defined in chapter I (section III-2-b) was set to 3.02 eV to reproduce DFT data.

$E_{A^{SIA}B^{SIA}}^{b}$ (eV)	Fe	Ni	Cr
Fe	0.00	-	-
Ni	-0.50	-0.90	-
Cr	0.10	-0.30	-0.05

Tab. IV-15: Interaction parameter values between dumbbell atoms, $E_{A^{SIA}B^{SIA}}^{b}$, where A^{SIA} (B^{SIA}) refers to elements A (B) positioned in interstitial sites.

Point defect formation energy (eV)	PIM	DFT
Fe-Fe	3.02	3.02
Ni-Ni	3.74	3.65
Cr-Cr	3.32	3.31
Fe-Ni	3.36	3.37
Fe-Cr	3.00	3.05
Ni-Cr	3.38	3.35

Tab. IV-16: Mean value of SIA formation energies calculated using the first parameterisation for our PIM presented from Tab. IV-13 to Tab. IV-15. These values are compared to DFT results obtained in Tab. III-4.

II-2   Prediction of our PIM

II-2-a   Properties of the dilute fcc Fe-Ni-Cr alloys

The prediction of our PIM for point defect and solute properties are compared to DFT results in Tab. IV-17 and in Tab. IV-18. It can be noted that, except for Cr-Cr interactions, all the binding energies are in reasonable agreement with DFT results obtained in the dilute fcc Ni matrix. However, the strong Fe-Fe and Fe-Cr repulsions couldn't be reproduced accurately in magnitude. In building our model, it was decided to put an emphasis in finding the best agreement for the binding energies in the dilute fcc Fe matrix since we want to model ternary alloys containing high proportions of Fe (Fe-10Ni-20Cr target system). In particular, we did not care too much that the worst agreement between our PIM predictions and DFT is for the binding energies between two Cr atoms in the pure Ni system, $E_{b}^{CrCr/Ni}$, because it is less important for the study of Fe-Ni-

Cr alloys near the composition of 316L SS. However, it should be borne in mind that, due to the lack of data, the AFM states are just supposed to be reliable for the calculation of binding energies in the γ-Fe system using DFT.

Regarding the migration barriers, although our PIM overestimates the migration energy in the pure fcc Ni system, the migration energies presented in Tab. IV-19 are in general in reasonable agreement with DFT data.

Binding energy (eV)	DFT	PIM
Fe-Fe	-0.16	-0.01
Cr-Cr	0.11	-0.10
Fe-Cr	-0.11	-0.02
V-Fe	-0.02	-0.02
V-Cr	-0.05	-0.04
V-V	0.02	0.02

Tab. IV-17: Binding energies calculated using our PIM in the pure fcc Ni system. These values are compared to DFT data available [TUCKER2008].

Binding energy (eV)	DFT	PIM
Ni-Ni	-0.01 to 0.11	-0.01
Cr-Cr	-0.1 to -0.01	-0.07
Ni-Cr	-0.01 to 0.05	0.01
V-Ni	0.02 to 0.09	0.01
V-Cr	-0.09 to 0.00	-0.01
V-V	0.04 to 0.18	0.05

Tab. IV-18: Binding energies calculated using our pair PIM in the pure fcc Fe system. These values are compared to DFT data available [KLAVER2012].

Formation energy (eV)	Pure fcc Fe	Pure fcc Ni
DFT	1.95	1.45
PIM	1.95	1.65

Tab. IV-19: Vacancy formation energies calculated using our PIM in the pure fcc systems. These values are compared to DFT data available [KLAVER2012, TUCKER2008].

The PIM limited to 1nn interactions presented above is a very simple cohesive model. As a result, relationships between energies can be found which can be summarized as follows:

> ➤ Ordering energies, Ω^{AB}, are proportional to the binding energies involving two alloying elements A in a solvent B, $E_b^{AA/B}$, as can be seen in Eq. IV-5 where z refers to the coordination number.

$$\Omega^{AB} = -zE_b^{AA/B} \qquad\qquad \text{Eq. IV-5}$$

> ➤ Binding energies involving two alloying elements A in a solvent B, $E_b^{AA/B}$, are equivalent to binding energies involving two alloying elements B in a solvent A, $E_b^{BB/A}$ (Eq. IV-6).

$$E_b^{AA/B} = E_b^{BB/A} \qquad\qquad \text{Eq. IV-6}$$

> ➤ The tendency of atoms A to segregate at a surface of vacancies in a solvent B, $E_{seg\_A<111>}^{B/V}$, is proportional to binding energies involving one vacancy and one solute atom A in a solvent B, $E_b^{VA/B}$, as shown in Eq. IV-7.

$$E_{seg\_A<111>}^{B/V} = 3E_b^{VA/B} \qquad\qquad \text{Eq. IV-7}$$

The choices we made when solving the linear systems used to deduce the interaction parameters have therefore some consequences which are listed below:

> ➤ The value assigned to the binding energies between two Ni atoms in the pure Fe system, $E_b^{NiNi/Fe}$ (–0.01 eV), imposes the values of the binding energy $E_b^{FeFe/Ni}$ (–0.01 eV) and the ordering energy Ω^{FeNi} (0.12 eV). Although DFT data available in dilute fcc Fe showed rather non-negligible attraction between pairs of Ni atoms of up to 0.1 eV at 1nn separation, a negative sign had to be assigned to this value in order to be in agreement with the repulsive interaction found for Fe-Fe pair in the pure Ni system but also with the ordering tendency observed in the fcc Fe-Ni alloys (formation of the FeNi$_3$ ordered phase up to about 600°C [CHUANG1986]).

> ➤ The value assigned to the binding energies between two Cr atoms in the pure fcc Fe system, $E_b^{CrCr/Fe}$ (–0.07 eV), is in agreement with the repulsion found using DFT.

However, it implies a strong ordering tendency between Fe and Cr atoms. In particular, this ordering tendency is stronger than the one obtained between Fe and Ni atoms.

➢ Values assigned to the binding energies between one vacancy and one Ni atom, $E_b^{VNi/Fe}$ (0.01 eV), and between one vacancy and one Cr atom, $E_b^{VCr/Fe}$ (−0.01 eV), impose the segregation behaviour at a surface which can be considered as a collection of vacancies. Indeed, Ni atoms will thus tend to deplete ($E_{seg\_Ni<111>}^{Fe/V}$ = −0.03 eV) while Cr atoms will tend to segregate ($E_{seg\_Cr<111>}^{Fe/V}$ = 0.03 eV) at the surface.

II-2-b   Substitutional formation energies in the Fe-10Ni-20Cr alloy

In Fig. IV-13 and in Fig. IV-14 we compare substitutional formation energies calculated using DFT to substitutional formation energies calculated using our PIM. The reference chemical potentials presented in Tab. IV-12 were used for comparison purpose. This results show clearly that we obtain the same evolution for the substitutional formation energies. Indeed, the same evolution as for DFT calculations was found with the number of 1nn Cr as well as the number of 1nn Fe presented from Fig. III-9 to Fig. III-13. Similarly, no clear trends are observed for substitutional formation energies involving one Fe and one Ni atom (Fig. III-9) and the number of 1nn Ni does not appear to play a significant role in substitutional formation energy values.
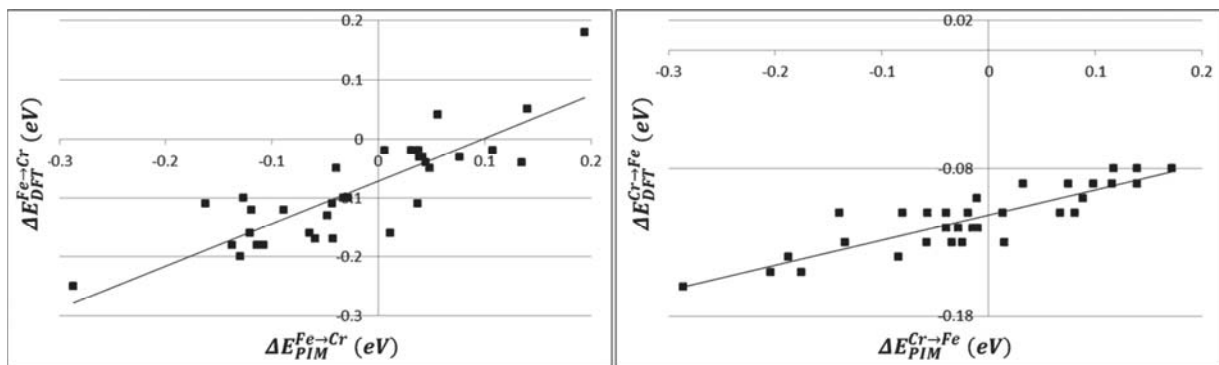
Fig. IV-13: Cr➔Fe substitutional formation energies using DFT, $\Delta E_{DFT}^{Cr\to Fe}$, as a function of the Cr➔Fe substitutional formation energies using our PIM, $\Delta E_{PIM}^{Cr\to Fe}$ (right figure). Fe➔Cr substitutional formation energies using DFT, $\Delta E_{DFT}^{Fe\to Cr}$, as a function of the Fe➔Cr substitutional formation energies using our PIM, $\Delta E_{PIM}^{Fe\to Cr}$ (left figure).
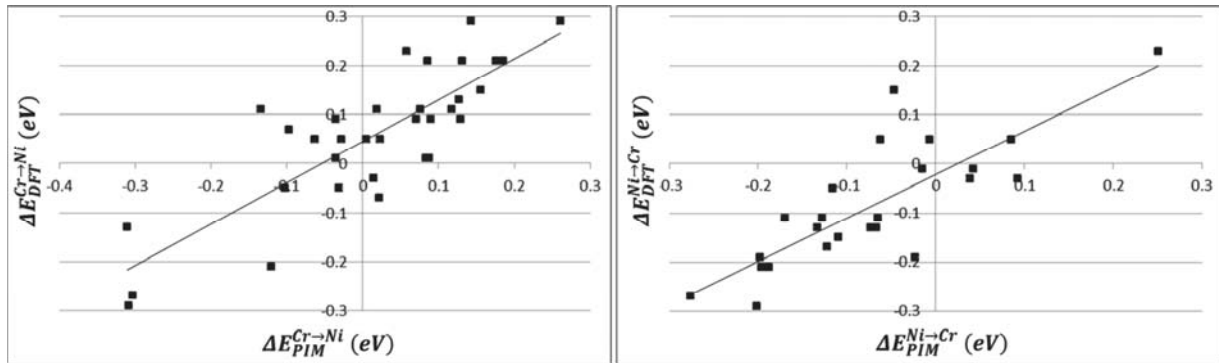
Fig. IV-14: Ni➔Cr substitutional formation energies using DFT, $\Delta E_{DFT}^{Ni \to Cr}$, as a function of the Ni➔Cr substitutional formation energies using our PIM, $\Delta E_{PIM}^{Ni \to Cr}$ (right figure). Cr➔Ni substitutional formation energies using DFT, $\Delta E_{DFT}^{Cr \to Ni}$, as a function of the Cr➔Ni substitutional formation energies using our PIM, $\Delta E_{PIM}^{Cr \to Ni}$ (left figure).

II-2-c   Correlation factors

As seen previously, the cohesive model was adjusted to reproduce as accurately as possible the high temperature diffusion experiments performed in Ni-Cr and Fe-Ni binaries as well as in Fe-Ni-Cr ternaries close to the Fe-10Ni-20Cr target composition. However, tracer diffusion measurements were performed at temperatures at which activation energies do not have a significant impact on diffusion coefficients (beyond 1000 K). Activation energies have however a significant impact at intermediate temperatures and drive the evolution of the diffusion coefficient at low temperatures. In particular, their relative values drive the exponential divergence between each element, with decreasing temperatures, and correlation effects are expected to increase.

In order to analyse the correlation effects occurring at lower temperatures, in Fig. IV-15 we present for the vacancy and the solute elements the correlation factors as the function of temperature in the $Fe_{39}Ni_{45}Cr_{16}$ alloy to compare with Barbe cutbond's model [BARBE2006] and in our model Fe-10Ni-20Cr alloy. AKMC simulations were performed in a system containing 4096 atoms including one vacancy and by making $2.0 \cdot 10^6$ measurements of at least 10 jumps per atom of each solute. At high temperatures, the correlation factors are close to 1 which indicates that correlation effects are small, i.e. that activation energies are small relative to thermal fluctuations, thus implying more or less a diffusion of solute elements by random walks. The correlation factors of Cr atoms have nevertheless the smallest values (about 0.6 in both cases),

165   Chapter IV. Cohesive models and RIS modelling

which is consistent with Cr atoms being the fastest diffusion elements, thus involving a preferential exchange between the vacancy and Cr atoms. The same behaviour can be observed for both ternary alloys which seem to indicate that migration properties are little affected by the alloy composition. The results found in the Fe-45Ni-13Cr can be compared to the calculation performed by Barbe [BARBE2006] using its model in the same system and for the same computational conditions. Results are found to be very similar especially at temperatures beyond 700 K. Barbe found however smaller correlation factor values at lower temperatures and our results is a closer match to calculations performed using a mean field approach. These results are consistent with the previous observations made in Fig. IV-12, i.e. that there is not enough variation in the SP energies. It can be mentioned that in its model, Barbe adjusted the slope of f_V factor to reproduce the effective migration energy of the vacancy at low temperature provided by Dimitrov [DIMITROV1982, DIMITROV1988]. Using our model, the effective migration energy is however underestimated.
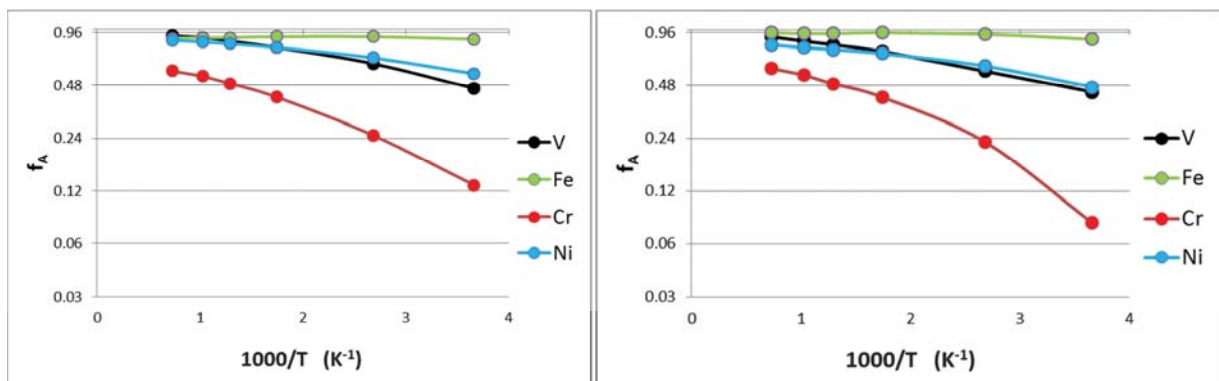
Fig. IV-15: Correlation coefficients of the vacancy and solute atoms, f_A (A refers to the element type), as a function of the temperature in the Fe-45Ni-13Cr system (left figure). Correlation coefficients of the vacancy and solute atoms, f_A, as a function of the temperature in the Fe-10Ni-20Cr system (right figure). Calculations performed at 273, 373, 573, 773, 973 and 1373 K in a system containing 4096 atoms ($8\times8\times16$ a_0^3) including one vacancy.

II-2-d   TNES modelling in the Fe-10Ni-20Cr alloy

To model TNES, we only need to consider vacancy mediated diffusion since this kind of segregation only involves vacancies in overconcentration. Thus, the set of 10 interaction parameters presented in Tab. IV-10 and in Tab. IV-11 between elements in perfect lattice sites (solute atoms and vacancy) has been used to perform AKMC simulations of TNES. In order to

166   Chapter IV. Cohesive models and RIS modelling

simulate TNES conditions, we introduced a vacancy in the matrix and let the system evolve. As mentioned previously, we derived a PIM based solely on the vacancy formation energy obtained using DFT calculations and the VASP code. As no data (DFT or experimental ones) for the interactions between the elements and the GB are available, the GB is assumed to behave as a surface, therefore we chose for the GB-solute interaction energies the surface-solute segregation energies. The values obtained from Eq. I-45 in the pure Fe system are −0.03 eV (repulsion) for ε_{GB-Cr} and 0.03 eV (binding) for ε_{GB-Ni}, which are not in agreement with the experimental results of TNES which show that Cr segregates at GB and Ni either depletes a little or does not do anything. The values for ε_{GB-Fe} are always set to zero in what follows and can be viewed as the reference energy for GB-solute interactions. From Fig. IV-16 to Fig. IV-18, we present a simulation performed in the Fe-10Ni-20Cr target system at 500 K which can be related to TNES, i.e. without irradiation. Note that however, because of the size of the box, the concentration of vacancies ($1.25 \cdot 10^{-5}$ at %) is much larger than the equilibrium concentration predicted by our model ($1.45 \cdot 10^{-8}$ at %). The evolution of solute concentration at the GB induced by the addition of one vacancy in a system containing 80,000 atoms ($20 \times 20 \times 50\ a_0^3$) as a function of AKMC time is presented along with MMC calculations. GB interaction energies were assigned to all lattice sites lying in the 5 atomic planes between the dashed lines presented in the figures. The MMC and AKMC profiles are found to be consistent with the GB interaction energies chosen since we observe a depletion of Cr atoms ($\varepsilon_{GB-Cr} = -0.03$ eV) and segregation of Ni atoms ($\varepsilon_{GB-Ni} = 0.03$ eV) at the GB, and therefore, as expected, in disagreement with TNES profiles. Although no interaction energies are considered between the GB and Fe atoms, Fe atoms are found to deplete at the GB using MMC owing to the fact that Ni atoms segregate more at the GB than Cr atoms deplete.
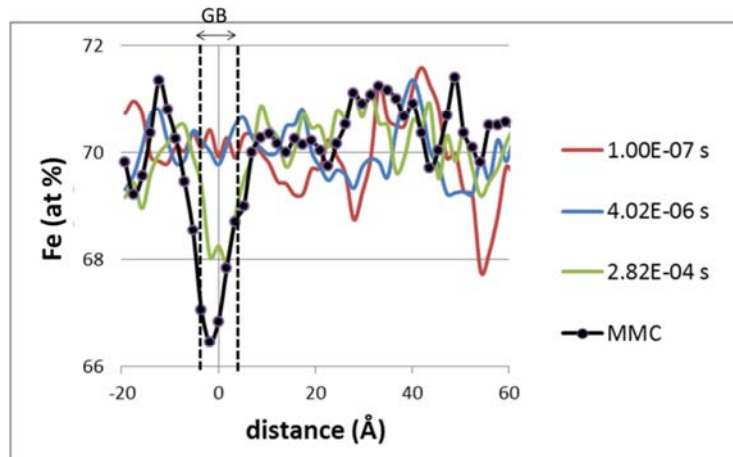
Fig. IV-16: TNES profiles of AKMC (coloured lines) and MMC (black line) simulations obtained for Fe atoms as a function of the distance from the GB at 500K in the fcc Fe-10Ni-20Cr alloy. Calculations performed in a system containing 80,000 atoms ($20{\times}20{\times}50\ a_0^3$).
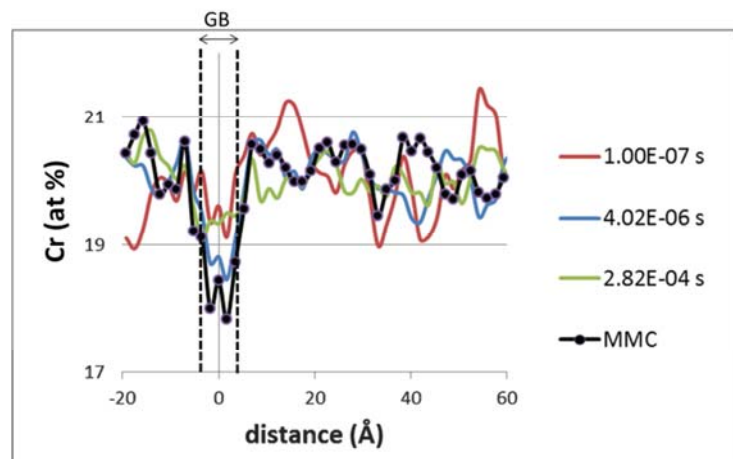
Fig. IV-17: TNES profiles of AKMC (coloured lines) and MMC (black line) simulations obtained for Cr atoms as a function of the distance from the GB at 500K in the fcc Fe-10Ni-20Cr alloy. Calculations performed in a system containing 80,000 atoms ($20{\times}20{\times}50\ a_0^3$).

168   Chapter IV. Cohesive models and RIS modelling
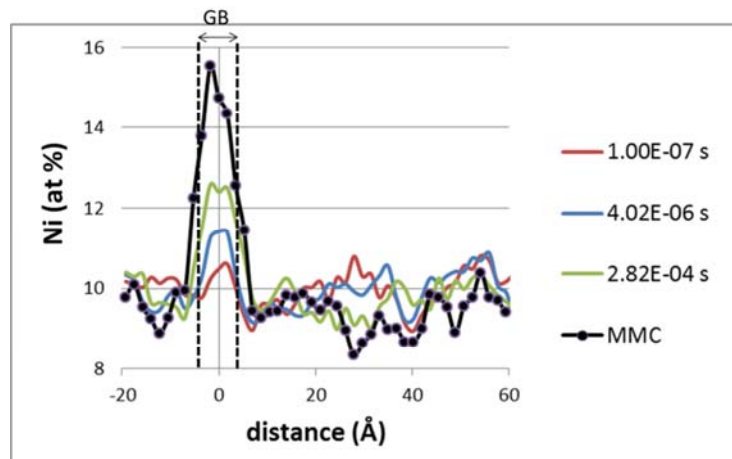
Fig. IV-18: TNES profiles of AKMC (coloured lines) and MMC (black line) simulations obtained for Ni atoms as a function of the distance from the GB at 500K in the fcc Fe-10Ni-20Cr alloy. Calculations performed in a system containing 80,000 atoms ($20 \times 20 \times 50$ a_0^3).

As the segregation profiles obtained previously are, as expected, in disagreement with the experimental trends but in agreement with the segregation energies, we then chose segregation energies in agreement with the experimental results for TNES, i.e. a value of 0.03 eV (binding) for ε_{GB-Cr} and -0.015 eV (repulsion) for ε_{GB-Ni}. AKMC simulations thus obtained are presented in Fig. IV-19 and show that the segregation profiles are now in agreement with the experimental data.
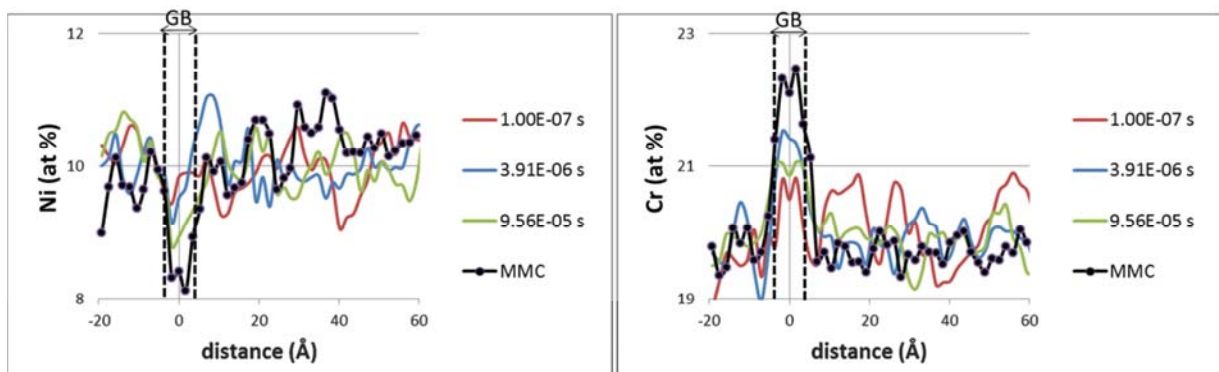
Fig. IV-19: TNES profiles of AKMC (coloured lines) and MMC (black line) simulations obtained for Ni atoms (left figure) and Cr atoms (right figure) as a function of the distance from the GB at 500K in the fcc Fe-10Ni-20Cr alloy. Calculations performed in a system containing 80,000 atoms ($20 \times 20 \times 50$ a_0^3).

169   Chapter IV. Cohesive models and RIS modelling

Furthermore, if we use a different model for the cohesive model and the activation barriers, i.e. if we use Barbe's cut-bond model, the trends observed are identical, indicating that it is indeed the solute-GB segregation energies which drive TNES (Fig. IV-20). The main difference between the two models (FISE and cut-bond) is the enrichment factor which is completely different.
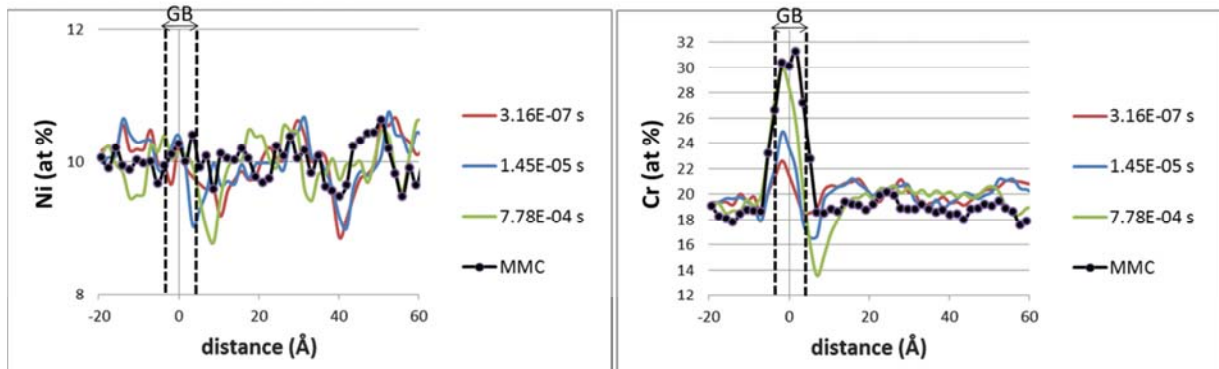
Fig. IV-20: TNES profiles of AKMC (coloured lines) and MMC (black line) simulations obtained for Ni atoms (left figure) and Cr atoms (right figure) as a function of the distance from the GB at 500K in the fcc Fe-10Ni-20Cr alloy using Barbe's cut-bond model. Calculations performed in a system containing 80,000 atoms ($20\times20\times50\ a_0^3$).

Finally, when the solute-GB segregation energy is set to 0 as it is the case for ε_{GB-Fe} in the previous simulations, the two models (FISE and cut-bond model) behave differently as can be seen in Fig. IV-21. The differences of MMC profiles obtained between our PIM and Barbe's model are consistent with the Legrand-Tréglia model [TREGLIA1988]. Indeed, this model predicts that a positive ordering energy promotes the segregation of elements with the highest content. When using Barbe's model, $\Omega^{FeCr} = 0$ eV and $\Omega^{NiCr} = 0.84$ eV, thus involving a strong segregation of Cr atoms associated with a strong depletion of Fe atoms. By contrast, when using our PIM, $\Omega^{FeCr} = 0.84$ eV and $\Omega^{NiCr} = 1.2$ eV, thus being in agreement with the less important depletion of Fe atoms observed in Fig. IV-21 compared to Barbe's model.

170   Chapter IV. Cohesive models and RIS modelling
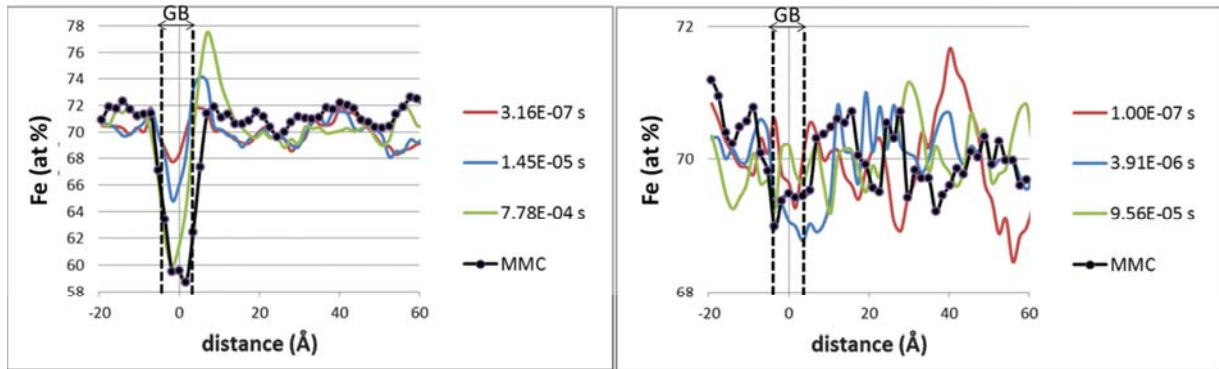
Fig. IV-21: TNES profiles of AKMC (coloured lines) and MMC (black line) simulations obtained for Fe atoms as a function of the distance from the GB using Barbe's cut-bond model (left figure) and using our model (right figure) at 500K in the fcc Fe-10Ni-20Cr alloy. Calculations performed in a system containing 80,000 atoms ($20 \times 20 \times 50\ a_0^3$).

II-2-e   RIS modelling in the Fe-10Ni-20Cr alloy

As irradiation creates Frenkel pairs, modelling of RIS requires the use of both vacancy and dumbbell mediated diffusion. Thus, the complete set of interaction parameters, i.e. the values presented from Tab. IV-13 to Tab. IV-15 for the dumbbell interactions along with those previously considered to simulate TNES (Tab. IV-10 and Tab. IV-11) have been used to perform AKMC simulations of RIS. For these simulations, the model also requires attempt frequencies and E_{a_0} migration energies for the SIA atoms (ν^{SIA} and $E_{a_0}^{SIA}$ respectively). In a first stage, we assumed that these parameters do not depend on the migrating atom. The values considered are listed in Tab. IV-20.

	Fe	Ni	Cr
$E_{a_0}^{SIA}$ (eV)	0.3	0.3	0.3
ν^{SIA} (s^{-1})	$2.0 \cdot 10^{16}$	$2.0 \cdot 10^{16}$	$2.0 \cdot 10^{16}$

Tab. IV-20: Attempt frequencies, ν^{SIA}, and migration energies $E_{a_0}^{SIA}$ values for SIA in our FISE model.

In these simulations, we used the same GB-solute interactions as those used to obtain the TNES profiles in agreement with experiments. Furthermore, interaction between the GB and the point defects, ε_{GB-V} and ε_{GB-SIA}, are assumed to be equal. These interactions are listed in Tab. IV-21.

171   Chapter IV. Cohesive models and RIS modelling

	GB-element interactions (eV)
ε_{GB-Fe}	0.00
ε_{GB-Ni}	-0.015
ε_{GB-Cr}	0.03
ε_{GB-V}	0.3
ε_{GB-SIA}	0.3

Tab. IV-21: Interaction energies between the GB sites and the vacancy (V), the different dumbbell types (SIA) and the solute atoms.

In these electron irradiation simulations, the Frenkel pairs were not correlated, i.e. the vacancy and its corresponding SIA were introduced randomly in the simulation box. The recombination between the vacancies and the SIAs was set to occur at 2nn separation.

In all the following RIS simulations, we considered the same set of pair interactions for the vacancy mediated diffusion, i.e. the one previously considered to simulate TNES (Tab. IV-10 and Tab. IV-11). The first parameterisation we tried for SIAs is based on the DFT results and more precisely on the relationships we obtained between the SIA formation energies and the local environment. Indeed, as previously mentioned in section II-1-d, the binding energies in Tab. IV-13 and in Tab. IV-14 were obtained as simple means of the parameter values obtained with various linear regressions summarized in Table III-7. Furthermore, the binding energies in Tab. IV-15 were adjusted to reproduce the average value of SIA formation energies. Fig. IV-22 represents the solute profile after an electron irradiation done at 0.63 dpa and 723K, with a flux of $2 \cdot 10^{-3}$ dpa/s using this first parameterisation. The value chosen for the flux was set so as to have only one Frenkel pair at the time in the simulation box. A depletion of Cr and Ni atoms is observed at the grain boundary region. This result is however not in agreement with experiment for which Ni enrichment is expected. In particular, the comparison with the results obtained previously for TNES modelled with the same simulation conditions presented in the same figure clearly shows that SIA mediated transport induces the Ni depletion observed in the RIS simulation which disagrees with experiments. This result could be expected as our DFT calculations presented in chapter III clearly show that both Cr and Ni atoms behave as oversized atoms. As the parameterisation used for this simulation reflects these DFT results, we found that the solute atoms are generally repelled from the compressive sites of ⟨100⟩ dumbbells, thus resulting in depletion of Cr and Ni atoms at the GB.

172   Chapter IV. Cohesive models and RIS modelling
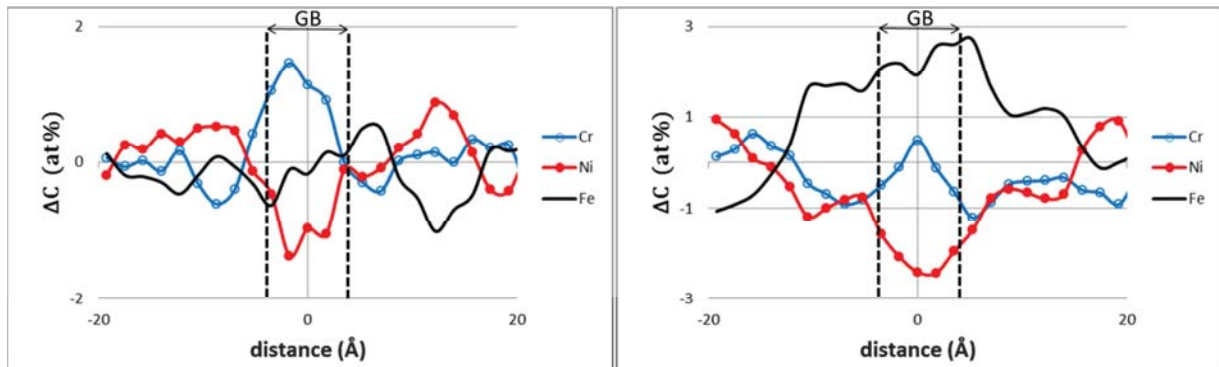
Fig. IV-22: AKMC RIS profiles (right figure) obtained using the first parameterisation, after an electron irradiation ($2 \cdot 10^{-3}$ dpa/s) at 0.63 dpa and 723 K for Fe (black line), Ni (blue line) and Cr (red line) atoms in the fcc Fe-10Ni-20Cr alloy. AKMC TNES profiles (left figure) for Fe (black line), Ni (blue line) and Cr (red line) atoms at 723K in the fcc Fe-10Ni-20Cr alloy. We consider the variation of composition, ΔC, as a function of the distance from the GB. Calculations performed in a system containing 80000 atoms ($20 \times 20 \times 50\ a_0^3$).

The second parameterisation is to test the influence of binding energies between dumbbell atoms and their 1nn (Tab. IV-13 and Tab. IV-14) on segregation behaviour. To this end, we considered a set of parameters also based on the DFT but inducing smaller variation with the local environment. We thus considered a parameterisation in which all the positive binding energies displayed in Tab. IV-13 and in Tab. IV-14 were set to the relatively small values of 0.02 eV while all negative values were set to −0.02 eV. The 6 remaining $E^b_{A^{SIA}B^{SIA}}$ parameters were deduced as done in section II-1-d, i.e. by adjusting them to reproduce the SIA formation energies. This second parameterisation is reported in Tab. IV-22 and the corresponding SIA formation energies are presented in Tab. IV-23.

173   Chapter IV. Cohesive models and RIS modelling

$E^b_{A^{SIA}B^{1nnc}}$ (eV)			
A^{SIA} \ B^{1nnc}	Fe	Ni	Cr
Fe	0.00	-0.02	0.02
Ni	0.00	0.02	0.02
Cr	0.00	-0.02	-0.02

$E^b_{A^{1nnt}SIA}$ (eV)	Fe	Ni	Cr
SIA	0.00	0.02	0.02

$E^b_{A^{SIA}B^{SIA}}$ (eV)	Fe	Ni	Cr
Fe	0.00	-	-
Ni	-0.50	-0.90	-
Cr	-0.05	-0.30	-0.30

Tab. IV-22: Full set of binding energies used for the second parameterisation. The first two tables refer to values obtained by setting all the positive (negative) binding energies displayed in Tab. IV-13 and in Tab. IV-14 to 0.02 eV (−0.02 eV). The third table refers to values adjusted to reproduce SIA formation energies presented in Tab. IV-23.

Point defect formation energy (eV)	PIM	DFT
Fe-Fe	3.02	3.02
Ni-Ni	3.76	3.65
Cr-Cr	3.41	3.31
Fe-Ni	3.33	3.37
Fe-Cr	3.13	3.05
Ni-Cr	3.32	3.35

Tab. IV-23: Mean value of SIA formation energies calculated using the second parameterisation presented in Tab. IV-22 and compared to DFT results obtained in Tab. III-4.

Fig. IV-23 represents the solute profile after an electron irradiation done at 0.63 dpa and 723K, with a flux of $2 \cdot 10^{-3}$ dpa/s using the second parameterisation. The same conclusions as those done when used the first parameterisation can be drawn. The depletion of Ni and Cr atoms are even more pronounced when using the second parameterisation.
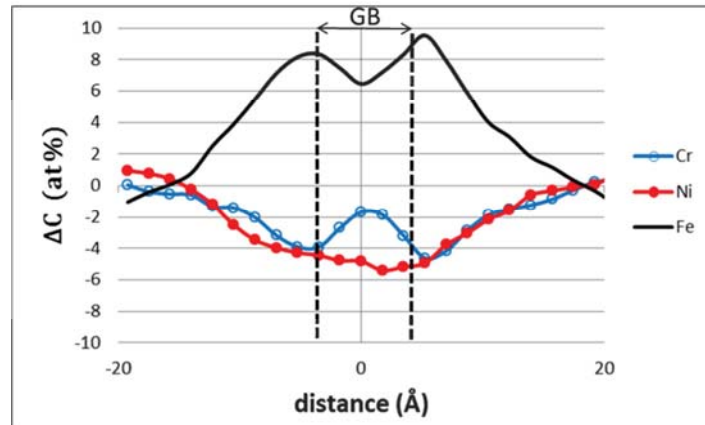
Fig. IV-23: AKMC RIS profiles obtained using the second parameterisation, after an electron irradiation ($2 \cdot 10^{-3}$ dpa/s) at 0.63 dpa and 723 K for Fe (black line), Ni (blue line) and Cr (red line) atoms in the fcc Fe-10Ni-20Cr alloy. We consider the variation of composition, ΔC, as a function of the distance from the GB. Calculations performed in a system containing 80,000 atoms ($20 \times 20 \times 50\ a_0^3$).

Following the same procedure as used in the second parameterisation, i.e. changing the binding energies between dumbbell atoms and their 1nn while capturing the DFT trends, we performed a systematic study by playing around with these binding energies as well as with the diffusion coefficients, but without ever being able to reproduce the experiments trends. In a last step, we then assessed the role of the cohesive model and more precisely the interaction parameters by setting all 18 parameters related to the SIAs to 0 (Tab. IV-24) and playing around with the diffusion coefficients only, i.e. the attempt frequency and the migration barrier. It can be noted that the SIA formation energies are not in agreement with DFT data anymore (Tab. IV-25) owing to the fact that $E_{A^{SIA}B^{SIA}}^{b}$ energies were not adjusted this time.

175   Chapter IV. Cohesive models and RIS modelling

$E^b_{A^{SIA}B^{SIA}}$ (eV)	Fe	Ni	Cr
Fe	0.00	-	-
Ni	0.00	0.00	-
Cr	0.00	0.00	0.00

$E^b_{A^{SIA}B^{1nnc}}$ (eV)			
A^{SIA} \ B^{1nnc}	Fe	Ni	Cr
Fe	0.00	0.00	0.00
Ni	0.00	0.00	0.00
Cr	0.00	0.00	0.00

$E^b_{A^{1nnt}SIA}$ (eV)	Fe	Ni	Cr
SIA	0.00	0.00	0.00

Tab. IV-24: Full set of binding energies used for the third parameterisation. All binding energies were set to 0.

Point defect formation energy (eV)	PIM	DFT
Fe-Fe	3.02	3.02
Ni-Ni	2.89	3.65
Cr-Cr	2.99	3.31
Fe-Ni	2.89	3.37
Fe-Cr	2.98	3.05
Ni-Cr	2.98	3.35

Tab. IV-25: Mean value of SIA formation energies calculated using the third parameterisation presented in Tab. IV-24 and compared to DFT results obtained in Tab. III-4.

When using the third parameterisation, the migration energies of Ni atoms in interstitial sites seem to rule the segregation behaviour. Indeed, when choosing $E^{SIA}_{a_0}$ in order to have a higher migration probability for Ni compared to Cr and Fe as previously done in rate theory models of the literature [KINOSHITA1996], we were able to obtain results in agreement with RIS experiments in 316L steels, i.e. Ni enrichment and Cr depletion. The evolution of segregation profiles when decreasing gradually $E^{SIA}_{a_0}$ for Ni atoms in interstitial sites (relative to the value of 0.3 eV presented in Tab. IV-20) is shown in Fig. IV-24 and in Fig. IV-25. The inversion of the segregation tendency of Cr atoms is observed compared to the simulation presented in Fig. IV-24. The preferential transport of Ni compared to Cr and Fe seems thus to be sufficient to have Ni segregation in agreement with experimental results.

The results obtained for the first two parameterisations (based on DFT) show that DFT seem a priori in disagreement with what one can expect to obtain agreement with RIS experiments. Such an observation has been reported in the Ni-Cr system by Choudhury et al. and Barnard et al. using a rate theory model [CHOUDHURY2011, BARNARD2012], in a system for which the magnetism of Ni is well reproduced and less complicated than Fe-Ni-Cr AFM1 system. In particular, when directly using DFT data available in the pure fcc Ni [TUCKER2008] as input parameters, Barnard could not reproduce the RIS experiments and had to adjust the pair interaction between dumbbells and Cr atoms to obtain an accurate model. When using our PIM, the first two parameterisations presented above which were designed to reproduce the SIA formation energies as well as the influence of the local environment (at least quantitatively), were not able to reproduce RIS experiments. Furthermore, whatever the parameter used, Ni enrichment was never obtained when adjusting parameters on the SIA formation energies obtained using DFT. This result is confirmed by the occurrence of Ni enrichment using the third parameterisation in which no adjustment on SIA formation energies is considered, thus proving their strong influence on segregation behaviour. Furthermore, the higher migration probability for Ni compared to Cr and Fe was found to be one of the controlling criteria to obtain the desired segregation when using the third parameterisation.
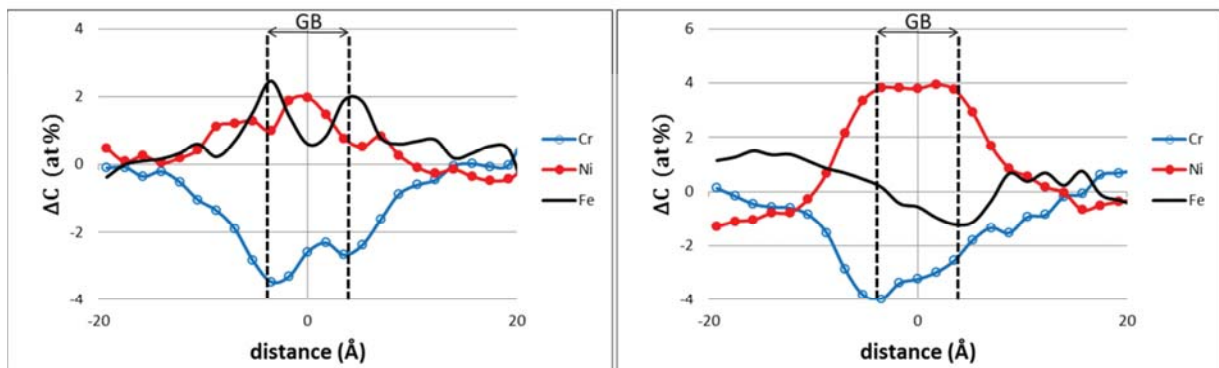
Fig. IV-24: AKMC RIS profiles obtained using the third parameterisation, after an electron irradiation ($2 \cdot 10^{-3}$ dpa/s) at 0.63 dpa and 723 K for Fe (black line), Ni (red line) and Cr (blue line) atoms in the fcc Fe-10Ni-20Cr alloy. We consider the variation of composition, ΔC, as a function of the distance from the GB using for the Ni atoms in interstitial sites $E_{a_0}^{SIA} = 0.25$ (left figure) and $E_{a_0}^{SIA} = 0.20$ (right figure). Calculations performed in a system containing 80000 atoms ($20 \times 20 \times 50$ a_0^3).

177   Chapter IV. Cohesive models and RIS modelling
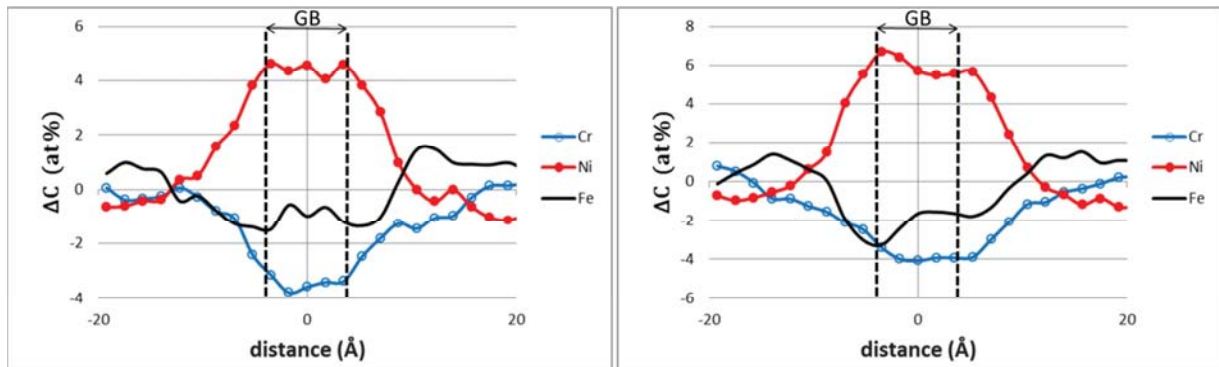
Fig. IV-25: AKMC RIS profiles obtained using the third parameterisation, after an electron irradiation ($2 \cdot 10^{-3}$ dpa/s) at 0.63 dpa for Fe (black line), Ni (red line) and Cr (blue line) atoms in the fcc Fe-10Ni-20Cr alloy. We consider the variation of composition, ΔC, as a function of the distance from the GB at 500 K (left figure) and 723 K (right figure) using for the Ni atoms in interstitial sites $E_{a_0}^{SIA} = 0.15$. Calculations performed in a system containing 80,000 atoms ($20 \times 20 \times 50 \ a_0^3$).

II-3   Conclusions

Our PIM provides a reasonable agreement with important properties for RIS modelling which can be summarized as follows:

> ➢ Binding energies calculated in dilute systems are in general in good agreement with DFT data. However, a few energies could not reproduce DFT data owing to the simplicity of the PIM. In particular, the binding energies between two Cr atoms in the pure Ni system, $E_b^{CrCr/Ni}$, could not be in agreement without having a strong impact on agreements obtained for the other binding energies. It has therefore been chosen to maintain this disagreement for $E_b^{CrCr/Ni}$, all the more so because this energy is less important for the study of Fe-Ni-Cr alloys near the composition of 316L SS. Furthermore, $E_b^{FeFe/Ni}$ and $E_b^{NiNi/Fe}$ binding energies which have the same values in the framework of the PIM, could not reproduce the non-negligible attraction between pairs of Ni atoms in pure γ-Fe and the strong repulsion between pairs of Fe atoms in pure γ-Ni both predicted by the DFT. It has therefore been chosen to consider weak repulsions for these binding energies in order to obtain an agreement with DFT data performed in the pure γ-Ni system but also with the occurrence of order in Fe-Ni [CHUANG1986].

178   Chapter IV. Cohesive models and RIS modelling

➢ Our PIM was found to be in good agreement with DFT calculations performed in the Fe-10Ni-20Cr target system presented in chapter III. Indeed, impact of the local environment on both substitutional formation and point defect formation energies is systematically qualitatively reproduced. The magnitude of these variations is however not always reproduced accurately.

➢ We reproduced the evolution of high temperature diffusion experiments in Fe-Ni and Cr-Ni binary alloys but it was impossible to adjust the diffusion experiment using a unique set of frequencies owing to the fact that the energy range obtained for the migration energies using the FISE model was too small. Given the fitting constraints, we showed that our model, which is only based on interaction parameters between elements positioned at perfect lattice sites, cannot capture alone both thermodynamic and kinetic aspects of Fe-Ni-Cr alloys. Atomistic models thus seem to require the partitioning of interactions between alloying elements and the vacancy positioned at the SP.

Our PIM was used to perform TNES and RIS simulations using AKMC. The most important results can be summarized as follows:

➢ TNES profiles of AKMC simulations are driven by the solute-GB interactions. We chose segregation energies in quantitative agreement with the experimental results for TNES, i.e. a value of 0.03 eV (binding) for ε_{GB-Cr} and -0.015 eV (repulsion) for ε_{GB-Ni}.

➢ RIS profiles obtained using parameterisations based on DFT data were found to be in strong disagreement with experiments. This result seems to indicate that our DFT data are not, at the moment, reliable for the study of RIS in the Fe-Ni-Cr system. In particular, the reproduction of SIA formation energies predicted by DFT with our model was found to prevent the occurrence of Ni segregation at the GB. A model, not based on DFT data, assuming no dependence of the SIA formation energies on the local environment, and in addition, in which Ni atoms have a higher migration probability (e.g. lower migration energy) than Cr and Fe atoms was found to be capable of reproducing the correct trends of solute enrichment at GBs.

179   Chapter IV. Cohesive models and RIS modelling

III   Conclusions and perspectives

We have tested a set of EAM potentials (provided by Bonny [BONNY]) dedicated to model the Fe-Ni-Cr system. These studies show the difficulty of building a relevant potential to investigate the RIS in Fe-Ni-Cr systems. In particular, MMC simulations using these potentials showed that the solid solution is not stable at the temperature range encountered in PWR reactors. Indeed, we observed for each potential strong tendency for either phase ordering or phase precipitation in the Fe-10Ni-20Cr target alloy, thus allowing for the appearance of the solid solution usually at too high temperatures. Moreover, a complete agreement with available DFT interaction energies in the pure fcc phase was also difficult to obtain. It can however be mentioned that DFT results obtained on these systems have to be used with care, as our work along with others [KLAVER2012] has shown DFT's limits in the ability to find a relevant reference state, thus limiting its predictive capabilities.

As none of the EAM potentials seemed appropriate for our purpose (the modelling of RIS) a cohesive model using pair interactions limited to 1nn separations at perfect lattice positions was built. Pair interactions were adjusted to reproduce DFT data in reasonable agreement. Adjustment on high temperature experiments were however not fully achieved, thus showing that atomistic models for the migration energies seem necessary to take into account the local environment at the SP position. We used our PIM to model TNES and found that, according to our model, it is the solute-GB segregation energies which drive TNES. We also found that the reproduction by our PIM of the SIA formation energies predicted by DFT in Fe-Ni-Cr alloys was found to be incompatible with the modelling of RIS. Agreement with RIS experiments was however obtained with SIA interactions which do not incorporate the DFT trends by assuming no interactions of the SIAs with solute atoms and by imposing higher migration probability for Ni atoms compared to Cr and Fe atoms.

However, before drawing hasty conclusions about the relevance of DFT data performed in the AFM1 reference state, it may be mentioned again that our PIM suffers from many weaknesses. Indeed, this PIM contains a total of only 30 pair interactions to model RIS and to capture chemical and magnetic properties of Fe-Ni-Cr alloys. These interactions are only taken into

---

account between 1nn whereas long range interactions can occur in such ternary systems [TUCKER2008]. Furthermore, interactions taken into account are only those of a collection of atoms positioned in a perfect lattice, thus considering implicitly the atomic relaxations via the DFT calculations. Finally both thermodynamic and kinetic data are adjusted using a unique data set, thus inducing strong fitting constraints. In particular, the use of the FISE model makes difficult the change of interaction parameters for the vacancy mediated diffusion because too many data are fitted. This constraint prevent from playing on the preferential transport of elements either via the inverse Kirkendall mechanism or via the drag mechanism, thus limiting the possibility to make some adjustments to fit with RIS experiments.

For all these reasons, further analysis should be conducted before to state that DFT data in the fcc AFM1 reference state are not reliable. In particular, a more accurate FISE model, i.e. which taken into account of SP environment, seems to be the minimum level of improvement to achieve in order to obtain better results. The cut bond model (instead of the FISE model used in this work) may also be used to achieve the partitioning between thermodynamic and kinetic information as it has been done previously by Barbe [BARBE2006], thus removing these strong fitting constraints. Indeed, in this case, the high temperature diffusion experiments could be adjusted much more easily. We could also adjust our data set on the effective migration energies of both the vacancy and the dumbbell obtained by Dimitrov [DIMITROV1982, DIMITROV1988], the adjustment of which has not been done in this work. Another possibility should be to perform many migration energy calculations using DFT in the AFM1 state, in order to find a relationship between the migration barriers and the local environment.

In the case where these further analyses would not lead to reliable results, we may call into question the reliability of the DFT data presented in this work for the RIS modelling. Further analysis would be to investigate more in detail both paramagnetic phase and non collinear configurations using VASP or another code. In particular, we need to determine if it is possible to retain these phases when relaxing the system. The re-investigation of effects of the functionals as well as the DFT simulation parameters may for instance be worth investigating. Another possible alternative should be to model the paramagnetic phase using CPA. Indeed, very promising results were obtained by Delcezg for the vacancy formation energy in concentrated and paramagnetic Fe-Ni-Cr systems [DELCEZG2012].

181   Chapter IV. Cohesive models and RIS modelling

182 Chapter IV. Cohesive models and RIS modelling

General conclusions and perspectives

The problem of segregation of alloy components is of considerable practical interest as grain boundary segregation of impurities can lead to temper embrittlement and thus intergranular fracture and segregation-induced precipitation can significantly change the alloy characteristics. As solute redistribution in a metallic alloy has to take place with the help of point defect migration, it is of no surprise that under irradiation, where a flux of point defects is generated through the material such segregations are observed. In the austenitic steels used, for instance, in the nuclear reactors, radiation induced segregation leads to a depletion of Cr atoms at grain boundaries, making these parts of the material more susceptible to corrosion and more precisely stress corrosion. Since its discovery forty years ago, RIS has generated a large number of experimental as well as theoretical works to understand the complicated connections existing between point defects and solute atom fluxes and the chain of events which leads to solute segregation. Most of the theoretical work was done at a continuum level using diffusion or rate equations that describe the fate of solute and point defect concentrations near sinks. In this description, the most important parameters are the diffusivities or transport coefficients which are not accurately known and depend very much on the alloy concentration. Diffusion being an atomic scale event, our work is an attempt at understanding and modelling at this scale the fate of solute atoms in austenitic steels. As steels are too complicated to model at the atomic scale, we chose to concentrate our effort on a model Fe-10Ni-20Cr alloy whose composition is representative of the austenitic steels used in nuclear reactors.

In this work we modelled RIS at the atomistic level using an AKMC model based on the rigid lattice approach and using different cohesive models. In a first step, we tested a set of six Fe-Ni-Cr potentials available in the framework of the PERFORM60 project. The study of these EAM potentials showed a rather low agreement with DFT data available and indicated that none of the potentials were able to reproduce the solid solution observed in 316L SS used for nuclear applications. In particular, the strong tendency for phase precipitation obtained for most of these potentials over a wide range of temperature (including temperatures well above operating

temperatures encountered in PWR reactors) makes their use difficult for the study of RIS. It was therefore decided to build a PIM.

For this purpose, we used DFT to calculate point defect formation energies and found that the local environment of point defect has a strong impact on the energy required to create it. We investigated this issue in depth. This study showed that the simple knowledge of the number of Ni and Cr atoms 1nn to point defects is sufficient to estimate with a reasonable agreement DFT data. The chemical composition of the first shell of atoms surrounding the point defects was therefore found to provide the biggest contribution to the formation energy values and that the position (tensile or compressive site) and thus magnetism usually intervenes at second order.

We in particular found that simple relationships between the formation energies and the chemical composition of the point defect vicinities can be obtained which we used to build our PIM. Interactions of Ni and Cr solutes with point defects thus obtained in austenitic in Fe-10Ni-20Cr are consistent with what would intuitively be expected of moderately oversized and undersized solutes, respectively.

Our model was also adjusted to reproduce high temperature diffusion experiments in Fe-Ni and Ni-Cr binaries. Although we have been able to reproduce the shape of the high temperature, we found that it was impossible to adjust the diffusion experiments using a unique set of pre-exponential factors. These conclusions along with the comparison of correlation coefficients calculated by Barbe show that our model behaves more like a mean field model. The comparison with Barbe's model (cut bond model) shows that this behaviour is primarily due the fact that our model predicts too small variations of the migration barriers as a function of the local environment.

Our work shows thus that a model fitted on data obtained for configurations where all the atoms are on lattice sites and not at the saddle point cannot capture alone both thermodynamic and kinetic aspect of Fe-Ni-Cr alloys in ASS. This study therefore shows that the modelling of RIS in ASS requires a more accurate description of point defect migration barriers and to better take into account the local chemical environment at the saddle point.

Our PIM was used to perform TNES and RIS simulations using AKMC. The solute-GB interactions were found to drive TNES. The reproduction by our PIM of DFT data for the SIAs was found to be incompatible with the modelling of RIS under electron irradiation. Agreement with RIS experiments was obtained using no specific binding energies of the dumbbells with the local chemical environment (e.g. without using the DFT data obtained on the SIA formation energies) and by imposing higher migration probability for Ni compared to Cr and Fe allow.

This work points thus out the need to perform further analysis to be able to state about the reliability of DFT data performed in the AFM1 reference state. One could envisage in a first step the use of either a more accurate FISE model, i.e. which taken into account of SP environment, or the cut bond model which gives the advantage of partitioning thermodynamic and kinetic information. Indeed, the high temperature diffusion experiments could be adjusted much more easily by using one of the two above mentioned models. Another possibility should be to perform many migration energy calculations using DFT in the AFM1 state in order to find a relationship between the migration barriers and the local environment. In the case where simple relationships between point defect positioned at saddle point location and their local environments could be found (as it is the case for point defect formation energies), these information could be incorporated into a more elaborated FISE model. In the case where these further analyses would not lead to reliable results, we may call into question the reliability of the DFT data presented in this work for the RIS modelling. Further analysis would be to investigate more in detail both paramagnetic phase and non collinear configurations using VASP or another code. In particular, we need to determine if it is possible to retain these phases when relaxing the system. The re-investigation of effects of the functionals as well as the DFT simulation parameters may for instance be worth investigating. Another possible alternative should be to model the paramagnetic phase using CPA which has yielded very promising results for the vacancy formation energy in concentrated and paramagnetic Fe-Ni-Cr systems.

The AKMC simulation of RIS has to be extended to neutron irradiation experiments with a flux of cascades. Furthermore, the model introduced for grain boundary can be extended to simulate segregation on loops as observed experimentally. Another improvement of the AKMC modelling

185   General conclusions and perspectives

can be the development of a longer range PIM model which would be necessary to model short range order (e.g. Ni2Cr phase) as observed in some Ni based alloys.

Finally, the Fe-Ni-Cr cohesive model has to be seen as an intermediate first step to investigate the complexity of ASS used in the nuclear industry. The following steps consist in adding step by step other alloying elements as it has been done by Ngayam Happy [NGAYAM HAPPY2010A, NGAYAM HAPPY2010B] in the case of ferritic steels. The addition of carbon, molybdenum and silicon is in particular of major interest for the study of RIS in ASS.

Annex 1: Grandjean's model

In order to model diffusion at the atomic scale, Grandjean [GRANJEAN1994] built a thermodynamic model to approximate the internal energy and entropy in concentrated alloys. This model have been built under the statistical assumption of Bragg-Williams, i.e. by not taking into account correlation between occupation numbers as in Eq. 1-1

$$\langle t_n^i t_m^j \rangle = \langle t_n^i \rangle \langle t_m^j \rangle \qquad \text{Eq. 1-1}$$

where t_n^i corresponds to the occupation number of the specie i in a site n. The calculation of the free energy can be calculated in a system containing several alloying elements and vacancies. Only pair interactions, ε_{AB}, are taken into account in this model.

We consider a binary system containing N elements, of which N_A atoms of A, N_B atoms of B and N_V vacancies, so that $N = N_A + N_B + N_V$. In the grand canonical ensemble, the chemical potential of the chemical potential of a species in the mixture can be defined as the slope of the free energy of the system with respect to a change in the number of moles of that species.

$$\mu^V = \frac{\partial F}{\partial N_V} \qquad \text{Eq. 1-2}$$

Thus, the chemical potential for the vacancy in a A-B binary, μ^V, is expressed as in Eq. 1-3 using this model.

$$\mu^V = k_B T log(C_V)$$

$$+ \frac{zC_A}{2} \{ C_A(2\varepsilon_{AV} - \varepsilon_{AA} - \varepsilon_{VV}) + C_B(2\varepsilon_{BV} - \varepsilon_{AB} - \varepsilon_{VV}) \} \qquad \text{Eq. 1-3}$$

$$+ \frac{zC_B}{2} \{ C_A(2\varepsilon_{BV} - \varepsilon_{BA} - \varepsilon_{VV}) + C_B(2\varepsilon_{BV} - \varepsilon_{BB} - \varepsilon_{VV}) \}$$

z refers to the coordination number, $C_A = N_A/N$ refers to the concentration of the species A and ε_{AB} refers to the pair interaction parameters between species A and B. As can be seen in Eq. 1-4, the chemical potential can therefore be connected to the vacancy formation energy in a pure

---

187   Annex 1. Grandjean's model

system A, $E_f^{V/A}$ (Eq. I-35), and to the ordering energy, Ω^{AB} (Eq. I-32), when using the relation $C_A + C_B = 1$.

$$\mu^V = k_B Tlog(C_V) + C_A \mathrm{E}_f^{V/A} + C_B \mathrm{E}_f^{V/B} + C_A C_B \,\Omega^{AB} \qquad \text{Eq. 1-4}$$

The Gibbs free energy of this system is minimized when μ^V is uniform and equal to zero. The $\mu^V = 0$ condition leads to the relation in Eq. 1-5.

$$C_V = exp\big(-\beta\big[C_A \mathrm{E}_f^{V/A} + C_B \mathrm{E}_f^{V/B} + C_A C_B \,\Omega^{AB}\big]\big) \qquad \text{Eq. 1-5}$$

Thus, the exponential term can be interpreted as the formation energy in an AB binary, $E_f^{V/AB}$, so that $E_f^{V/AB} = C_A E_f^{V/A} + C_B E_f^{V/B} + C_A C_B \,\Omega^{AB}$.

The same development can be done in a ternary alloy A-B-C. The chemical potential for the vacancy in a ABC ternary, μ^V, is expressed as in Eq. 1-6 using this model.

$$\mu^V = k_B Tlog(C_V)$$

$$+\frac{zC_A}{2}\{C_A(2\varepsilon_{AV} - \varepsilon_{AA} - \varepsilon_{VV}) + C_B(2\varepsilon_{BV} - \varepsilon_{AB} - \varepsilon_{VV}) + C_C(2\varepsilon_{CV} - \varepsilon_{AC} - \varepsilon_{VV})\}$$

$$\qquad\qquad\qquad\qquad\qquad\qquad\qquad\qquad\qquad\qquad\qquad\qquad \text{Eq. 1-6}$$

$$+\frac{zC_B}{2}\{C_A(2\varepsilon_{AV} - \varepsilon_{BA} - \varepsilon_{VV}) + C_B(2\varepsilon_{BV} - \varepsilon_{BB} - \varepsilon_{VV}) + C_C(2\varepsilon_{CV} - \varepsilon_{BC} - \varepsilon_{VV})\}$$

$$+\frac{zC_C}{2}\{C_A(2\varepsilon_{AV} - \varepsilon_{CA} - \varepsilon_{VV}) + C_B(2\varepsilon_{BV} - \varepsilon_{CB} - \varepsilon_{VV}) + C_C(2\varepsilon_{CV} - \varepsilon_{CC} - \varepsilon_{VV})\}$$

Again, using the relation $C_A + C_B + C_C = 1$, the chemical potential can therefore be connected to the vacancy formation energy of pure elements and to ordering energies of the three possible binaries that we can form with a ternary alloy, as can be seen in Eq. 1-7.

$$\mu^V = k_B Tlog(C_V) + C_A \mathrm{E}_f^{V/A} + C_B \mathrm{E}_f^{V/B} + C_C \mathrm{E}_f^{V/B} + C_A C_B \Omega^{AB} + C_A C_C \Omega^{AC} + C_B C_C \Omega^{BC} \qquad \text{Eq. 1-7}$$

Applying the $\mu^V = 0$ condition leads to the relation in Eq. 1-8.

$$C_V = exp\big(-\beta\big[C_A \mathrm{E}_f^{V/A} + C_B \mathrm{E}_f^{V/B} + C_C \mathrm{E}_f^{V/B} + C_A C_B \Omega^{AB} + C_A C_C \Omega^{AC} + C_B C_C \Omega^{BC}\big]\big) \qquad \text{Eq. 1-8}$$

188   Annex 1. Grandjean's model

Thus, the exponential term can be interpreted as the formation energy in an A-B binary, $E_f^{V/ABC}$,

so that $E_f^{V/ABC} = C_A E_f^{V/A} + C_B E_f^{V/B} + C_C E_f^{V/B} + C_A C_B \Omega^{AB} + C_A C_C \Omega^{AC} + C_B C_C \Omega^{BC}$.

189   Annex 1. Grandjean's model

190   Annex 1. Grandjean's model

Annex 2: SQS configurations

Final atomic positions for SQSa in the fct AFM1 phase (CONTCAR file using VASP):

```
Fe-10Ni-20Cr SQS-A
 3.50000000000000000
     4.0750975954635482      0.0013022976811032      0.0002820526359305
     0.0013144755911132      4.0038706245068783     -0.0005387894177150
     0.0002742367307578     -0.0005386056177541      3.9905934519239610
 180   50   26
Direct
  0.0006146389409436  -0.0000109961805953   0.2509615957951394
  0.9986733342598260   0.1254881333232295   0.1256980578227261
  0.9993010357833189   0.1271221927997956   0.3723968321363631
  0.0007502547557716   0.1290444131830525   0.8740675853923916
  0.0002892363587518   0.2487417113538211   0.0018093417917546
  0.9990594217636548   0.2487639996684341   0.2492516009232418
  0.9983745482729381   0.2496419517448157   0.4997945465677026
  0.9993414529178547   0.2524207285875116   0.7501809528032019
  0.9995761197872630   0.3734659678411776   0.1257022150301789
  0.9982428774020499   0.3763775531342922   0.6242719874902344
  0.0012705752457500   0.5006692699068632   0.2469864247511698
  0.9989276947750855   0.4992638116324954   0.5026296105283986
  0.9979269358402902   0.5001229593564152   0.7474906234508981
  0.0010461769926043   0.6254379145593952   0.1257406403161795
  0.0004223687607592   0.6232785125431248   0.6229509564695032
  0.0006303374965184   0.7490370227102142   0.0035464314832629
  0.0003181718997870   0.7496006431185062   0.2494903116341227
  0.0007102854530657   0.7516226254917759   0.5018581502411409
  0.9994919635999625   0.8728639126789770   0.1259819911726510
  0.0011169117571369   0.8737224989020275   0.3741326003379166
  0.9995614194604936   0.8732993676713476   0.6232708535548159
  0.2496715977709658   0.9994645571555708   0.4994070206497538
  0.2517514729494325   0.0001019316229304   0.7495424123424361
  0.2501573689847586   0.1250909268615527   0.1252971516292829
  0.2517369686570512   0.1240388675777495   0.3764679800945096
  0.2500756951292988   0.1235723557339596   0.6253778605032326
  0.2502796712965917   0.1268598461606110   0.8722319300480698
  0.2507310957513680   0.2488823445377495   0.7504494292033846
  0.2501471101382333   0.3767355469321627   0.1258362785682604
  0.2511230626986104   0.3786996895572107   0.3759933175609647
  0.2507397756349430   0.3768499825642228   0.8719822978205235
  0.2521018180620129   0.5000939244009717  -0.0003674200978604
  0.2514943538139108   0.5008404783954647   0.2496845815380887
  0.2521846245566575   0.5025678199436626   0.5001816458008186
  0.2532530156179757   0.5021825145888059   0.7501526936212358
  0.2516765863406170   0.6274067198294756   0.1259117429462520
  0.2514252691989074   0.6268553891017844   0.3770230693600435
```

```
0.2509119940634664    0.6251189401903110    0.6245655593205998
0.2502444711168802    0.6243679614818802    0.8735971358303035
0.2488500825982680    0.7470493045312007    0.9996733343877431
0.2484752622256969    0.7494005087179557    0.2516603346309289
0.2507396922915626    0.7492466878418158    0.5017532792022232
0.2490922423361009    0.7499614655779239    0.7480300367918196
0.2491547707310044    0.8714811382967891    0.3785418349247183
0.2507480594293139    0.8742512332002940    0.6243209294370964
0.2481638009679682    0.8711213810634442    0.8721092480720047
0.5009640118023243    0.9985826312407647    0.9995646689332125
0.5016564182128227    0.9985505079694642    0.2516316209961409
0.5004265007978534    0.9976650205240064    0.5003324369765564
0.5015814453069146    0.1241755329451197    0.3763839549591094
0.4977461626661368    0.2499724780123199    0.9980853760228062
0.4988983756551269    0.2508747183681480    0.2521404080074765
0.5009173695144885    0.2521325842642343    0.4981662559813375
0.4986937347776324    0.3746977888274720    0.1233108545607599
0.4998203994467463    0.3773140147635580    0.3757123689090918
0.5006290143850436    0.3777208746635267    0.6243643431408789
0.4982047782697337    0.3761154288196695    0.8757621163126386
0.4979897624293172    0.4993670754484856    0.9986007736415736
0.5004037005761663    0.4988957727939810    0.5013707917537330
0.4977567235714537    0.5008665253526029    0.7492239182873039
0.4990587924074366    0.6251883242461015    0.6238267120055031
0.4984289595054124    0.6263601866192895    0.8769502491219903
0.4999209119093598    0.7506906016567981    0.9987674500596161
0.5010595498182538    0.7523932357997292    0.2504197550436594
0.5013013219377295    0.7498701273719575    0.5002397132259510
0.4996106818439740    0.7521761141236185    0.7505432047577630
0.5007028612821786    0.8760217105968430    0.1250051924346855
0.5003945394883520    0.8738321163124125    0.3757363391698276
0.5004477054216170    0.8727585153856162    0.6235098459893297
0.4992833121804913    0.8738925666082166    0.8764472760603055
0.7498375684754274    0.9982245462268393    0.9986980178592108
0.7494780736027565    0.9995979867978001    0.2508213967384818
0.7497452817712410    0.0005802262720191    0.7489159246062821
0.7504465612755044    0.1248786406028390    0.1252695138648940
0.7490095261351911    0.1257490929163472    0.3735626954356296
0.7487269294400120    0.1273041749649543    0.6246254737529610
0.7495162396572084    0.1234278722491402    0.8740876218837620
0.7524568511415078    0.2482413435127058    0.9995558296766706
0.7518896800509497    0.2491686957196771    0.2502461101770711
0.7505511816700429    0.2493203198337578    0.5000557935323083
0.7537610002323507    0.2482603646545940    0.7501179621487779
0.7514709869114644    0.3764222189077042    0.3755818642138509
0.7499144006507873    0.5020442065400949    0.9989628417905720
0.7486097539355200    0.4989306418534076    0.2511228836116770
0.7498002669931434    0.5004749168874688    0.4997613772674707
0.7501144881886070    0.5013891113032014    0.7485928476776935
0.7499125592869338    0.6243458948935930    0.1269239723081439
0.7498734902541662    0.6240533404969513    0.6233688439168332
```

192   Annex 2. SQS configurations

```
0.7506621486597107    0.6244321746485374    0.8741474033019266
0.7504308790247664    0.7494296057061034    0.7490816761582345
0.7487304564775279    0.8792323516738867    0.1263671458525870
0.7508244336525880    0.8738111156737977    0.3734706805267814
0.7501655625101272    0.8734524135272663    0.6275514414966977
0.7519754153718452    0.8746808513228388    0.8736572324997003
0.6244230654289448    0.9985632401423715    0.1247834152391552
0.6256028183021409    0.1265862549815322    0.5020188700506754
0.6256822959135863    0.2492914735342922    0.6234139658567146
0.6267077202760214    0.3748572643612104    0.9986769735121949
0.6246135109502369    0.3761482745301543    0.2502249585524570
0.6253878750635022    0.3767300555984577    0.5009801789139197
0.6247403411627429    0.4969913073941451    0.3740665586862329
0.6243819733911053    0.4978149965100126    0.6260536255391986
0.6241644550304185    0.6282775241981130    0.0002997219064656
0.6237632624633667    0.6263492953126495    0.2514972662507895
0.6255364271426939    0.7483333438935322    0.1251163450060681
0.6254094210422279    0.7524643646688728    0.3733059124750541
0.6260193873220887    0.7513693325435633    0.6257717295722638
0.6252288867499235    0.7517883240341409    0.8781377416555922
0.6258602053061292    0.8726528477746669    0.0005453349662231
0.6261075835075708    0.8729712327839946    0.2492664984267531
0.6246585109636138    0.8698474707307182    0.5003965843074437
0.6253664153023326    0.8733175053370618    0.7496657912485316
0.3743558576398416    0.9980932813834499    0.1254313674852016
0.3756383594002444    0.9976508827141818    0.3769727260962085
0.3762682233677695    0.1252831513470674    0.4985935306802508
0.3748960245055984    0.1248608448991300    0.7485388908501190
0.3753681787202132    0.2520028729333265    0.1247014181572194
0.3756700723385777    0.2526025874575319    0.3769394299779244
0.3750528436599602    0.2470409548747955    0.6245848388676186
0.3712654999061807    0.3730268821660176    0.9980349393032982
0.3754061863146219    0.3740934050338692    0.2508144983424181
0.3750453549890743    0.3747913377586455    0.5013681444912911
0.3750710007464551    0.3775060302629565    0.7490552494328369
0.3761171903432081    0.5024998120155332    0.6226916898190569
0.3749098861771746    0.5006731310424148    0.8759969775912844
0.3737812753800408    0.6272193036714723    0.9995408266055918
0.3745688268535882    0.6282039843880095    0.2517400127247233
0.3776643962619738    0.6264821417489651    0.5000324640910493
0.3740721113699092    0.6279982810889903    0.7500377337841529
0.3751744570578125    0.7499383559520654    0.1250599034909001
0.3734536716678750    0.7491528856937152    0.3749754950571140
0.3753336125754033    0.7494516860019418    0.6233314416281328
0.3738829646893478    0.7484542093892984    0.8773737335821559
0.3734664082663823    0.8741705485065419    0.9998286614206435
0.3743594086865591    0.8743939960737694    0.2513018614099818
0.3740625214701908    0.8727923636811433    0.4991921848985146
0.8737828834679977    0.0013461787211127    0.3764521627531415
0.8743975458440718    0.0009689625982757    0.6197524030917921
0.8773344288620285    0.9968231851759036    0.8784440557419614
```

193   Annex 2. SQS configurations

```
0.8756676987126806    0.1257661149548975    0.2540446505230610
0.8746671098461337    0.1252532573944426    0.4968370804902898
0.8741628672580918    0.2493025612357678    0.1264883476468470
0.8745053762279106    0.2515068483569963    0.3746906380188263
0.8745909147762301    0.3744413247659777    0.0013750881989873
0.8751251717434451    0.3745689700898855    0.2525305541497453
0.8757254098236364    0.3760947445881290    0.4993056049087668
0.8735196186924935    0.3786026736127936    0.7461402864518054
0.8742465694526353    0.4984908229738738    0.3745477747127997
0.8762293833774744    0.5005888147243955    0.6233906721248886
0.8721826597052248    0.5025316408306476    0.8755131876874848
0.8741669468149996    0.6273112744424920    0.0022698616201697
0.8741780134481278    0.6263105640518408    0.2528560627808243
0.8732812032579759    0.6242748436301466    0.4999625508333320
0.8760332615908084    0.6261757579940407    0.7458320082678542
0.8740976809891114    0.7498378546019341    0.1252060738351013
0.8768148476219610    0.7484229754256871    0.3764391189858658
0.8759392079496551    0.7479047787197229    0.6220106046716791
0.8757424651885566    0.8741338843604239    0.0008973011215455
0.8765824957746441    0.8738544854433288    0.5001732719806178
0.1253061506529844    0.9996206218388882    0.3732111273961987
0.1255443522024354    0.9973468463680288    0.6256800880499794
0.1260941785593625    0.9993952519446357    0.8755838276318938
0.1254819325374156    0.1279372442316224    0.9967836112530803
0.1259754744088207    0.1264678335950369    0.2512400698097422
0.1264732435478298    0.2464063571175626    0.1253396748246099
0.1244801957513269    0.2505555844518534    0.3759628895826930
0.1240506730771963    0.2534541555684545    0.6236872347197088
0.1273808803899624    0.2516777092310289    0.8748686761066260
0.1239590221457435    0.3753660959109664    0.5012117077279662
0.1250507182004459    0.3747756788710660    0.7500794167658897
0.1262543352473221    0.5001930246658221    0.1237202975250627
0.1243888689299351    0.5000783588650449    0.6252469039945636
0.1257824402510687    0.4999780129658138    0.8712916765245347
0.1251989992994023    0.6253140409274551    0.5038355370146999
0.1255959167070927    0.6256668580407455    0.7496188092570755
0.1242983333093493    0.7506496014163434    0.1274616703491274
0.1243161122647775    0.7469593992980718    0.6253684910676331
0.1250691189808840    0.7509853832280383    0.8715312429659859
0.1248724292313050    0.8754025239278049    0.2539618530024920
0.1244266438514158    0.8757513588229230    0.7485815326088795
0.0027293109555847    0.0020952742565438    0.9991306280690614
0.1203093249318397    0.0009186291744319    0.1262133720779602
0.9986208419881619    0.0023975713247856    0.4989868373264341
0.1263862581890808    0.1245855698477464    0.7511115974268858
0.1260974437193717    0.3772685966855152    0.9985796352521488
0.9971689190993717    0.3752213538328560    0.3755517679428061
0.1267563086781273    0.6236853095183889   -0.0002025366973016
0.1266858098075823    0.6240874719307988    0.2489446602284960
0.1245808737506083    0.7492066039789306    0.3771506124109748
0.1265329489764757    0.8735438093176353    0.5014924682658081
```

194   Annex 2. SQS configurations

```
0.0009469326403064    0.7475683331395897    0.7474555887597518
0.0004892914696086    0.8738531706985765    0.8776220828940348
0.2470436088771152    0.0016383882265138    0.0002284362448250
0.3764426748123201    0.1262017239088810    0.0022328072551488
0.2499455077702536    0.9983189751971920    0.2517686120193308
0.3746317854662545    0.1255352025433028    0.2518187819522442
0.3740070309731271    0.9994557192117233    0.6218737686662542
0.2481827615123932    0.2488254671170922    0.0002927597468091
0.3746603903001174    0.2529814552102357    0.8714720007826877
0.3723678596493009    0.4993830944932178    0.1257368762871897
0.3725097911152178    0.4993562883567904    0.3753571288073765
0.3719267611004559    0.8686684747727991    0.7516412307313242
0.6245171203288309    0.1241674150648107    0.0031676188074643
0.6230928356840721    0.9959389196010237    0.3795293485040846
0.6250616092617038    0.1253194535601865    0.2478717100236973
0.4999659332587800    0.1299443903885958    0.6227856923077569
0.6258747336680102    0.9980856493039353    0.6231390207645882
0.4984737735687616    0.9948678640252189    0.7481854530069867
0.4993796260888945    0.1225911957988313    0.8708325106521057
0.6265291651857496    0.9945776426702211    0.8729560114857543
0.6253430863790017    0.1293176900267332    0.7505881068067261
0.6263233551304505    0.2533649645842684    0.8760253394438960
0.6237563642232451    0.3730372671552400    0.7489342500908077
0.4986080143325560    0.6296727452866820    0.1259678862675702
0.5021306375025566    0.4972119200518625    0.2499700670119837
0.5022985789162250    0.6268541025359980    0.3722620093420510
0.6235414281246995    0.6233889161931067    0.5018644783814273
0.8746940501033592    0.9999112564572255    0.1249153774858823
0.7533354693556192    0.9980877095271734    0.4996221537319310
0.7508137857115613    0.3742292590563671    0.1206878301002458
0.7522165111887672    0.3771329703020445    0.6260654084505812
0.8749452156251248    0.2484796523187192    0.6254884222331187
0.7533418659332219    0.3798077901030124    0.8753499898517227
0.8719111995103328    0.2500831542019707    0.8742966172126568
0.7476722196307415    0.6213650441188530    0.3738711617114912
0.7494246697629199    0.7503753526580024    0.0027317165395968
0.7471835446345790    0.7511182680145340    0.2473961239832742
0.8776840898434006    0.8726803890108898    0.2533030569169715
0.7507359056839621    0.7544694702370478    0.4994487670171551
0.8719616098791445    0.8741557714644737    0.7462043465691583
0.0008845971884258    0.1256838773118826    0.6259202827027927
0.1244068724150696    0.1246101202969899    0.5000558923051220
0.9997049260628185    0.9980921941516996    0.7497203486167990
0.1247264847274638    0.3742912631634797    0.2511567792737334
0.9991531428547282    0.3760144680596893    0.8739884350926213
0.9995147832840342    0.4994353931751680    0.0004043975792806
0.9998263624178284    0.6239841827744018    0.3763791901371578
0.1251101953035922    0.5000861578072409    0.3767400854957280
0.0005402552557540    0.6239850189661029    0.8754046610684227
0.1254550309300603    0.8736983778380917    0.9995718563704382
0.3745166186431351    0.9993548947107596    0.8750876902073990
```

195   Annex 2. SQS configurations

```
0.2504458074030964    0.2511297409545745    0.2519714257408796
0.2501855585339918    0.2505408379486129    0.5001864071749250
0.2503835209873479    0.3761264960493511    0.6256787348829449
0.2489500991298544    0.8740926716861172    0.1259179776231334
0.4990890694673155    0.1241062669592817    0.1255120112288348
0.6238599793456215    0.2519577338723587    0.1247297898646429
0.6257929341304241    0.2516411075414095    0.3746372521832954
0.4991447803441843    0.2518768447285019    0.7493180867826094
0.6245263648415912    0.5005383086637677    0.1236648484839115
0.6244112559557653    0.5013847082877496    0.8757919790129843
0.6236716737525030    0.6260759434444961    0.7503402848056760
0.8748173756714795    0.1237382581345089    0.9996690171247985
0.8750283696668656    0.1225192385708854    0.7501012795266998
0.8739920057675697    0.5006840216401547    0.1263468086674242
0.8761344414806544    0.7483053986162603    0.8757205256387203
```

Final atomic positions for SQSb in the fct AFM1 phase (CONTCAR file using VASP):

```
Fe-10Ni-20Cr SQS-B
3.51799999999999979
     4.0633252983483548     0.0005206839759465     0.0004813608008942
     0.0005285534729527     3.9767162621963674     0.0017080019610555
     0.0004923457159452     0.0017120298780450     3.9707236576412317
 180   50   26
Direct
-0.0001033631537302    0.9995120075354990    0.0001716323610964
 0.0020129237443450    0.9977124302257527    0.2512228372327254
 0.0005624401350433    0.1212186866935417    0.1264785577969218
 0.9977557198116334    0.1259942452003507    0.8731036009357681
-0.0000660718602573    0.2515912574932232    0.4990598236274753
 0.9974063067549699    0.2509476871722496    0.7527844486800014
 0.9997325440910829    0.3790309320136217    0.1254710728213570
 0.9995976227183752    0.3756787122051734    0.3773169070305985
 0.9978053258025003    0.3736994648869427    0.8753848895175587
 0.9992865542284025    0.4987548398022929    0.9983588897970028
 0.0004751823159808    0.4994563544904523    0.2527624749075639
 0.0018196122624942    0.5024037066158993    0.4993035570101024
 0.0018346032756443    0.6254058444793194    0.3739035662587282
 0.0008630009691751    0.6274360437034686    0.6233019181728001
 0.0003853815735951    0.6259644764489489    0.8778029022516564
 0.0007579287657616    0.7513423544934480    0.9982883516519201
 0.0012434196760376    0.7518791497810449    0.2506690096919335
 0.0016082427606174    0.7503434152679459    0.4992022972166035
 0.0002490926378629    0.7479017647323907    0.7506937438298842
 0.0010258813159867    0.8728336893403638    0.1256494189183824
 0.0016285486151822    0.8740953009081361    0.3727373081461587
 0.0000715871449812    0.8715837964395482    0.6251274697406265
 0.9993871039007266    0.8736193631289750    0.8756410152467453
 0.5001533777064626    0.0007561406826402    0.9975597301863597
```

```
0.5002396887225510    0.0022984218265582    0.7496535371080925
0.4982517863807127    0.1248477458327362    0.1209718098793782
0.4985414492260844    0.1248948995045814    0.3764591196445096
0.4986080401050203    0.1248683520287930    0.6282053143649112
0.4999332974885547    0.1237890817130278    0.8751775046662864
0.4988519548119318    0.2473248799275570    0.9978056338173029
0.4990309307867263    0.2500360969734273    0.2499280019464975
0.5006272826503049    0.2501946832665667    0.7506178810091979
0.4994619446030027    0.3782216806950395    0.3736868011527115
0.5010216612249264    0.3754066312747517    0.6271447037357772
0.5001086778582142    0.3760635645839945    0.8771247789550687
0.5004466408000189    0.5020314624432013    0.9981401640965230
0.4984312660908446    0.5007715214825980    0.2496482279747507
0.4993676862135276    0.4979823094088511    0.4995125338886857
0.5004780097079397    0.4976269591833707    0.7508744911789415
0.5001249413723140    0.6252420538765158    0.1261364890707651
0.5002072731697973    0.6254423296070867    0.8752369466466589
0.5004236208831959    0.7497309554153976    0.9983570939656533
0.4990901402061666    0.7476190076086362    0.2468402123932708
0.4996329225774631    0.7506980010681714    0.7525825331121218
0.5001042385792513    0.8748330019356058    0.8755021660360724
0.2478971228756943    0.9997714684467328    0.2488771508149686
0.2492919929537264    0.9973288699696014    0.7514107589181180
0.2489010825152394    0.1254000210148145    0.1242559107180744
0.2498025675265307    0.1252457047090693    0.3783461808320983
0.2524134542580910    0.2486614564303810    0.0007184300160762
0.2514171253211971    0.2503069772277078    0.4987861408388302
0.2494954580001512    0.2538706379274557    0.7491812450092034
0.2512328675591131    0.3745506953417498    0.1212945531877340
0.2515488522409526    0.3766080509455145    0.3770910384606966
0.2489950287063715    0.3733904143241343    0.6235841009246252
0.2499012243663837    0.3735673105709542    0.8771785253959152
0.2501123190242237    0.4984923869116896    0.0000431130345335
0.2510466925332775    0.5005767381528288    0.4986958724638450
0.2526141834097204    0.6244734662850747    0.3741440013406296
0.2512754059369692    0.6219352246920393    0.6236437849346520
0.2500558961214979    0.6260878774735106    0.8793848440269618
0.2493216840038324    0.7528881589999168    0.9992174181250841
0.2491101418665488    0.7490404580987365    0.2507150074723895
0.2500298020363158    0.8718978370727082    0.1266251260823751
0.2506974722051518    0.8739055566874716    0.3720339094965057
0.2514733883272384    0.8785062838752401    0.6282253873466926
0.2495254081182993    0.8729006599695260    0.8730766336356433
0.7504221421202133    0.9967114576995103    0.0029474430259675
0.7503768058083108    0.9997075210955830    0.2502291420855631
0.7502569049281584    0.0003781712775265    0.5010315739697965
0.7508582692499338    0.9964824653458033    0.7472256832122877
0.7507817364881603    0.1246791206669526    0.1251496435934509
0.7510781044360239    0.1244504863132782    0.3748887338901314
0.7513175775875356    0.1232371885352515    0.6243896575119280
0.7499103315029096    0.2501931829552322    0.0024779083017540
```

```
0.7499862630099208    0.2468899292284958    0.2504162136471459
0.7479541906023683    0.2461213818535498    0.5001806081714739
0.7507989242301153    0.3758323808984053    0.1264281053633307
0.7505320675172666    0.3758481236922456    0.8760683836169272
0.7493089548076923    0.5000045458767971    0.9988522933465667
0.7497533271174207    0.5011757809600493    0.2499847979384301
0.7494234468379174    0.5045153595886168    0.4995809810949428
0.7508991876402596    0.5017497149018466    0.7526827671464619
0.7481717722928352    0.6264686327287117    0.3736285736192343
0.7511189806287738    0.6268715517795648    0.6241823400792638
0.7504785508346655    0.6266559459823806    0.8769951807006798
0.7502190541444526    0.7515887944292287    0.9997070653510454
0.7496747159045068    0.7523927513606615    0.2524475575313035
0.7488238878059866    0.7493714762126950    0.4993588649889727
0.7519317733669342    0.7509769359674626    0.7498308561993694
0.7493754049538223    0.8737515610162084    0.1273243441918198
0.7494167314264736    0.8742547372383304    0.3740526613990056
0.7495077513642252    0.8739455657607191    0.6235389906739365
0.7499713374693812    0.8742128186131106    0.8757698403144552
0.8743436090971517    0.9984110974537583    0.3737934930843326
0.8760068007312521    0.9960934427196242    0.6226443954528257
0.8763215375487300    0.1262568294176676    0.0031530278414896
0.8766024662259014    0.1268919594451417    0.2528226078931585
0.8750982363919645    0.2481393737797565    0.1274858390826523
0.8746397751773776    0.2510611926527301    0.3734553609502156
0.8734519876471506    0.2520646598461047    0.6245514549648191
0.8750973885777458    0.3730486354493410    0.2497177583930114
0.8744090757487696    0.3739285218654436    0.5003350180336299
0.8742081560864371    0.5025584828982936    0.6229913783232808
0.8761801903332178    0.6282726093805053    0.0012292142053794
0.8758691484056407    0.6264064974383448    0.4974908502701415
0.8747565815605143    0.6252945736256929    0.7500717019862446
0.8759497050208128    0.7526107691365694    0.3757015141802466
0.8760305087133938    0.7468515992811710    0.8751255573340743
0.8756707710876072    0.8730562620281985    0.2530477892005696
0.8745932159709633    0.8772659413402375    0.4972602810928183
0.1258825026433192    0.9961857249290064    0.3734649337779825
0.1245731321002177    0.1291875998364452    0.9992714923995946
0.1242722935064483    0.1263711546556284    0.2537190961590371
0.1239617013135851    0.1267254919525152    0.7462689163666893
0.1235540072627444    0.2457745554788674    0.1252621918992668
0.1247180690986533    0.2493308857144947    0.3747149136646960
0.1228604582689924    0.2477418351963391    0.8740004568523481
0.1249057675288012    0.4998505559161344    0.1270680862253002
0.1264664624429744    0.5046687766678614    0.3748484747578317
0.1254452178171744    0.5016774221450583    0.8737215525038826
0.1255305639650478    0.6232621751742139    0.2471396660969816
0.1270754545265684    0.6250295425643744    0.4984637523791883
0.1263420573130605    0.6270832696202677    0.7525527160976203
0.1243400066874646    0.7528862504423347    0.1264138283316474
0.1255351852210836    0.7482775313341692    0.6228871372815887
```

198   Annex 2. SQS configurations

```
0.1243710588124629    0.7514420956424154    0.8746839205893481
0.1265516233362896    0.8715145656324843    0.9993755144017269
0.1259004931175022    0.8740755028706387    0.2496406650189818
0.1263467071198697    0.8778738974805921    0.5012809156359127
0.6249523299024768    0.0032117624536501    0.1248680221853900
0.6247983667649092    0.0003102319095627    0.3740100445476225
0.6249028835803391    0.0005848779425441    0.6261066840372702
0.6263326068421359    0.0005190993853537    0.8736087366895573
0.6252612006084994    0.1238455537455634    0.0002397975928457
0.6244798685456647    0.1261538715769725    0.2506750039006743
0.6243530325420823    0.1213326619478972    0.4979555088834996
0.6260198824990590    0.1214763636112016    0.7509609994392700
0.6229708096288044    0.2468368097925950    0.1245092436446695
0.6254848345862979    0.2493024917447283    0.3763713239832838
0.6248431403596768    0.3741206216242403    0.0047008135976369
0.6268031934386696    0.3766649821181925    0.4967493035979593
0.6272895028088938    0.3744762554361115    0.7491229786387672
0.6245600434927360    0.5002506141407644    0.1235938263874475
0.6240819075730510    0.5023215766527259    0.3750593472597937
0.6245546234106013    0.6276866460924521    0.0018795916759482
0.6241695220903160    0.6248145834251274    0.2500106474254680
0.6226657081442692    0.6266029119601730    0.4998140974623408
0.6256143186365690    0.7497740897374604    0.1264453871051663
0.6240552936387127    0.7489794632557080    0.3753754297276749
0.6239253784732078    0.7519014729017578    0.6234913163406178
0.6263708391596093    0.7504547284176646    0.8738978899695945
0.6245892078716807    0.8748864559641258    0.2500044744794703
0.6242320200655156    0.8748550134905321    0.5001201729696844
0.6252821250945215    0.8745802541190237    0.7495192091680672
0.3737858394036560    0.9979229620833249    0.6274963644898228
0.3751376648885361    0.9988559357328665    0.8737256871393694
0.3759348053806577    0.1294804321212835    0.2487025069510564
0.3743941034286002    0.1236109555303283    0.7483318954582104
0.3763203056086181    0.2520393676322387    0.1249789823753614
0.3747517703033086    0.2528190846498486    0.3713338552127233
0.3753815508614850    0.2513620130904659    0.6290172618328138
0.3745687441117264    0.3767602295039450    0.0015996643123632
0.3754020739070981    0.3745170476754654    0.2461878747463661
0.3732018356793076    0.3733058347825832    0.5022984842803231
0.3745088158831382    0.3787125348327931    0.7498290340477277
0.3748574966503472    0.5002091834088375    0.1263183432065547
0.3738033856541824    0.5013005487623060    0.6237384064858260
0.3758518782039058    0.4979517196424143    0.8737771417638536
0.3750119836225180    0.6259414736938492    0.2476521370231535
0.3746935414275758    0.6262423066878772    0.5026100899766337
0.3736157315176779    0.6246876687356145    0.7507055348517218
0.3745144839466121    0.7514128269604404    0.1249429159459306
0.3740813820873139    0.7483326614093926    0.3749218281911601
0.3741923676262929    0.7501719505541762    0.6255725113503005
0.3731806538884191    0.7515798114013041    0.8742219484648205
0.3740186943991924    0.8751958811734255    0.9974356253835762
```

```
 0.3739991186068503    0.8701977224498146    0.2489851458918329
 0.3751442591175288    0.8747746379045631    0.5003404231511848
 0.3748390059954452    0.8739142127725537    0.7509874853646016
 0.1239088840045374    0.0000488486765411    0.1263267151391374
 0.9999185446248996    0.1244474987279040    0.3770870676094986
 0.9989073740478175    0.9933961557270595    0.4975027721986857
-0.0008493457435369    0.1259963886773479    0.6250570244761882
 0.1245348620271591    0.9979826070993785    0.6264965766381676
 0.1287994802280083    0.1252307445554521    0.4981786591182234
 0.0010277817693115    0.2499609910942533    0.0059331346060267
 0.9990118285249763    0.2512136200486782    0.2475736342918019
 0.1243793016804924    0.2541918341835044    0.6278832345558369
 0.1267245185604111    0.3734067590359392    0.4935228495225339
 0.0056477610399938    0.6249343817569407    0.1257711099199652
 0.1236046612972539    0.6258013427572295    0.9979047465486526
 0.1260881064861405    0.5037260487177029    0.6244562153081412
 0.1247619908958655    0.7500172318966332    0.3735896845648078
 0.1231817337481143    0.8723558199069085    0.7508374399490918
 0.2489197461146730    0.9983504401032348    0.9983215250863172
 0.3753492291953635    0.1237154899761912    0.0012658627157742
 0.2533754728332781    0.9931394661258147    0.4957093010023916
 0.2531470289108493    0.1249226698393247    0.6277139484615060
 0.3757864955395182    0.1281988115700810    0.4997144169678992
 0.3745996270433434    0.2528945203906238    0.8715423100029941
 0.2515231805140870    0.6277932171832464    0.1241518076965322
 0.2488706948459947    0.4992071173593357    0.2495571585774400
 0.3763250853970975    0.4996454645276260    0.3755697802356492
 0.2537572100697729    0.5017776791515248    0.7534492342908501
 0.2530209386271218    0.7508071675938162    0.5032108122845450
 0.2514757188092331    0.7444889299045359    0.7490294439350509
 0.4990222183406762    0.9979065999092744    0.4996015703958052
 0.4996219965520383    0.3753459459171167    0.1218166929303280
 0.6234383800964514    0.2477489463505910    0.6238407964400603
 0.5020078544677747    0.6250570384840084    0.3744259465119461
 0.4984523287788337    0.6249104463819390    0.6257991637672072
 0.6262403430121116    0.5011839784807582    0.8767808840395483
 0.6267773035933938    0.8744434674201194    0.9997065724546974
 0.4975556951800140    0.7535288929434062    0.4997880218152502
 0.4995211864671372    0.8733132824510975    0.6314703757500199
 0.8692503964520625    0.1255220635068960    0.4996522852573656
 0.7486818849092106    0.1226582786020270    0.8765458637740557
 0.8743985740620762    0.1237811733961563    0.7447070788133736
 0.7507145616487170    0.3746991886315633    0.3772001722808673
 0.7484137718979386    0.3763075077639455    0.6222834775626805
 0.8752178874795674    0.2492072800474710    0.8778587658330591
 0.8766338537417739    0.3757946741297606    0.7470837271851581
 0.8744592912838397    0.5001511510004738    0.1235874947231289
 0.8751144193812316    0.6274676472256980    0.2538328141692090
 0.8713876381178502    0.5018943089085514    0.8783514434957106
 0.8735718669628163    0.7483420452882708    0.1267936364496794
 0.8730313560042495    0.8737554003482292    0.9996365128629685
```

200   Annex 2. SQS configurations

```
0.8754572602307117    0.7470116866822161    0.6207927001460153
0.8754974856764680    0.8748763046766798    0.7515727721901617
0.9990728229865274    0.9983028701534856    0.7499288953536799
0.1229288581944304    0.9998025363191537    0.8756083620519031
0.1239711088734984    0.3753338418534509    0.9999278315406450
0.1252310596143883    0.3749685179908303    0.2502258481683029
0.0006221405606621    0.3763629603751862    0.6244284172056837
0.1240465410593742    0.3767091318637509    0.7520472459185835
0.9991909962616470    0.5029207777182966    0.7501815777359720
0.3728437678135416    0.9986640860654672    0.1253603248694215
0.3748442415522474    0.9998221376972239    0.3730946467878810
0.2492224912730579    0.1260501560033688    0.8730840870318390
0.2505367098680555    0.2504977451724537    0.2501679869438009
0.3749256736370278    0.6248702642560564    0.9994826319746896
0.4995962129702021    0.0019471125541970    0.2486650727929175
0.6248293645777235    0.3744650856077721    0.2500377203547835
0.4998673618440652    0.2511287649574475    0.4992982616074699
0.6253650986337769    0.2502786393969539    0.8755911468998907
0.6248829425429938    0.4999987958095885    0.6245847233420081
0.6251205356322667    0.6263736132727141    0.7491228068362310
0.5004731244036157    0.8754248224518459    0.1238920975662957
0.4991050252168752    0.8739389130129745    0.3728331552088796
0.8761988624222165    0.9988881304395343    0.1272775479408665
0.8744696813994625    0.0012912058121987    0.8757952858687904
0.8747627617533144    0.3737235750862120    0.0015199826240201
0.7501566423563225    0.2494490207117908    0.7496001842713839
0.7505668163524509    0.6260391972999273    0.1244881392518089
0.8742738617721143    0.4988167248319085    0.3753136022506479
```

201   Annex 2. SQS configurations

202 Annex 2. SQS configurations

Annex 3: Thermodynamic calculation of chemical potentials

When we consider a mixture defined by $\sum x_i \langle A_i \rangle$, so that $\sum x_i = 1$ (A_i refer to the atomic species and x_i refer to their molar fractions), In the general case, the molar free enthalpy can be expressed as in Eq. 3-1

$$G_m = G^0 + G^{id} + G^{\chi S} + G^{surf} + G^{mag} + \cdots \qquad \text{Eq. 3-1}$$

where G^0 is the standard term which depends on the choice made for the standard states, G^{id} is the ideal contribution, $G^{\chi S}$ is the excess contribution, G^{surf} is the contribution dur to the surface and G^{mag} is the contribution due to the magnetic ordering. Both G^{surf} and G^{mag} occurs in tis expression only if surface effects (e.g. small particles) and magnetic effects (e.g. ferromagnetic ordering) are significant, which will not be the case here. Thus, in the austenitic Fe-10Ni-20Cr alloy, we can rewrite Eq. 3-1 as:

$$G_m = G^{id} + G^{\chi S} \qquad \text{Eq. 3-2}$$

I   Expression for the excess contribution of the free enthalpy for a binary

Several equations exist to calculate the excess contribution of the free enthalpy, $G^{\chi S1}$. We focus here the Redlich-Kister development [REDLICH1948] which is widely used in thermodynamics. The equation for the binary is presented in Eq. 3-3.

$$G^{\chi S1} = x_1 x_2 \sum_{i=0}^{+\infty} L^{(i)} (x_1 - x_2)^i \qquad \text{Eq. 3-3}$$

For a binary system we posit that:

$$x_2 = x, \;\; x_1 = 1 - x \qquad \text{Eq. 3-4}$$

Thus, Eq. 3-3 can be rewritten as:

$$G^{\chi S1} = x(1-x) \sum_{i=0}^{+\infty} L^{(i)} (1-2x)^i \qquad \text{Eq. 3-5}$$

It is worth noting that the $L^{(i)}$ coefficients $\left(L^{(0)}, L^{(1)}, L^{(2)}, \dots\right)$ can be interpreted as the interactions between neighbouring species (first, second and third nearest neighbours respectively).

In a ternary alloy, the calculation of the excess contribution of the free enthalpy, $G^{\chi S1}$, consists in combining three Redlich-Kister developments (Eq. 3-3) for the three possible binaries, $G_{12}^{\chi S}$, $G_{13}^{\chi S}$ and $G_{23}^{\chi S}$.

$$G_m = G^{id} + G^{\chi S1} = G^{id} + G_{12}^{\chi S1} + G_{13}^{\chi S1} + G_{23}^{\chi S1} \qquad \text{Eq. 3-6}$$

Sometimes, this combination may be not sufficient so that the calculation of G_m for a ternary requires the use ternary interaction term, $G^{\chi S2}$, presented in Eq. 3-7.

$$G^{\chi S2} = x_1 x_2 x_3 (x_1 L_1 + x_2 L_2 + x_3 L_3) \qquad \text{Eq. 3-7}$$

In general, we posit $L = L_1 = L_2 = L_3$ so that Eq. 3-7 can be rewritten as:

$$G^{\chi S2} = L x_1 x_2 x_3 \qquad \text{Eq. 3-8}$$

II   Calculation of chemical potentials in the austenitic Fe-10Ni-20Cr alloy

The chemical potential of a species in the mixture can be defined as the slope of the free energy of the system with respect to a change in the number of moles of that species. Thus, In order to calculate the chemical potentials of species in the austenitic Fe-10Ni-20Cr alloy, we use the Eq. 3-9

$$\mu_i = G_m + \sum_{j=2}^{n} (\delta_{ij} - x_j) \left(\frac{\partial G_m}{\partial x_j} \right) \qquad \text{Eq. 3-9}$$

204   Annex 3. Thermodynamic calculation of chemical potentials

where δ_{ij} is the Kronecker symbol so that $\delta_{ij} = 1$ when $i = j$ and $\delta_{ij} = 0$ when $\delta_{ij} \neq 1$. Thus, in a ternary alloy, the chemical potentials of the three species can be expressed as in the following equations:

$$\mu_1 = G_m - x_2 \left(\frac{\partial G_m}{\partial x_2} \right)_{T,P,x_3} - x_3 \left(\frac{\partial G_m}{\partial x_3} \right)_{T,P,x_2} \qquad \text{Eq. 3-10}$$

$$\mu_2 = G_m + (1 - x_2) \left(\frac{\partial G_m}{\partial x_2} \right)_{T,P,x_3} - x_3 \left(\frac{\partial G_m}{\partial x_3} \right)_{T,P,x_2} \qquad \text{Eq. 3-11}$$

$$\mu_3 = G_m - x_2 \left(\frac{\partial G_m}{\partial x_2} \right)_{T,P,x_3} + (1 - x_3) \left(\frac{\partial G_m}{\partial x_3} \right)_{T,P,x_2} \qquad \text{Eq. 3-12}$$

In what follows, equation are developed in the general case, i.e. when $G^{\chi S1} \neq 0$ and $G^{\chi S2} \neq 0$.

From Eq. 3-13 to Eq. 3-15 are presented the chemical potentials for the $G^{\chi S1}$ term obtained by using the Eq. 3-9.

$$\mu_1^{\chi S1} = \sum_v \left\{ L_{12}^{(v)} x_2 (x_1 - x_2)^{v-1} \left[(x_1 - x_2)(x_2 + x_3) + v x_1 (2 x_2 + x_3) \right] \right.$$

$$+ L_{13}^{(v)} x_3 (x_1 - x_3)^{v-1} \left[(x_1 - x_3)(x_2 + x_3) + v x_1 (2 x_3 + x_2) \right] \right\} \qquad \text{Eq. 3-13}$$

$$- L_{23}^{(v)} (1 + v) x_2 x_3 (x_2 - x_3)^v$$

$$\mu_2^{\chi S1} = \sum_{\nu} \left\{ L_{12}^{(\nu)} x_1 (x_1 - x_2)^{\nu-1} \left[(x_1 - x_2)(x_1 + x_3) - \nu x_2 (2\, x_1 + x_3) \right] \right.$$

$$\left. + L_{23}^{(\nu)} x_3 (x_2 - x_3)^{\nu-1} \left[(x_2 - x_3)(x_1 + x_3) + \nu x_2 (2\, x_3 + x_1) \right] \right\} \qquad \text{Eq. 3-14}$$

$$- L_{13}^{(\nu)} (1 + \nu) x_1\, x_3\, (x_1 - x_3)^{\nu}$$

$$\mu_3^{\chi S1} = \sum_{\nu} \left\{ L_{13}^{(\nu)} x_1 (x_1 - x_3)^{\nu-1} \left[(x_1 - x_3)(x_1 + x_2) - \nu x_3 (2\, x_1 + x_2) \right] \right.$$

$$\left. + L_{23}^{(\nu)} x_2 (x_2 - x_3)^{\nu-1} \left[(x_2 - x_3)(x_1 + x_2) - \nu x_3 (2\, x_2 + x_1) \right] \right\} \qquad \text{Eq. 3-15}$$

$$- L_{12}^{(\nu)} (1 + \nu) x_1\, x_2\, (x_1 - x_2)^{\nu}$$

It has to be noted that, in order to avoid complicating the above formulas, we kept x_1 variable, but in the practical case, x_1 variable has to be replaced by $1 - x_2 - x_3$.

Considering the case where $L_1 \neq L_2 \neq L_3$ (Eq. 3-7), the chemical potentials for the $G^{\chi S2}$ term are presented from Eq. 3-16 to Eq. 3-18.

$$\mu_1^{\chi S2} = x_2\, x_3 [L_1 x_1 (2 - 3x_1) + (L_2 x_2 + L_3 x_3)(1 - 3x_1)] \qquad \text{Eq. 3-16}$$

$$\mu_2^{\chi S2} = x_1\, x_3 [L_2 x_2 (2 - 3x_2) + (L_1 x_1 + L_3 x_3)(1 - 3x_2)] \qquad \text{Eq. 3-17}$$

$$\mu_3^{\chi S2} = x_1\, x_2 [L_3 x_3 (2 - 3x_3) + (L_1 x_1 + L_2 x_2)(1 - 3x_3)] \qquad \text{Eq. 3-18}$$

Considering the case where $L = L_1 = L_2 = L_3$ (Eq. 3-8), the chemical potentials for the $G^{\chi S2}$ term are presented from Eq. 3-19 to Eq. 3-21

$$\mu_1^{\chi S2} = L x_2\, x_3 (1 - 2x_1) \qquad \text{Eq. 3-19}$$

$$\mu_2^{XS2} = Lx_1\, x_3(1 - 2x_2) \qquad\qquad \text{Eq. 3-20}$$

$$\mu_3^{XS2} = Lx_1\, x_2(1 - 2x_3) \qquad\qquad \text{Eq. 3-21}$$

The chemical potentials presented from Eq. 3-13 to Eq. 3-15 and from Eq. 3-19 to Eq. 3-21 can be verified using the Euler's formula presented in Eq. 3-22.

$$G = \sum x_1 \mu_1 \qquad\qquad \text{Eq. 3-22}$$

III   <u>Numeric application</u>

It can be noted that by convention, elements are numbered in alphabetic order and then, in what follows, Cr=1, Fe=2 and Ni=3. In what follows, $L_{12}^{(0)}$ coefficient will refer to interactions between Cr and Fe atoms positioned at 1nn position. Similarly, Cr, Fe and Ni concentration will be labelled x_1, x_2 and x_3 respectively.

The parameters may be taken at least from four different papers [KJELLQVIST2008, MIETINNEN1999, HILLERT1991, BYEONG-JOO1983] in which authors built a model where both Fe-Ni and Fe-Cr binaries were modelled equally ($L_{12}^{(v)}$ and $L_{23}^{(v)}$ .coefficients). These empirical parameters are summarized in Tab. 3-1 which display:

- ➢ Coefficients obtained by Kjellqvist in the γ-Cr-Fe-Ni-O [KJELLQVIST2008].
- ➢ Coefficients obtained by Mietinnen in the γ-Fe-Cr-Ni system [MIETINNEN1999].
- ➢ Coefficients obtained by Hillert in the γ-Fe-Cr-Ni-C system [HILLERT1990, HILLERT1991].
- ➢ Coefficients obtained by Byeong-Joo in the γ-Fe-Cr-Ni system [BYEONG-JOO1983].

reference	L coefficient (J/mol)			
	[KJELLQVIST2008]	[MIETINNEN1999]	[HILLERT1990, HILLERT1991]	[BYEONG-JOO1983]
$L_{12}^{(0)}$	$10\,833 - 7.477T$	$10\,833 - 7.477T$	$10\,833 - 7.477T$	$10\,833 - 7.477T$
$L_{12}^{(1)}$	1410	1410	1410	1410
$L_{23}^{(0)}$	$-12054.355 + 3.27413T$	$-12054.355 + 3.27413T$	$-12054.355 + 3.27413T$	$-12054.355 + 3.27413T$
$L_{23}^{(1)}$	$11082.13 - 4.45077T$	$11082.13 - 4.45077T$	$11082.13 - 4.45077T$	$11082.13 - 4.45077T$
$L_{23}^{(2)}$	-725.805174	-725.805174	-725.805174	-725.805174
$L_{13}^{(0)}$	$8030 - 12.8801T$	$8030 - 12.8801T$	$8030 - 12.8801T$	$17170 - 11.8199T$
$L_{13}^{(1)}$	$33080 - 16.0362T$	$33080 - 16.0362\,T$	$29895 - 16.3838T$	$34418 - 11.8577T$
L_1		$10000 - 10T$		
L_2		-6500		
L_3		48000		
L	$16580 - 9.783T$		1618	$-2673 - 2.04145T$

Tab. 3-1: Available parameters for the L coefficients in the γ-Cr–Fe–Ni–O system [KJELLQVIST2008], in the γ-Cr–Fe–Ni system [MIETINNEN1999, BYEONG-JOO1983], in the γ-Cr–Fe–Ni–C system [HILLERT1990, HILLERT1991].

The chemical potentials as well as the activity coefficients were calculated using these four different sets of parameters in the austenitic Fe-10Ni-20Cr alloy, i.e. so that $x_1 = 0.2$, $x_2 = 0.7$ and $x_3 = 0.1$.

The numeric applications are presented from Fig. 3-1 to Fig. 3-3 for the chemical potentials. As can be seen, despite the difficulty of calculating a chemical potential and despite the fact that L coefficients are determined empirically, agreement between the different models is good. Chemical potential values of Cr atoms are substantially positive on a wide range of temperatures. These values significantly reduce with increasing temperature and become negative far beyond the operating conditions of temperatures encountered in nuclear reactors. The chemical potential of Fe atoms displays a similar behaviour than the chemical potential of Cr atoms. Indeed, although chemical potential values of Fe atoms are about one order of magnitude smaller than those of Cr atoms, they also decreases with increasing temperatures and becomes negative at temperatures above 1000 K. Finally, Chemical potential values of Ni atoms stay negative on the full range of temperatures investigated in Fig. 3-3.

The chemical potential represents the macroscopic manifestation of microscopic interactions between atoms and the medium in in which they have been introduced. The more the microscopic interactions with the medium are repulsive, the more these atoms will tend to move toward another less hostile medium, e.g. the point defect sinks. To be more specific, chemical potential always tend to decrease its value by moving toward another medium where its chemical potential will be smaller, i.e. that interactions with that medium will be less repulsive. It has to be

remembered however that the calculated chemical potentials correspond, in fact, to the difference $\mu_i - \mu_i^0$, where we assumed that $\mu_i^0 = 0$. In other words, we estimate the stability of elements in the austenitic Fe-10Ni-20Cr alloy. Knowing that the more the potential is negative the more stable is the element, we can conclude that for each data set considered here, Ni atoms are stable in the austenitic Fe-10Ni-20Cr alloy while both Cr and Fe atoms have on average repulsive interaction.

These results are consistent with experimental results obtained for TNES in austenitic stainless steels, i.e. the segregation of Cr atoms and the depletion of Ni atoms at defect sinks [ALLEN2007]. This is consistent with the fact that μ_{Ni} is negative, indicating that Ni atoms tend to stay in the medium while μ_{Cr} is positive, indicating that Cr atoms tend to segregate at the point defect sinks.
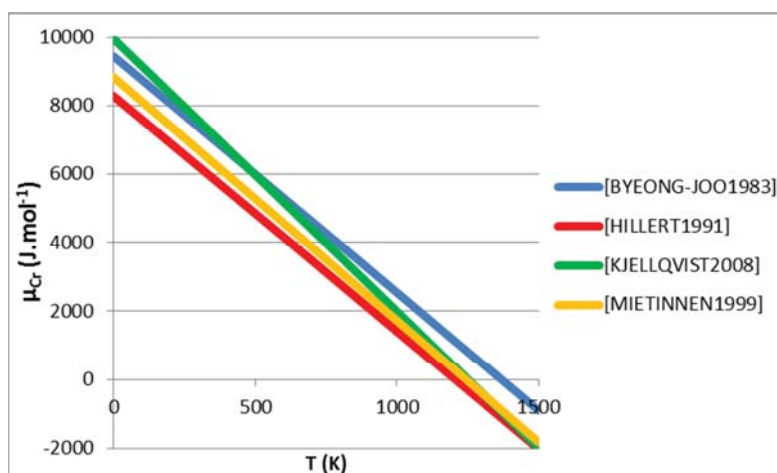
Fig. 3-1: Cr chemical potential,μ_{Cr}, as a function of the temperature, calculated in the austenitic Fe-10Ni-20Cr, using different sets of parameters [KJELLQVIST2008, MIETINNEN1999, HILLERT1991, BYEONG-JOO1983].

209   Annex 3. Thermodynamic calculation of chemical potentials
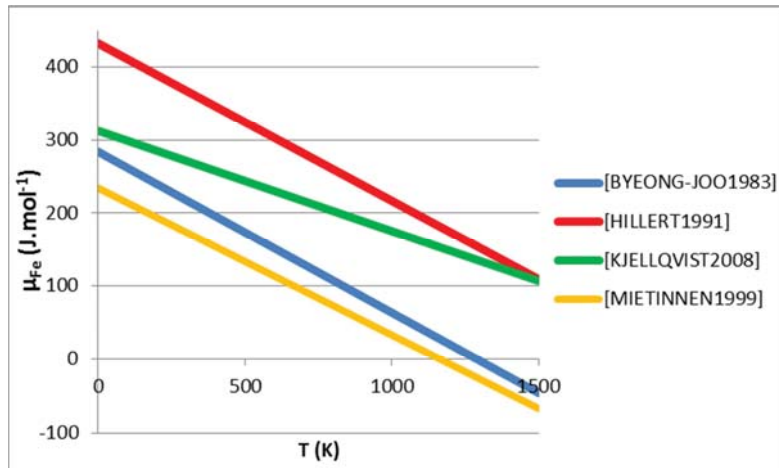
Fig. 3-2: Fe chemical potentials, μ_{Fe}, as a function of the temperature, calculated in the austenitic Fe-10Ni-20Cr, using different sets of parameters [KJELLQVIST2008, MIETINNEN1999, HILLERT1991, BYEONG-JOO1983].
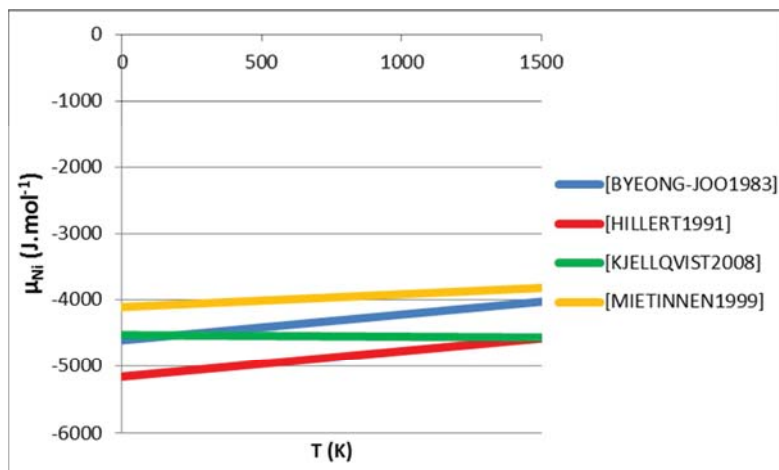
Fig. 3-3: Ni chemical potentials, μ_{Ni}, as a function of the temperature, calculated in the austenitic Fe-10Ni-20Cr, using different sets of parameters [KJELLQVIST2008, MIETINNEN1999, HILLERT1991, BYEONG-JOO1983].

210   Annex 3. Thermodynamic calculation of chemical potentials

Annex 4: Calculation of binding energies using MD

Distance	Cohesive model	Binding energy (eV)					
		V-V	Fe-V	Cr-V	Fe-Fe	Cr-Cr	Fe-Cr
1nn	DFT	0.02	-0.02	-0.05	-0.11	0.04	-0.16
	P-100819	0.17	-0.06	0.09	-0.07	0.1	0.14
	P-100826	-0.06	0	0	0.22	0.05	0.16
	P-100831	0.17	0.06	0.22	0	0.14	0.2
	P-110307	0.33	0.03	0	-0.01	0.01	0
	P-20120216	0.12	-0.11	-0.03	-0.09	0.06	-0.08
2nn	DFT	0.12	-0.01	0.01	0.02	0.11	0.01
	P-100819	0.02	0.03	0	-0.03	0.02	0.07
	P-100826	0.04	-0.01	0.01	-0.02	-0.04	0.02
	P-100831	0.02	0.01	-0.04	0.11	0.06	0.21
	P-110307	0	-0.03	-0.02	0	-0.01	0
	P-20120216	0.04	0	0.01	0.02	0.04	0

Tab. 4-1: Binding energies calculated in the pure γ-Ni system using MD. Results are compared to DFT data [TUCKER2008]. We consider five different Fe-Ni-Cr potentials presented in Tab. IV-1.

Distance	Cohesive model	Binding energy (eV)					
		V-V	Ni-V	Cr-V	Ni-Ni	Cr-Cr	Ni-Cr
1nn	DFT	0.04 to 0.18	0.02 to 0.09	-0.09 to 0.00	-0.01 to 0.11	-0.10 to -0.01	-0.01 to 0.05
	P-100819	0.28	0.15	-0.15	0.09	-0.15	0
	P-100826	0.28	0.06	-0.04	0.01	0.04	-0.05
	P-100831	0.29	0.14	-0.15	0.10	-0.14	0
	P-110307	0.32	-0.03	-0.04	-0.01	0	-0.02
	P-20120216	0.24	0.02	0.06	-0.08	0.13	-0.01
2nn	DFT	-0.09 to 0.02	-0.01 to 0.03	-0.08 to 0.00	-0.01 to 0.07	-0.01 to 0.02	-0.03 to -0.01
	P-100819	-0.04	-0.1	-0.02	-0.07	0.03	0.01
	P-100826	-0.04	-0.02	0.02	0.03	0.06	0.06
	P-100831	-0.04	-0.09	-0.02	-0.04	0.03	0.03
	P-110307	0.09	0.03	0.01	0	0.01	0
	P-20120216	0.04	0.01	0.01	0.04	0.06	0.02

Tab. 4-2: Binding energies calculated in the pure γ-Fe system using MD. Results are compared to DFT data [KLAVER2012]. We consider five different Fe-Ni-Cr potentials presented in Tab. IV-1.

211   Annex 4. Calculation of binding energies using MD

Distance	Cohesive model	Binding energy (eV)					
		V-V	Fe-V	Cr-V	Fe-Fe	Cr-Cr	Fe-Cr
1nn	P-100819	0.02	0.09	0.19	0.09	0.09	0.12
	P-100826	0.2	0.05	0.01	0.22	0.14	0.1
	P-100831	0.02	0.21	0.32	0.16	0.13	0.2
	P-110307	0	0	0.01	0	0	0
	P-20120216	0.12	0	0.01	0	0	0.01
2nn	P-100819	0	0.01	0.02	0.09	0.07	0.16
	P-100826	0.02	0.05	0.01	0.03	0	0.06
	P-100831	0	0.02	0.01	0.2	0.13	0.29
	P-110307	0.01	0	0.01	0	0.01	0
	P-20120216	0.03	0	0	0.01	0.01	0.01

Tab. 4-3: Absolute value of the difference of binding energies calculated using MD (Tab. 4-1) and using the rigid lattice approach (Tab. IV-2), in the pure γ-Ni system. We consider five different Fe-Ni-Cr potentials presented in Tab. IV-1. Results are compared to DFT data [TUCKER2008].

Distance	Cohesive model	Binding energy (eV)					
		V-V	Ni-V	Cr-V	Ni-Ni	Cr-Cr	Ni-Cr
1nn	P-100819	0	0.07	0.01	0.01	0.01	0.01
	P-100826	0	0.01	0	0.02	0	0
	P-100831	0.01	0.07	0.01	0	0.02	0.02
	P-110307	0.02	0.01	0.01	0	0.01	0.01
	P-20120216	0.14	0.01	0	0.01	0.01	0
2nn	P-100819	0	0.01	0	0.07	0.02	0.02
	P-100826	0	0	0.01	0.01	0	0
	P-100831	0	0	0	0.09	0.02	0.03
	P-110307	0.01	0	0	0	0	0
	P-20120216	0.01	0.01	0.02	0.01	0	0

Tab. 4-4: Absolute value of the difference of binding energies calculated using MD (Tab. 4-2) and using the rigid lattice approach (Tab. IV-3), in the pure γ-Fe system. We consider five different Fe-Ni-Cr potentials presented in Tab. IV-1. Results are compared to DFT data [KLAVER2012].

List of references

[ABRAHAMS1962] S. C. Abrahams, L. Guttman, J. S. Kasper, Phys. Rev. 127 (1962) 2052.

[ABRIKOSOV2007] I. A. Abrikosov, A. E. Kissavos, F. Liot, B. Alling, S. I. Simak, O. Peil, A. V. Ruban, Phys. Rev. B 76 (2007) 014434.

[ACKLAND1997] G. J. Ackland, D. J. Bacon, A. F. Calder, T. Harry, Phil. Mag. A 75 (1997) 713.

[ACKLAND2004] G. J. Ackland, M. I. Mendelev, D. J. Srolovitz, S. Han, A. V. Barashev, J. Phys.: Condens. Matter. 16 (2004) 1.

[ADJANOR2011] G. Adjanor, M. Athènes, J. M. Rodgers, J. Chem. Phys. 135 (2011) 044127.

[ALLEN1997] T. R. Allen, G. S. Was, E. A. Kenik, J. Nucl. Mater. 244 (1997) 278−294.

[ALLEN1998A] T. R. Allen, J. T. Busby, G. S.Was, E. A. Kenik, J. Nucl. Mater. 255 (1998) 44–58.

[ALLEN1998B] T. R. Allen, G. S. Was, Acta. Metall. 46 (1998) 3679−3691.

[ALLEN2007] T. R. Allen, L. Tan, G. S. Was, E. A. Kenik, J. Nucl. Mater. 361 (2007) 174–183.

[ALLNATT1982] A. R. Allnatt, J. Phys. C 15 (1982) 5605.

[ALLNATT1983] A. R. Allnatt, A. Barbu, A. D. Franklin, A. B. Lidiard, Acta. Metall. 31 (1983) 1307.

[ALLNATT1984] A. R. Allnatt, E. L. Allnatt, Phil. Mag. A 49 (1984) 625.

[ALLNATT1987] A. R. Allnatt, A. B. Lidiard, Rep. Prog. Phys. 50 (1987) 373.

[ALLNATT1993] A. R. Allnatt, A. B. Lidiard, Atomic Transport in Solids (Cambridge University Press, 1993), p. 572.

[AL TOOQ] Z. Al Tooq, S. Kenny, PERFORM60 project (private communication).

[ANDERSEN1980] H. C. Andersen, J. Chem. Phys. 72 (1980) 2384−2393.

[ANTHONY1968] T. R. Anthony, R. E. Hanneman, Scr. Metall. 2 (1968) 611−614.

[ANTHONY1969] T. R. Anthony, Acta. Metall. 17 (1969) 603−609.

[ANTHONY1970A] T. R. Anthony, J. Appl. Phys. 41 (1970) 3969−3976.

[ANTHONY1970B] T. R. Anthony, Phys. Rev. B 2 (1970) 264.

[ANTHONY1970C] T. R. Anthony, Acta. Metall. 18 (1970) 307−314.

[ARDELL2008] A. J. Ardell, Materials Issues for Generation IV Systems, NATO Science for Peace and Security Series B: Physics and Biophysics (Springer Netherlands, 2008) pp 285−310

[ARTSISHEVSKAYA2008] L. P. Artsishevskaya, E. A. Ibragimov, Y. P. Selisski, M. N. Sorokin, Izv. Akad. Nauk. SSSR Met. 4 (1968) 158.

[ASTM1993] ASTM, Annual Book of ASTM Standards 12.02 (1993) E693–E701.

[ASTM1994] ASTM, Annual Book of ASTM Standards, 12.02 (1994) E693.

[BARASHEV2005] A. V. Barashev, Phil. Mag. 85 (2005) 1539–1555.

[BARASHEV2006] A. V. Barashev, A. C. Arokiam, Phil. Mag. Lett. 86 (2006) 321–332.

[BARBE2006] V. Barbe, doctoral thesis, Ecole Centrale des Arts et Manufactures «Ecole Centrale Paris » (2006).

[BARBE2006B] V. Barbe, M. Nastar, Phil. Mag. 86 (2006) 3503.

[BARBU1980] A. Barbu, Acta Metall. 28 (1980) 499.

[BARNARD2012] L. Barnard, J. D. Tucker, S. Choudhury, T. R. Allen, D. Morgan, J. Nucl. Mater. 425 (2012) 8−15

[BAER1958] V. H. G. Baer, Z. Metallkde. 12−49 (1958) 614−622.

[BELOVA2003] I. V. Belova, G. E. Murch, Phil. Mag. 83 (2003) 377.

[BENKADDOUR1994] A. Benkaddour, C. Dimitrov, O. Dimitrov, J. Nucl. Mater. 217 (1994) 118−126.

[BENNETT1976] C. H. Bennett, J. Comp. Phys. 22 (1976) 245.

[BLÖCHL1994] P. E. Blöchl, Phys. Rev. B 50 (1994) 17953.

[BOCQUET2002] J. Bocquet, Defect and Diffusion Forum 203−205 (2002) 81−112.

[BONNY] G. Bonny, D. Terentyev, L. Malerba, PERFORM60 project (private communication).

214   List of references

[BONNY2011A] G. Bonny, R. C. Pasianot, D. Terentyev, L. Malerba, Phil. Mag. 91 (2011) 1724.

[BONNY2011B] G. Bonny, D. Terentyev, R. C. Pasianot, S. Poncé, A. Bakaev, Modelling Simul. Mater. Sci. Eng. 19 (2011) 085008.

[BORTZ1975] A. B. Bortz, M. H. Kalos, J. L. Lebowitz, J. Comp. Phys. 17 (1975) 10.

[BURKE2007] K. Burke, The ABC of DFT (University of California, Irvine, 2007).

[BUSBY2002] J. T. Busby, G. S. Was, E. A. Kenik, J. Nucl. Mater. 302 (2002) 20.

[BYEONG−JOO1983] L. Byeong−Joo, J. Korean Inst. Metals 31 (1983) 480−489.

[CARLING2000] K. Carling, G. Wahnstrom, T. R. Mattsson, A. E. Mattsson, N. Sandberg, G. Grimvall, Phys. Rev. Lett. 85 (2000) 3862.

[CHUANG1986] Y. Chuang, K. Hsieh, A. Chang, Met. Trans. A 17A (1986) 1373.

[COSTA2012] D. Costa, doctoral thesis, Université des Sciences et Technologies de Lille (2012).

[COTTENIER2002] S. Cottenier, B. De Vries, J. Meersschaut, M Rots, J. Phys.: Condens. Matter 14 (2002) 3275–3283.

[DAMCOTT1995] D. L. Damcott, T. R. Allen, G. S. Was, J. Nucl. Mater. 225 (1995) 97−107.

[DAW1984] M. S. Daw, M. I. Baskes, Phys. Rev. B 29 (1984) 6443.

[DEDERICHS1978] P. H. Dederichs, C. Lehman, H. R. Schober, A. Scholz, R. Zeller, J. Nucl. Mater. 69&70 (1978) 176.

[DE FONTAINE1979] D. de Fontaine, solid state physics 34 (1979) 73–274.

[DELCZEG2012] L. Delczeg, B. Johansson, L. Vitos, Phys. Rev. B 85 (2012) 174101.

[DE SCHEPPER1983] L. De Schepper, D. Segers, L. Dorikens−Vanpraet, M. Dorikens, G. Knuyt, L. M. Stals, P. Moser, Phys. Rev. B 27 (1983) 5257.

[DIMELFI1980] R. J. Dimelfi, J. M. Kramer, J. Nucl. Mater. 89 (1980) 338−346.

[DIMITROV1981] C. Dimitrov, M. Tenti, O. Dimitrov, J. Phys. F: Metal Phys. 11 (1981) 753−65.

[DIMITROV1982] O. Dimitrov, C. Dimitrov, J. Nucl. Mater. 105 (1982) 39−47.

215   List of references

[DIMITROV1984] C. Dimitrov, O. Dimitrov, J. Phys. F: Metal Phys. 14 (1984) 793−811.

[DIMITROV1987] C. Dimitrov, A. Benkaddour, O. Dimitrov, C. Corbel, P. Moser, Materials Science Forum. 15−18 (1987) 1275−1280.

[DIMITROV1988] C. Dimitrov, O. Dimitrov, J. Nucl. Mater. 152 (1988) 21−29.

[DIMITROV1991] C. Dimitrov, A. Benka, C. Cor, P. Moser, Annales de chimie 16 (1991) 319−324.

[DIMITROV1993] O. Dimitrov, C. Dimitrov, B. Sitaud, Annales de chimie 18 (1993) 263−270.

[DOMAIN] C. Domain, C. S. Becquart, PERFORM60 project (private communication).

[DOMAIN2001A] C. Domain, C. S. Becquart, J. C. Van Duysen, Mater. Res. Soc. Symp. Proc. 650 (2001) R3.25.1.

[DOMAIN2001B] C. Domain, C. S. Becquart, Phys. Rev. B 65 (2001) 024103.

[DOMAIN2004] C. Domain, C. S. Becquart, J. Foct, Phys. Rev. B 69 (2004) 144112.

[DOMAIN2005] C. Domain, C. S. Becquart, Phys. Rev. B 71 (2005) 214109.

[DUDAREV2005] S. L. Dudarev, P. M. Derlet, J. Phys.: Condens. Matter 17 (2005) 1.

[DUH1998] T. S. Duh, J. J. Kai, F. R. Chen, L. H. Wang, J. Nucl. Mater. 258−263 (1998) 2064.

[DUH2001] T. S. Duh, J. J. Kai, F. R. Chen, L. H. Wang, J. Nucl. Mater. 294 (2001) 267.

[EHRHART1974] P. Ehrhart, H. G. Haubold, W. Schilling, Adv. in Sol. State Phys. XIV, 87 (1974).

[EHRHART1991] P. Ehrhart, Atomic Defects in Metals (Springer−Verlag, Berlin, New York, 1991), 25, p. 88.

[EYRING1931] H. Eyring, M. Polanyi, Zeitschrift fur Physikalische Chemie 12 (1931) 279.

[EYRING1935] H. Eyring, J. Chem. Phys. 3 (1935) 107.

[FAULKNER1982] J. S. Faulkner, Prog. Mater. Sci. 27 (1982) 1.

[FORSCH1974] K. Forsch, J. Hemmerich, H. Knoell, G. Lucki, Phys. Status Solidi A 23 (1974) 223.

[FRENKEL1996] D. Frenkel, B. Smit, Academic Press (1996).

[FUKUYA2004] K. Fukuya, M. Nakano, K. Fujii, T. Torimaru, J Nucl Sci Technol. 41 (2004) 594.

[FURDERER1987] K. Fürderer et al., Mater. Sci. Forum 15–18 (1987) 125.

[GEAR1971] C. W. Gear, Numerical initial value problems in ordinary differential equations, Prentice−Hall, Englewood, NJ (1971).

[GRANJEAN1994] Y. Grandjean, P. Bellon, G. Martin. Phys. Rev. B 50 (1994) 4228.

[GRANJEAN1995] Y. Grandjean, doctoral thesis, Université de Paris VII, 1995.

[GRUJICIC1993] M. Grujicic, X. W. Zhou, Calphad 17 (1993) 383.

[HACKETT2009A] M. J. Hackett, J. T. Busby, M. K. Miller, G. S. Was, J. nucl. Mater. 389 (2009) 265−278.

[HACKETT2009B] M. J. Hackett, R. Najafabadi, G. S. Was, J. nucl. Mater. 389 (2009) 279−287.

[HAFNER2001] R. Hafner, D. Spisák, R. Lorenz, J. Hafner, J. Phys.: Cond. Matter 13 (2001) L239.

[HAFNER2002] R. Hafner, D. Spisák, R. Lorenz, J. Hafner, Phys. Rev. B 65 (2002) 184432.

[HERPER1999] H. C. Herper, E. Hoffmann, P. Entel, Phys. Rev. B 60 (1999) 3839.

[HILLERT1990] M. Hillert, C. Qiu, Met. Trans. A 21A (1990) 1673−1680.

[HILLERT1991] M. Hillert, C. Qiu, Met. Trans. A 22A (1991) 2187−2198.

[HINES2009] W. A. Hines, P. Shanthakumar, T. Huang, J. I. Budnick, R. L. Miller, D. M. Pease, D. M. Perry, Phys. Status Solidi B 246 (2009) 2154−2158.

[HOHENBERG1964] P. Hohenberg, W. Kohn, Phys. Rev. B 136 (1964) B864.

[HUGUENIN1987] D. Huguenin, A. Berroudji, C. Mairy, F. Vanoni, J. Hillairet, Materials Science Forum 15−18 (1987) 1269−1274.

[HUGUENIN1989] D. Huguenin, P. Moser, F. Vanoni, J. nucl. Mater. 169 (1989) 73−78.

[JANOTTI2004] A. Janotti, M. Krcmar, C. L. Fu, R. C. Reed, Phys. Rev. Lett. 92 (2004) 85901.

[JIANG2003] D. E. Jiang, E. A. Carter, Phys. Rev. B 67 (2003) 214103.

[JIN2012] S. Jin, L. Guo, F. Luo, Z. Yao, S. Ma, R. Tang, scripta mater. 68 (2013) 138.

[JOHNSON1976] R. A. Johnson, N. Q. Lam, Phys. Rev. B 13 (1976) 4364.

217   List of references

[KAI2004] J. J. Kai, F. R. Chen, T. S. Duh, Mater. Trans. 45 (2004) 40.

[KATO1992] T. Kato, H. Takahashi, M. Izumiya, J. Nucl. Mater. 189 (1992) 167−174.

[KARMAZIN1982] L. Karmazin, Mat. Sci. Eng. A 54 (1982) 247−256.

[KENIK2012] E. A. Kenik, J. T. Busby, Mat. Sci. Eng. R 73 (2012) 67–83.

[KING1966] H. W. King, J. Mater. Sci. 1 (l966) 79.

[KINOSHITA1996] H. Kinoshita, S. Watanabe, S. Mochizuki, N. Sakaguchi, H. Takahashi, J. nucl. Mater. 239 (1996) 205−209.

[KJELLQVIST2008] L. Kjellqvist, M. Selleby, B. Sundman, Calphad, 32 (2008) 577−592.

[KLAVER2006] T. P. C. Klaver, R. Drautz, M. W. Finnis, Phys. Rev. B 74 (2006) 094435.

[KLAVER2012] T. P. C. Klaver, D. J. Hepburn, G. J. Ackland, Phys. Rev. B 85 (2012) 174111.

[KOIWA1983] M. Koiwa, S. Ishioka, Phil. Mag. A 47 (1983) 927.

[KONG2006] L. T. Kong, B. X. Liu, J. Alloys and Comp. 414 (2006) 36−41.

[KRCMAR2005] M. Krcmar, C. L. Fu, A. Janotti, R. C. Reed, Acta Mater. 53 (2005) 2369.

[KRESSE1993] G. Kresse, J. Hafner, Phys. Rev. B 47 (1993) 558.

[KRESSE1994] G. Kresse, J. Hafner, Phys. Rev. B 49 (1994) 14251.

[KRESSE1996A] G. Kresse, J. Furthmüller, Phys. Rev. B 54 (1996) 11169.

[KRESSE1996B] G. Kresse, J. Furthmüller, Comput. Mater. Sci. 6 (1996) 15.

[KRESSE1999] G. Kresse, D. Joubert, Phys. Rev. B 59 (1999) 1758.

[LAM1981] N. Q. Lam, H. Wiedersich, J. nucl. Mater. 103 (1981) 433.

[LAM1982] N. Q. Lam, A. Kumar, H. Wiedersich, Effects of Radiation on Materials: Eleventh Conf., eds., H.R. Brager and J.S. Perrin (ASTM STP782, American Society for Testing and Materials, 1982) p. 985.

[LE BOUAR2002] Y. Le Bouar, F. Soisson, Phys. Rev. B 65 (2002) 094103.

[LECLAIRE1956] A. D. LeClaire, A. B. Lidiard, Philos. Mag. 1 (1956) 518.

218   List of references

[LIDIARD1955] A. B. Lidiard, Philos. Mag. 46 (1955) 1218.

[LULA1986] R. A. Lula, J. G. Parr, A. Hanson, Stainless Steel (American Society for Metals, Ohio, Metals Park, 1986).

[MAIER1978] K. Maier, H. Metz, D. Herlach, H. E. Schaefer, J. Nucl. Mater. 69−70 (1978) 589.

[MAJUMDAR1983] A. K. Majumdar, P. V. Blanckenhagen, J. Magn. Mater. 40 (1983) 227.

[MAJUMDAR1984] A. K. Majumdar, P. V. Blanckenhagen, Phys. Rev. B 29 (1984) 4079.

[MALERBA2006] L. Malerba, J. Nucl. Mater. 351 (2006) 28−38.

[MALERBA2010] L. Malerba, M. C. Marinica, N. Anento, C. Björkas, H. Nguyen, C. Domain, F. Djurabekova, P. Olsson, K. Nordlund, A. Serra, D. Terentyev, F. Willaime, C. Becquart, J. Nucl. Mater. 406 (2010) 19−38.

[MANNING1959] J. R. Manning, Phys. Rev. 116 (1959) 819.

[MANNING1962] J. R. Manning, Phys. Rev. 128 (1962) 2169.

[MANNING1964] J. R. Manning, Phys. Rev. 136 (1964) 1758.

[MARUCCO1994] A. Marucco, Mat. Sci. Eng. A 189 (1994) 267−276 .

[MARWICK1978] A. D. Marwick, J. Phys.: Metal. Phys. 8 (1978) 1849−1861.

[MAZIASZ1993] P. J. Maziasz, J. Nucl. Mater. 205 (1993) 118−145.

[MATTER1979] H. Matter, J. Winter, W. Triftshäuser, Appl. Phys. 20 (1979) 135.

[MATTSSON2002] T. R. Mattsson, A. E. Mattsson, Phys. Rev. B 66 (2002) 214110.

[MENDELEV2003] M. I. Mendelev, A. Han, D. J. Srolovitz, G. J. Ackland, D. Y. Sun, M. Asta, Phil. Mag. A 83 (2003) 3977.

[METHFESSEL1989] M. Methfessel and A. T. Paxton, Phys. Rev. B 40 (1989) 3616.

[METROPOLIS1949] N. Metropolis, S. Ulam, J. Am. Stat. Assoc. 44 (1949) 335.

[METROPOLIS1953] N. Metropolis, A. W. Rosenbluth, M. N. Rosenbluth, A. H. Teller, E. J. J. Teller, Chem. Phys. 21 (1953) 1087.

[MEYERHEIM2005] H. L. Meyerheim, R. Popescu, D. Sander, J. Kirschner, Phys. Rev. B 71 (2005) 035409.

219 List of references

[MIETINNEN1999] J. Mietinnen, Calphad, 23 (1999) 231−348.

[MILLION1981] B. Million , J. Ruzickova, J. Velisek, J. Vrestal, Mat. Sci. Eng. 50 (1981) 43−52.

[MILLION1985] B. Million, J. Ruzickova, J. Velisek, Mater. Sci. Eng 72 (1985) 85.

[MISHIN2004] Y. Mishin, Acta Mater. 52 (2004) 1451.

[NAKATA1987] K. Nakata, I. Masaoka, J. Nucl. Mater. 150 (1987) 186.

[NASH1991] P. Nash, Binary Alloy Phase Diagrams 2 (T .B. Massalski, ASM Inter., Ohio, 1991) pp 1298−1302.

[NASTAR1998] M. Nastar, P. Bellon, G. Martin, J. Ruste, Proc. Mater. Res. Soc. Symposium 481 (1998) 383.

[NASTAR2000] M. Nastar, V. Yu. Dobretsov, G. Martin, Phil. Mag. A 80 (2000) 155.

[NASTAR2005] M. Nastar, Phil. Mag. 85 (2005) 641−647.

[NASTAR2012] M. Nastar, F. Soisson, Comprehensive Nuclear Materials 1 (2012) 471−496.

[NORGETT1975] M. J. Norgett, M. T. Robinson, I. M. Torrens, Nucl. Eng. Des. 33 (1975) 50−54.

[NOSE1984A] S. Nose, J. Chem. Phys. 81 (1984) 511.

[NOSE1984B] S. Nose, Molec. Phys. 52 (1984) 255.

[OLSSON2006] P. Olsson, I. A. Abrikosov, J. Wallenius, Phys. Rev. B 73 (2006) 104416.

[OLSSON2005] P. Olsson, J. Wallenius, C. Domain, K. Nordlund, L. Malerba, Phys. Rev. B 72 (2005) 214119.

[OLSSON2007] P. Olsson, C. Domain, J. Wallenius, Phys. Rev. B 75 (2007) 014110.

[OLSSON2010] P. Olsson, T. P. C. Klaver, C. Domain, Phys. Rev. B 81 (2010) 054102.

[OKAMOTO1973] P. R. Okamoto, S. D. Harkness, J. J. Laidler, Trans. Am. Nucl. Soc. 16 (1973) 70.

[OKAMOTO1974] P.R. Okamoto, H. Wiedersich, J. Nucl. Mater. 53 (1974) 336.

[OKAMOTO1979] P. R. Okamoto, L. E. Rehn, J. Nucl. Mater. 83 (1979) 2−23.

[OKAMURA1983] Y. Okamura, A. R. Alnatt, J. Phys. C 16 (1983) 1841.

[PECHENKIN1999] V. A. Pechenkin, I. A. Stepanov, Mater. Sci. Forum 294–296 (1999) 771.

[PERDEW1981] J. P. Perdew, A. Zunger, Phys. Rev. B 23 (1981) 5048.

[PERDEW1991] J. P. Perdew, Electronic Structure of Solids, Akademie Verlag, Berlin (1991).

[PERDEW1992] J. P. Perdew, Y. Wang, Phys. Rev. B 45 (1992) 13244.

[PERDEW1996] J. P. Perdew, K. Burke, M. Ernzerhof, Phys. Rev. Lett. 77 (1996) 3865.

[PERKS1986] J. M. Perks, A. D. Marwick, C. A. English, AERE R (1986) 12121.

[PITKÄNEN2009] H. Pitkänen, M. Alatalo, A. Puisto, M. Ropo, K. Kokko, M. P. J. Punkkinen, P. Olsson, B. Johansson, S. Hertzman, L. Vitos, Phys. Rev. B 79 (2009) 024108.

[POSTNIKOV2003] A. V. Postnikov, P. Entel, J. M. Soler, Eur. Phys. J. D 25 (2003) 261.

[RAYNOR1988] G. V. Raynor, V. G. Rivlin, Cr−Fe−Ni Phase Equilibria in Iron Ternary Alloys (Institute of Metals, London, 1988) p 316−332.

[REDLICH1948] O. Redlich, A. Kister, Ind. Eng. Chem. 40 (1948) 345.

[REHN1978] L.E. Rehn, P.R. Okamoto, D.I. Potter, H. Wiedersich, J. Nucl. Mater. 74 (1978) 242.

[ROTHMAN1980] S. J. Rothman, L. J. Nowicki, G. E. Murch, J. Phys. F: Metal Phys. 10 (1980) 383.

[RUICKOVA1981] J. Ruickova, B. Million. Mat. Sci. Eng. 50 (1981) 59.

[SAKAGUCHI2004] N. Sakaguchi, S. Watanabe, H. Takahashi, R. G. Faulkner, J. Nucl. Mater. 329–333 (2004) 1166–1169

[SCHAEFER1977] H. E. Schaefer, K. Maier, M. Weller, D. Herlach, H. Seeger, J. Diehl, Scripta Metall. 11 (1977) 803.

[SCHILLING1978] W. Schilling, J. Nucl. Mater. 69−70 (1978) 465−489.

[SCHMAUDER2002] S. Schmauder, P. Binkele, Comput. Mater. Sci. 24 (2002) 42.

[SEEGER1998] A. Seeger, Phys. Stat. Sol. A 167 (1998) 289.

[CHOUDHURY2011] S. Choudhury, L. Barnard, J. D. Tucker, T. R. Allen, B. D. Wirth, M. Asta, D. Morgan, J. Nucl. Mater. 411 (2011) 1‑14

[SIMONEN1999] E. P. Simonen, S. M. Brunemmer, Materials Science Forum 294−296 (1999) 755−758.

221   List of references

[SMEDSKJAER1981] L. C. Smedskjaer, M. J. Fluss, D. G. Legnini, M. K. Chason, R. W. Siegel, J. Phy. F 11 (1981) 2221.

[SMITH1989] R. W. Smith, G. S. Was, Phys. Rev. B 40 (1989) 10322.

[SOISSON1996] F. Soisson, A. Barbu, G. Martin, Acta Mater. 44 (1996) 3789.

[SOISSON2000] F. Soisson, G. Martin, Phys. Rev. B 62 (2000) 203.

[SPIŠÁK2000] D. Spišák, J. Hafner, Phys. Rev. B 61 (2000) 16129.

[SPIŠÁK2002] D. Spišák, J. Hafner, Phys. Rev. Lett. 88 (2002) 056101.

[STEPANOV2004] I. A. Stepanov, V. A. Pechenkin, Y. V. Konobeev, J. Nucl. Mater. 329–333 (2004) 1214–1218.

[STRAALSUND1974] J. L. Straalsund, J. F. Bates, Metallur. Trans. 5 (1974) 493.

[TABATA1981] T. Tabata, H. Fujita, H. Ishii, K. Igaki, M. Isshik, Scripta Metall. 15 (1981) 1317.

[TERENTYEV2008] D. A. Terentyev, T. P. C. Klaver, P. Olsson, M. C. Marinica, F. Willaime, C. Domain, L. Malerba, Phys. Rev. Lett. 100 (2008) 145503.

[TERENTYEV2011] D. Terentyev, X. He, E. Zhurkin, A. Bakaev, J. Nucl. Mater. 408 (2011) 161–170.

[TREGLIA1988] G. Tréglia, B. Legrand, F. Ducastelle, Europhys. Lett. 7 (1988) 575.

[TSUNODA1989] Y. Tsunoda, J. Phys.: Condens. Matter 1 (1989) 10427.

[TSUNODA2009] Y. Tsunoda, H. Nogami, M. Takasaka, Phys. Rev. B 76 (2007) 054419.

[TUCKER2008] J. D. Tucker, doctoral thesis, University of Wisconsin−Madison (2008).

[TUCKER2010] J. D. Tucker, R. Najafabadi, T. R. Allen, D. Morgan, J. Nucl. Mater. 405 (2010) 216.

[VINCENT2006A] E. Vincent, doctoral thesis, Université des Sciences et Technologies de Lille (2006).

[VINCENT2006B] E. Vincent, C. S. Becquart, C. Domain, J. Nucl. Mater. 351 (2006) 88.

[VINCENT2008] E. Vincent, C. S. Becquart, C. Domain, C. Pareige, P. Pareige, J. Nucl. Mater. 373 (2008) 387.

[VITOS2003] L. Vitos, P. A. Korzhavyi, B. Johansson, Nat. Mater. 2 (2003) 25.

[VITOS2006] L. Vitos, P. A. Korzhavyi, B. Johansson, Phys. Rev. Lett. 96 (2006) 117210.

[VITOS2009] L. Vitos, B. Johansson, Phys. Rev. B 79 (2009) 024415.

[VOLGIN2012] A. Volgin, doctoral thesis, Université de Rouen (2012).

[VOSKO1980] S. H. Vosko, L. Wilk, M. Nusair, Can. J. Phys. 58 (1980) 1200.

[WAS1992] G. S. Was and P. L. Andresen, JOM 44 (1992) 8.

[WAS1994A] G. S. Was, T. Allen, Mater. Charact. 32 (1994) 239.

[WAS1994B] G. S. Was, S. M. Bruemmer, J. Nucl. Mater. 216 (1994) 326.

[WATANABE1997] S. Watanabe, N. Sakaguchi, K. Kurome, M. Nakamura, H. Takahashi, J. Nucl. Mater. 240 (1997) 251.

[WATANABE2000A] S. Watanabe, Y. Takahashi, Jour. de Phys. IV (2000) Pr6−173.

[WATANABE2000B] S. Watanabe, Y. Takamatsu, N. Sakaguchi, H. Takahashi, J. Nucl. Mater. 283–287 (2000) 152.

[WIEDERSICH1979] H. Wiedersich, P. R. Okamoto, N. Q. Lam, J. Nucl. Mater. 83 (1979) 98−108.

[WIDOM1963] B. Widom, J. Chem. Phys. 39 (1963) 2802.

[WIMMER2008] E. Wimmer, W. Wolf, J. Sticht, P. Saxe, C. B. Geller, R. Najafabadi, G. A. Young, Phys. Rev. B 77 (2008) 134305.

[WIRTH1999] B. D. Wirth, G. R. Odette, Mater. Res. Soc. Symp. Proc. 540 (1999) 637.

[WOLLENBERGER1983] H. J. Wollenberger, Physical Metallurgy Chapter 17: Point Defects, edited by R. W. Cahn and P. Haasen (North Holland Physics Publishing, 1983) Part II, pp. 1139−221.

[YOUNG1966] W. M. Young, E. W. Elcock, Proc. Phys. Soc. 89 (1966) 735.

[YOUNG1978] F. W. Young Jr., J. Nucl. Mater. 69&70 (1978) 310−330.

[ZOUARI2012] M. Zouari, doctoral thesis, Université de Grenoble (2012).

[ZUNGER1990] A. Zunger, S. H. Wei, L. G. Ferreira, J. E. Bernard, Phys. Rev. Lett. 65 (1990) 353.

[ZHURKIN] E. Zhurkin, M. Hou, PERFORM60 project (private communication).

[ZHURKIN2011] E. Zhurkin, D. Terentyev, M. Hou, L. Malerba, G. Bonny, J. Nucl. Mater. 417 (2011) 1082–1085.

223   List of references